Speed and Contrast in Magnetic Resonance Imaging

David W. Carmichael

University College London,

Department of Medical Physics and Bioengineering,

London, U.K.

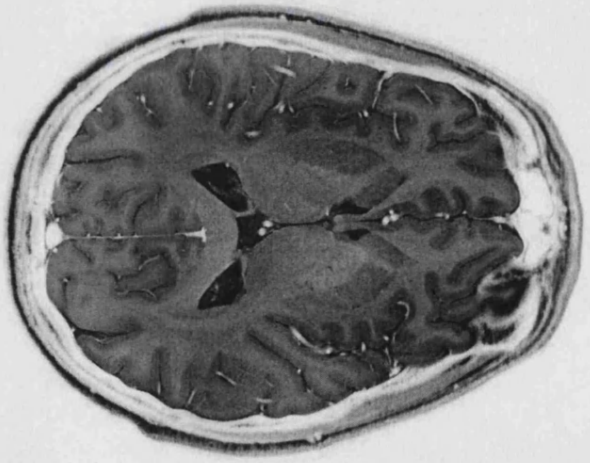

PhD Thesis

Submitted for Doctor of Philosophy Degree

November 2003

ProQuest LLC
789 East Eisenhower Parkway
P.O. Box 1346
Ann Arbor, MI 48106-1346

Abstract

The four main projects presented in this thesis investigate different aspects of speed and contrast in MRI.

Firstly, a new method called SPENT is described that is used to investigate the homogeneity of tissue. The resulting images appear bright in regions where pixel's underlying magnetisation is non-uniform and dark in regions where it is uniform. The aim of this section is to investigate the contrast produced using SPENT images and evaluate their potential for obtaining structural information beyond that normally available.

Secondly, the structure and strength of bone as predicted using MRI is compared to Young's Modulus, a measure of biomechanical strength, and bone mineral density measured by DEXA. Direct MR-image based structural assessment of excised trabecular bone samples is compared to the relaxation parameters (R_2 / R_2') and SPENT for the determination of bone strength.

Thirdly, a 200MHz / 4.7 T multiple receiver coil is evaluated for its Signal to Noise Ratio (SNR) performance both for standard and parallel imaging. This entails the development of software for accurate mapping of coil sensitivity, SNR estimation and for combining the images from each array coil element. The software and coil developed are shown to enable a reduction in imaging time using the SENSE (SENSitivity Encoding) technique. Fast Spin Echo (FSE) images are presented demonstrating the array coil used at 4.7 T obtains in vivo images of humans with improved quality.

Finally, new pulse sequences are presented that produce multiple images in rapid succession. These multiple images are acquired with a reduced data matrix that corresponds to several shorter periods of data acquisition. The multiple images are combined to produce full matrix images. The most promising application for these techniques is in improving the performance of Gradient Echo-Echo Planar Imaging (GE-EPI) at high field. Segmenting the acquisition in this way provides an increase in image quality without many of the problems associated with other methods to segment the EPI acquisition.

Foreword

Before continuing further I have to acknowledge the help and support of many people.

I would not have started, let alone finished this PhD if it were not for Roger Ordidge. He has always been prepared to help me, not only with this project, but both personally and academically for the past 5 years. For his ideas, incite, enthusiasm, patience and kindness I will always be grateful.

I have also been fortunate to be surrounded by a great number of people from UCL who have given their time and assistance over the last three years. Firstly, in the Bloomsbury Laboratory, both Andrew Priest and Alan Bainbridge started working when I commenced my PhD. I have learnt a lot from both of them, and I am thankful for their help over the last 3 years. We were all lucky to have joined John Thornton, who has also provided me with a good deal of help and prudent advice, as have Ern Cady, Daniel West and Quyen Nguyen. I must thank Marios Yiannakas from City University for all his time, effort and good humour during hours spent in the basement. Secondly, from the Wellcome High Field Laboratory, it has been great to have the experience of Dave Thomas, Harry Parkes, Paul Kinchesh and recently Maria Fernandez-Seara to call on in addition to that of Bob Turner my second supervisor. I must particularly mention Enrico De Vita, my fellow PhD student, who has been tireless both in his own work and in assisting me with mine. Enrico has provided good company with Karin Shmueli and Oli Gearing for my time in the other basement. I must also thank Billy Raven, Stewart Morrison and Denzil Booth from the Medical Physics workshop who have helped me make all sorts of bits of equipment.

Finally, a special mention must go to my parents for their love and support over the last quarter of a century and to Emilie for everything, I could not have done it without you.

Contents

List of Figures

List of Tables

1. Introduction

In this chapter the development of Nuclear Magnetic Resonance (NMR) and its use for taking images, normally called Magnetic Resonance Imaging (MRI), is briefly summarised. The aims of the work presented here are then outlined within this context.

1.1 The Development of MRI

In 1946 Bloch [1] and Purcell [2] discovered that some atomic nuclei were able to resonantly absorb and subsequently emit radiation when placed in a magnetic field. The resonant frequencies were characteristic of the nuclei observed and proportional to the strength of the magnetic field used. Soon after this, it was found that observable nuclei in different molecules resonated at different frequencies due to their different chemical environments. This phenomenon, reported by Proctor and Yu [3] and Dickinson [4], was able to determine not only which molecules were present in a sample but also their relative concentrations. Magnetic Resonance Spectroscopy (MRS) has subsequently become vital for the non-invasive investigation of molecular structure and concentration both in vivo and in vitro. In 1976, over twenty-five years after Bloch and Purcell's original discovery, Lauterbur first used the principles of NMR to take an image [5]. Smaller magnetic fields with linear gradients were used to encode spins with a variation in frequency and phase that depended linearly on position; Magnetic Resonance Imaging (MRI) was born. MRI quickly progressed with the first in vivo human image produced by a group in Nottingham in 1976 [6] led by Mansfield. Both Lauterbur and Mansfield received the Nobel Prize in 2003 for their contribution to the development of MRI. Due to the relatively low strength of the NMR signal only the most abundant NMR visible nucleus, Hydrogen (^{1}H), has been used routinely used for medical imaging. While recent advances have been made in imaging other nuclei [7] it is exclusively ^{1}H MRI that is described here. One of the great strengths of ^{1}H MRI is that the different physical properties of tissue in the body can be used to produce a range of contrast levels, making different tissue easily differentiated. While the abundance of water within tissue can provide some of this contrast, the environment of the observed ^{1}H nuclei provides extra sensitivity that can be manipulated through various parameters.

Very briefly, these include T_1, $T_1\rho$, T_2, T_2*, Diffusion Weighted Imaging (DWI) and Magnetisation Transfer (MT) that respectively give sensitivity to spin-lattice relaxation that changes with molecular environment, spin-spin relaxation dependant on how free water is to move, local magnetic fields, how free water is to diffuse in a given direction and how energy is transferred between bound and free water.

1.2 The Limitations of MRI

A continued need has been found for increasing the speed of MRI image acquisition. In recent years imaging of the heart and bowels has become possible, because these systems are constantly moving, an image must be taken in a period that allows little movement. The challenge of observing these dynamic systems has spurred the development of faster imaging sequences and hardware.

One new application for rapid imaging is functional MRI (fMRI) where a local change in blood volume and oxygenation causes a change in local magnetic fields (seen in T_2* contrast changes) called Blood Oxygenation Level Dependent contrast (BOLD) [8,9]. The observation of this regional change with time can be used to chart brain activity. This necessitates the acquisition of images over most of the brain every few seconds for an extended period. Hence the repetition speed of the scans needs to be maximised, while achieving the best possible sensitivity to the small changes in T_2*. BOLD contrast is increased by the use of higher field magnets however image quality can suffer. The challenge is to maintain the level of image quality while increasing the sensitivity to BOLD afforded by higher fields; this may be achieved through more rapid image acquisition or via several shorter periods of image acquisition in a similar time period.

Time is often the biggest limitation in MRI. Fourier encoding, first introduced by Lauterbur [5], has proved a very efficient technique, but it necessitates the acquisition of data while a series of magnetic field gradients are applied. The time Fourier encoding requires limits the speed of image formation. Both targeting less information, and increasing the information gathered in a given time, can be used to increase speed. Both of these aspects of time saving are investigated in this work.

A continued need for changing the contrast in an MRI image has been also found. The ability to see a difference between tissues, or between the same tissue at different points through development or disease has applications in medicine [10]. Recent advances include diffusion weighted imaging where the signal is sensitised to the diffusion of water through a sample [11-13]. This technique is the earliest indicator of tissue at risk in neonatal hypoxic-ischaemia and stroke [14-16]. Thus, any new way of using MRI to better characterise tissue is important. As MRI scanners become more widely available, the ability to characterise tissue that is normally investigated clinically with other methods (often using invasive techniques and ionising radiation) is an important goal. MRI / MRS allows the non-invasive measurement of many conditions, providing a unique tool to safely diagnose, and monitor disease in vivo.

1.3 Outline and Aims

In chapter 2, an outline of NMR theory and MRI principles are given. This chapter draws on the well-established work of many others and so is kept brief. The aim of this chapter is to introduce and summarise the basic theory of NMR and MRI that will be used throughout the thesis.

In chapter 3, a new method called SPENT (Sub Pixel Enhancement of Non-uniform Tissue) is described, which is used to investigate the homogeneity of tissue. The resulting images have bright pixels in regions where the underlying magnetisation is non-uniform, and dark pixels in regions where the underlying magnetisation is uniform. This contrast, sensitive to sub-pixel structure is achieved through the application of an extra linear magnetic field gradient during a 2DFT pulse sequence, or, through filtering the acquired (time domain) signal. The aim of this chapter is to investigate the contrast produced in SPENT images and evaluate its potential for obtaining structural information not normally available from an object.

Rather than producing different 'contrast' in images, SPENT obtains images that are sensitive to structures of a certain size. If these images can directly give information on structure, normally only available through a full image acquisition followed by image processing, then a saving in time both in image acquisition and in post processing could be realised.

In chapter 4, the structure and strength of bone is investigated using MRI in excised human samples. This is compared to the Young's Modulus, a measure of biomechanical strength, and Bone Mineral Density (BMD) obtained from the same samples. In vivo, BMD is commonly measured using Dual Energy X-ray Absorptiometry (DEXA), which uses ionising radiation and is limited in accuracy because it can only measure 'area' density as opposed to the 'true' density from within a volume. The key question for this section is whether MR parameters can be used to predict bone strength as accurately as DEXA without the drawbacks? Bone structure is beyond the resolution normally available on clinical machines and so MR-image based structural assessment of trabecular bone has proved difficult. Both SPENT and the relaxation parameters

(R_2/R_2') are investigated as a way of determining bone strength without requiring high resolution or highly uniform images.

In chapter 5, a 200MHz / 4.7 T multiple receiver coil is evaluated for its Signal to Noise Ratio (SNR) performance both for standard and parallel imaging. An increase in SNR provides better image quality. When combined with a high field strength array coils form part of a more sensitive system for signal detection. This extra sensitivity to signal (increased SNR) is used to obtain Fast Spin Echo (FSE), in vivo images of humans with increased resolution and improved quality. Alternatively, the array coils can be used to trade some of the SNR for increased speed. This is important at high field where some imaging techniques improve in image quality with shorter acquisition periods. This entailed the development of software for accurate mapping of coil sensitivity, SNR estimation and for combining the multiple images. The software and coil developed are shown to enable an imaging time reduction using the SENSE (SENSitivity Encoding) technique.

In chapter 6, the aim is to introduce a number of novel ways to produce multiple images in rapid succession. Different variations in spatial sensitivity to the signal from an object are deliberately imposed on the multiple images obtained. The multiple images can be acquired with a reduced data matrix that corresponds to several shorter periods of data acquisition. The multiple reduced data matrices are combined in various ways to produce full matrix images with the variations in sensitivity removed. The main advantage of these techniques lies in applications where several shorter periods of data acquisition (as opposed to a single longer acquisition) saves time or enhances image

quality. The most promising application is in improving the performance of Gradient Echo-Echo Planar Imaging at high field.

In chapter 7, a summary of the thesis and its main conclusions are given with particular reference to the future development of the work presented here.

1.4 References

1. Bloch, F., Hansen, W. W., & Packard, M. 1946, "Nuclear induction", *Physical Review*, vol. 69, p. 127.

2. Purcell, E. M., Torrey, H. C., & Pound, R. V. 1946, "Resonance absorption by nuclear magnetic moments in a solid", *Physical Review*, vol. 69, p. 37.

3. Proctor, W. G. & Yu, F. C. 1950, "The dependence of a nuclear magnetic resonance frequency upon chemical compound", *Physical Review*, vol. 77, p. 717.

4. Dickinson, W. G. 1950, "Dependence of the 19F nuclear resonance position on chemical compound", *Physical Review*, vol. 77, p. 736.

5. Lauterbur, P. 1973, "Image formation by induced local interactions: examples employing nuclear magnetic resonance", *Nature*, vol. 242, pp. 190-191.

6. Mansfield, P. and Maudsley, A. A. 1976, "Planar and line-scan spin imaging by NMR.", *Proc.19th AMPERE congress, Heidelberg*, vol. 247-252.

7. Foster, M. A. & Hutchison, J. M. S. 1987, *Practical NMR imaging* IRL Press, Oxford.

8. Ogawa, S., Lee, T. M., Kay, A. R., & Tank, D. W. 1990, "Brain magnetic resonance imaging with contrast dependent on blood oxygenation", *Proceedings Of The National Academy Of Sciences Of The United States Of America*, vol. 87, pp. 9868-9872.

9. Turner, R. & Ordidge, R. J. 2000, "Technical challenges of functional magnetic resonance imaging", *IEEE Eng Med Biol.Mag.*, vol. 19, no. 5, pp. 42-54.

10. Gadian, D. G. 1995, *NMR and its applications to living systems*, 2nd edn, Oxford University Press, Oxford.

11. Torrey, H. C. 1956, "Bloch equations with diffusion terms", *Physical Review*, vol. 104, no. 3, pp. 563-565.

12. Stejskal, E. O. 1965, "Use of spin echoes in a pulsed magnetic field gradient to study anisotropic, restricted diffusion and flow", *Journal of Chemical Physics*, vol. 43, no. 10, pp. 3597-3603.

13. Le Bihan, D., Breton, E., Lallemand, D., Grenier, P., Cabanis, E., & Laval-Jeantet, M. 1986, "MR imaging of intravoxel incoherent motions: application to diffusion and perfusion in neurologic disorders", *Radiology*, vol. 161, pp. 401-407.

14. Moseley, M. E., Cohen, M. S., Mintorovich, J., Chileuit, L., Shimizu, H., Kucharczyk, J., Wendland, M. F., & Weinstein, P. R. 1990, "Early detection of regional cerebral ischaemia in cats: comparison

of diffusion- and T2-weighted magnetic resonance imaging and spectroscopy", *Magnetic Resonance In Medicine*, vol. 14, pp. 330-346.

15. Le Bihan, D. & Turner, R. 1992, "Diffusion and perfusion," in *Magnetic Resonance Imaging*, 2nd edn, vol. 1 D. D. Stark & W. G. Bradley, eds., Mosby, St Louis, pp. 335-371.

16. Thornton, J. S., Ordidge, R. J., Penrice, J., Cady, E. B., Amess, P. N., Punwani, S., Clemence, M., & Wyatt, J. S. 1997, "Anisotropic water diffusion in white and gray matter of the neonatal piglet brain before and after transient hypoxia-ischaemia", *Magnetic Resonance In Medicine*, vol. 15, no. 4, pp. 433-440.

2. Theory of NMR and MRI

In this chapter an outline of NMR theory and MRI principles are given. This section is kept brief because the subject matter is well established and has been summarised by, amongst others, Brown and Semelka [1], Haacke et al [2], Cady [3], Webb [4], Gadian [5] and Foster and Hutchison [6].

2.1 Simple Spin Physics

2.1.1 Spin

All fundamental particles such as electrons share a quantum mechanical property called 'spin'. While this property is not fully explained by any classical analogue, it can be described as a magnetic dipole arising from the rotation of a charged particle about a principal axis. For this reason, it is termed magnetic angular momentum. Electrons and quarks, the particles that make up atoms, all have spin (S) of ½ and a particle with spin ½ can have spin states (m_z) of +½ (↑) or –½ (↓).

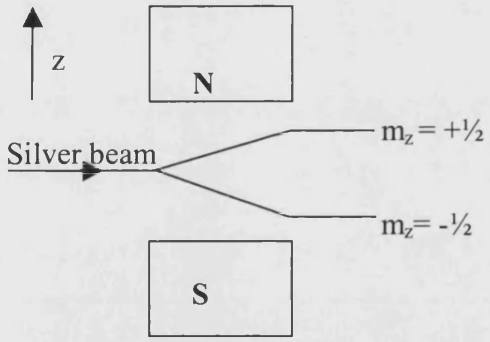

Figure 2.1 Stern and Gerlach Experiment
A beam of silver ions is split by a magnetic field due to the spin of its outer electron.

Stern and Gerlach first demonstrated this in a classic experiment where a beam of silver ions, with a single electron in their outer shells, was split by an inhomogeneous magnetic field. The ions formed two discrete beams corresponding to the two spin states that the outer electron of the atom may take up. Each of the spin states forms a discrete energy level when the ions are placed in a magnetic field.

2.1.2 Nuclear Spin

The spin of the many electrons around an atomic nucleus adds up to give a total spin for the atom. The spin of the various quarks that make up nucleons (i.e. protons and

neutrons) also add up to give a total spin; this property 'isospin' exhibits very similar behaviour to spin. Nucleons all have isospin (I) of ½ with the directional component (I_z) of ±½. Atomic nuclei can be examined in terms of their net spin angular momentum, a sum of their constituent nucleon isospin. The nuclei fall into three main categories: Firstly, nuclei with even numbers of protons and nucleons have I=0, no energy level splitting and no NMR signal. Secondly, atomic nuclei with even numbers of nucleons and an odd number of protons have I=integer and give short lived, more complex NMR signals. Lastly, nuclei with an odd number of nucleons have I=½ integer; these are NMR visible and behave in an analogous way to the silver ion where only the single outer electron contributes to the net spin. The nucleus is made up of constituent particles that move around. This means that a nucleus can have orbital angular momentum in addition to spin angular momentum. The combined property is termed the nuclear angular momentum (J) and has the dependence on the nuclear quantum number (I) shown below.

$$|\mathbf{J}| = \sqrt{\mathbf{I(I+1)}}\hbar$$
$$\mathbf{J}_z = \mathbf{I}_z\hbar \qquad (2\text{-}1)$$

Where I_z=-I, -I+1, ..., I-1, I *and* $\hbar = h/2\pi$, h= *Planck constant*

Associated with this angular momentum J is a magnetic moment (μ) called the nuclear magneton

$$\mu = \gamma\mathbf{J} \qquad (2\text{-}2)$$

where γ is the gyro-magnetic ratio, a constant giving the frequency change with field strength that is dependent on nuclear structure. The hydrogen nucleus is a single proton and so has isospin I=½ and no orbital angular momentum. This results in a simple dipole moment with $J=\sqrt{(3/2)}.\hbar$ and $J_z=\pm½\hbar$ from equation 2-2.

2.2 Energy

2.2.1 Transition Between Energy Levels

In a static magnetic field (B_0) the hydrogen nucleus, like any dipole, will tend to align parallel or anti parallel to the magnetic field (see figure 2.2). There is then a component of the dipole in the direction of the applied field (μ_z). This is the nuclear angular momentum coupling with the magnetic field. The potential energy (E) of these two states, a nuclear form of the Zeeman Effect, is different. To induce a transition of a spin from one state to the other energy must be supplied at ΔE, the difference in energy between the two states.

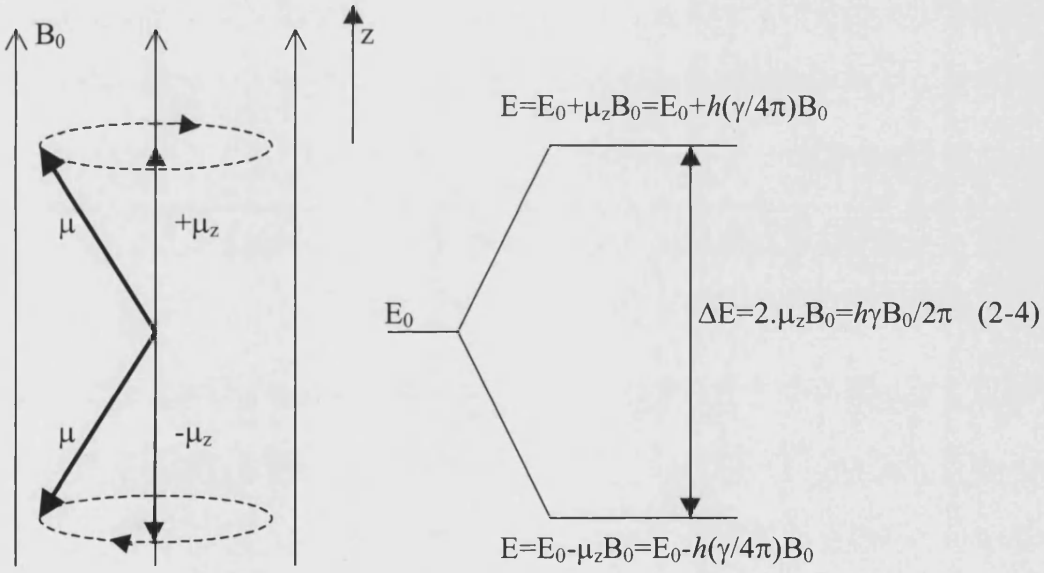

Figure 2.2 Zeeman splitting of nuclear energy states
A hydrogen nucleus behaves as a dipole when placed in a static magnetic field B_0.The energy level of the hydrogen nucleus is split.

The De Broglie relationship equates the energy E of an electromagnetic wave to its frequency υ

$$\mathbf{E = h\nu} \qquad (2\text{-}3)$$

Thus it can be seen from figure 2.2 that the transition energy ΔE is

$$\Delta E = h \gamma |B_0| / 2\pi \qquad (2\text{-}4)$$

Using 2-3 to relate this transition energy ΔE to a resonant frequency (i.e. $E=\Delta E$) gives

$$|\omega_0| = \gamma |B_0| \qquad (2\text{-}5)$$

The transition energy of nuclei in a magnetic field B_0 corresponds to an electromagnetic wave with an angular frequency of ω_0. This is called the Larmor frequency and is in the Radio Frequency (RF) range for magnetic fields in the order of 1Tesla.

2.2.2 Precession

In classical physics, the rotation of any magnetic dipole about the direction of an applied magnetic field is described by Larmor precession (see figure 2.2). Precession can be fully described by quantum mechanics [7], but a more intuitive classical approach yields the same results for the hydrogen nucleus (see section 2.3). The energy for NMR transition is supplied in the form of an oscillating magnetic field perpendicular to B_0. As B_0 lies along z, this is a magnetic field rotating in the xy plane at ω_0.

2.2.3 The Boltzmann Distribution

The nuclei observed in NMR samples can take up one of the two energy states described previously. A nucleus aligns with B_0 with a probability P_+, the nucleus can take up the opposite alignment with a corresponding probability P_-. Any number of the 'N' nuclei in a sample may take up each state so that the populations are N_+ and N_- respectively. The probabilities and populations are described by classical Boltzmann statistics. The probability is thus related to the energy of a given state in the following manner

$$P(E) = Ae^{(-E/kT)} \qquad (2\text{-}6)$$

Where k is the Boltzmann constant, T is absolute temperature and A is a constant related to the number of particles in the system. So for N spins the ratio of the occupancy in two states (N_-/N_+) is the same as the ratio of the probabilities (P_-/P_+).

$$\frac{\mathbf{N_-}}{\mathbf{N_+}} = \frac{\mathbf{P_-}}{\mathbf{P_+}} = \frac{\mathbf{Ae^{(-E_-/kT)}}}{\mathbf{Ae^{(-E_+/kT)}}} = \mathbf{e^{(-\Delta E/kT)}} \qquad (2\text{-}7)$$

Using equation 2-4 in figure 2.2 and the fact that $N = N_- + N_+$

$$\mathbf{N_+ - N_- = N \tanh\left(\frac{\gamma\hbar|B_0|}{2kT}\right)}$$

$\gamma\hbar|\mathbf{B_0}| \ll \mathbf{kT}$ and $\tanh(\varphi) \approx \varphi$, hence to a close approximation

$$\mathbf{N_+ - N_- = \frac{N\gamma\hbar|B_0|}{2kT}} \qquad (2\text{-}8)$$

The net magnetisation (M) is equal to the vector sum of the magnetic moments (μ) from all the nuclei placed in the magnetic field.

$$\mathbf{|M| = N_+\mu_+ + N_-\mu_-}$$

$$\mathbf{|M| = \frac{\gamma\hbar}{2}(N_+ - N_-)}$$

Substituting 2-8 gives

$$\mathbf{|M| = \frac{N\gamma^2\hbar^2|B_0|}{4kT}} \qquad (2\text{-}9)$$

At the values of field strength and temperature commonly used, the populations of the two states are very similar, typically to within a few parts per million. The bulk magnetisation M, used to generate the NMR signal, is proportional to this difference making NMR an insensitive technique. Fortunately, the abundance of protons in vivo is very large of the order of Avogadro's number (~6e23).

2.3 Classical Description of Magnetic Moments in Applied Magnetic Fields

2.3.1 The Classical Behaviour of Magnetisation in a Static Magnetic Field

It has been stated in section 2.2.2 that the rate of precession of a spin around the direction of an applied field is described by the Larmor frequency. This comes from the classical model of the interaction of a magnetic dipole (μ) with a static magnetic field (B_0). A dipole in a magnetic field experiences no net force but a torque (τ) given by

$$\boldsymbol{\tau} = \boldsymbol{\mu} \times \mathbf{B}_0 \qquad (2\text{-}10)$$

Just as a force is given by the rate of change of momentum, the torque is the rate of change of angular momentum (J) with time (t)

$$\frac{\mathbf{dJ}}{\mathbf{dt}} = \boldsymbol{\mu} \times \mathbf{B}_0$$

From equation 2-2 we have the equation of motion for a dipole in a magnetic field

$$\frac{\mathbf{d}\boldsymbol{\mu}}{\mathbf{dt}} = \gamma \boldsymbol{\mu} \times \mathbf{B}_0 \qquad (2\text{-}11)$$

The equation of motion 2-11 can now be used to examine the rate of precession.

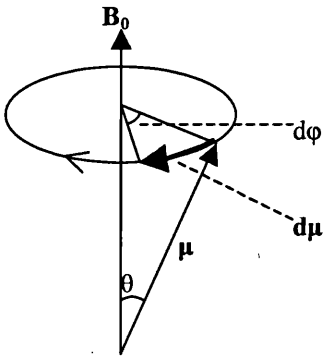

Figure 2.3 The motion of a dipole in a static magnetic field $\mathbf{B}_0$

From figure 2.3 it can be seen that

$$|\mathbf{d}\boldsymbol{\mu}| = \boldsymbol{\mu} \sin\theta |\mathbf{d}\varphi|$$

With equation 2-11 giving

$$|\mathbf{d}\boldsymbol{\mu}| = \gamma |\boldsymbol{\mu} \times \mathbf{B}_0| \mathbf{dt} = \gamma \mu \mathbf{B}_0 \sin\theta \mathbf{dt}$$

Equating the two expressions above then gives the expected Larmor precession at an angular frequency ω_0

$$|\omega_0| = \left|\frac{d\varphi}{dt}\right| = \gamma|\mathbf{B}_0| \qquad (2\text{-}12)$$

Note that this is the same as equation 2-5. The frequency of precession is the same as the frequency of electromagnetic radiation needed to excite a transition between energy states. The cross product of $\mu \times B_0$ will produce a vector perpendicular to plane formed by μ and B_0 such that the tip of the μ will rotate in a clockwise direction. If B_0 is defined to be in the z-direction then the motion of μ will, in a clockwise direction, trace out a circle in the xy-plane. This direction is defined by the cross product as being negative giving

$$\omega_0 = -\gamma|\mathbf{B}_0| \qquad (2\text{-}13)$$

2.3.2 The Rotating Reference Frame

The Larmor frequency, ω_0, is the same for both the dipole precession and the magnetic field needed to excite transition. It is often useful to view interactions in a reference frame that is also rotating so that results are not complicated by periodic motion. If we go back to the equation of motion for a dipole in a static magnetic field

$$\left(\frac{d\boldsymbol{\mu}}{dt}\right) = \gamma\boldsymbol{\mu} \times \mathbf{B}_0 \qquad (2\text{-}14)$$

we can use a co-ordinate system that is rotating at an angular velocity Ω and derive the motion of the dipole in this reference frame

$$\left(\frac{d\boldsymbol{\mu}}{dt}\right)_{rot} = \gamma\boldsymbol{\mu} \times \mathbf{B}_0 - \boldsymbol{\Omega} \times \boldsymbol{\mu} \qquad (2\text{-}15)$$

Since AxB = - (BxA)

$$\left(\frac{d\mu}{dt}\right)_{rot} = \gamma\mu \times \mathbf{B}_0 + \mu \times \Omega$$
$$\left(\frac{d\mathbf{M}}{dt}\right)_{rot} = \mu \times (\gamma \mathbf{B}_0 + \Omega) \qquad (2\text{-}16)$$

This is the same as an effective magnetic field of B_{eff} in the rotating reference frame

$$\mathbf{B}_{eff} = \mathbf{B}_0 + \frac{\Omega}{\gamma} \qquad (2\text{-}17)$$

It is now simple to consider a reference frame in which $\Omega = \omega_0 = -\gamma B_0$. In the rotating reference frame the field is zero and the magnetic moment is static. The magnetic moment is thus rotating at the Larmor frequency in the laboratory frame.

2.3.3 Radio Frequency Pulses (RF pulses)

Now the concept of the rotating reference frame has been introduced it is simple to consider the effects of a rotating magnetic field (B_1) applied perpendicular to the static magnetic field. If B_1 is rotating at the Larmor frequency ω_0 and $\Omega = \omega_0 = -\gamma B_0$, the effective field in the rotating reference frame is given by

$$\mathbf{B}_{eff} = \mathbf{B}_0 + \frac{\omega_0}{\gamma} + \mathbf{B}_1 = \mathbf{B}_0 - \frac{\gamma \mathbf{B}_0}{\gamma} + \mathbf{B}_1 = \mathbf{B}_1 \qquad (2\text{-}18)$$

A magnetic moment in this field will be rotated about B_1 with an angular frequency ω.

$$|\omega| = \left|\frac{d\theta}{dt}\right| = |\gamma \mathbf{B}_1| \qquad (2\text{-}19)$$

From equation 2-19 it can be seen that when the B_1 field is applied for a time t the moment is rotated by an angle θ given by

$$|\theta| = |\gamma \mathbf{B}_1| t \qquad (2\text{-}20)$$

When energy is supplied to spins on resonance ($\omega = \omega_0$), in the rotating reference frame the moment is tipped through an angle θ that can be manipulated by varying the strength and duration of the B_1 field applied. These periods of applied B_1 are termed RF pulses.

2.4 Relaxation and The Bloch Equations

A classical model has been used above to understand the way that isolated spins behave in static and RF magnetic fields. In order to provide a useful description of MRI, this model needs to be modified to determine how large groups of interacting spins will behave. Consider the net magnetisation M, introduced in section 2.2.3, this has the familiar equation of motion we examined for individual magnetic moments

$$\frac{\mathbf{dM}}{\mathbf{dt}} = \gamma \mathbf{M} \times \mathbf{B}_0$$

If we define the static magnetic field as being in the longitudinal or z-direction ($B_0=B_z$), the net magnetisation has a longitudinal component M_z and a transverse component M_{xy}. The motion of the components that make up the magnetisation in the static magnetic field can then be described by the following equations

$$\frac{\mathbf{dM}_z}{\mathbf{dt}} = 0, \quad \frac{\mathbf{dM}_{xy}}{\mathbf{dt}} = \gamma \mathbf{M}_{xy} \times \mathbf{B}_z \qquad (2\text{-}21)$$

The equilibrium net magnetisation, M_0, has a magnitude given by equation 2-9 and is aligned with the direction of the main magnetic field, B_0 (see figure 2.4). Thus, at equilibrium

$$\mathbf{M}_z = \mathbf{M}_0 = |\mathbf{M}_0|.\mathbf{z}, \quad \mathbf{M}_{xy} = 0 \qquad (2\text{-}22)$$

The basis of pulsed NMR is to excite the magnetisation with on-resonance RF pulses. In section 2.3.3, the effect of these pulses on a magnetic moment was seen to be a rotation through an angle θ; the same rotation is applied to the bulk magnetisation by the RF pulse. This rotation changes the relative components of the magnetisation (M_{xy} *and* M_z) such that the transverse component (M_{xy}) is non-zero. The magnetisation then returns to its equilibrium position over time in what is termed relaxation. During its return to equilibrium, the transverse magnetisation rotates at the Larmor frequency producing a plane polarised wave that can be detected to form the NMR signal.

2.4.1 Spin-Lattice Relaxation and its Time Constant T_1

Spin-lattice relaxation causes the magnetisation M to return to its equilibrium position via the exchange of energy between spins and their surrounding molecular environment (or lattice). Molecular tumbling produces small rapidly oscillating (around the Larmor frequency) variations in the size and direction of B_0. A magnetic moment in this oscillating B_0 field will have transitions induced between spin states. Due to the bias in probability of transition between states towards a particular direction, the change in the population of states will on average return the magnetisation to its equilibrium position.

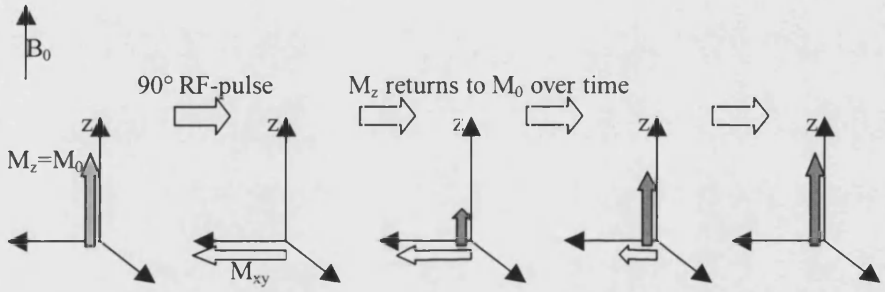

Figure 2.4 The return of longitudinal (z) magnetisation after an RF-pulse
The equilibrium magnetisation has a magnitude M_0 and is aligned with the direction of B_0 (the z-axis is chosen to lie in this direction). After the 90° RF-pulse the magnetisation is all transverse (xy) plane. The longitudinal magnetisation then returns to its equilibrium value over time.

The change in M_z with time is expressed mathematically below.

$$\frac{dM_z}{dt} = -\frac{(M_0 - M_z)}{T_i} \qquad (2\text{-}23)$$

The constant T_1 in equation 2-23 is determined by experiment. The solution of this equation is that of an exponential return to equilibrium described by the following equation

$$M_z(t) = M_0 + (M_z(0) - M_0) \cdot \exp\left(-\frac{t}{T_1}\right) \qquad (2\text{-}24)$$

2.4.2 Spin-Spin Relaxation and its Time Constant T_2

The equilibrium value of the transverse magnetisation M_{xy} (from equation 2-20) is zero because the magnetic moments that make up M_{xy} are randomly orientated. After an RF pulse has been applied there is coherent transverse magnetisation M_{xy}, see figure 2.5 below. The coherence is gradually lost (dephased) as components of the transverse magnetisation obtain different phase. The molecular tumbling described above causes the exchange of energy between spins and this process results in a gradual loss of phase coherence. In contrast to longitudinal relaxation where biased transition occurs between spin states, transverse relaxation does not need to involve a change in the relative population of spin states. In addition, the primary component in the loss of M_{xy} coherence in biological samples occurs through the exposure of spins to local, low frequency fluctuations in the magnetic field. This extra component of T_2 relaxation ensures that T_2 is always shorter than T_1.

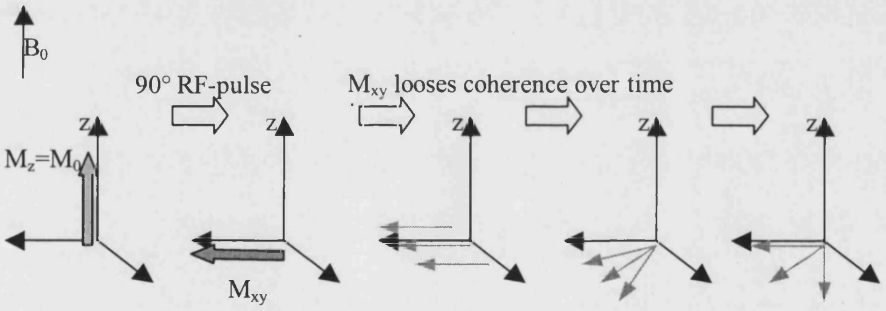

Figure 2.5 The loss of transverse magnetisation after an RF-pulse
After the 90° RF-pulse the magnetisation is all transverse (xy) plane. The transverse magnetisation then loses its coherence over time.

The rate of change of M_{xy} is described mathematically below

$$\frac{dM_{xy}}{dt} = -\frac{M_{xy}}{T_2} \qquad (2\text{-}25)$$

The solution of this equation for the development of the net transverse magnetisation with time shows an exponential decay to zero

$$M_{xy}(t) = M_{xy}(0) \cdot \exp\left(-\frac{t}{T_2}\right) \qquad (2\text{-}26)$$

Transverse magnetisation can also lose coherence through spatial variation in the main magnetic field B_0, causing a variation in spin's angular velocities that is temporally invariant. This dephasing is reversible and characterised by T_2'. The combination of T_2 and T_2' is measured in MRI, it has its own relaxation parameter T_2* and a decay described by equation 2-26 with the substitution of T_2* for T_2.

2.5 How to Localise Signal; Standard Imaging Principles

There have been many different techniques developed to localise signal and form images in MRI. The three main components of localisation, described below, are employed in nearly all MR imaging techniques currently used. The hardware required must produce a linearly varying magnetic field (constant magnetic field gradient) that may be applied in 3 orthogonal directions. The application of these fields causes the resonant frequency of the magnetisation to be spatially dependent. To form images an RF-transmitter and receiver is used in conjunction with the main magnetic field and the constant gradient set.

2.5.1 The Fourier Transform

The Fourier Transform [8,9] (FT) is fundamental to the spatial localisation technique called Fourier encoding. Applying a Fourier Transform to a signal ($g(t)$) that is a function of time (t) yields a set of complex exponential functions with frequencies that make up a complete set of harmonics (n) where $n=1,2,3..\infty$. A continuous function ($f(x)$)

makes up the coefficients of the exponentials that describe *g(t)*. Here the Fourier Transform is defined

$$\mathbf{f(x) = \int g(t) \cdot e^{i\theta} dt}$$

$$\mathbf{g(t) = \int f(x) \cdot e^{-i\theta} dx} \qquad (2\text{-}28)$$

Normally, in MRI conjugate variables such as $\theta=kx$ or $\theta=\omega t$ are used (see section 2.6.2). These integrals can describe non-periodic functions. In MRI a finite set of terms is collected forming a finite series. This produces a periodic function and so has implications for representing an object without error.

An important property of the FT is the convolution theorem [8]. This states that if two functions each have a Fourier transform, then the Fourier transform of the product of the two functions is the convolution of their individual Fourier transforms.

2.5.2 Slice Selection

When a RF pulse is applied it will excite all the spins that have a resonant frequency within the bandwidth (*BW*) of the pulse. This means in a uniform static magnetic field B_0, all spins will be excited if the pulse is on-resonance. Slice selection works by exciting all the spins in a given plane within a three-dimensional (3D) object, then only two-dimensional (2D) encoding is needed to obtain an image from that plane. If a slice is desired, through a plane in a given direction (for example z), a constant magnetic field gradient (G_z) must be applied perpendicular to the plane. This means that the resonant frequency of the spins (ω) is dependant on their position (z) with a frequency given by

$$\mathbf{\omega(z) = \gamma(B_0 + G_z \cdot z)} \qquad (2\text{-}29)$$

Where the magnetic field acts in the z-direction and $G_z=dB_z/dz$. If the RF pulse has a bandwidth BW and a central frequency ω_{slice}

$$\begin{aligned} \mathbf{BW} &= \gamma(\mathbf{G_z}.\Delta \mathbf{z}) \\ \omega_{\mathbf{slice}} &= \gamma.(\mathbf{B_0} + \mathbf{G_z}.\mathbf{z_{slice}}) \end{aligned} \qquad (2\text{-}30)$$

Rearranging 2-30 gives

$$\Delta \mathbf{z} = \frac{\mathbf{BW}}{\gamma.\mathbf{G_z}}$$

$$\mathbf{z_{slice}} = \frac{\omega_{\mathbf{slice}} - \gamma \mathbf{B_0}}{\gamma \mathbf{G_z}}$$

A slice of thickness Δz, centred at position z_{slice} is excited. The gradient amplitude and the pulse BW govern the slice thickness; the slice position is determined by the central frequency of the RF pulse ω_{slice} and the gradient amplitude G_z. After a slice gradient has been applied the phase of the spins across its thickness become dispersed. This is because the transverse magnetisation created during the RF pulse experiences the slice selective gradient that is applied and so spins precess at slightly different rates across the slice. To refocuses this dephasing, a gradient of opposite polarity is applied for the same period that the transverse magnetisation experienced the slice selective gradient.

2.5.3 Frequency Encoding

The basis of frequency encoding is that, in the presence of an applied constant magnetic field gradient (here G_x), the signal from a sample can be measured as shown in figure 2.6. The angular frequency ω and magnitude function $f(\omega)$ directly correspond to the position x and the magnitude of the magnetisation $g(x)$ respectively. The Fourier Transform (FT) of the signal evolution with time during the application of the gradient is a projection of the sample.

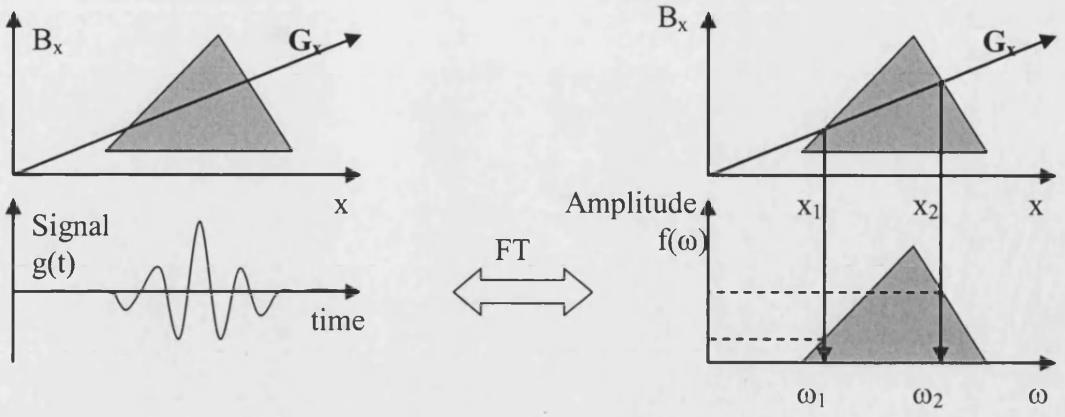

Figure 2.6 Frequency Encoding
A linearly varying magnetic field B_x of gradient strength G_x is applied across an object. The signal from the object measured over time can then be Fourier Transformed to produce a representation of the object in frequency, corresponding to position, and amplitude, corresponding to the objects magnetisation. The level of magnetisation the object possesses is normally associated with a larger object or a greater density of protons.

The signal is received (often called the readout) after a slice selective 90° RF pulse has brought a 2D plane of spins, perpendicular to G_x, into the transverse plane. A secondary effect of applying the gradient is that the phase as well as the frequency of the spins is dependent on position and time within the readout. A gradient with half the area and opposite polarity is applied before the readout. This means that the spins will have phase coherence in the centre of the readout. Thus, the acquired signal will have maximum signal intensity in the centre of the readout and a full, symmetrical echo [10] will be sampled. The reason for this read preparation gradient is further illustrated in the later section 2.6.2 on k-space.

2.5.4 Phase Encoding

In conjunction with frequency encoding and slice selection, phase encoding is applied along the third orthogonal dimension to localise signal from a 3D object. A linear magnetic field gradient is applied for a fixed time in the phase encoding direction;

consequently the spin dipoles precess with a different frequency for a fixed period. This applies a linear phase shift to the magnetisation in the phase encoding direction. The phase shift applied across the object is stepped in factors of 2π, with the number of steps being the same as the number of pixels in this direction. Phase encoding is a similar process to frequency encoding in that the spin density is the Fourier Transform of the acquired signal (see figure 2.6). See the following k-space section for further explanation.

2.6 Tools for Describing Sequences

A typical MRI experiment consists of a large number of RF pulses and magnetic field gradients that are switched on and off (pulsed) in a sequence, normally termed the pulse sequence. There are a number of ways to represent pulse sequences and the signals they acquire. These are necessary to explain the different strategies that may be employed to gain the correct signals, for subsequent correct images. Three commonly used pulse sequences are described in this chapter. They are i) the 2-Dimensional Fourier Transform (2DFT), which is a simple sequence used to illustrate pulse sequences diagrams ii) Echo Planar Imaging (EPI) a very rapid technique, and iii) The Fast Spin Echo (FSE) method that is frequently used clinically, because it provides high quality images in a reasonable time. The FSE and EPI methods are more complicated, so their description is left to the end of the chapter.

2.6.1 Sequence Diagrams

MRI experiments that are performed have five main components: The transmitted RF pulses, linear magnetic field gradients in the x, y and z directions and the RF receiver with its sampling rate and duration. Each component can be represented on a time line

to make a simple pictorial representation of the sequence of gradients, pulses and anticipated echoes. Here four axes are used with a single axis representing RF transmission and reception. The sampling function applied is shown in the frequency encode direction or x-axis. Magnetic field gradients in a direction (m) are represented by shapes that have a height proportional to the gradient magnitude G_m (where $G_m=dB_z/dm$) and a length proportional to gradient pulse duration.

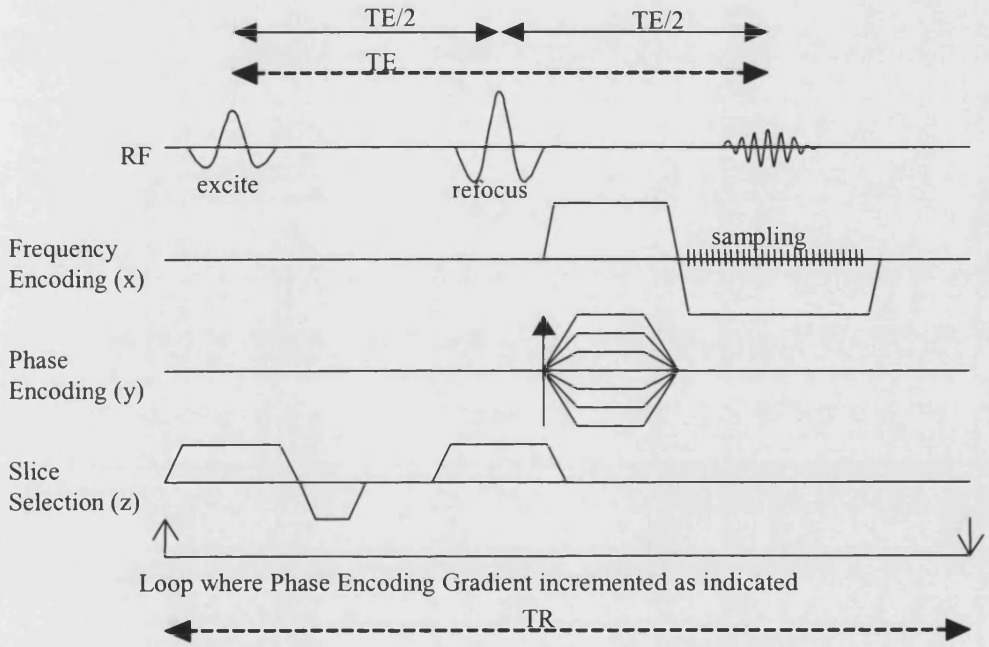

Figure 2.7 A spin echo 2DFT sequence diagram
The application of RF and gradient pulses during the acquisition of an image are represented on different axes.

A 2DFT experiment is shown in figure 2.7. The RF line shows the application of a pulse to excite the spins in a slice (determined by the amplitude of the slice selection gradient for a given RF pulse) followed by a refocusing RF pulse. The refocusing pulse is positioned at time TE/2 to reverse any phase evolution from constant local fields at the echo time (TE). This is called a spin echo and the signal will be T_2 weighted. With the omission of the refocusing pulse an image can still be generated, but the image has

different contrast (T_2* weighted), sensitive to local susceptibility gradients. In the 2DFT method, one line of data is read out for each different phase encoding gradient. There is a time TR between the start of each phase encoding (PE) loop, which allows the longitudinal magnetisation to recover before it is used again in the acquisition of next segment of data. The TR is thus typically of the order of T_1 to make sure a reasonable amount of the magnetisation has relaxed and can then be used for the next excitation. The total scan time for the 2DFT is *TR*nPE* where *nPE* is the number of PE steps.

2.6.2 K-Space

To gain a more exact and intuitive description of how spatial localisation is achieved the concept of k-space is introduced. The relationship between the applied gradients, the magnetisation and its net signal is made clearer in k-space. This is because the Fourier Transform (FT) connects the density of spins in real space (also called image space or the frequency domain) to their rate of precession in Fourier space (called k-space or the time domain).

The position in k-space at a time t (see figure 2.9) is given by indices k_x and k_y, which are related to the applied linear field gradients G_x and G_y in the following manner

$$\mathbf{k_x(t) = \gamma \int_0^t G_x(t)dt}$$
$$\mathbf{k_y(t) = \gamma \int_0^t G_y(t)dt} \qquad (2\text{-}31)$$

The signal (S) that is received at a point in time is the integral of the magnetisation distribution M_{xy} over space (here over x and y). The magnetisation will have been affected by relaxation, pulse sequence parameters, and by the characteristics of the hardware employed. However, while these factors modulate the function *M(x,y)* to

change the appearance of the image obtained, they do not alter what is considered here. The magnetisation has been modulated by the application of gradients G_x and G_y to give

$$S(t) = \iint M(x,y) \cdot \exp\left(i\gamma \left[|B_0| t + x \int_0^t G_x(t)dt + y \int_0^t G_y(t)dt \right] \right) dxdy \quad (2\text{-}32)$$

But, equations 2-31 above with a demodulated [4] receive signal (S'), such that oscillations at the Larmor frequency ω_0 are removed, yields

$$S'(k_x, k_y) = \iint M(x,y) \cdot \exp(i(k_x x + k_y y)) dxdy \quad (2\text{-}34)$$

If the signal has been measured the magnetisation distribution $M(x,y)$ is then simply the Fourier Transform pair of the above equation

$$M(x,y) = \iint S'(k_x, k_y) \cdot \exp(-i(k_x x + k_y y)) dk_x dk_y \quad (2\text{-}35)$$

The signal can only be sampled at discrete points in time so the integral above will form a discreet sum. Now the relationship between k-space $S(k_x,k_y)$ and image space $M(x,y)$ is known, the points in k-space that need to be sampled can be deduced (often called the Nyquist sampling criteria [11], also see the next section). This can be thought of as the convolution [8] of the continuous functions in equation 2-35 above with a comb function. The FT of a comb function is another comb function with a reciprocal period. The image must have a spatial extent or 'Field of View' (FoV) that is as large as the object (FoV_{min}), so in the image domain the comb function must repeat at not more than once every FoV_{min}. The distance in frequency space Δk_{min} is then the reciprocal period $2\pi/FoV_{min}$.

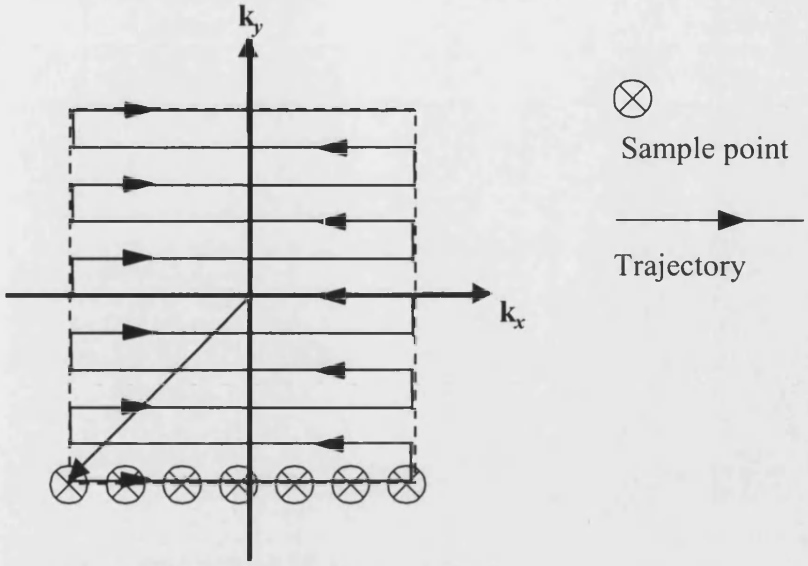

Figure 2.8 A trajectory through k-space
The application of gradients is described by the traversal of k-space; a construct that links applied gradients, the expected signal and the image obtained.

Similarly, for a desired resolution of λ, $M(k_x,k_y)$ must be sampled over an area $2\pi/\lambda$. This leads to grid of points in k-space that must be sampled using gradients that take a trajectory passing through them, such as that shown in figure 2.8. The way that k-space is sampled is fundamental to a technique. In the 2DFT experiment each line along k_x is sampled individually in a separate TR, the magnetisation is then left to recover before the next line is acquired. The reason for the preparation gradients in the frequency and phase encoding directions are clear from figure 2.8; these take the magnetisation to bottom corner of k-space, from which point the trajectory can start. In the EPI experiment (see section 2.8) the line in figure 2.8 is followed through the complete trajectory in a single readout. The read gradient reversals switch the k_x direction and the phase encoding gradient 'blips' jump the magnetisation to the next line.

2.6.3 Discrete Fourier Encoding: Aliasing

When an analogue signal is digitised, the rate at which it is sampled has important implications that are explored in figure 2.9 below. In section 2.5.1, it was stated that any

continuous signal could be represented by an infinite number of harmonics. Instead, a digitised signal is made up of a finite number of harmonics. The sampling rate *Ts* determines the range of frequency components, often called the bandwidth '*BW*' (*BW=1/Ts*), which can be measured in a signal. The higher frequency components are still measured, but they appear as low frequency signal. This superposition of signals that are at different frequencies is called aliasing.

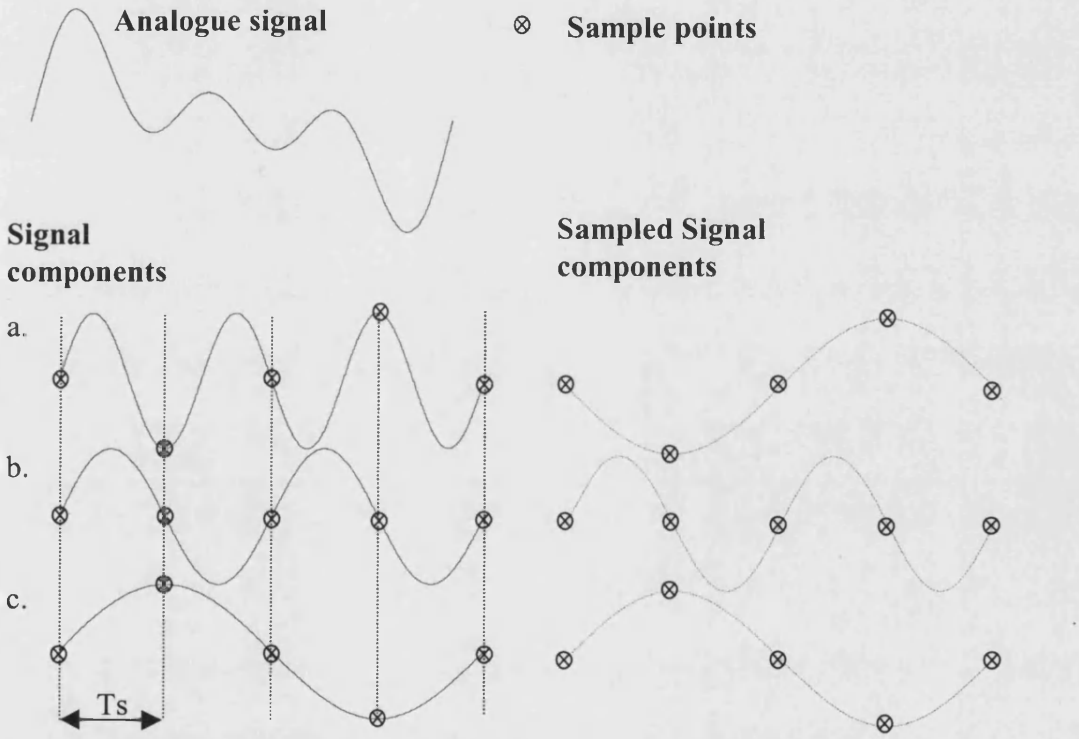

Figure 2.9 Sampling and Aliasing of Signals
An analogue (or continuous) signal is presented at the top. This signal can be described by 3 sinusoidal components '*a*', '*b*'and '*c*' seen on the left hand side with a solid line. The signal is sampled at points in time '*Ts*' apart. A sinusoidal dotted line is drawn through the sampled points on the right hand side. It becomes clear that while components *b* and *c* are accurately described by the sampled points, component *a* is represented by a lower frequency signal. Components *a* and *c* are aliased, the higher frequency component *c* appears at the lower frequency of *a*. The sampled signal in this example up will simply be component *b*. This is because sampled signals *a* and *c* will destructively interfere. The frequency of *b* is the Nyquist frequency *Fn*, which is the maximum frequency that can measured using a sampling frequency *Fs*. From the figure it can be seen that *Fn = 2*Fs = 1/Ts i.e. Fn= 1/(2Ts)*.

The ideas in figure 2.9 are important when considering how to best sample the receiver signal generated during an MRI experiment. The receive bandwidth determines the frequencies (and levels, since most of the signal is normally concentrated at low frequencies) of signal and noise that are obtained. However, as described in section 2.6.2, sampling in k-space is also fundamental to correct signal localisation using Fourier encoding.

The frequency of precession of the magnetisation in an object is related to its position (see figure 2.6). When the MR signal is not sampled correctly aliasing occurs. This means that the signal from an object is assigned to an incorrect spatial position in the image. Restating some of the discussion in section 2.6.2, the applied magnetic field gradients make the frequency and phase of the magnetisation depend on spatial position. To correctly produce an image, the signal from different positions in space must be sampled with a frequency that allows them to be distinguished. E.g. $\Delta k_{min}=\gamma G_m Ts$ and the FoV is simply $2\pi/\Delta k_{min}$, so for a correct FoV the gradient size and sample time must be balanced. Larger gradients mean lower sample times can be used while maintaining the FoV. Lower sample times mean that the receiver bandwidth is reduced. A lower receiver bandwidth is desirable because the signal tends to be entirely within a low range of frequencies while the noise is distributed among all frequencies. This means a low bandwidth has a higher Signal to Noise Ratio (SNR).

2.6.4 Discrete Fourier Encoding: The Point Spread Function (PSF)

K-space is sampled discretely, but it is also sampled over a finite area. The convolution theorem means that these sampling functions can be considered as separate filters that are applied to a continuous, infinite k-space (k-space is not sampled to infinity because

it would take an infinite time!). The filter that is applied in k-space is normally a 'box' filter (e.g. in 1D, $-k_{max}:k_{max}=1$, all other values $=0$). This means that the signal from each spatial position, represented by a pixel, is distributed in image space by the FT of the 'box' filter that has been applied. The distribution of signal, which is the FT of the k-space filter applied by sampling a discrete area, is called the Point Spread Function (PSF).

In figure 2.10 a box function is shown, which is also sampled at discreet positions indicated by the crosses. The FT of the box filter produces a sinc function. With the points that are sampled this produces an oscillating spread of signal intensity across the image that decreases with distance. The contribution to every other pixel is zero. When a wider region of k-space is acquired it is like applying a wider box function. This makes the PSF reciprocally narrower i.e. the PSF will be the same function, but it will be spread over half the physical distance.

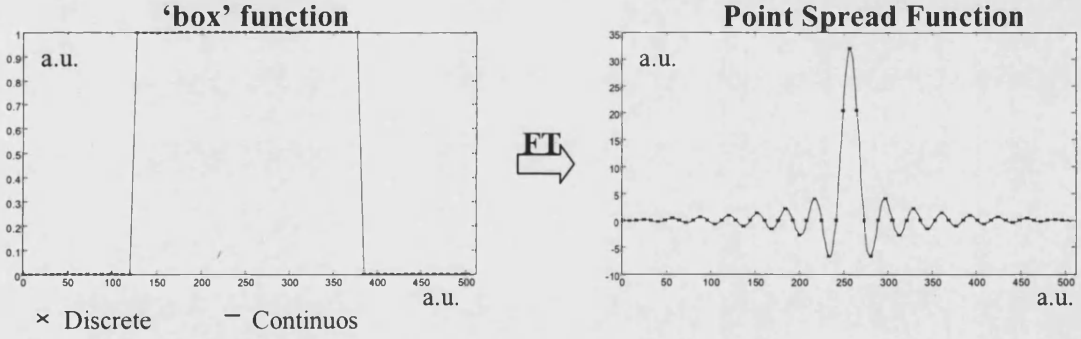

Figure 2.10 The Point Spread Function (PSF)
On the left hand side a box function over a finite region is displayed. This continuous function is actually sampled (as represented by the crosses). The continuous line has infinite bounds. When a signal is sampled using this function it produces the PSF displayed on the right hand side. The function is a sinc and it is sampled at the points given by a cross. The nearest pixels have the largest values the function then decreases with distance. However, due to the sampling every other sampled position (or pixel in the image) is zero. When signal from a given position in space is sampled it will be distributed throughout the image according to the point spread function.

2.6.5 Phase Graphs

Phase graphs, first published by Hennig [12,13], are an elegant way of describing the evolution of magnetisation during the application of repeated RF pulses. Simple vectors of magnetisation may describe the spin echo, but echoes created by dephased magnetisation can quickly become too complicated.

Consider magnetisation that is dephased by a gradient so that it forms a complete disk in the transverse plane, see figure 2.11. If the magnetisation experiences 180° RF pulse (2.11a), and the same gradient both before and after the pulse, then the magnetisation is refocused for a spin echo at an equal time later. If however, the magnetisation experiences no RF pulse, the magnetisation is further dephased by 2π creating a disk of magnetisation with two windings (2.11b). The third possibility is that the magnetisation experiences a 90° RF pulse (2.11c). In this case, the magnetisation that is perpendicular to the plane of the RF field is rotated onto the longitudinal axis, while the rest of the magnetisation remains in the transverse plane. The continued application of the gradient will again form an echo, though it is a different species that is hard to describe with just a few magnetisation vectors.

To keep track of the transfer of magnetisation, and potential echo formation, from repeated RF pulses of varying angles, a diagram called a phase graph is used (illustrated in figure 2.12). The phase graph is made up of vertical lines that represent RF pulses. The flow of longitudinal magnetisation between states given by Z and Z^*, representing magnetisation wrapped in a clockwise or counter clockwise orientation respectively, is represented by the dotted lines. Similarly, the transverse magnetisation is represented by the solid lines, with states F and F^* representing magnetisation wrapped in a clockwise

or counter clockwise orientation respectively. To observe the formation of an echo one of the *F/F** states must cross through the u,v line.

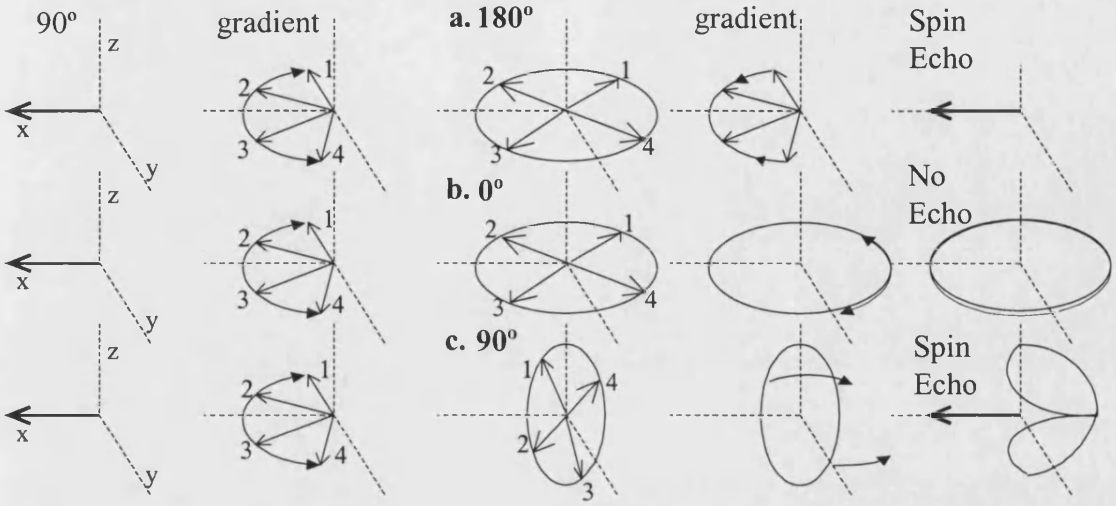

Figure 2.11 The development of magnetisation under the application of different RF pulses
The evolution of magnetisation is considered during the application of different pairs of RF pulses. Different echoes are produced depending on the angles of the pulses used.
a. At the top a spin echo is formed from a 90-180 set of pulses. The 180 pulse reverses the positions of the vectors. After the application of the same gradient they are all returned to there starting positions and a spin echo is formed.
b. In the middle, no echo is formed from the application of a 90-0 set of pulses. The gradient simply dephases the magnetisation.
c. At the bottom, another spin echo is formed from a 90-90 set of pulses. The second 90 pulse reverses the position of some of the magnetisation as with the 180 pulse (a). This component of the magnetisation forms a spin echo - it has been refocused as if it has seen a 180 pulse. However, some of the magnetisation is rotated on to the z-axis, does not experience the gradient and is not involved in forming the echo.

In figure 2.12a, the formation of a normal spin echo (*SE*) is seen from the application of a 90°-180° pulse train. The *SE* occurs at a time equal to twice the spacing between the first two pulses. The component of magnetisation that forms the *SE* is one compete disk of magnetisation at the 180° pulse, represented by the F_1 state. It is then converted to the F^*_1 state by the 180° pulse. The continuous gradient then refocuses this magnetisation by bringing it through the *u,v* line.

In figure 2.12b, no echo is formed from the application of a 90°-0° pulse train. The magnetisation is wrapped further by the gradient, and goes from the F_1 state to the F_2 state.

A spin echo can also be formed by a pair of 90° RF pulses, see figure 2.12c. The transverse magnetisation produced by the first 90° pulse is split into two states by the application of a further 90° RF pulse. The first state present after the second 90° pulse is F^*_1, which forms the *SE*. The second is the longitudinal magnetisation in state Z_1. The longitudinal magnetisation can be brought back into the transverse plane ($Z_1 \rightarrow F^*_1$ in 2.12c) by a third 90° pulse, which forms another kind of echo termed the stimulated echo *STE*.

In figure 2.12d, a full series of pulses that have an arbitrary angle are used. All the different lines represent all the different states for the magnetisation. This diagram shows how a complex series of pulses quickly builds up a large number of states. Designing a pulse sequence containing a number of pulses requires the different states to be, firstly, anticipated, and secondarily, carefully selected, using the appropriate choice of RF pulses and gradients. The phase diagram allows this to be achieved with relative ease.

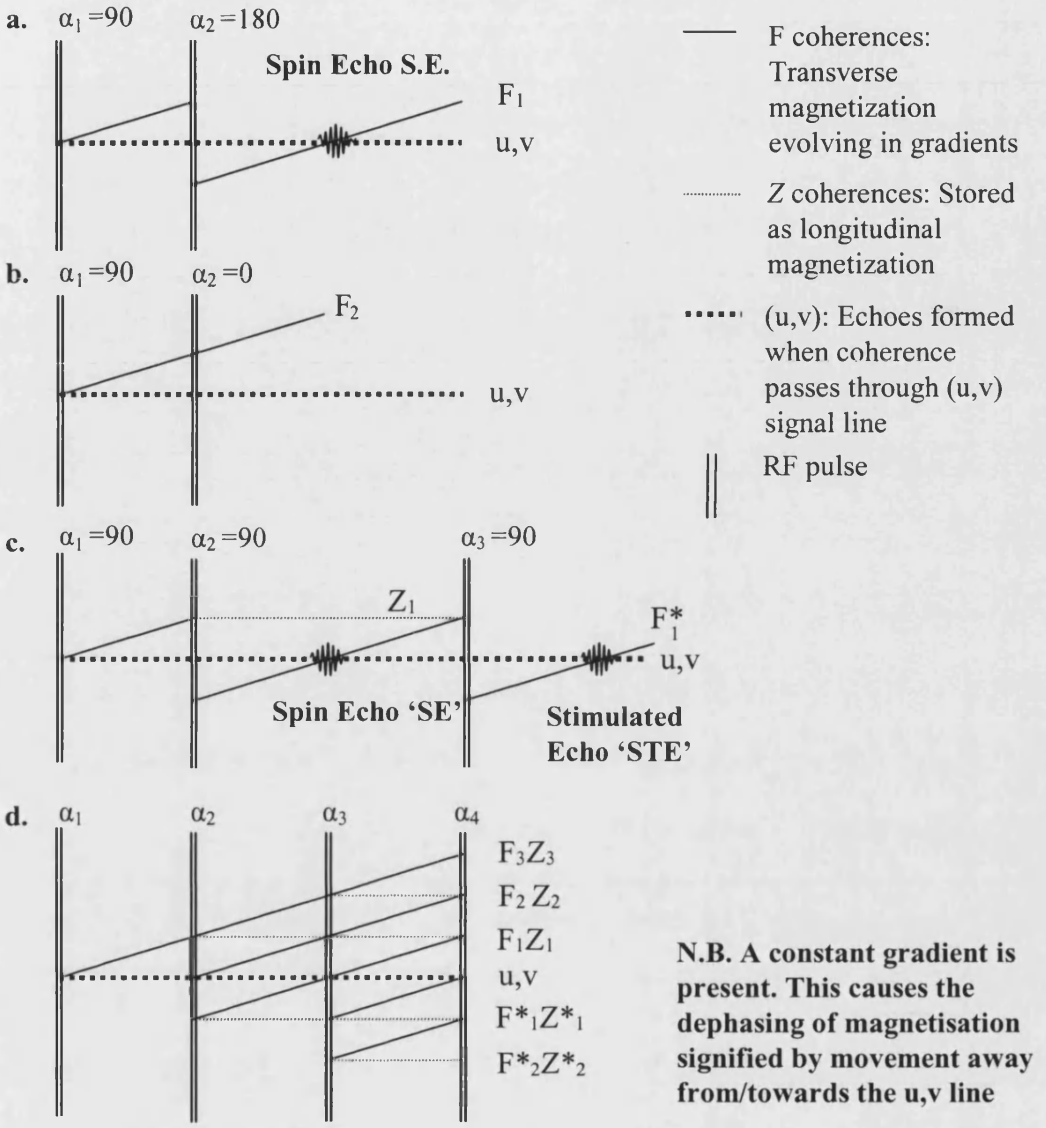

Figure 2.12 The Phase Graph

The development of magnetisation is charted through the α° RF pulses. The figures 2.12a-c mirror the development of magnetisation in figure 2.11a-c. The dotted lines represent the *Z*, longitudinal magnetisation states. The solid lines represent the *F* transverse magnetisation states. An echo is seen when one of the states passes the u,v line

a. The formation of a spin echo from a 90-180 pulse train

b. No echo is formed from a 90-0 pulse train, the magnetisation is further dephased. This is represented by the F_2 state as opposed to the F_1 state in figure 2.12a.

c. The formation of a spin echo from a 90-90 pulse train is seen. However, this is not the same as in 2.12a, there is also a component of longitudinal magnetisation represented by the Z_1 state. The application of a further 90 pulse brings the *Z* magnetisation back to the transverse plane where it forms a stimulated echo.

d. All the different components of magnetisation created during the application of repeated RF pulses are shown.

2.7 Parallel Imaging and Sensitivity Encoding

Modern MRI, using the principles of Fourier encoding, has been extremely successful. However, this approach has also set limits on the speed of image acquisition: a certain number of points in k-space must be sampled, and, as only one point can be sampled at any one time, a certain k-space trajectory must be followed. The trajectory takes a finite time limited by hardware performance [11] and physiological boundaries [14]. The limiting factors normally cited are the time it takes to sample a point, the minimum number of points required to form an image, the strength of the gradients and how rapidly they may be switched. To circumvent these limitations a group of new techniques has been developed that are termed Parallel Imaging (PI).

PI uses multiple coils to simultaneously receive signals from an object. Each receive signal is modulated by the spatial sensitivity of the coil. If these spatial sensitivities are known, their difference can be used to assign the spatial position of the signal, reducing the amount of Fourier encoding that is necessary for the correct reconstruction of an image. All PI methods use this principle, but there are various ways in which the sensitivity information can be used to reconstruct an image.

2.7.1 Image Domain or SENSE-Type Techniques

SENSitivity Encoding or SENSE [15] is performed in the image domain and so it is the most intuitive to understand, thus it is more fully described here. A simple two-coil introduction is given in figure 2.13 below. Two coils pick up signal from an object and two images are obtained, one from each coil. These images may be acquired with a reduced FoV by sampling the signal in k-space less densely. This means that signals from different spatial positions (*a* and *b* in figure 2.13) are aliased. However, because

the aliased signal (from the same spatial position in the two images *I1* and *I2*) is weighted differently, the relative contributions from the two aliased spatial positions can be determined provided the sensitivity functions (*S1* and *S2*) are known.

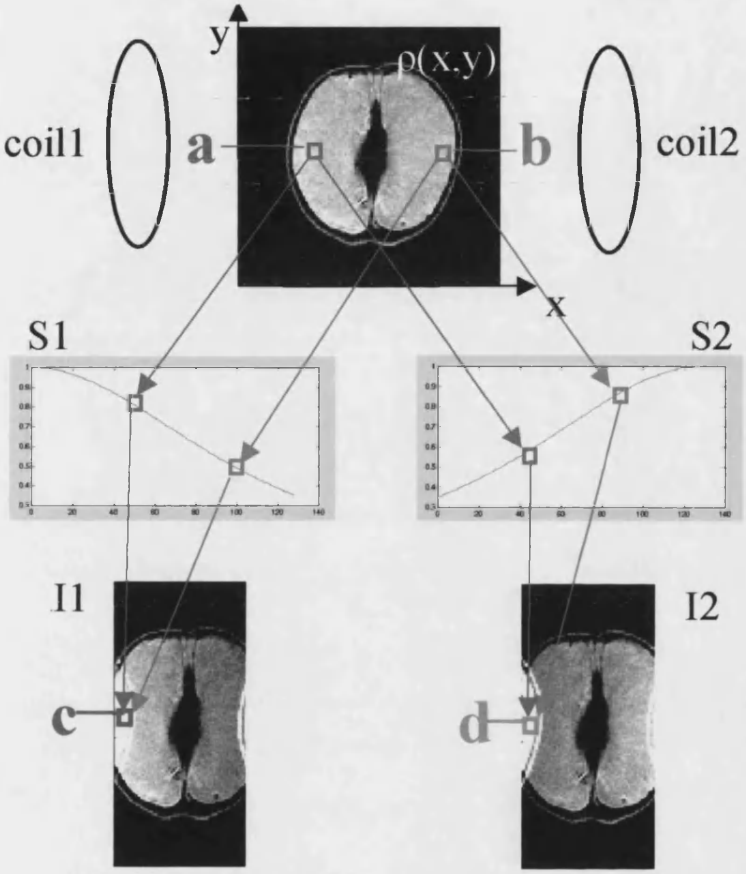

$$I1(c,y) = S1(a,y) * \rho(a,y) + S1(b,y) * \rho(b,y)$$

$$I2(d,y) = S2(a,y) * \rho(a,y) + S2(b,y) * \rho(b,y)$$

Object with spin density $\rho(x,y)$ in the FoV_{full} is imaged using two coils.

Two positions a & b are highlighted to track what happens to signal from these positions.

The spin density is weighted by the sensitivity of each coil S1 and S2. Profiles of S1 and S2 with x are shown.

Two images are generated I1 & I2 that have a reduced FoV. The aliased signal from positions a and b is shown in pixels c and d in the reduced FoV.

The signal in c and d is weighted by the different functions S1 and S2.

If we know S1 and S2 we can get $\rho(x,y)$ over the full FoV from images I1 and I2 by solving these simultaneous equations.

Figure 2.13 Principle of SENSE

Generalising, SENSE relies on the acquisition of multiple images (*I*), with each image acquired by a different receiver (*r*). These images contain information about spin density (ρ) modulated by a spatial weighting from the coil (*S*). To shorten scan time in conventional Fourier imaging the same area of k-space is sampled less densely, leading to images with a reduced FoV (*fovr*), but the same resolution. Pixels in the *fovr* images now contain weighted information from several positions [15]. If in each image the

weightings are significantly different they may be used to separate the aliased signal. So in the Cartesian case, where x and y give position and the number of positions aliased is n, individual images are represented by the following equation

$$\begin{pmatrix} \mathbf{I}_1 \\ \mathbf{I}_2 \\ \dots \\ \mathbf{I}_r \end{pmatrix} = \begin{pmatrix} \mathbf{S}_{1(x,y)} & \mathbf{S}_{1(x+fovr,y)} & \dots & \mathbf{S}_{1(x+(n\times fovr),y)} \\ \mathbf{S}_{2(x,y)} & \mathbf{S}_{2(x+fovr,y)} & \dots & \mathbf{S}_{2(x+(n\times fovr),y)} \\ \dots & \dots & \dots & \dots \\ \mathbf{S}_{r(x,y)} & \mathbf{S}_{r(x+fovr,y)} & \dots & \mathbf{S}_{r(x+(n\times fovr),y)} \end{pmatrix} \times \begin{pmatrix} \boldsymbol{\rho}_{(x,y)} \\ \boldsymbol{\rho}_{(x+fovr,y)} \\ \dots \\ \boldsymbol{\rho}_{(x+(n\times fovr))} \end{pmatrix} \quad (2\text{-}37)$$

or

$$\mathbf{I} = \mathbf{S} \times \boldsymbol{\rho} \quad (2\text{-}38)$$

This enables us to obtain a full FoV image by inverting the sensitivity matrix S.

$$\boldsymbol{\rho} = \mathbf{S}^{-1} \times \mathbf{I} \quad (2\text{-}39)$$

The SENSE technique has a more complicated Signal to Noise Ratio (SNR) performance than conventional Fourier imaging. There are two main factors that reduce the signal to noise: firstly, the degree of speed up given by the Reduction factor (R). R is ratio of the number of k-space lines acquired with the *fovr* to the number of k-space lines for a full FoV acquisition. The second consideration is how good the sensitivity functions are at separating the signal. This is related to how independent the different views of the coils are (in the ideal case each coil would receive signal from one spatial region only and an unaliased image would be formed of a part of the FoV) and is also dependent on the degree of aliasing. Mathematically, the extra SNR penalty for having to separate the signals is given by the g-factor (g), which can be calculated from knowledge of the sensitivity functions and the level and correlation of noise in the receivers. This is discussed more full in section 5.2.5. From reference [15], the SNR for SENSE is given with respect to the noise performance of a coil array with no reduction in sampling SNR_{full}

$$\mathbf{SNR_R} = \frac{\mathbf{SNR_{full}}}{\sqrt{\mathbf{R}} \times \mathbf{g}} \qquad (2\text{-}40)$$

It should be noted that the SNR performance of the array itself has certain characteristics, so when considering overall SNR first the SNR_{full} performance of the array must be taken into consideration. This can also be derived from the sensitivity functions and the receiver noise characteristics, and is explored further in section 5.2.5.

2.7.2 Frequency Domain or SMASH-Type Techniques

Methods that use the sensitivity information in the time domain are called SMASH [16] type techniques after one of the first methods to produce images in a reduced time using multiple receivers: Simultaneous Acquisition of Spatial Harmonics. As the name suggests, in this approach the modulation on the magnetisation normally imposed by phase encoding is partly replaced using the complex coil sensitivities. The coil sensitivities available are always low frequency, which means that k-space lines are required over the whole of k-space. A partial sampling of k-space is then used with the sensitivity data to 'fill in the gaps' and calculate a full matrix of k-space data.

Rather than trying to create a combination of coil sensitivity functions that replicates phase encoding, the signal in the time domain can simply be considered an object's signal modulated by an encoding function. The time domain signal is a product of the spin density and an encoding function (in a very similar way to equation 2-37). The encoding matrix can be inverted (like in equation 2-39) to obtain the spin density. This is the basis of Generalised SMASH [17] and unifies the time and frequency domain approaches. There are also a number of hybrid techniques, which bridge the gap between using all the k-space lines together (as in SENSE and Generalised SMASH) and using each line individually (as in SMASH). The various related reconstruction

approaches include GRAPPA [18], G-SMASH [19] and SPACE-RIP [20] in addition to those already mentioned.

2.8 Echo Planar Imaging (EPI)

Mansfield first introduced Echo Planar Imaging in 1977 [21]. This, the most rapid of imaging techniques, was conceived well in advance of its routine application. EPI is now used for performing studies of, for example, diffusion, perfusion and BOLD functional activation.

An EPI diagram is shown in figure 2.14. A gradient echo is formed when the transverse magnetisation is dephased and then rephased by linear magnetic field gradients alone. The EPI experiment involves a single RF pulse followed by a train of gradient echoes that are read out by applying a series of gradients with equal areas and opposite magnitude. Each echo has a different net phase encoding gradient due to the extra gradients (blips) applied between the readout gradient reversals [22]. This is in contrast with the 2DFT experiment (figure 2.7), where each phase encoding step requires a separate excitation of the magnetisation (and a subsequent wait for it to relax). Here, EPI acquires all the PE steps in one TR making it a much faster technique than the 2DFT. This implementation of EPI is termed 'single-shot' because it requires only one excitation of the magnetisation to obtain an image.

The echo time TE is centred on the middle PE step where the net phase encoding gradient is zero. It is clear that because each echo is at a different position in time, the magnetisation will have experienced different amounts of dephasing from local

susceptibility gradients. This inconsistency between successive echoes has associated problems that will be discussed at greater length later.

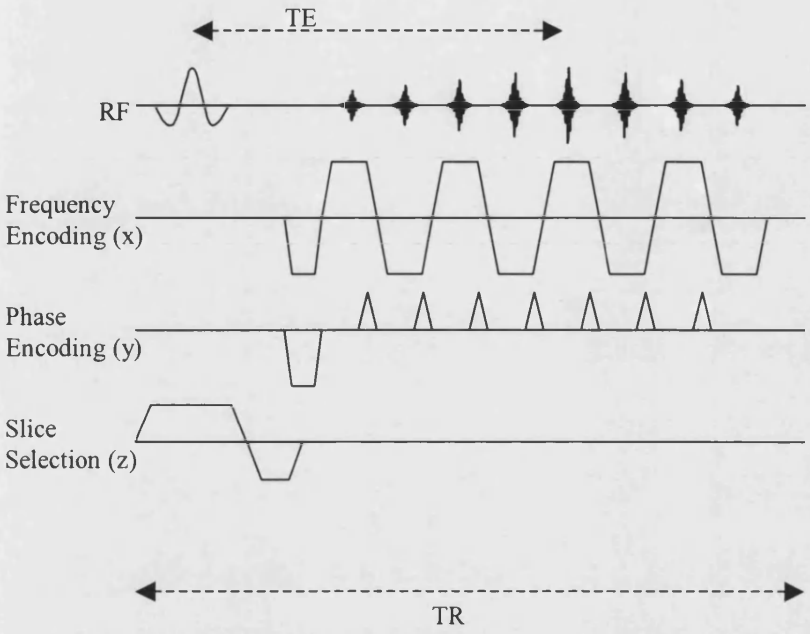

Figure 2.14 A Blipped Echo Planar sequence diagram
The Echo Planar experiment forms a set of echoes with a single RF excitation. EPI uses Phase Encoding between a series of readout gradients with alternating polarity.

EPI has one major advantage: its speed; an image can typically be obtained in 50ms using modern hardware. EPI is able to take multiple images (slices) over a large volume in a few seconds, allowing a dynamic system to be imaged repeatedly. This also enables motion to be frozen, particularly important in Diffusion Weighted Imaging for example, which is highly motion sensitive [23].

2.8.1 EPI Problems

EPI can suffer from a number of problems that are directly related to its strategy of full k-space coverage in a single-shot. EPI readouts are naturally longer than for other pulse sequences, because a greater distance through k-space must be travelled. Further

problems are associated with having reversed the direction travelled through k-space in alternate lines; see reference [24] for a full description of EPI artefacts and their causes.

Blurring of image detail occurs because of T_2^*/T_2 decay over the length of the acquisition. This is because the PSF of an image is made considerably worse by the extra filter that is imposed in k-space by relaxation of the magnetisation over the length of the readout. This is a greater problem at higher field where T_2^* is shorter and the stronger filter imposed results in a worse PSF. Shortening the readout duration reduces this problem leading to a sharper image.

Distortion is the result of local susceptibility gradients and chemical shifts that cause spins from a particular spatial position to precess with a different frequency than expected in the presence of a linear magnetic gradient field. In an EPI acquisition, these local susceptibility gradients are significant in size when compared to the gradients encoding along the phase direction, causing an error in the assignment of spin position. In 2DFT images the receiver bandwidth is kept as low as possible, this is to maximise SNR as discussed in section 2.6.3. In EPI, large readout gradients (G_{ro}) are used to get through k-space more quickly and so a high receiver bandwidth ($BW_{receiver}$) must be used i.e. $2\pi/FoV_{ro}=\Delta k_{ro}=\gamma G_{ro}Ts= \gamma G_{ro}(1/BW_{receiver})$, a large G_{ro} is used for EPI so an equal increase in the $BW_{receiver}$ is required to maintain the readout direction FoV (FoV_{ro}), where Δk_{ro} is the distance in k-space between sampled points in the readout direction and Ts is the time between sampled points.

The Phase Encoding direction (*PE*) in an EPI acquisition is somewhat like a second readout direction. The points are readout consecutively in time Ts_{PE} and so also have a

bandwidth (BW_{PE}) in this direction of $1/Ts_{PE}$. The bandwidth per pixel is the BW_{PE} divided by the number of PE steps. This corresponds to the frequency difference between the harmonics measured using N sample points with a sample time of Ts (i.e. $1/N.Ts$). In EPI, Ts_{PE} is typically long (of the order of 1ms) and there are 64 points on the phase encoding axis, this means BW_{PE}/N_{PE} is typically ~1000/64Hz. Susceptibility gradients in the human head of 1 part per million at 4.7 T (^{1}H frequency=200MHz) corresponds to a frequency of 200Hz. Thus, susceptibility gradients can cause significant distortion of the spatial position of magnetisation in the PE direction. To reduce distortion, the bandwidth per point along the phase encoding axis must be increased.

The dephasing of signal from within a voxel causes dropout. The amount of dephasing is dependant on the local field inhomogeneity. In regions where susceptibility gradients are strong, the magnetisation within a voxel can become completely incoherent. This means that no signal is seen from this region, often described as a region of 'dropout'. To reduce this problem the amount of dephasing across a voxel can be reduced by making the voxel smaller, or by reducing the time that the local fields have to dephase the signal by minimising the echo time TE.

In EPI, ghosting is normally produced by a mismatch between echoes formed by read gradients of opposite magnitude. Gradient inconsistencies, eddy currents and susceptibility gradients can all contribute to this mismatch. Hardware improvement or corrections can both reduce the artefact level [24]. One way to correct for mismatches is to employ a reference scan (or navigator echo) [23]. The echo train used for the EPI acquisition is performed without PE gradients. A series of echoes is formed that can

alternately be reversed in time. Any shift in time between them (in k-space) will produce a corresponding linear phase shift in image space. The phase of the Fourier transformed echoes can be compared. The difference may then be used to correct all subsequent acquisitions.

2.8.2 EPI Variants

The basic idea of EPI is to travel through the whole of k-space in a single image acquisition, one example of the gradients required to do this is shown in figure 2.14. However, a number of other strategies may be employed to perform the same function [25], some of which are briefly summarised.

Firstly, different gradient pulse shapes can be used in the readout direction, the most popular of which are trapezoidal (as in figure 2.14). This produces linear k-space sampling except when signal is sampled during the gradient ramps (at the edges of k-space in the readout direction). The major disadvantages of trapezoids are that rapid gradient switching is required between the lobes of opposite polarity. This is hardware intensive and is associated with high acoustic noise levels and eddy currents. Alternatively, sinusoidal readout gradients may be used. These are slightly smaller on average and so the readout will be longer. However, sinusoidal pulse shapes do not require such rapid switching and acoustic noise is reduced. In addition, they tend to be less affected by eddy currents that can cause ghosting in the images. With uniform sampling in time, a non-uniform readout gradient amplitude in time produces non-uniform sampling in k-space. The reconstruction process used must take this into account (normally the data is regridded-using interpolation, alternatively, a trajectory based reconstruction method could be used [26]).

Secondly, different phase encoding gradients may be employed. Blipped gradients like those in figure 2.14 are the most common. These 'jump' the trajectory to the next k-space line before it is readout. Alternatively, a constant gradient may be applied. This causes a zigzag trajectory across k-space that again requires more processing for correct image reconstruction. One other method is to apply a sinusoidal phase encoding gradient. This can be employed alongside a sinusoidal readout gradient to form a spiral k-space trajectory. The amount of very fast gradient switching that is required using this method is lowered. Also, the signal can be sampled continuously during the readout period, which compensates for the lower average gradient amplitude obtained using the sinusoidal readout gradient when compared to a trapezoidal readout gradient. The major advantage of the spiral trajectory is that the phase encoding bandwidth is significantly increased and correspondingly distortion is significantly reduced.

A further group of EPI pulse sequences are also used. These are segmented EPI sequences that aim to split the coverage of k-space into several separate readouts. Different groups of k-space lines are acquired in separate readouts; for two segments every other line of the standard k-space coverage is readout, then, the remaining lines are acquired in a separate readout. Some sequences aim to acquire the different lines in a single-shot using different components of the magnetisation. The segments can be readout consecutively by using a 45° RF pulse and acquisition followed directly by a 90° RF pulse and acquisition. This method is susceptible to differences between the segments caused by RF inhomogeneity and phase evolution during the sequence that cause ghosting artefacts. Alternatively, if a steady state is achieved by the repeated application of RF pulses then many different segments may be readout consecutively. A

more robust strategy is to allow the magnetisation to relax fully before acquiring each segment, though this entails a penalty in temporal resolution that would be unacceptable for many applications. Furthermore, these multi-shot segmented methods suffer from reduced tolerance to motion. Segmented acquisitions have the advantage of reduced blurring and distortion within the images. However, because they involve the combination of data from different readouts (in k-space), any mismatch or discontinuity in the k-space data leads to ghosting artefacts in the image that can be severe.

2.9 The Fast Spin Echo (FSE) Method

The FSE technique is a variant of RARE, Rapid Acquisition with Relaxation Enhancement [27]. This sequence is used routinely in clinical MRI, so there is a wealth of information describing the sequence. This work is not about the FSE sequence, but it is used to obtain images in chapter 5. A brief introduction of the FSE technique is included in this section to illustrate some of the choices that can be made and their possible implications see references [28-32] for more details.

The idea behind the FSE is to use repeated 180° RF pulses, to successively refocus the magnetisation, and form a train of spin echoes. Each echo in the train can be used to acquire a different k-space line. The acquisition time can then be reduced by a factor equal to the number of echoes used in the RF pulse train.

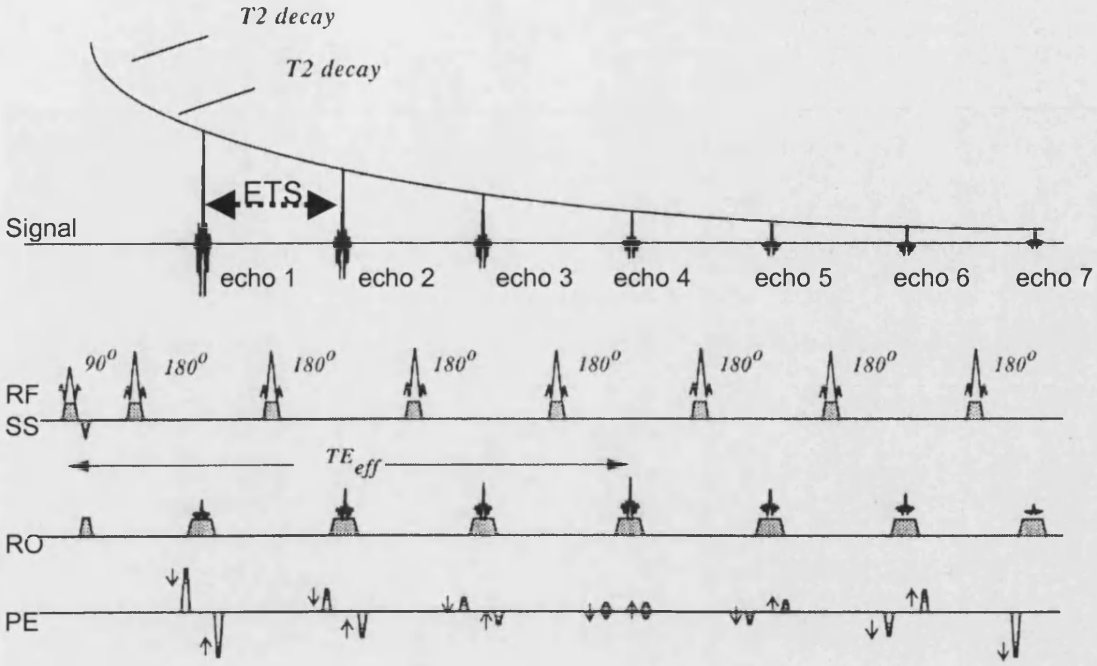

Figure 2.15 A Fast Spin Echo Pulse sequence
The Fast Spin Echo (FSE) experiment forms a set of echoes with a single RF excitation. Each echo is formed by the application of a 180 RF pulse. The echoes each have a different phase encoding gradient to acquire a different line of k-space. Each echo also has different relaxation characteristics (and so amplitude) that is dependent on the position of the echo within the echo train. The effective echo time is the echo time at which the centre of k-space is read out.

There are a number of factors that can be varied in the FSE sequence above. Some of the most important are summarised below.

- Number of echoes
- Inter Echo Time (ETS in figure 2.15)
- Effective echo time (i.e. which echo in the train to use for the central line of k-space)
- K-space ordering (i.e. which echo in the train to use for all the other k-space lines)
- Choice of encoding gradients, their position and balance (i.e. refocusing scheme)
- RF pulse characteristics such as amplitude, bandwidth, number and position.
- Number, order and distance between slices

The choice of these parameters is important because they alter the SAR (see next section), image contrast, the PSF and the SNR of the resulting image, in addition to the total acquisition time. Thus, to obtain the best possible FSE images a careful choice of parameters must be made to balance the positive and negative effects that the various factors can produce.

T_2 weighting is the main contributor to image contrast in most FSE images. However, Magnetisation Transfer (MT) and direct saturation can also contribute significantly. Fat often appears brighter in FSE images due to J modulation effects. As with 2DFT images, diffusion weighting can also be a factor [29].

2.10 RF Effects: SAR and RF Penetration Effects with Reference to Field Strength

Later in this work a number of techniques are considered for use at high field strength (>1.5T). The consideration of RF non-uniformity and power deposition must be made for the reasons outlined in this section.

When an RF field interacts with tissue in the body energy is absorbed. MRI is termed non-invasive because the most important known effect of this interaction is heating. Thus, one of the most important limits on an acquisition is the Specific Absorption Rate (SAR). This is a measure of the energy deposited in tissue and is governed by the likely temperature changes induced from this exposure [33]. For the human head 4W/Kg is the current safety limit for a period of 15 minutes. It should also be noted that there are two slightly different considerations to be made. Firstly, what is the overall energy deposition and secondly, what is the distribution of this deposition [34-36]. Particular

care must be taken over structures that receive a lot of RF power but which do not have mechanisms for redistributing the heat such as high levels of perfusion.

In pulse sequence design and implementation the level of SAR must be considered. SAR is particularly important in sequences that use many high power pulses in a short period of time such as the FSE. At higher field strength there are two factors to consider. Firstly, the RF Power is generally increased because the frequency (and so energy see section 2.2) required for spin transitions is higher. Secondly, at higher field strength RF distribution tends to become less uniform and so local regions of excess RF deposition are more likely [35-37].

RF coils have been designed that have high levels of uniformity such as the birdcage [38] and TEM coil [39]. RF coils tend to produce a lower level of uniformity at higher field, because the wavelength of the field produced is of a similar size to the coil elements. Standing waves can be produced in the elements creating a variation in performance along their length. While distributed capacitance can reduce this problem, it is hard to eliminate using capacitors that have a capacitance within a reasonable range.

At higher field strengths the RF field is also non-uniform because of interactions between the coil and the RF field. RF tends not to penetrate samples in the same way when frequencies used are of the order of MHz. The electric field produced by conductive samples can produce magnetic fields that distort and attenuate the B_1 field created by the RF coil alone. When the wavelength of the applied RF field is small compared to the size of a sample, and if it has a reasonable dielectric constant, modified

B_1 fields are produced in the sample. The sample and coil interact in a complicated manner both producing fields and inducing current in each other [35-37].

2.11 References

1. Brown, M. A. & Semelka, R. C. 1999, *MRI : basic principles and applications*, 2nd ed edn, New York ; Chichester : Wiley-Liss.

2. Haacke, E. M., Brown, R. W., Thompson, M. R., & Venkatesan, R. 1999, *Magnetic Resonance Imaging Physical Principles and Sequence design*, 1 edn, John Wiley and Sons, New York, USA.

3. Cady, E. B. 1990, *Clinical Magnetic Resonance Spectroscopy* Plenum Press, New York.

4. Webb, S. 1990, *The Physics of medical imaging*, Repr. with corr. edn, Bristol : Hilger.

5. Gadian, D. G. 1995, *NMR and its applications to living systems*, 2nd edn, Oxford University Press, Oxford.

6. Foster, M. A. & Hutchison, J. M. S. 1987, *Practical NMR imaging* IRL Press, Oxford.

7. Haacke, E. M., Brown, R. W., Thompson, M. R., & Venkatesan, R. 1999, "The quantum mechanical basis of precession and excitation," in *Magnetic Resonance Imaging Physical Principles and Sequence design*, 1 edn, E. M. Haacke et al., eds., John Wiley and Sons, New York, USA.

8. Boas, M. L. 1983, *Mathematical methods in the physical sciences*, 2nd ed edn, New York ; Chichester : Wiley.

9. Haacke, E. M., Brown, R. W., Thompson, M. R., & Venkatesan, R. 1999, "The Continuous and Discrete Fourier Transforms," in *Magnetic Resonance Imaging Physical Principles and Sequence design*, 1 edn, E. M. Haacke et al., eds., John Wiley and Sons, New York, USA, pp. 207-230.

10. Hahn, E. L. 1950, "Spin Echoes", *Physical Review*, vol. 80, pp. 580-594.

11. Haacke, E. M., Brown, R. W., Thompson, M. R., & Venkatesan, R. 1999, "Sampling and Aliasing in Image Reconstruction," in *Magnetic Resonance Imaging Physical Principles and Sequence design*, 1 edn, E. M. Haacke et al., eds., John Wiley and Sons, New York, USA, pp. 231-264.

12. Hennig, J. 1991, "Echoes - How to generate, recognize, use or avoid them in MR-imaging sequences. Part II: Echoes in imaging sequences", *Concepts in Magnetic Resonance*, vol. 3, pp. 179-192.

13. Hennig, J. 1991, "Echoes - How to generate, recognize, use or avoid them in MR-imaging sequences. Part I: Fundamental and not so fundamental properties of spin echoes", *Concepts in Magnetic Resonance*, vol. 3, pp. 125-143.

14. Irnich, W. & Schmitt, F. 1995, "Magnetostimulation in MRI", *Magn Reson.Med.*, vol. 33, no. 5, pp. 619-623.

15. Pruessmann, K. P., Weiger, M., Scheidegger, M. B., & Boesiger, P. 1999, "SENSE: sensitivity encoding for fast MRI", *Magnetic Resonance In Medicine*, vol. 42, no. 5, pp. 952-962.

16. Sodickson, D. K. & Manning, W. J. 1997, "Simultaneous acquisition of spatial harmonics (SMASH): fast imaging with radiofrequency coil arrays", *Magnetic Resonance In Medicine*, vol. 38, no. 4, pp. 591-603.

17. Sodickson, D. K. & McKenzie, C. A. 2001, "A generalized approach to parallel magnetic resonance imaging", *Med.Phys.* , vol. 28, no. 8, pp. 1629-1643.

18. Griswold, M. A., Jakob, P. M., Heidemann, R. M., Nittka, M., Jellus, V., Wang, J., Kiefer, B., & Haase, A. 2002, "Generalized autocalibrating partially parallel acquisitions (GRAPPA)", *Magn Reson.Med*, vol. 47, no. 6, pp. 1202-1210.

19. Bydder, M., Larkman, D. J., & Hajnal, J. V. 2002, "Generalized SMASH imaging", *Magnetic Resonance In Medicine*, vol. 47, no. 1, pp. 160-170.

20. Kyriakos, W. E., Panych, L. P., Kacher, D. F., Westin, C. F., Bao, S. M., Mulkern, R. V., & Jolesz, F. A. 2000, "Sensitivity profiles from an array of coils for encoding and reconstruction in parallel (SPACE RIP)", *Magnetic Resonance In Medicine*, vol. 44, no. 2, pp. 301-308.

21. Mansfield, P. 1977, "Multi-planar image formation using NMR spin echoes", *Journal of Physics C* p. L55-L58.

22. Schmitt, F., Stehling, M. K., & Turner, R. 1998, *Echo-planar imaging* Heidelberg: Springer-Verlag, Berlin.

23. Ordidge, R. J., Helpern, J. A., Qing, Z. X., Knight, R. A., & Nagesh, V. 1994, "Correction of motional artefacts in diffusion-weighted MR images using navigator echoes", *Magnetic Resonance In Medicine*, vol. 12, no. 3, pp. 455-460.

24. Fischer, H. & Ladebeck, R. 1998, "Echo-Planar Imaging Image Artefacts," in *Echo-planar imaging*, F. Schmitt, M. K. Stehling, & R. Turner, eds., pp. 180-200.

25. Wielopolski, P. A., Schmitt, F., & Stehling, M. K. 1998, "Echo-Planar Pulse Sequences," in *Echo-planar imaging*, F. Schmitt, M. K. Stehling, & R. Turner, eds., pp. 65-134.

26. Turner, R., Howseman, A. M., Rees, G. E., Josephs, O., & Friston, K. 1998, "Functional magnetic resonance imaging of the human brain: data acquisition and analysis", *Experimental Brain Research*, vol. 123, pp. 5-12.

27. Hennig, J., Nauerth, A., & Friedburg, H. 1986, "RARE imaging: a fast imaging method for clinical MR", *Magnetic Resonance In Medicine*, vol. 3, pp. 823-833.

28. Constable, R. T. & Gore, J. C. 1992, "The loss of small objects in variable TE imaging: implications for FSE, RARE, and EPI", *Magn Reson.Med.*, vol. 28, no. 1, pp. 9-24.

29. Constable, R. T., Smith, R. C., & Gore, J. C. 1992, "Signal-to-noise and contrast in fast spin echo (FSE) and inversion recovery FSE imaging", *J.Comput.Assist.Tomogr.*, vol. 16, no. 1, pp. 41-47.

30. Garwood, M. & Ke, Y. 1991, "Symmetric pulses to induce arbitrary flip angles with compensation for RF inhomogeneity and resonance offsets", *Journal Of Magnetic Resonance*, vol. 94, pp. 511-525.

31. Mulkern, R. V., Melki, P. S., Jakab, P., Higuchi, N., & Jolesz, F. A. 1991, "Phase-encode order and its effect on contrast and artifact in single-shot RARE sequences", *Med.Phys.*, vol. 18, no. 5, pp. 1032-1037.

32. Mulkern, R. V., Wong, S. T., Winalski, C., & Jolesz, F. A. 1990, "Contrast manipulation and artifact assessment of 2D and 3D RARE sequences", *Magn Reson.Imaging*, vol. 8, no. 5, pp. 557-566.

33. Shellock, F. G. 2002, "Magnetic resonance safety update 2002: implants and devices", *Journal of Magnetic Resonance Imaging*, vol. 16, no. 5, pp. 485-496.

34. Shellock, F. G., Schaefer, D. J., & Gordon, C. J. 1986, "Effect of a 1.5 T static magnetic field on body temperature of man", *Magnetic Resonance In Medicine*, vol. 3, no. 4, pp. 644-647.

35. Sled, J. G. & Pike, G. B. 1998, "Standing-wave and RF penetration artefacts caused by elliptic geometry: an electrodynamic analysis of MRI", *IEEE Trans.Med.Imaging*, vol. 17, no. 4, pp. 653-662.

36. Ibrahim, T. S., Lee, R., Abduljalil, A. M., Baertlein, B. A., & Robitaille, P. M. 2001, "Dielectric resonances and B(1) field inhomogeneity in UHFMRI: computational analysis and experimental findings", *Magn Reson.Imaging*, vol. 19, no. 2, pp. 219-226.

37. Kangarlu, A., Baertlein, B. A., Lee, R., Ibrahim, T., Yang, L., Abduljalil, A. M., & Robitaille, P. M. 1999, "Dielectric resonance phenomena in ultra high field MRI", *J.Comput.Assist.Tomogr.*, vol. 23, no. 6, pp. 821-831.

38. Hayes, C. E., Edelstein, W. A., Schenck, J. F., Mueller, O. M., & Eash, M. 1985, "An efficient, highly homogeneous radiofrequency coil for whole-body NMR imaging at 1.5T", *Journal Of Magnetic Resonance*, vol. 63, pp. 622-628.

39. Vaughan, J. T., Adriany, G., Garwood, M., Yacoub, E., Duong, T., DelaBarre, L., Andersen, P., & Ugurbil, K. 2002, "Detunable transverse electromagnetic (TEM) volume coil for high-field NMR", *Magnetic Resonance In Medicine*, vol. 47, no. 5, pp. 990-1000.

3. SPENT: Sub Pixel Enhancement of Non-uniform Tissue

In this chapter, a new method called Sub Pixel Enhancement of Non-uniform Tissue (SPENT) is introduced that produces an original form of contrast sensitive to variations in the distribution of magnetisation across a voxel. An image is obtained that has a 2π phase wrap applied across each voxel. This leads to a coherent signal only when there is a non-uniform magnetisation distribution within a voxel. The homogeneity of magnetisation within voxels can be investigated in different directions by applying the phase wrap in different directions.

SPENT is investigated as an original technique for the extraction of information about the structure of a sample with reference to the following questions

- How does new contrast produced in SPENT images behave?
- Does SPENT improve the visualisation of pixels that lie on the boundary of two tissue types and contain a partial volume of each?
- Is SPENT a more efficient way of targeting k-space for certain structural information than a standard image acquisition?
- Can SPENT images provide a global measure of structure within a sample?

The assistance of Marios Yiannakas in the preparation of the bone samples used in this chapter is acknowledged.

3.1 Background and Introduction

In this chapter, to accurately consider the differences between SPENT and standard images a number of terms need to be defined. The term 'resolution' is defined as $\lambda_{min}=2\pi/k_{max}$ (as in section 2.6.2), λ_{min} is the length of a pixel in a given direction. The term 'true resolution' of an image (akin to the ability to resolve two point sources) is determined by the resolution, but also by the Signal to Noise Ratio (SNR) and Point Spread Function (PSF) of the image pixels. A pixel is the point in an image that represents an area of the object. A voxel is defined here as the volume of magnetisation in the object that is represented by a pixel. Bleeding is where signal in a pixel originates from other surrounding voxels rather than the voxel represented by the image pixel.

Diffusion-Weighted MRI (DWI) [1-3] is routinely used to probe structure that is smaller than the size of a voxel, typically examining structures of several microns. This is achieved by making the signal inside a voxel sensitive to the microscopic, intra-voxel movement of water. SPENT [4] aims to investigate structures that are at the limits of standard image resolution by making the appearance of a pixel sensitive to a non-uniform magnetisation distribution within its voxel. This contrast, achieved by applying a 2π phase wrap across each voxel, could be useful for assessing the structure of a sample.

In k-space the majority of the signal lies in the centre, where the main low frequency features of an object are encoded. In higher frequency regions of k-space smaller details of an object are to be found, however, the SNR of this information is usually decreased. To image at the highest possible resolution, k-space is normally sampled up to the point at which no more useful information is acquired; at this point the SNR in k-space is too

low [5,6]. Normally, the k-space data is then Fourier transformed (FT'd) to produce an image.

If a region of k-space contains certain information, it is possible to target this by sampling the desired region with greater efficiency. This idea has been used in keyhole methods [7,8]. These methods are often used to study dynamic information to enable a better time resolution or image quality. Similarly, in a high resolution image the smaller structures on the limits of resolution are found in higher frequency regions of k-space; SPENT aims to target these regions and sample them with a greater efficiency.

SPENT should produce signal in samples that have regular structures such as edges between tissue types. If the SPENT signal changes when there are more or less of these structures, it might produce a global measure of the structure contained within the sample without requiring the image processing techniques that are normally used. From a time domain perspective, if an object contains some regular sized structures these will produce signal in a certain region of k-space. The smaller the size of the structures, the further out in k-space the signal will lie. SPENT, by sampling a higher region of k-space and reconstructing it independently could sensitise images to the level of structure within the object.

The discrete nature of k-space sampling means that the signal at each position in the frequency domain is convolved with the Fourier transform of the sampling window applied in the time domain. The result is that each pixel has a PSF that describes the distribution of signal across an image originating from a particular spatial region of the object (see section 2.6.4). The signal in a pixel with a defined PSF is then a sum of the

signal from both the voxel at the pixel's position and a contribution of signal from all the other voxels. The largest additional contribution is normally from neighbouring voxels.

When an isolated voxel contains a different spin density, the averaging effect of signal contributions from surrounding voxels can greatly reduce its pixels contrast relative to surrounding pixels. One example of this is when a pixel contains a Partial Volume (PV) of two tissue types. The difference in pixel signal intensity can be much less than the corresponding difference in voxel spin density. However, it may be possible to use different reconstruction schemes to display the higher frequency information about a PV pixel better, by altering the effects of the PSF and the resulting bleeding of signal from bright neighbouring pixels.

In the following chapter, SPENT is introduced by considering the effect of acquiring an image when an extra gradient is applied within a standard sequence to produce a 2π phase wrap across each image pixel. This is then illustrated in terms of k-space coverage in two ways. Firstly, the different ways to cover the same, or a similar area of k-space, are discussed. Furthermore, the reduced region of k-space that is sampled for a SPENT image is used to obtain the same information as is present in a high resolution image. If structural information can be obtained from SEPNT images, the different ways to cover k-space could be used to enable a reduction in scan time or a correspondingly increase in SNR.

3.2 Theory

The idea behind SPENT is that structure below the resolution of a pixel may be investigated by making the imaging experiment sensitive to the level of homogeneity within a voxel. In figure 3.1, the meaning of magnetisation homogeneity within a voxel is investigated.

a. A homogeneous 2D voxel that contains a uniform magnetisation distribution and no structure.

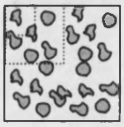

b. This voxel does contain structure but over the size of the pixel the magnetisation distribution is quite homogeneous.

c. A smaller voxel contain the same structure starts to have a less homogeneous magnetisation distribution.

d. As the structures approach the size of the voxel the magnetisation distribution is non-uniform.

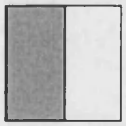

e. A voxel containing a distribution of magnetisation that is completely uniform in the up down direction, but, is highly non-uniform in the left right direction.

Figure 3.1 Homogeneity, describing how uniform the magnetisation distribution is within a voxel
Various different distributions of spins are seen in a-e. Within the voxel, how homogeneous the magnetisation distribution is depends on the distribution of spins. Structures that are uniform do not always have a uniform magnetisation distribution within the voxel, especially when the voxel size is similar to the structure size.

Different distributions of magnetisation (or spins) have different levels of homogeneity - compare figures 3.1a-e. There are two main factors that describe the distribution of spins. Firstly, there is the overall spin density (i.e. 3.1a and 3.1e clearly have different spin densities). Secondly, there is the way that the spins are distributed (i.e. 3.1e and 3.1b have similar overall spin densities but quite different levels of homogeneity). It is

also noted that the distribution in 3.1e is completely homogeneous in one direction while being highly non-uniform in the other. Additionally, the same distribution is seen to exhibit different levels of homogeneity depending on its scale relative to the voxel size in 3.1b-d.

SPENT aims to make the signal intensity in an image sensitive to some of the differences between the spin density distributions seen in figure 3.1. This can be achieved by applying an extra gradient within a standard Spin Echo (SE) sequence as shown in figure 3.2, which generates a phase wrap of 2π per voxel.

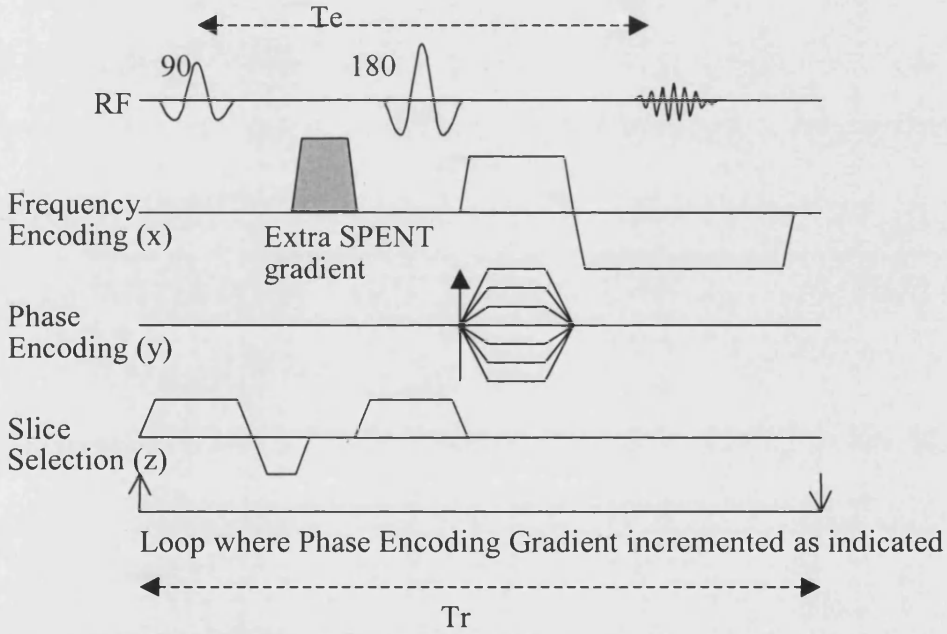

Figure 3.1 The SPENT pulse sequence diagram
An extra gradient is applied within a 2DFT Spin Echo sequence.

In figure 3.3, the progression of magnetisation for a uniform and a non-uniform voxel is shown. For the voxel with a uniform spin density in the direction of the applied gradient, spins experience a field that is dependent on their position and so precess at different rates, causing intra-voxel dephasing. The gradient is applied until there is a phase dispersion of 2π across each voxel. In the uniform voxel in figure 3.3, the

components of magnetisation at different positions are equal in magnitude, and thus when summed, no coherent magnetisation remains. The voxels net magnetisation (of zero) then contributes no signal and, in the image, the pixel is dark. If the voxel has a non-uniform spin density the components of the magnetisation have a non-zero sum; this produces a coherent signal and a bright pixel in the image. Thus, pixel signal intensity reflects voxel homogeneity in the direction of the applied gradient.

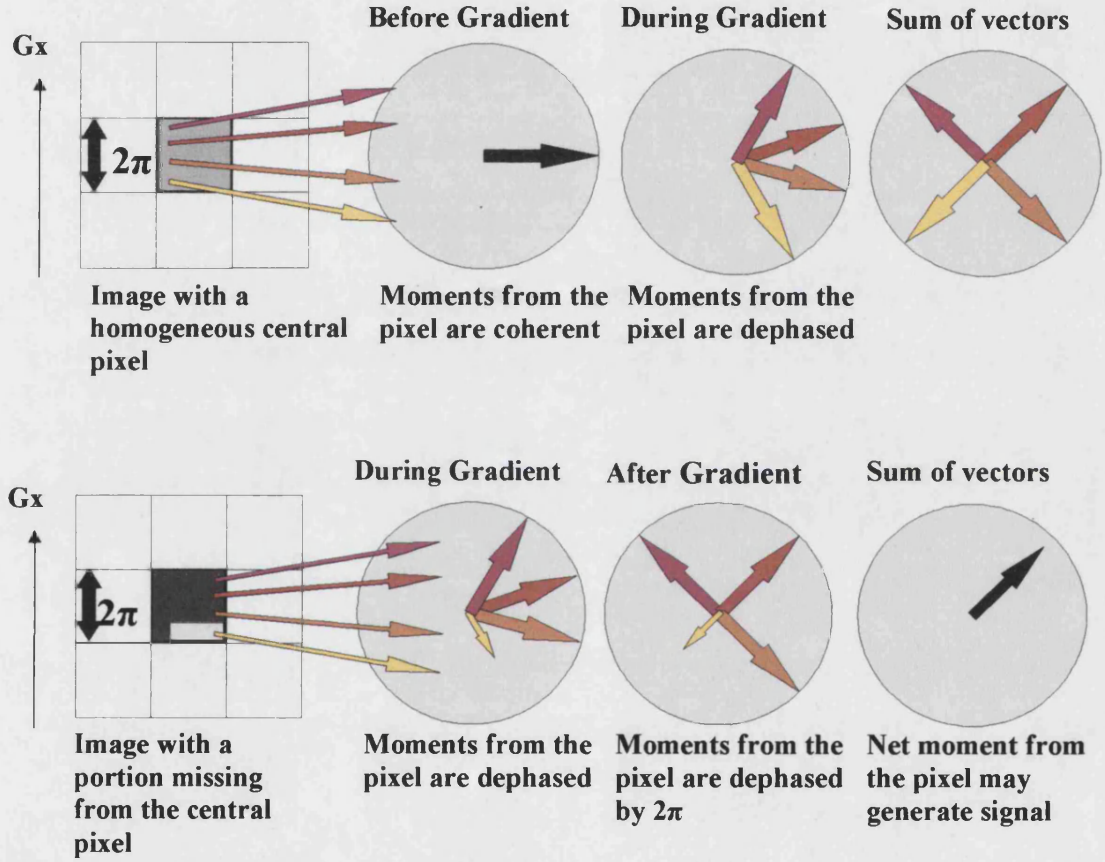

Figure 3.2 How SPENT works
Top left to right, a homogeneous pixel in an image has its magnetisation dephased by a gradient such that no signal is produced. Bottom left to right, the signal from a non-uniform pixel is dephased by the same amount and a coherent signal can be seen.

The gradient can be applied in each direction (read/phase/slice or *x*/*y*/*z*) making the image sensitive to voxel homogeneity in each direction. Here, the SPENT sequence is

used with proton density weighted spin echo images, because this does not expose the magnetisation to any loss of coherence other than from spin density inhomogeneity.

The SPENT sequence can also be considered in terms of the k-space area that is sampled to create an image. The area in k-space that is traversed in an acquisition (from section 2.6.2) gives the resolution of the image. A standard image acquisition will examine a region like that seen in figure 3.4a with the centre of k-space lying in the centre of the sampled region. The application of the extra gradient in SPENT takes a section of the same size but displaced by $2\pi/\lambda$ (remembering λ is the image resolution in that direction), which is the next section of k-space often referred to as a 'tile'.

Application of the gradient in the x-direction acquires the next tile along the k_x axis; its application in the y-direction acquires the next tile along the k_y axis. The data for two SPENT images and a standard image could be obtained in three separate experiments, each acquiring the tiles seen in figure 3.4a. However, this is not the most efficient sampling regime.

The main time factor in a 2DFT acquisition is the number of phase encoding (*npe*) steps needed to generate the image data. This is because each phase encoding (PE) step requires a separate excitation (and subsequent relaxation time (TR) before the next excitation) of the magnetisation. From section 2.6.1, *scan time= TR*npe*. Figure 3.4b shows a different scheme for k-space traversal that uses 2/3 of the PE steps that are needed in 3-4a. Two sections of k-space are acquired, each section uses a longer readout length and the direction of the readout is switched between the acquisition of the two tiles. This regime gains 4 SPENT images and a standard image taken with 2 averages.

Provided the longer readout is short compared to T_2, and that the TR is sufficiently long to allow enough slices to be gained for a specific application, there is little penalty from extending the readout length.

A further alternative would be to acquire an image at a higher resolution. This acquisition is represented in k-space by figure 3.4c. In addition to being able to produce a high resolution image, the same data can be used to produce 8 sub images equivalent to the application of a SPENT gradient in the *x, -x, y, -y, xy, -xy, x-y, -x -y* directions and a standard image: All 9 sub images have 1/3 of the resolution of the high resolution image. Reconstructing the data in separate tiles to form SPENT images may reduce the bleeding effect of signal contributions from surrounding voxels that can reduce the contrast of a pixel when it contains a PV. This is because the SPENT image pixels should have less bleeding from bright neighbouring voxels, as they do not contain bulk regions of high signal intensity that are produced by the centre of k-space. However, sampling a discrete area of k-space will have an effect on the distribution of signal from a voxel in the object due to the PSF. The different ways of reconstructing the high resolution k-space data, therefore, represent ways of changing the averaging of signal that occurs in a pixel through both the PSF and image combination.

The SPENT gradient can be applied in the slice direction to gain an idea of the levels of voxel uniformity found in this direction. In the *z*-direction a separate acquisition is required to form a SPENT image. One alternative to the acquisition of a standard and SPENT image would simply be to excite thinner slices for a corresponding improvement in resolution.

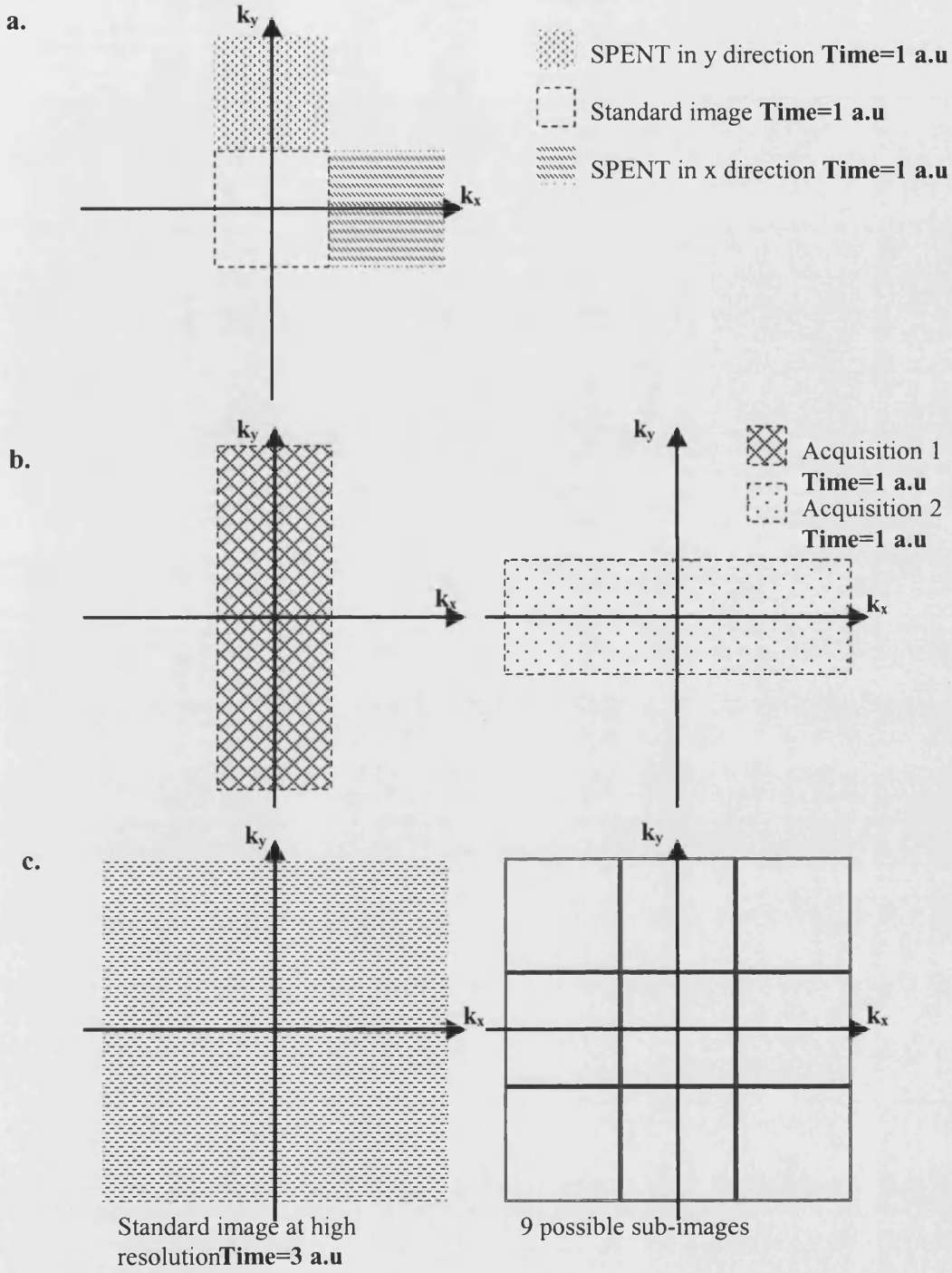

Figure 3.4 SPENT and high resolution image acquisitions represented in k-space
From the top, diagram a, the different tiles in k-space are seen that are obtained with a standard Spin Echo sequence and with the SPENT sequence with the extra gradient applied in the x and y directions respectively. In figure b a more efficient scheme of k-space traversal is demonstrated. In contrast, figure c shows a high resolution image acquisition. This can be divided into separate tiles forming a lower resolution image and 8 possible SPENT images.

A second way to examine thinner slices is through the use of Fourier encoding in the slice direction. This approach is used in slab selection and 3D methods. The application of the 2π phase wrap in SPENT is identical to a phase encoding step in these other methods. Hence, there is no obvious advantage in terms of k-space sampling efficiency. It should be noted that the ideas of SPENT and of the filtering and tiling of k-space seen in figure 3.4, can be generalised to include the slice direction. If SPENT images can give a direct measure of structure from a sample then it could become desirable to apply SPENT in the z-direction.

3.3 Methods

3.3.1 Simulating SPENT

A 1D simulation of the SPENT sequence in figure 3.2 was developed in MatLab (Mathworks, Natick, MA). A sample was modelled as a discrete set of magnetic moments. Gradients and RF pulses were treated as vector rotations of the magnetisation; T_1 and T_2 relaxation were not considered. A sum over the set of magnetic moments replicates the signal expected during the application of the readout gradients. The FoV, resolution and SPENT gradient were controllable parameters. This enabled sections of k-space to be sampled as a 1D representation of the sampling regime in figure 3.4a.

The magnetisation distribution of the sample was modelled using 2048 discrete points. An object was created using a box function with gaussian edges to avoid excessive Gibbs ringing, see example in figure 3.5a. The sample distribution was altered to contain a region with zero magnetisation and this region could be varied in size. The size of the region was displayed as percentage PV given by *100*(region size)/(voxel size)*. The sample was imaged with a matrix of 64 points and with a FoV that covered

the full width of the sample, this meant there were 32 magnetic moments per pixel. The fid generated by the simulation was filtered to avoid excessive ringing created from the PV.

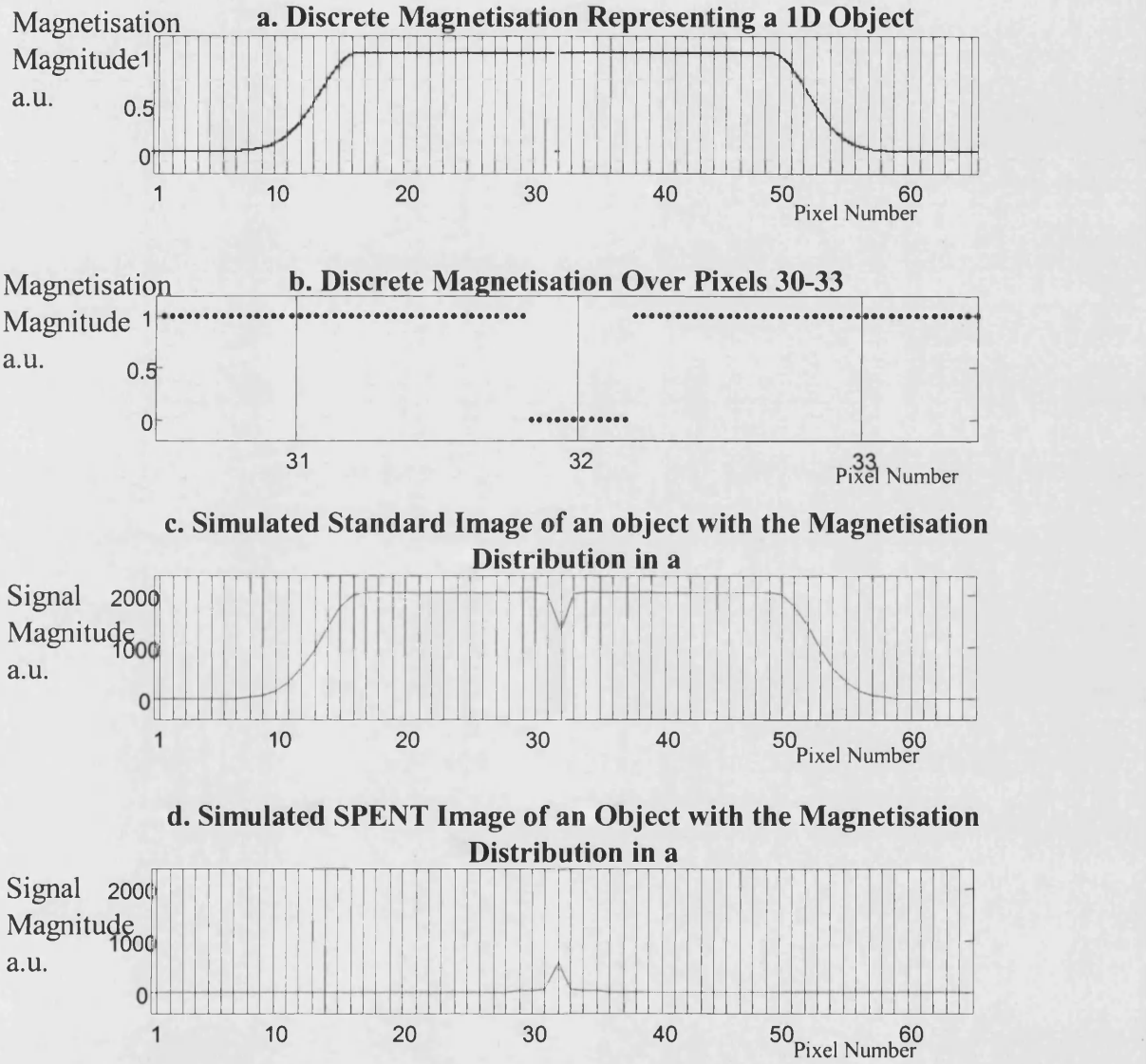

Figure 3.5 A simulation to produce standard and SPENT images of an object containing a non-uniform region of magnetisation

From the top, 3.5a shows the discrete distribution of magnetisation used in the simulation. The gridlines represent the centre of a pixel. Examining pixels 30-33 more closely, in 3.5b; the discrete positions and a region containing a partial volume are clearly seen centred on pixel 32, further highlighting the distribution of magnetisation used. In 3.5c the standard image produced with this magnetisation is shown with the SPENT image in 3.5d.

In figure 3.5, the gridlines show the position of the centre of each pixel. Pixel 32, in figure 3.5b, can be seen to contain 32 magnetic moments. The central 12 magnetic moments of pixel 32 having a magnitude of zero, simulating a voxel with a PV. The signal in the time domain is generated for different magnetisation distributions, containing different degrees of PV. This was repeated for SPENT and standard acquisitions. The time domain data was then reconstructed to obtain 1D images. Figure 3.5c shows an example of a standard image that was generated with the magnetisation distribution in figure 3.5a & b. An example of a SPENT image that was generated with the same magnetisation distribution is seen in figure 3.5d.

To investigate the Signal to Noise Ratio (SNR) and Contrast to Noise Ratio (CNR), pseudo-random noise was added to the simulated signal at a constant level. The noise was calculated for each pixel by taking the standard deviation of the signal for a set of one thousand images, the signal being the mean value over the same set. The contrast was taken as the difference between the signal in the PV pixel and the average signal from a neighbouring region of 12 pixels that lay within the sample, but that did not include the PV.

To demonstrate whether SPENT images can be used to produce a global measure of structure, a second simulation was developed. This examined the global signal produced in SPENT images by certain structures within an object. To simulate the continuous signal produced by an object in k-space, a large image matrix was constructed that contained an object at very high resolution within a large FoV. This will subsequently be referred to as the object. To simulate the k-space that this would produce the object is Fourier transformed. The high resolution k-space data is then sub-sampled both in area

and sampling density to simulate discrete sampling of continuous k-space data. If the original matrix is large in comparison to the sub-sampled version, this should provide a reasonable approximation.

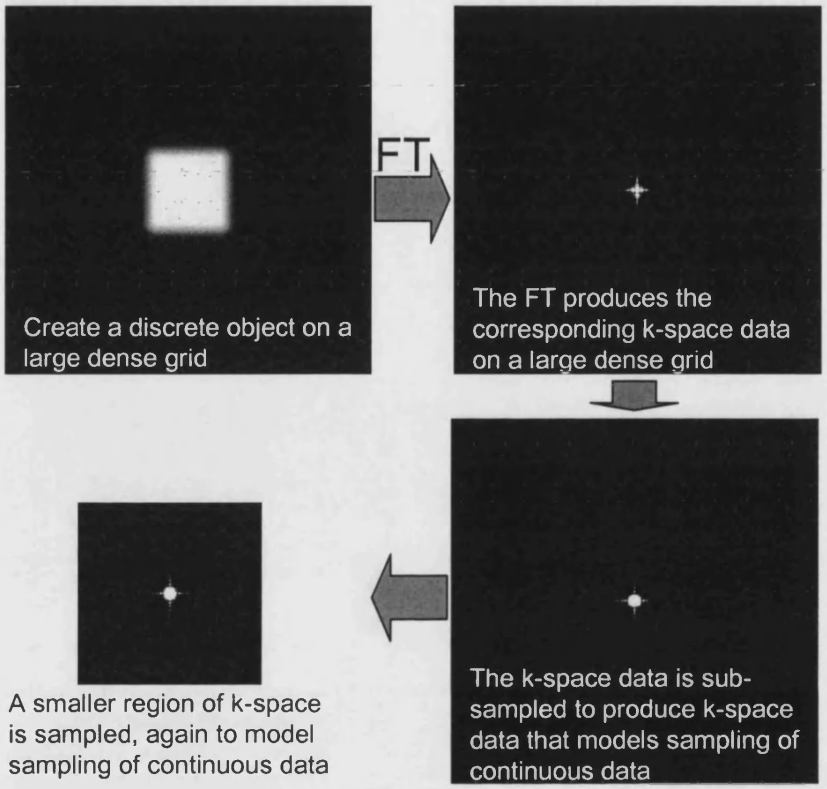

Figure 3.6A Simulating SPENT – generating k-space data
In the top left an object is created that has some structure. The object is created on a fine mesh, and over a wide FoV. The FT of this object produces the corresponding k-space data. To simulate sampling k-space, the data is sub-sampled and a reduced area is taken.

The smaller region of k-space produced in figure 3.6A is used to create images in figure 3.6B below. These images have a smaller FoV and lower resolution than the original object. In figure 3.6B, three different images (or sets of images) are produced from the same k-space data. Firstly, the whole region is FT'd to produce an image in the conventional manner. Secondly, the data was split into 9 equal tiles and FT'd to produce 9 individual images. The central image is the same as a 1/3 resolution standard image. The other images are equivalent to SPENT images with a gradient applied to produce a

2π phase wrap across each pixel in the direction of the centre of each tile from the centre of k-space.

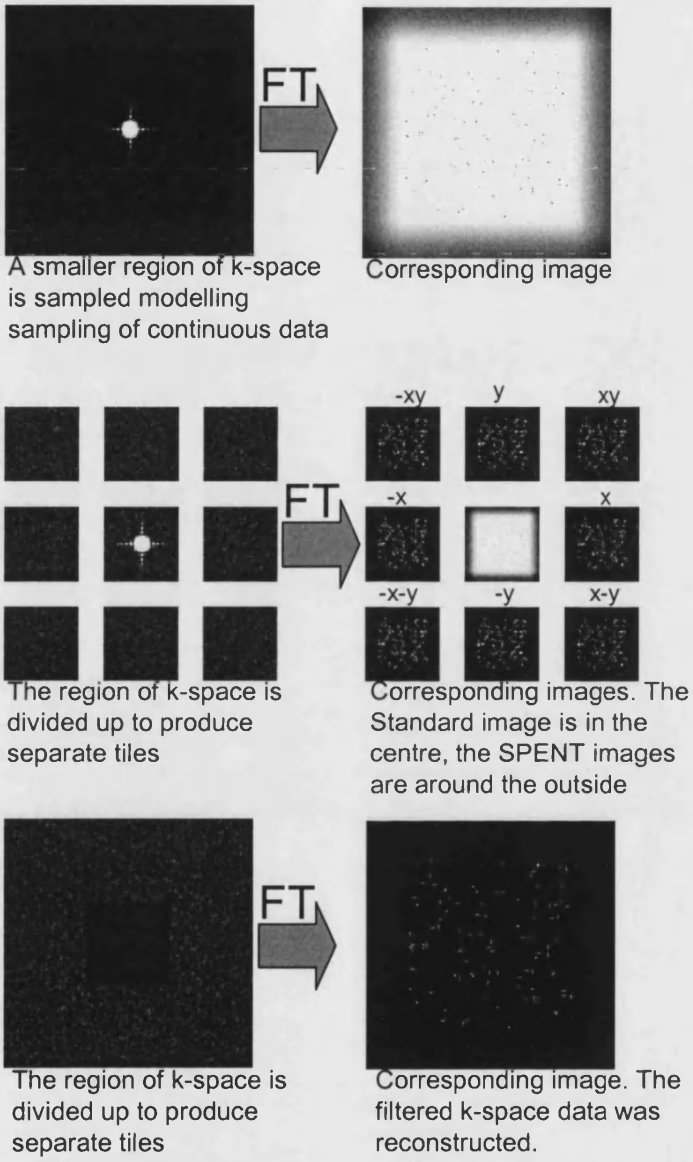

Figure 3.6B Simulating SPENT: using the simulated k-space data to produce SPENT images

On the left hand side, the k-space data obtained using the process illustrated in figure 3.6A is used in different ways. The corresponding images that are produced are seen on the right hand side. At the top the full k-space area is used to produce an image. In the middle, the k-space region is separated in to 9 equal sized tiles. This produces a standard image of 1/3 resolution of the image above and 8 SPENT images with 1/3 resolution of the image above.

In figure 3.6B, the various images produced show different behaviour. At the top, a higher resolution image demonstrates that there was some structure in the object. There were small holes in the original object (3.6A top left) that are displayed as darker pixels in the image at the top right of figure 3.6B. The tiled images in the centre right of figure 3.6B are quite different. The central image of the set shows a similar image to the one above only with a reduced resolution. The SPENT images around it have bright pixels where there is non-uniformity due to the holes in the original object. At the bottom of figure 3.6B a filtered image is seen where the central tile is made equal to zero. This creates an image similar to the SPENT images, with only the pixels containing holes appearing bright. However, the image formed by filtering k-space has a higher resolution than the SPENT images formed from the k-space tiles.

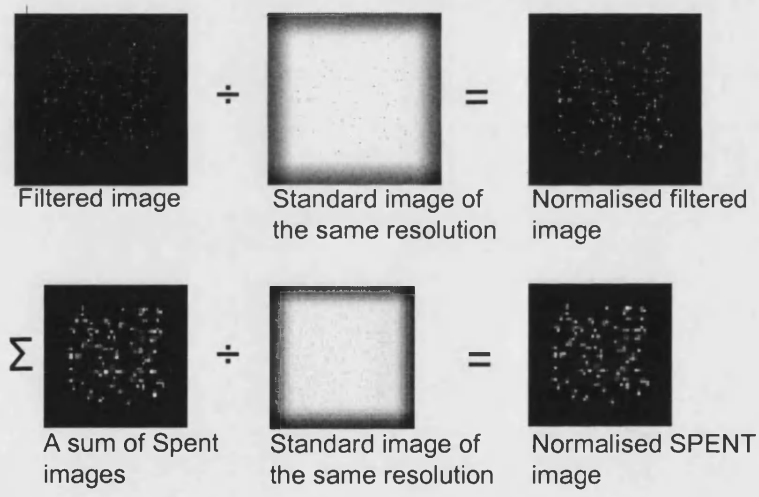

Figure 3.6C Simulating SPENT: extracting structural information from the SPENT images
The images obtained in figure 3.6B are used to gain a measure of structure. This is achieved by dividing the filtered image (from the filtered k-space region) by the standard image of the same resolution along the top row of images. On the lower row the SPENT image pixel values from a sum of the 8 SPENT images (from the 8 k-space tiles in figure 3.6B) is divided by the standard image of the same resolution (from the central k-space tiles in figure 3.6B). These images can have their global signal level measured and used to compare to structural parameters.

In figure 3.6C, the images produced by filtering and tiling k-space were divided by a standard image of the same resolution. This produces images that should have a signal intensity related to the structure in a pixel. These are called Normalised SPENT (N-SPENT) images. The global N-SPENT signal can be measured within an object or region and investigated as a correlate to structural parameters of the sample.

The simulation allowed images to be produced with different densities of holes and different sized holes lying within the original object. The holes were positioned randomly within the object. The simulation could then be run repeatedly to check that the result was not affected by the specific structure generated in any particular run. An object of 3600 pixels was created originally and this was Fourier transformed to create the time domain data. This was sub-sampled by a factor of 3 in density. The central 1/8 of the area was taken and used to obtain images. The object was varied to contain 100 different sized holes ranging from 1-10 original pixels. The simulation was also repeated with different densities of holes of 1 pixel in the original object.

3.3.2 Imaging with SPENT

A high resolution 2DFT proton density weighted image was taken of a 1.5 cm^3 bone cube. The bone cube was cut from an excised femoral head before having the marrow removed and replaced with water (see chapter 4, especially section 4.3.2 for further information on bone, its structure and its preparation). Bone is close to being MR invisible and so it forms a binary distribution of image pixel intensities with water; pixels containing bone will be dark and those containing water will be light. However, a third set of pixels will contain a partial volume (of bone and water) and will appear with intermediate signal intensity.

Experiments were performed using a 7 T, 12cm bore, Bruker Avance spectrometer using a standard spin echo sequence with the following parameters TE/TR=20/1162ms, 3cm FoV, 192x192 matrix, 1mm slice thickness. The image was reconstructed in several ways. Firstly, as in figure 3.4c, the k-space data was separated into 9 tiles of 64x64 data points and then each tile was reconstructed individually. This produces 8 separate SPENT images and a low resolution standard image.

The 8 SPENT images were summed and divided by the spin density image to give a measure of voxel homogeneity. This measure should be independent of both the direction of the structures in the xy plane and of the overall spin density of the voxel and is called a Normalised SPENT (N-SPENT) image. Secondly, a standard 2D Fourier Transform was performed on the full data matrix to obtain a full resolution image. Thirdly, a 2D box filter was applied to the full k-space data matrix. This makes the central third of k-space equal to zero while the rest remains unaltered; applying a 2D Fourier Transform to this data produced an additional image. The filtered image was processed in a similar way to the SPENT images; the filtered image was divided by the full resolution image to gain a representation of the homogeneity of a voxel.

To compare the filtered image and the combined SPENT images, the resolution of the filtered image was reduced to the same level as the tiled images. This was achieved by taking the mean value of the signal from 3x3 pixels to form a new larger pixel with the resolution of the SPENT images. The difference between the images formed from filtering and tiling was compared by subtraction after the mean value of each image had been normalised.

3.4 Results

3.4.1 Simulation Results

Figures 3.5a & b show an example magnetisation distribution that was used in the simulation. The 1D images that were created using this distribution are seen in figure 3.5c, for a standard image acquisition and figure 3.5d, for a SPENT image acquisition.

In figure 3.5c, the standard image accurately represents the overall shape of the magnetisation distribution. The non-uniform voxel (number 32) contains 20/32 of the magnetisation of its neighbours, but while a reduction in signal is clearly visible from pixel 32, its value is greater than 20/32 of the signal in the nearby pixels. The adjacent pixels (number 31 and 33) also show a reduction in signal, though they have a full quota of magnetisation. This demonstrates the signal 'bleed' that occurs between pixels in MR images that reduces the contrast of a pixel with a lower spin density, especially when it is surrounded by bright pixels. Figure 3.5d shows a SPENT image of the same object. Here, only the non-uniform voxel (32) is bright; both the background and the homogeneous regions of the sample appear dark. Again some signal can be seen to bleed, only now it is from pixel 32 into the surrounding pixels 31 and 33.

Standard and SPENT images like those in figure 3.5 were generated. In each, a different sized region of zero magnetisation was created, centred on pixel 32. In figure 3.7, the signal strength in pixels 31-33 was investigated as a function of partial volume (PV). In figures 3.7 and 3.8 the level of PV ranges from 0% for a completely full voxel, through 100% for a completely empty voxel. 150% is the maximum value and this is for a region of zero magnetisation of 1.5 voxels length, again centred on pixel 32.

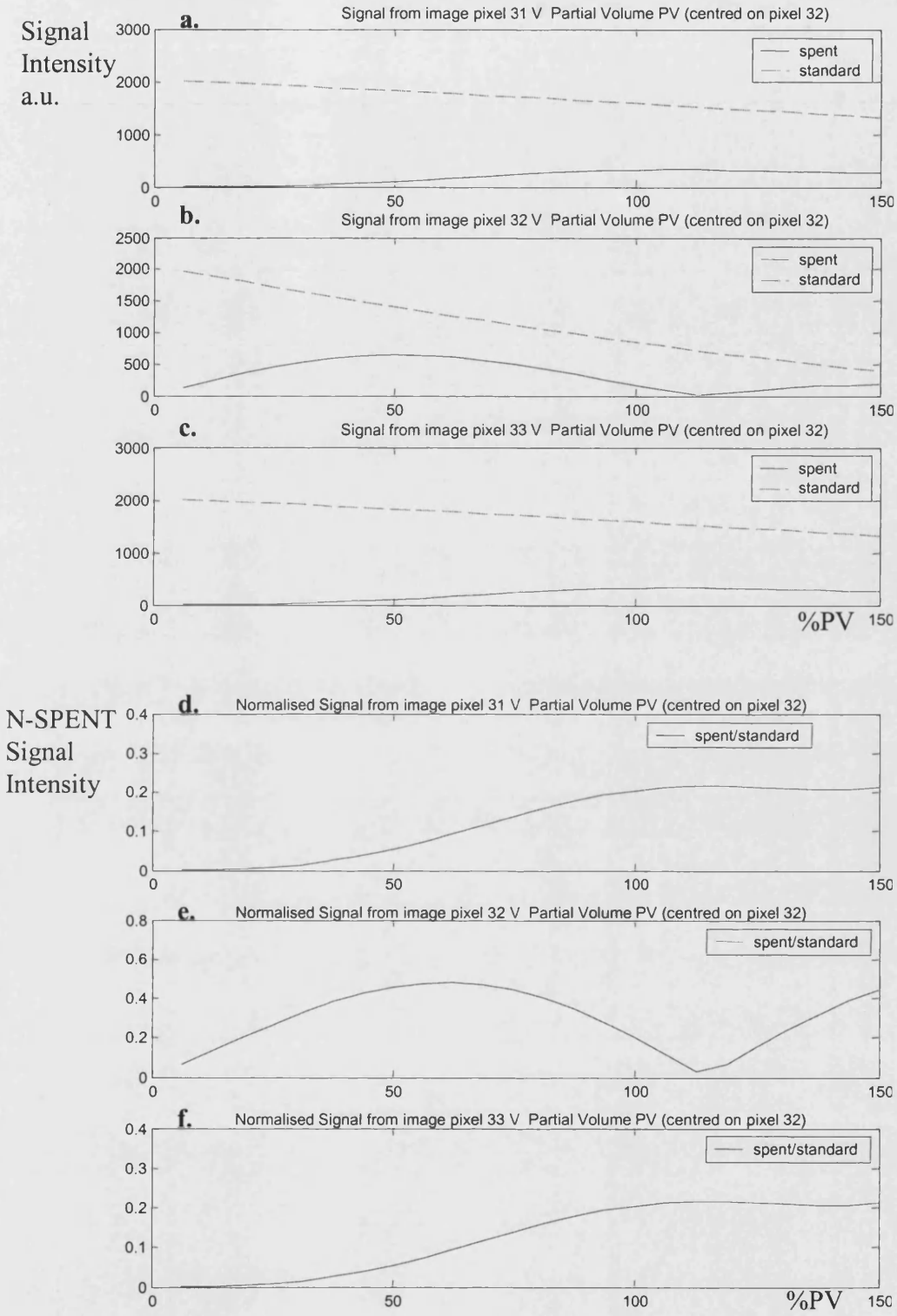

Figure 3.7 Signal from a non-uniform pixel in standard and SPENT images
The signal in a pixel is investigated with partial volume for simulated standard and SPENT 1D images. This is done for pixel 32 that contains the partial volume and for the two adjacent pixels 31 and 33. The top three plots show the magnitude signal from the SPENT and standard image pixels. The bottom three plots show the signal ratio (N-SPENT value) over the same three pixels.

The behaviour of the signal with PV is quite different for a standard image (dotted line) than for a SPENT image (continuous line). In the voxel containing the PV (32, figure 3.7b), the signal in the standard image pixel is seen to drop as the size of the PV increases. This relationship is approximately linear; however, when the voxel contains no magnetisation nearly half the signal level is still present in the pixel. This is because the signal bleeds in from magnetisation in surrounding voxels by an amount determined by the pixel's PSF. In contrast for SPENT, a full voxel (0% PV) containing uniform magnetisation produces a pixel with no signal. As the PV increases, so does the signal level in the SPENT image pixel 32, until it reaches a maximum when at ~50% PV, the signal then decreases to zero as the PV passes 100%.

The surrounding pixels (31 and 33, figures 3.7a and c) also show changes in signal intensity, despite the PV being completely contained within a different voxel for a PV<100%. In the standard images, the signal in the adjacent pixels falls as PV increases, because more signal bleeds out of voxels 31 and 33 than bleeds in from their surrounding voxels. In the SPENT images, the signal in the adjacent pixels increases, because the amount of signal that bleeds out of voxel 32 increases with PV. The SPENT image signal in the adjacent pixels 31 and 33 then continues to increase as the PV region enters these voxels.

The SPENT images were divided by the standard image to make Normalised SPENT (N-SPENT) images. These Normalised SPENT (N-SPENT) values are displayed against PV in figure 3.7d-f, for pixels 31-33. The shape of the signal response with PV is similar to the pure SPENT signal in the same pixel with values lying between 0 and 0.5. The simulation was run for several different densities of magnetic moments and the

signal intensity was calculated as in figure 3.7. The different magnetic moment densities changed the signal level of the SPENT and standard images. However, the N-SPENT contrast was not altered by quantity of magnetisation, it was only altered by the distribution (or PV size in this simulation). This result indicates that the N-SPENT images give a measure of sub-pixel uniformity that is independent of the amount of magnetisation contained within a voxel.

To assess the ability of both a SPENT and a standard image to distinguish a voxel containing a PV, the CNR was calculated for two different noise levels over a range of PV values.

In figure 3.8a, the noise level added to the image was low in comparison to the signal. The CNR with PV for each type of image is significantly different. The CNR with PV of the SPENT image pixels follows the form of the SPENT signal with PV (in figure 3.7), with most contrast found when the pixel has a PV of around 50%. This is a spin distribution within a pixel like that shown in figure 3.1a. The standard image shows a more linear relationship between CNR and PV, the largest CNR possible (where there is a pixel with zero signal amongst pixels with maximum signal) does not occur even with a region of zero magnetisation of 1.5 voxels (150% PV). This demonstrates the true image resolution is not as high as the pixel size may suggest. SPENT exhibits a higher CNR for a PV of 0-50% in figure 3.8a; this advantage is diminished when the noise level is higher as shown by figure 3.8b. This is because the SPENT signal is contrasted against a background of rectified noise: as the noise increases, the SPENT signal becomes closer to the average background level.

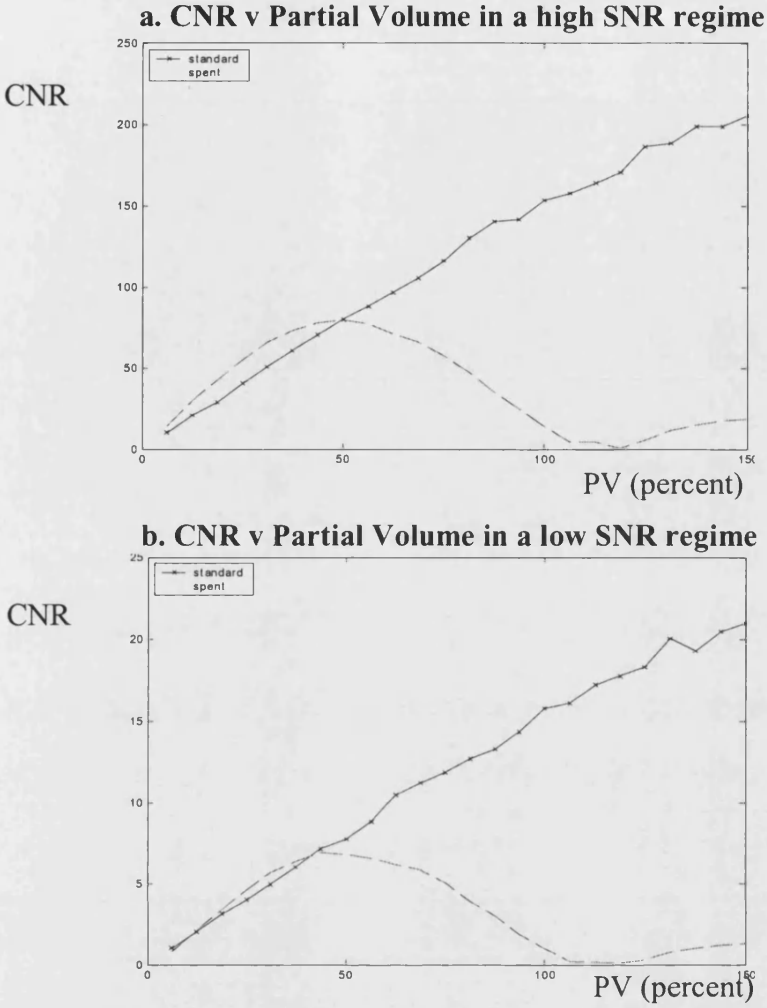

Figure 3.8 Contrast to Noise Ratio (CNR) from a non-uniform pixel in both a standard and a SPENT image
The figures above demonstrate how the CNR behaves as the level of partial volume changes within the pixel for a standard and a SPENT image. Figure 3.8a shows the signal change for a high SNR image, 3.8b shows the same result for a lower SNR regime.

In figure 3.9, the results of the simulation to examine the variation in global N-SPENT signal with sample structure are displayed. In the top graph, different densities of holes in the object were plotted against the global N-SPENT signal. A hole is a pixel of *signal=0*, as opposed to a pixel of *signal=1* in the surrounding object. The holes were randomly distributed through the object. The SPENT images that were used had a resolution of 1/3 compared to the sub-sampled data. The different SPENT directions *x*

and -x (see figure 3.6B) were displayed using different markers. This showed that the x and $-x$ directions contained the same information, which suggests that only one of these tiles of data needs to be acquired. It was also noted that all the directions gave the same response. This might be expected, because the structure in the object is approximately uniform with direction. In a uniform structure, it may be possible to extract all the desired information from two of the 9 tiles in figure 3.6B. The images from different directions can be combined by adding the N-SPENT images together. The N-SPENT signal increases with hole density in a non-linear fashion.

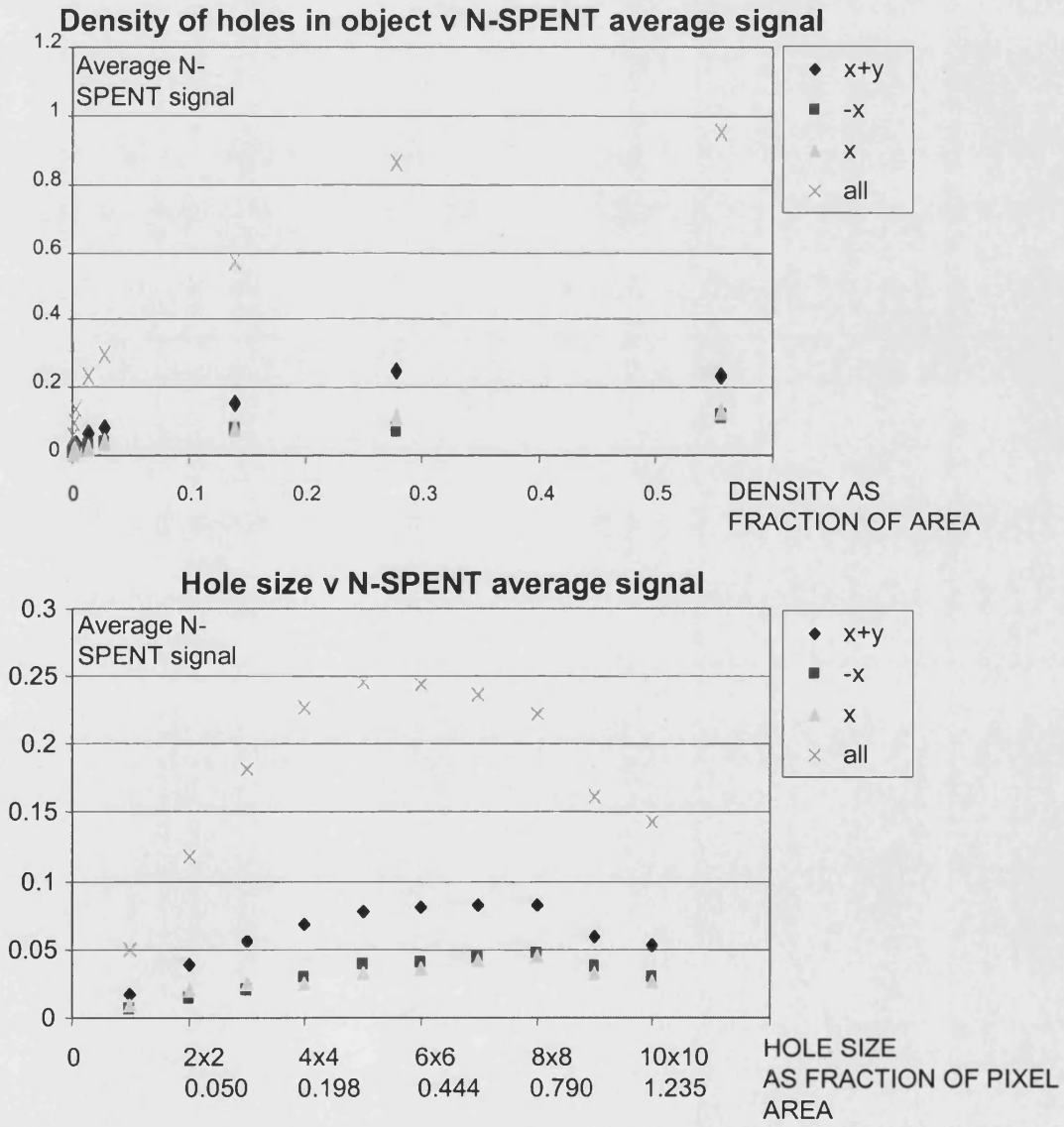

Figure 3.9 The simulated variation of global N-SPENT signal with structure of a sample

In the lower graph in figure 3.9, the same number of holes was generated, but the holes were increased in size from 1 to 10 pixels in the original object. This corresponds to a PV of between 0 and 124% (1.235 as a fraction in figure 3.9) because the image pixels are the same size as 9^2 pixels in the original object. Again, an initial increase in signal was seen with increased hole size, until the hole is significant in size compared to the pixel size. This graph follows a similar form to the 1D simulation in figure 3.7. There were some small differences between the N-SPENT signal in different directions with hole size.

3.4.2 Imaging Results

A high resolution image data set was acquired on a sample of trabecular bone. This was used to generate the nine images in figure 3.10. The central tile forms a standard proton density weighted image. The other 8 images have effectively had a 2π phase wrap imposed across each voxel in the directions indicated. This is because the gradient applied in the pulse sequence (in figure 3.2) is the correct size to acquire the adjacent k-space tile (as shown in figure 3.4a).

The signal in the SPENT images was bright where there was a non-uniform voxel, such as in the bone region or at the edges of the container. In contrast, there was no signal in the SPENT images from the homogeneous regions of pure water. In addition, the SPENT direction of the image indicated in figure 3.10 makes a difference to the image produced. The SPENT image pixels were bright when an edge cut through the voxel perpendicular to the SPENT direction. This is because the voxel was not uniform in the direction perpendicular to the structure.

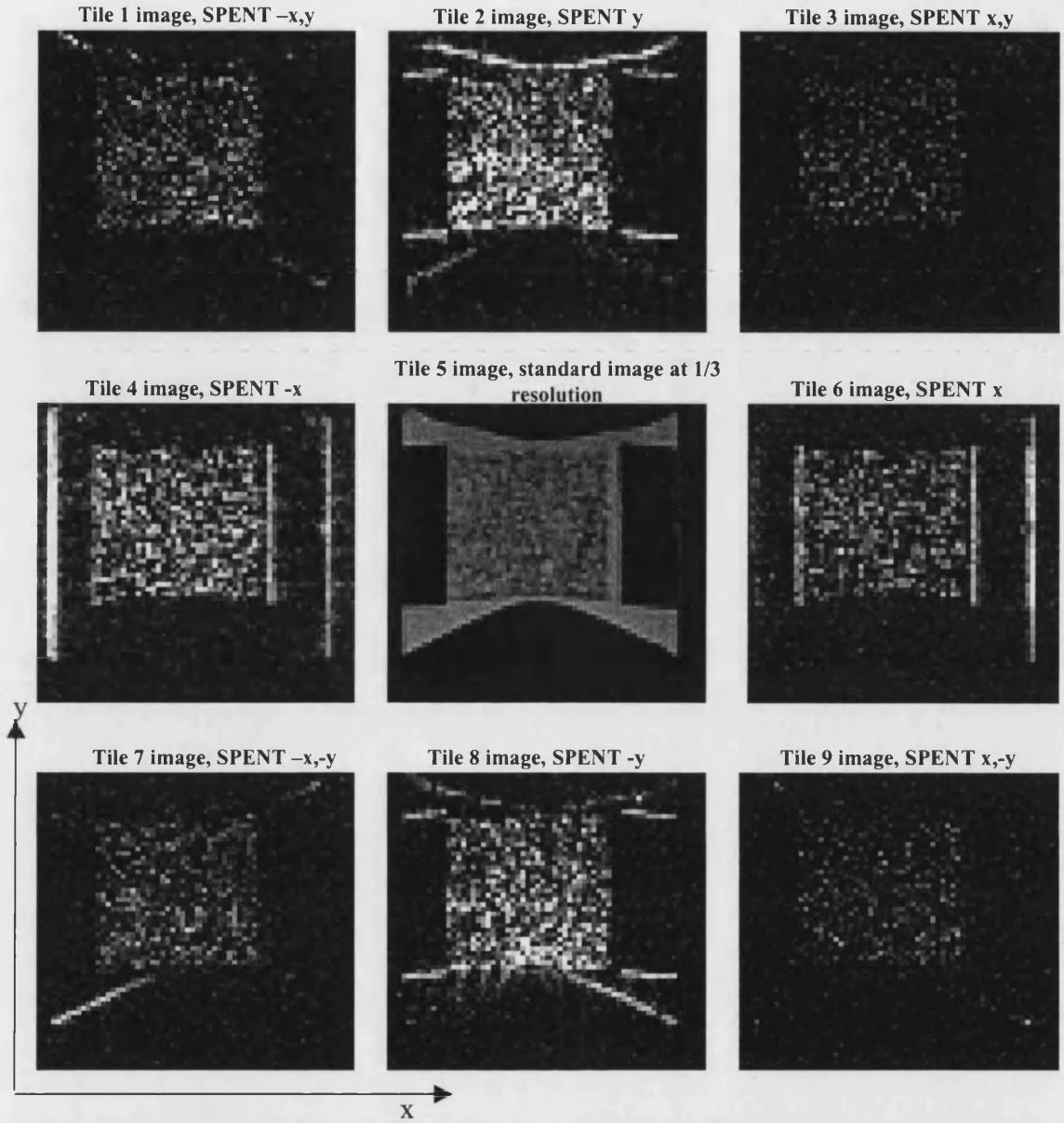

Figure 3.10 Nine 64x64 images created from different tiles of a 192x192 matrix in k-space

A high resolution data set is used to generate nine images by dividing up the raw spectrum into 9 sections (see figure 3.4c). The central tile forms a standard proton density weighted image. The other 8 images have had a 2π phase wrap imposed across each pixel in the directions indicated. The signal in these SPENT images is then bright where there is a non-uniform pixel such as in the bone region or at the edges of the container. In contrast there is no signal in the SPENT images from the homogeneous regions of pure water.

In figure 3.11a, the SPENT images were summed to give an overall measurement of homogeneity independent of direction. In figure 3.11b, the summed SPENT image

(3.11a) was divided by the standard low resolution image (tile 5 image from figure 3.10 that is formed with the central tile of the k-space that is filtered figure 3.12b) to obtain an N-SPENT image.

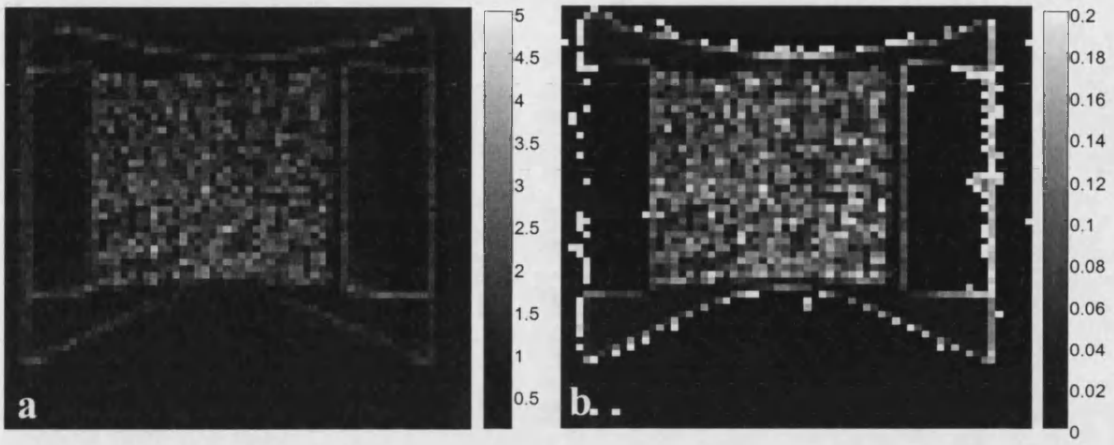

Figure 3.11 An averaged SPENT image and a normalised averaged (N-SPENT) image are created from the tiled images in figure 3.10
a. To gain a measure of the homogeneity of the pixels in all directions, the SPENT images from each of the 8 directions are averaged to form a new image
b. The averaged SPENT image is divided by the standard image. This divides out any dependence on spin density to obtain an image of spin density uniformity over the scale of a pixel.

In figure 3.12a, the same data was used to form a single high resolution image. The central 1/3 of the k-space data was then filtered and an image formed by Fourier transforming the filtered k-space data. This image uses exactly the same information that was used to make the combined SPENT image (figure 3.11a). The filtered k-space data is shown in figure 3.12b, with the image it creates in figure 3.12c. The filtered image (3.12c) was then divided by the standard image (3.12a) to obtain figure 3.12d; this produced a 'normalised' image in a similar way to the N-SPENT images. The normalised filtered image highlights the edges and inhomogeneities of the bone while leaving background and water regions dark in a similar manner to the N-SPENT image. However, the filtered image resolution is much higher than in the N-SPENT image with little visible reduction in image quality.

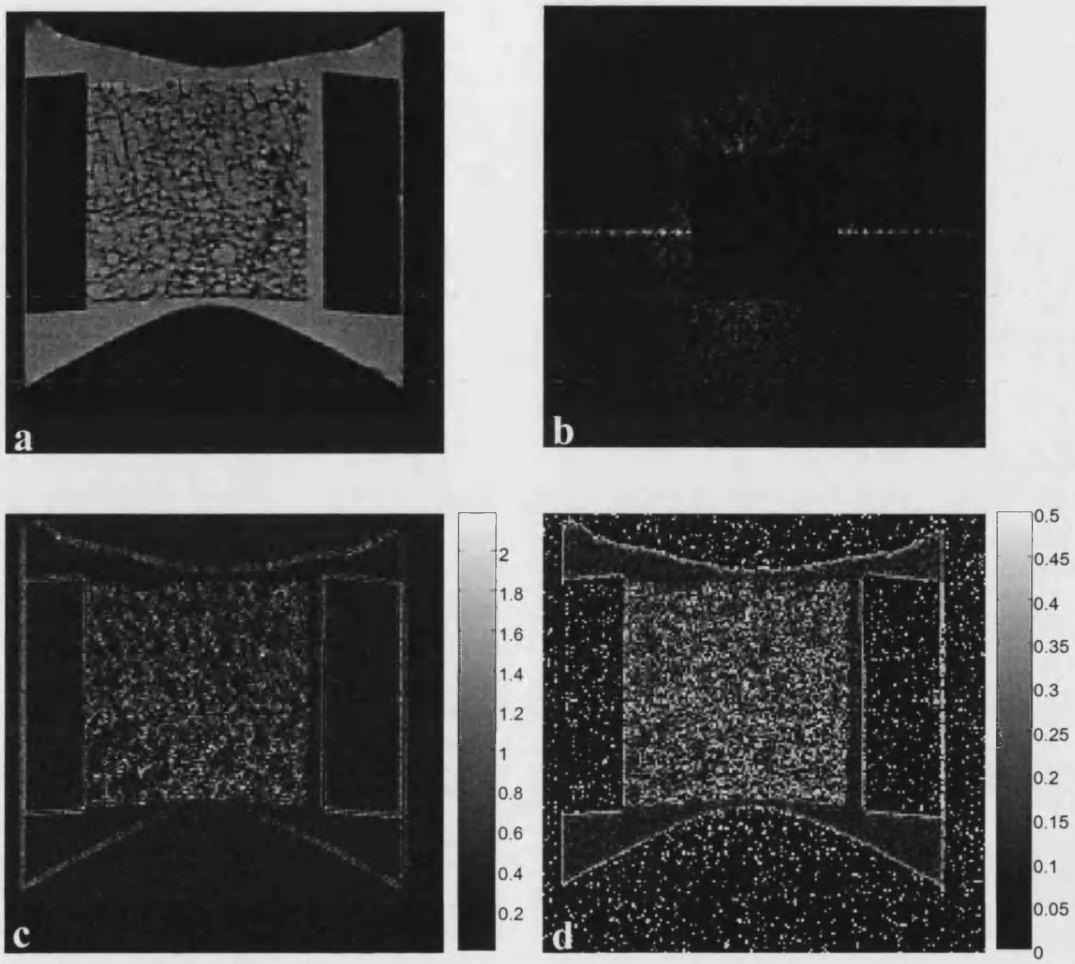

Figure 3.12 High Resolution images created from a 192x192 matrix in k-space 3.12a is a high resolution image. The k-space data used to reconstruct the image is filtered in 3.12b. 3.12c shows the image formed by reconstructing the filtered k-space data. 3.12d is the filtered image (c) divided by the high resolution image (a).

In figure 3.13c, a difference image was taken between the two 'normalised' images. First the filtered image resolution was reduced to the same resolution as the N-SPENT image by averaging pixel values together. The two images, figure 3.13a & b appear to be similar and pick out similar features: areas of uniform water appear dark and edges are clearly defined. Despite both images having been formed from the same data, there are also some clear differences between them, as demonstrated by the non-zero difference image. Broad regions do remain similar, represented by the grey areas in

figure 3.13c. However, some individual features have quite large differences in signal intensity between the images seen as black or white pixels in the difference image.

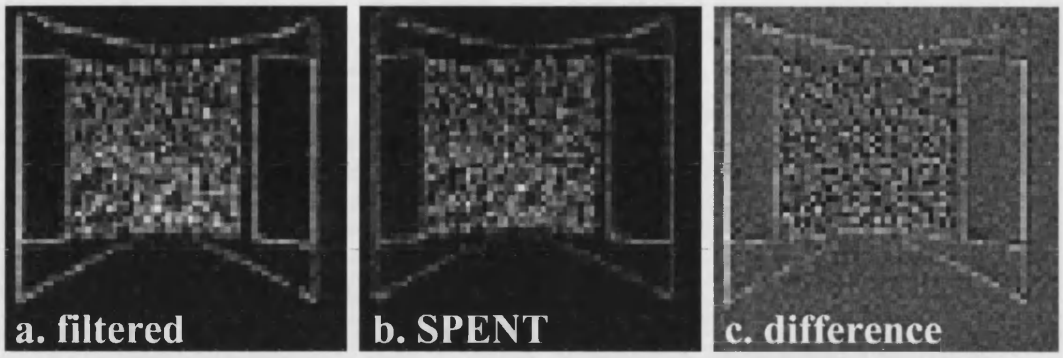

Figure 3.13 A comparison of the averaged SPENT image and the averaged filtered image
The difference image (c) shows the percentage difference between a and b and is scaled between -20% and +20%.

3.5 Discussion

To resolve smaller structures higher frequency regions of k-space must be sampled. However, these regions have lower SNR. When taking a high resolution image there is a point at which it is no longer worth acquiring data. This is because the SNR of the data degrades image quality without adding useful information about smaller structures. To improve the imaging of smaller structures it is necessary to measure the higher frequency regions of k-space with better SNR.

Increased SNR may be achieved by averaging in k-space or image space. However, image acquisition must normally be performed in a limited period and the speed of k-space traversal is fixed by gradient performance. This means improvements in resolution can normally only be achieved via more efficient sampling. A secondary consideration relates to the true resolution of the images. In MR images, signal from a physical position is distributed in an image: the PSF is used to describe this distribution. This means that in a bright region of an image corresponding to a high proton density a

small region of low proton density appears 'filled in' by signal from surrounding voxels and so is hard to resolve.

Some structural features of a sample may be related to the magnetisation homogeneity of the pixels in SPENT images. If so, SPENT images may be useful for extracting structural information. The non-linear contrast behaviour even for the simple structure used, seen in the simulation results (figure 4.9), suggests that the relationship between structure and N-SPENT signal may be complicated, especially in real, more complex structures.

The main points that need to be addressed in this section are: i) can SPENT improve resolution or probe sub-voxel structures beyond what a high resolution image could achieve in the same acquisition time? ii) Are there any improvements in the ability to resolve small structures in SPENT images as compared to standard images, due to differences in the PSF and bleed of signal between pixels? And, iii) is SPENT a simple way to extract architectural or structural information about a sample without the need for complicated and potentially biased image processing methods?

3.5.1 Can SPENT Improve Resolution or Probe Sub-Voxel Structures Beyond What a High Resolution Image Could Achieve in the Same Acquisition Time?

To improve the resolution of smaller structures k-space must be sampled with greater SNR by sampling more efficiently. In figure 3.4, various regimes for image acquisition were presented. Firstly, a low resolution image could be acquired. Alternatively, an image acquisition could be performed with 3 times the resolution. This data could be used to reconstruct a high resolution image, or, the separate tiles could be used to form a

standard, lower resolution image and 8 SPENT images. A time saving of 1/3 can be made to the acquisition while sampling 5/9 of the area to gain the low resolution image with two averages and a further 4 SPENT images. The time saving of 1/3 can be made, but this comes at a cost to the amount of information collected. If similar structural information about an object was obtained in the different SPENT images, time saving strategies could be employed, and a significant time saving would be possible. This would be particularly useful if regular structures allowed some structural information to be gained from a few of the k-space tiles/SPENT directions.

3.5.2 Are There Any Improvements in the Ability to Resolve Small Structures Using SPENT Images Compared to Standard Images?

The performance of a SPENT image was examined and compared with a standard image of the same resolution. The signal and contrast were investigated as a function of partial volume. In figure 3.7, the difference in the contrast is clear: The SPENT image pixels display a signal dependence that is non-linear and is most sensitive to a 50% partial volume. This is the point at which the voxel has the greatest level of non-uniformity and so the pixel signal is representative of the level of sub-voxel uniformity.

In some structures, the non-uniform voxel is surrounded with voxels containing full magnetisation. In the standard image, this means there is signal bleed into the non-uniform pixel. This is in contrast to the SPENT image where signal bleeds out of an isolated bright pixel. The PSF is the same for these two images and so the signal bleed out in the bright SPENT image pixel is the same as the bleed in seen in the standard image. The standard image shows less contrast than the SPENT image over low PV values (see figure 3.8) because there are more bright pixels making a significant

contribution to 'filling in' the signal. The contrast to noise ratio for a pixel with PV (figure 3.8) demonstrates that any advantage from the 'filling in' effect appears to be minimal in the low SNR regime in which SPENT would be most likely to find application. This is because the signal in a SPENT image pixel is seen against a background of rectified noise, lessening the contrast between a pixel with a PV and the surrounding dark pixels. The standard image resolved small structures with a higher CNR. This suggests that, to resolve a structure, the best strategy is to take the highest resolution standard image possible in a certain time, while maintaining the SNR of the image at a certain level.

3.5.3 Can SPENT be Used to Display Structural Information About a Sample?

If the CNR for a PV in a SPENT image was no better than in a standard image, was there any advantage to processing the high resolution image data to gain architectural information about a sample by creating filtered, or SPENT images from the data? There were three choices used here.

Firstly, the most obvious approach was to create a full resolution image like that in figure 3.10a. The advantages of this were that the full amount of information was used and that the PSF of the image pixels was minimised due to the larger window in k-space. The high resolution image can be used with various processing procedures to gain estimates of structural parameters such as, in the case of a bone cube, surface area and trabecular thickness. The potential disadvantages of this approach are that good SNR is necessary to gain accurate global measures of structural parameters. Also, the structural parameters can be affected by user dependent variables such as threshold

levels and the details of the structure in the higher k-space regions are dominated by the stronger, lower frequency components.

Secondly, the high resolution k-space data was filtered to obtain an image of edges and inhomogeneous regions. This removed the influence of the lower frequency components and maintained the pixel resolution while using the same data as the combined SPENT image.

Thirdly, a combined SPENT image was itself used to obtain a 1/3 lower resolution image sensitive to sub voxel non-uniformity. The filtered data, and the image generated from it, was displayed in figure 3.12. The image (3.12c) clearly picks out smaller structures without showing any of the broader regions of homogeneous water; the contrast appears similar to the SPENT image (figure 3.11a) but with a greater resolution. The filtered image pixels have a worse PSF than in the standard high resolution image because of the k-space filter that is applied. However, the quality of the filtered image appears high and the contrast shows pixels that are on the edge of a structure. In contrast, the combined SPENT image (figure 3.11) had a lower resolution and its pixels containing an edge or PV appeared bright, even though on a standard image of the same resolution the edge or PV cannot be clearly identified.

The similarity between the information displayed in the filtered and SPENT images was demonstrated in figure 3.11, where the filtered image had been averaged to be at the same resolution as the SPENT image. Many similar structures are seen with lower signal apparent in the less homogeneous regions. The filtered image seems to show similar information to the SPENT image while assigning the signal to a more accurate

position in space, though for a global measure of structure this may not be required. Both ways of displaying the higher frequency data were normalised to produce the 'uniformity maps' in figures 3.11b and 3.12d. The N-SPENT map should give a measure of magnetisation distribution that is independent of the amount of magnetisation in a given voxel.

The relationship between N-SPENT signal and structure was investigated by using a simulation of randomly distributed holes in an object of uniform spin density. The size and density of the holes was varied and the global N-SPENT signal was measured. The N-SPENT signal increased with both size and density of the holes. The exact relationship between the structural parameters (size and density) was not simple even in the basic model used here (see figure 3.9). In addition to the structural parameters of the sample, the size of the pixels used in the SPENT images also appears to make some difference. In each different structure and especially in more complicated ones, the relationship between the global N-SPENT signal and structural parameters of a sample are likely to be complicated. However, in general the global N-SPENT signal should increase with the size and density of the structures in the object when the structure is around the size of a pixel.

3.6 Preliminary Conclusions and Future Work

SPENT does not intrinsically improve resolution or probe sub-voxel structures beyond those attainable with the highest resolution image possible in a given time because neither sampling efficiency nor SNR is intrinsically increased. The advantage of SPENT is that signal bleed into pixels is reduced in regions of high signal intensity.

However, simulations show SPENT does not increase the CNR of pixels containing a PV.

The SPENT images represent a simple way to extract architectural or structural information about the sample without the need for complicated and potentially biased image processing methods. In general, the N-SPENT signal increased with the level of structure in a simple model.

Further work is required to ascertain the exact relation and quality of the SPENT or filtered image information to existing measures of structure. This is also likely to be highly dependent on the structure of the samples that are imaged.

3.7 References

1. Torrey, H. C. 1956, "Bloch equations with diffusion terms", *Physical Review*, vol. 104, no. 3, pp. 563-565.

2. Le Bihan, D. 1991, "Molecular diffusion nuclear magnetic resonance imaging", *Magnetic Resonance Quarterly*, vol. 7, pp. 1-30.

3. Stejskal, E. O. & Tanner, J. E. 1965, "Spin diffusion measurements: spin echoes in the presence of a time dependent field gradient", *Journal of Chemical Physics*, vol. 42, pp. 288-292.

4. Carmichael, D. W., Ordidge, R. J., and Yiannakas, M. 2002, "SPENT (Sub Pixel Enhancement of Non-Uniform Tissue): A New Pulse Sequence and its Application to Bone Imaging", *Proc.10th Annual Meeting of the ISMRM*, vol. 296.

5. Watts, R. & Wang, Y. 2002, "k-space interpretation of the Rose Model: noise limitation on the detectable resolution in MRI", *Magn Reson.Med*, vol. 48, no. 3, pp. 550-554.

6. Haacke, E. M., Brown, R. W., Thompson, M. R., & Venkatesan, R. 1999, "Signal Contrast and Noise," in *Magnetic Resonance Imaging Physical Principles and Sequence design*, 1 edn, E. M. Haacke et al., eds., John Wiley and Sons, New York, USA, pp. 331-378.

7. van Vaals, J. J., Brummer, M. E., Dixon, W. T., Tuithof, H. H., Engels, H., Nelson, R. C., Gerety, B. M., Chezmar, J. L., & den Boer, J. A. 1993, ""Keyhole" method for accelerating imaging of contrast agent uptake", *J.Magn Reson.Imaging*, vol. 3, no. 4, pp. 671-675.

8. Gao, J. H., Xiong, J., Lai, S., Haacke, E. M., Woldorff, M. G., Li, J., & Fox, P. T. 1996, "Improving the temporal resolution of functional MR imaging using keyhole techniques", *Magn Reson.Med*, vol. 35, no. 6, pp. 854-860.

4. Assessing the Structure of Bone with MRI

Osteoporosis is a disease that affects millions of people worldwide and is becoming progressively more common as the worlds population ages. To assess the disease Bone Mineral Density (BMD) is normally used as a predictive measure of bone strength. This is normally achieved using Dual-Energy X-ray Absoptiometry (DEXA). DEXA is limited by its accuracy; it measures 'area' density rather than 'true' density. In addition, it imparts a dose of radiation. MRI can provide a non-invasive investigation of bone density and structure. However, MRI assessment of bone has been limited in a clinical setting by the resolution and sensitivity of the images available.

The main aim of this chapter was to investigate the use of MRI to assess the structure, and most importantly, strength of trabecular bone. Excised samples were used, both to enable a direct measure of bone strength and to remove complicating factors, present in vivo such as the composition of fat in the bone. MR relaxation rate constants R_2 and R_2', SPENT and bone volume calculated from MR images were compared to i) the Young's Modulus (YM) of the bone that is a measure of the bones biomechanical strength, and ii) Bone Mineral Density (BMD) measured using both DEXA and by weighing.

The assistance of Marios Yiannakas is acknowledged in this section.

4.1 Background

Osteoporosis is a disease that affects the skeletal system and is strongly associated with increased age. The disease is a large and growing problem: 'Osteoporotic fractures are a frequent and important cause of disability and medical costs worldwide' [1], with the cost for osteoporotic fractures estimated at $13·8 billion in 1995 ($17 billion dollars in 2001) in the USA [1,2]. Due to the association of osteoporosis with age, this figure is set to rise as the average age of the world's population increases. While there are genetic factors that can cause the early onset of osteoporosis [3] it is a universal problem from middle age onwards. The main danger to people with osteoporosis is a bone fracture that can result in increased chances of disability and morbidity. The most common sites for fractures are the hip, vertebrae, upper femur and wrist. All these sites predominantly contain trabecular bone [4,5] that consists of an interconnecting network of plates and rods to form a strong and lightweight structure. The trabecular bone is present in regions that take a mechanical load. While it is not surprising that the regions that carry high loads are more prone to fracture, trabecular bone also responds up to eight times faster to metabolic stimuli and exhibits the earliest changes in bone volume [6] due to osteoporosis.

In osteoporosis, there is a degeneration of bone that can be characterised by two factors. These is a loss of both bone mineral content and bone volume [1] that occurs via the constant process of bone turnover. This process can change the mass and architecture of the bone, though the exact relation of bone turnover to bone strength is complex [7,8].

A number of methods have been used to determine fracture risk that can be classified into two groups. Firstly, there are techniques to measure the change in Bone Mineral

Density (BMD); these include Radiographic Absorptiometry (RA), Single or Dual Photon Absorptiometry (S/DPA), Single or Dual Energy X-ray Absorptiometry (S/DEXA). All of these methods measure the rate of absorption of photons at various energies. BMD provides a good degree of correlation with fracture risk [9-11]. However, BMD does not take into account bone architecture, which is an important factor in bone strength [12,13]. These BMD measurements are also limited by accuracy and precision; other tissue types, such as cortical bone, contaminate most accessible sites for measurement. In addition, the density is measured over an area, so the size or width of bone at a given site in a given subject also contributes to the measured BMD. The 'true' BMD would be measured within a well-defined volume only containing trabecular bone.

Studies have used BMD measured by DEXA because it is the conventional method for assessing fracture risk. It is noted here that this technique is limited to a measurement of density area, is not the only determinant of strength and imparts a radiation dose. Although the radiation dose imparted is not prohibitively high, DEXA is not an ideal technique for screening patients, or for studying disease. It would therefore, be desirable to use an alternative method to obtain BMD.

Computed Tomography (CT) and Magnetic Resonance Imaging (MRI) can provide structural measurements of the bone from high resolution images. From the images estimates of Bone Volume Fraction (BVF – very similar to BMD) can be made. While CT can provide a good assessment of BVF and bone architecture, to do so accurately requires a significant radiation dose and is often beyond the capabilities of a standard clinical CT scanner [14]. MRI can provide high quality information on BVF and

architecture and crucially, it is the only non-invasive way of gaining this level of information. This makes MRI invaluable in research, and in a more clinical setting, for investigating osteoporosis. However, MRI is limited by sensitivity and cost. The resolution and Signal to Noise Ratio (SNR) required to accurately assess bone structure and volume in vivo is difficult to achieve on standard machines, and has only been performed in peripheral sites of the skeleton [15,16].

4.2 Introduction

MRI has been used to determine the fracture risk of bone in two distinct ways. The first relies on the acquisition of high resolution structural images. This normally requires an imaging resolution that can resolve trabecular structures that are typically of the order of 200 microns. The images can then be processed to derive a large range of structural parameters. The most common is Bone Volume Fraction (BVF) that gives a measure of the ratio of bone to marrow, which has been performed in samples [5,17,18] and in vivo [15,16,19-21]. The BVF has also been estimated using low resolution MR, by directly calculating the fraction of bone present from the signal intensity [22]. The BVF gives a measure of bone structure that is similar to BMD because the density of bone is reasonably consistent in comparison to changes in bone volume in osteoporosis. Thus, a change in density normally results from a change in bone volume. It is noted that the mineral content of bone can vary without producing large changes in bone volume particularly in some diseases.

Architecture is also important in determining bone strength [12,13] and a whole range of structural parameters have been measured from the high resolution MR images and correlated to bone strength and BMD [16,19,23-29]. The parameters that are commonly

used are BVF, mean trabecular width and mean trabecular spacing. More complex parameters such as three dimensional connectivity [23], fabric tensor [12] in three dimensions and texture related parameters such as fractal dimension [30,31] are also used. Most of these processes rely on image segmentation by thresholding to obtain a binary image of voxels containing bone and water / marrow respectively. Sub-voxel processing is often used to reduce blurring due to voxels containing a partial volume, which reduce the accuracy of the image segmentation and the subsequent structural measures that are obtained.

There are two large drawbacks with all of the methods stated above. All these methods require good image uniformity and all but the work in reference [22] require high quality, high resolution images of the bone. At clinical field strengths images at this resolution are not reliably obtainable in a reasonable time scale. It is also noted that the work done so far in vivo has been limited to peripheral sites such as the heel and wrist. Further problems arise from non-uniform images that can result from coil loading or RF penetration effects. To accurately segment an image, or to map directly from signal intensity to bone density, the images must be uniformly sensitive to signal over a large volume in patients. Additionally, generating more complicated results from more complicated image processing methods presents a greater challenge for the widespread use of these techniques in a more clinical environment.

Secondly, relaxation parameters have been measured and used to infer bone strength. The relaxation rate R_2' ($1/T_2'$ described in section 2.4.2), characterised by a loss of coherence through spatial variation in the main magnetic field B_0, is generally regarded as the most useful. The relaxation rate R_2 is considered not to be strongly related to

bone structure or density. The effect of bone structure on the local magnetic field has been both modelled and simulated showing that R_2' will be altered by the bones structure and the orientation of this structure to the main magnetic field [32-34]. R_2' and R_2 have been measured in samples [18,32,35-37] and in vivo [19,38-40]. Unlike R_2', R_2 is not thought to be directly related to bone structure. The level of anisotropy in bone architecture has been investigated with both structural and relaxation parameters [27,37,41,42]. The work presented here follows the body of work outlined above, and investigates the relationship between R_2', R_2, BVF, BMD and Young's Modulus. In addition, SPENT is investigated as a means for extracting architectural information from low resolution images. Bone samples are used in this study to eliminate contaminating effects of marrow composition and variability. Thus, only the effects of the bones structure are apparent in the various results presented here.

The question that this, and future work in the same area must address, is whether MRI can reliably measure fracture risk to produce simple easily interpreted results? This must be achieved at clinical field strength and in different body sites including the femoral head. In this work, an investigation of MR relaxometry and SPENT is described as a promising alternative to DEXA for measuring bone fracture risk.

4.3 Methods

4.3.1 RF Coil and Pod

The requirements for imaging bone were good SNR and a reasonable level of B_1 uniformity. A saddle coil [43] was built that retained close coupling to the sample while offering a good level of B_1 uniformity in the imaging region. The coil was tuned to ^1H at 300 MHz for imaging at 7 T. The coil was fixed to a Perspex pod that just fitted the

magnet bore size of 12 cm, so that when inserted down the bore the coil centre matched the magnet bore centre in the *x*,*y* directions. The *z* position of the coil could be adjusted by sliding the entire pod down the magnet bore. The coil was mounted on a cylindrical tube with a diameter sufficient to just fit a standard 50ml syringe inside.

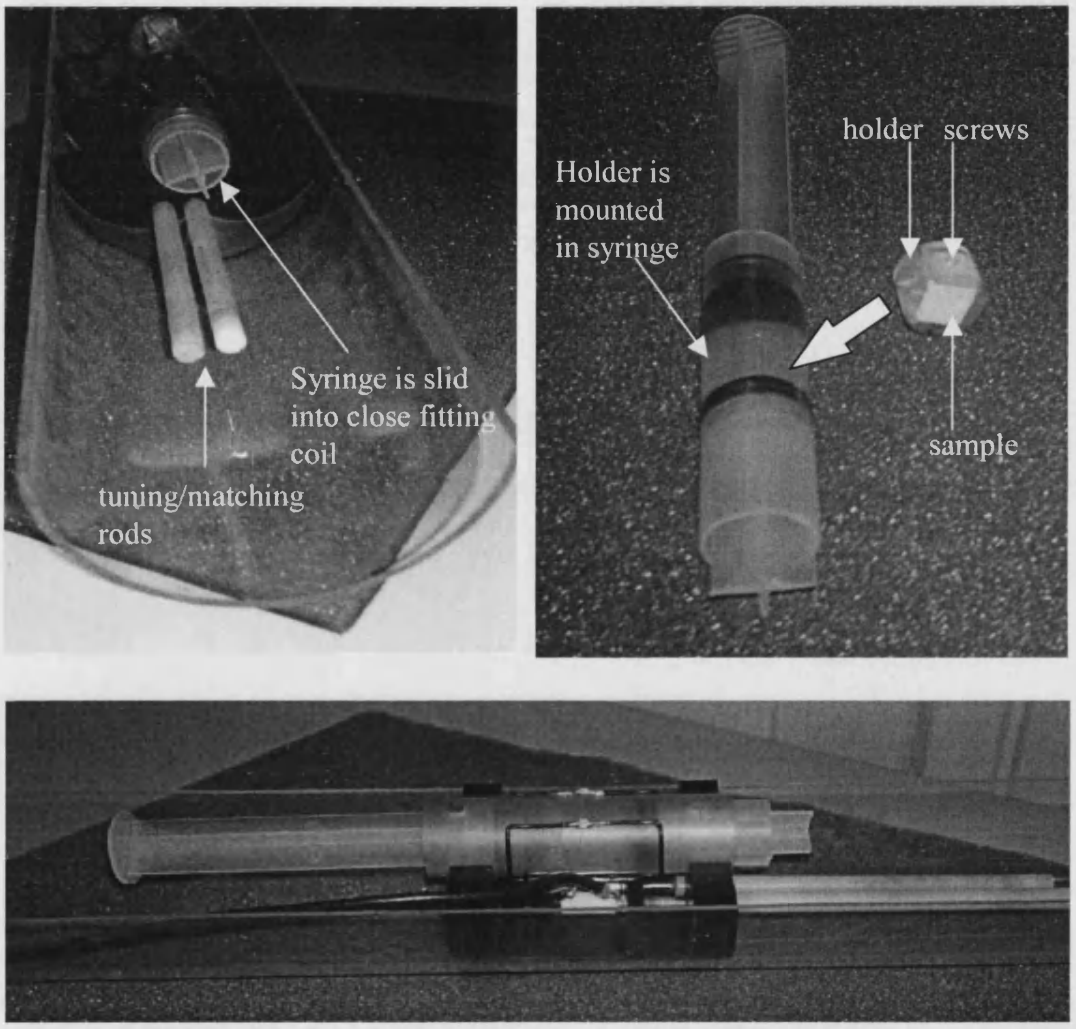

Figure 4.1 The experimental apparatus

A saddle coil was built into a pod that allowed easy positioning of the sample in the centre of the magnet bore. The sample was held in a Perspex holder that was the correct size to fit in a syringe. The syringe was then easily mounted within the coil.

The 1.5cm^3 sample needed to be positioned accurately in the centre of the magnet to ensure good B_0 homogeneity. This also ensured that measurements would be more

accurate and repeatable. It was necessary to ensure that the bone samples were fully immersed in water and contained no air bubbles either inside the bone cube or in it's near surroundings. To perform this task a plastic holding device was created. This was a precisely cut plastic cylinder with a square hole for the cubes to be inserted into. The bone cube could then be secured with plastic screws so that it fitted securely in the ring. The ring with a sample inside could then be slid into the 50 ml syringe. The syringe had its nose cut off so that it had two similar open sides. Two syringe handles were then inserted one at either end so that the sample could not move. The entire operation of fixing the sample into the syringe was performed under water to avoid the introduction of air. To remove any air or excess water in the syringe a needle could be inserted and pressure applied to the handle. This will force the excess air or water out via the needle. Once the sample was secured in the syringe it could be slid into the coil, which in turn could be positioned to place the cube repeatedly in the magnets iso-centre. The bone cubes were cut and positioned so that the majority of their trabecular bone structure was in the same direction as the B_0 field. The approximate direction of the majority of the bone structure is also termed the 'direction of trabecular flow' in his work. This was the readout direction used for the SPENT image acquisitions discussed later. Due it being the readout direction it is termed the *x*-direction in later sections i.e. the *x*-direction as used later in this chapter is the direction of trabecular flow, but it is not what is normally termed the *x*-direction in the MR scanner.

4.3.2 Trabecular Bone Samples

The trabecular bone samples were prepared using an established technique [44]. The samples used were 1.5cm^3 cubes cut from an excised human femoral head, in a location determined on the basis of two perpendicular radiographs. The femur was chosen due to

the accessibility of samples (because of the number of hip replacements) and its strong trabecular architecture. It is also where other studies have found the greatest level of sensitivity to osteoporotic changes in turnover [6] and is the site which has the greatest cost both financially, and in terms of disability, from osteoporotic fractures [45]. The area chosen to collect samples was carefully selected to lie in a region at the top of femur above Ward's triangle, as shown in figure 4.2, where there is a well-defined orientation of both stress and trabecular flow.

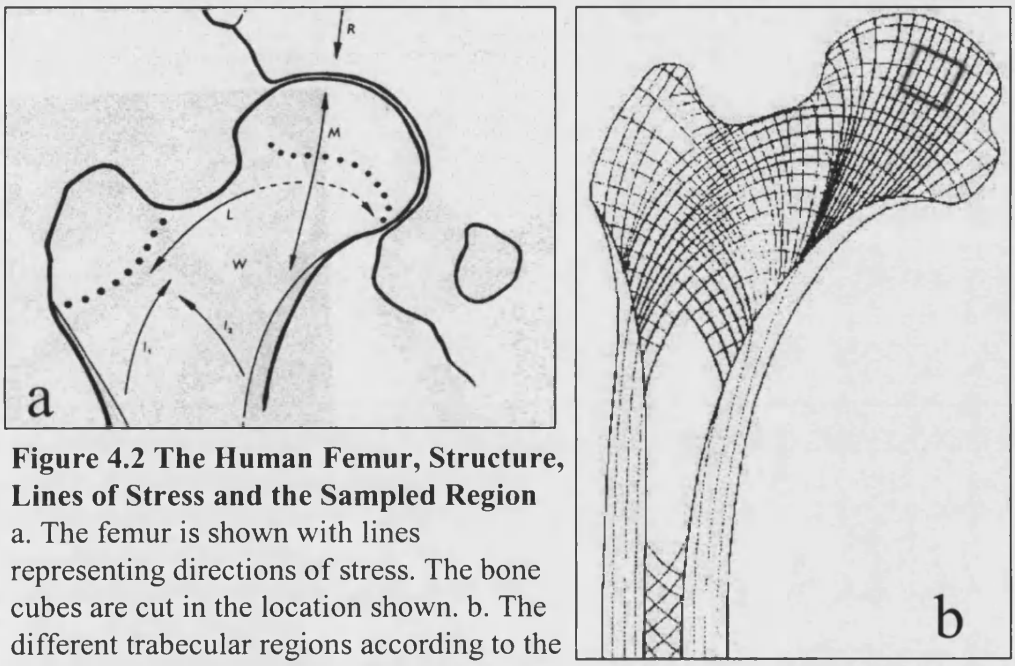

Figure 4.2 The Human Femur, Structure, Lines of Stress and the Sampled Region
a. The femur is shown with lines representing directions of stress. The bone cubes are cut in the location shown. b. The different trabecular regions according to the distribution of stress (From Whitehouse & Dyson, 1974, p422).

The cubes were cut using an Isomet 1000 precision saw with a diamond blade. Then, once cut, the marrow lipids were removed from the samples. The samples required the removal of marrow because the cutting process allows some of the marrow to escape and yellow marrow can degrade with exposure to oxygen in air. The introduction of any small air bubbles in the cutting process could dramatically change MR measurements and image quality. The cubes had their marrow removed via a process of emersion in an

enzyme-based detergent (Alconox Terg-a-zyme) and a 40°C temperature controlled ultrasonic bath.

The size of the bone cubes was determined by the ability to penetrate the sample and remove the fat effectively. The samples were verified as being clean by immersing them in ethanol, then pouring the ethanol into water. When no fat dissolves from the sample into the ethanol, it will form a clear solution with water. To image the bone samples the fat was replaced with water. The cleaned samples were immersed in a beaker of water before being placed in a vacuum pump (Edwards No 5, High Vacuum International, U.K.) to ensure the water fully penetrates the sample and that no gas remains. This process was normally achieved in 45-60 minutes.

4.3.3 MR Measurements

All measurements were performed on a 7 T, 12cm bore, Bruker Avance spectrometer running under Paravision 2.0. A number of standard sequences supplied by the manufacturer were used.

An adapted Spin Echo (SE) sequence (MSME_mod) was used to measure T_2. The level of diffusion was predicted to be a significant factor affecting the measured value of T_2 due to the sample being filled with free water. This would not normally be such a strong influence because water protons in marrow are much less mobile. The sequence was changed to minimise the effect of diffusion on the T_2 value. This was achieved by putting gradient dephasing and refocusing lobes as close together as possible and making the spacing between these lobes invariant with echo time (TE). Three different echo times were chosen to sample a significant portion of the decay.

The sequence was tested in two modes. Firstly, three different images with different TE values are obtained in separate acquisitions. Initially the TE values used were 20ms, 40ms and 60ms. Secondly, three images were formed from multiple echoes obtained in the same acquisition by the insertion of extra 180° RF pulses. The echo times used were 20ms, 40ms and 60ms with an image being formed at each. The other parameters used were FoV=3cm / TR=3000ms / Matrix size=96x96 / 16 adjacent slices acquired in an interlaced order / slice thickness=1mm. Both protocols achieved a precise measurement (see table 4.1). While there would be a time advantage for using a multiple echo sequence in vivo, there were less time constraints for the imaging protocol used in the samples. Here, the multiple single echo approach was used on all the samples to obtain values of T_2 because it was considered more robust to any variation in B_1. Following the repeated measurement test the TE values used on all the samples were 20, 50 and 80ms to enable a more precise measurement of T_2 values of ~100ms.

A standard gradient echo sequence supplied by the manufacturer (GEFI_BIO) was used to obtain T_2* weighted images. Three different images were taken in separate acquisitions with different TE times of 5ms, 15ms and 25ms. The other imaging parameters used were FoV=3cm / TR=2000 / Matrix size=96x96 / 30° flip angle.

2D and 3D structural imaging was performed using methods and parameters that would potentially be possible in vivo. 2D multi-slice imaging has been shown to be less accurate for the assessment of bone architecture, however it can provide spin echo images in a reasonable time scale. The alternative is to use a fast 3D Gradient Echo (3D-GE) sequence, for this purpose a 3D FLASH [46] sequence was used. Both 2D and 3D images were obtained at two different resolutions in 10 minutes maximum scan

time. This limit was imposed to make the resolution and SNR of the images obtained at the 7 T field strength used here in the samples, approach the capabilities of clinical scanners in the future. 3D spin echo sequences were not available with sufficient image quality and resolution using the hardware and time limitations imposed in this work, thus they are unlikely to be available in a more clinical setting. The 2D images were acquired with an in-plane resolution of 176 and 195 microns with a 500 micron slice thickness (256x256 matrix, 4.5 / 5cm FoV for 176 / 195 micron resolutions respectively, 46 0.35mm slices, TR/TE=2339.2/21.6ms). The 3D images were acquired with a resolution of 176 and 195 microns in all directions (256x256x256 matrix, 4.5 / 5cm FoV for 176 / 195 micron resolutions respectively, TR/TE=9.16/4.23ms, 30° flip angle).

SPENT gives information on the structure of a sample and is sensitive to voxels containing a partial volume such as those on the edge of a bone/water interface (as described in chapter 3). SPENT images were obtained in different directions for a low resolution, spin echo, multislice sequence by applying an extra gradient in the desired direction to produce a 2π phase wrap across each pixel. The imaging parameters used were FoV=3cm, 96x96 matrix/128x128 matrix, 1mm slice thickness, TE=20ms, TR=1162ms. In addition, SPENT images could also be created by filtering the 3D and 2D high resolution k-space data to obtain images from different tiles (see figure 3.3 and images in figure 3.7). This was used to investigate the SPENT images dependence on resolution.

4.3.4 Image Processing

4.3.4.1 R_2 and R_2' Calculation

Three T_2 weighted images at different echo times were obtained. A square region containing pure bone was selected in the images over all the slices containing pure bone (as in figure 4.3 for the SPENT images). From equation 2-26 we know that the signal intensity S decays according to

$$S = S_0 \cdot \exp\left(-TE/T_2\right) \tag{4-1}$$

Taking the natural log gives

$$\log(S) \propto -TE/T_2 \tag{4-2}$$

The log of the total signal intensity from the volume selected varies linearly with echo time. A first order 'least squares' polynomial fit to the data can then determine the overall T_2 value. The T_2 was also calculated on a pixel-by-pixel and slice-by-slice basis over the same volume.

Exactly the same process was repeated with the T_2* weighted images to obtain a value of T_2* for each sample. The value of R_2' were then derived using the following equations

$$1/T_2^* = R_2^* = 1/T_2 + 1/T_2' = R_2 + R_2' \tag{4-3}$$

To address the precision of the relaxation measurements a sample was scanned repeatedly. The sample was removed from the magnet, the standard setup procedure of tuning and matching the coil, shimming, setting the centre frequency and calibrating the amplifier attenuation for accurate 90° and 180° RF pulses was repeated each time. R_2, R_2' and R_2* were measured 10 times. In table 1, the standard deviation was typically a few percent of the mean value with the R_2 measurement being the least precise. The

reduced accuracy of R_2 was assigned to the use of less than optimal values of TE (20, 40 & 60ms) to measure a longer T_2 decay of around 200ms for the sample scanned repeatedly. In the subsequent protocol, used on all the samples, TE values of 20, 50 and 80ms were used as previously described. Overall the precision of the relaxation measurements in table 1 is high, typically 2-4%.

	s.d.(ms^{-1})	Mean (ms^{-1})	Estimated error on a single measurement
R_2	0.0002167	0.0049995	4.3%
R_2'	0.0017975	0.0704605	2.6%
R_2^*	0.0017392	0.0754600	2.3%

Table 4.1 The precision of relaxation measurements

4.3.4.2 SPENT Calculation

The SPENT signal was generated for each direction *x*, *y* and *z* corresponding to read, phase and slice directions respectively. This was achieved using a low resolution (for the 7 T system used) proton density weighted, multislice, spin echo sequence. A standard image with the same imaging parameters (e.g. TE, TR) was also acquired.

As described in chapter 3, a Normalised-SPENT (N-SPENT) image was derived by dividing the SPENT image by the standard image. This should remove the dependence on proton density and coil sensitivity that is present in the SPENT image signal to obtain contrast dependent only on the level of sub-pixel uniformity. The N-SPENT images can have a mean value taken over a region of the object. This should give some measure of the structure within a region.

The average N-SPENT value was calculated for each sample over a volume only containing bone (see figure 4.3). This was performed for each SPENT direction

individually (*x*, *y* and *z*) and for the combined in-plane directions (*xy*) and for all three directions combined (*xyz*).

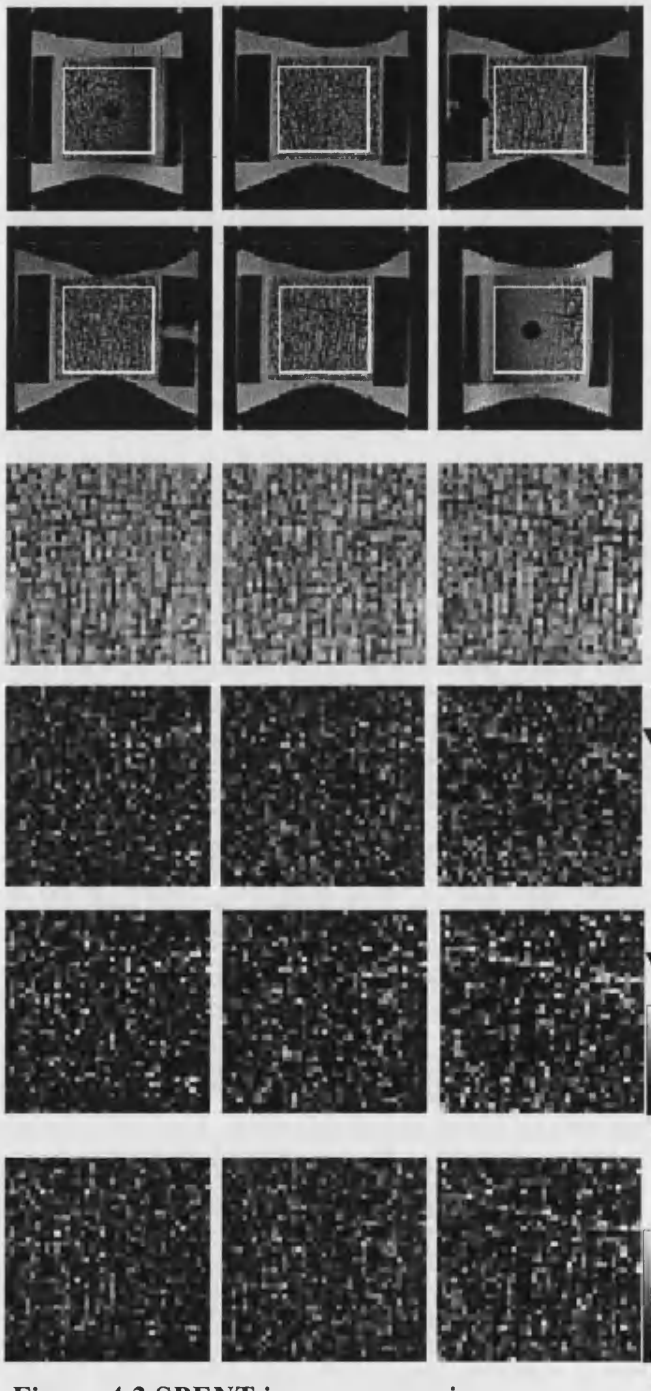

A. A region is selected (here shown over a number of slices at different positions through the sample)

Only the slices that contain pure bone are selected to give a volume of interest

B. Regions of pure bone – normal images and corresponding SPENT images over the same region

C. SPENT images (gradient applied in direction indicated with arrow) over the same region

D. N-SPENT x-direction images (direction on image indicated by arrow).

E. N-SPENT xyz-direction combined images

The mean value over these regions is taken to get a global measure of homogeneity

Figure 4.3 SPENT image processing
From the top, a number of different slices through the volume are displayed. A square roi is selected lying entirely within the bone (A). Slices that contain only bone are also selected so that a volume of pure bone is selected (B). The SPENT image for the same region is shown (C). The N-SPENT images for x (D) and xyz (E) are then shown. The mean value over this volume can be calculated for the different N-SPENT images to obtain a global measure of homogeneity

A further calculation was performed to look at the effect of resolution on the N-SPENT signal. The 3D data sets that were acquired were processed using a program developed in Matlab. The idea was to use different sized volumes of the raw k-space data to generate different resolution images. The central portions of the 195 micron, 256^3 datasets were taken. This was performed for 4 different resolutions corresponding to the central 255^3, 192^3, 126^3 and 66^3 points in k-space. Each of these data cubes can be split into 27 further sub-cubes (like a rubix cube!) of data. The central sub-cube can be FT'd to produce a 'standard' 3D image with 1/3 of the resolution. All the other cubes can be FT'd to obtain 3D SPENT images. The SPENT images are sensitised to structure in a direction specified by the vector joining the centre of k-space to the centre of the 'SPENT' sub-cube, see figure 4.4.

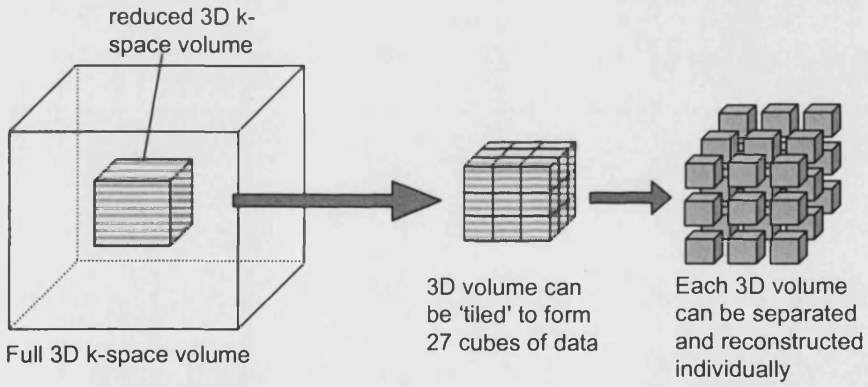

Figure 4.4 Separating k-space data into separate cubes
On the left hand side a 3D k-space region is represented. This could be FT'd to produce a 3D image. Alternatively a smaller region of the k-space data can be taken and this will form an image of lower resolution. The data can be separated into separate 'tiles' (like in figure 3.4c, only in 3D). The central cube can be FT'd to obtain a standard image of 1/3 the resolution, the others will form SPENT images in different directions.

The resolution of the 255^3, 192^3, 126^3 and 66^3 k-space data cubes was 196, 260, 396 and 756 (to 3s.f.) microns respectively. The SPENT images divide k-space into 27 separate sections that will have a further 1/3 reduction in resolution (in all directions) when they

are Fourier transformed to produce images. As described earlier pixel wise division of a SPENT image by the same resolution standard image produced N-SPENT images. A global measure of the N-SPENT signal intensity was taken over a region of interest. This was achieved by selecting a square region of interest in the *xy*-plane over all the volume. All the planes in the z-direction that contained pure bone were then selected to obtain a 3D volume of pure bone. The volume that was selected using the 195 micron image was applied to all the lower resolution images to take a very similar region of interest for each of the different resolution data sets. This process was performed on 10 samples.

4.3.4.3 Bone Volume Fraction (BVF) Calculation

The BVF was extracted from the 3D images using MatLab. Each 3D volume of data was loaded and Fourier transformed to create a 3D image. A 3D volume of pure bone was selected from these images. This was achieved by selecting a square region of interest in the *xy*-plane over all the volume. All the planes in the *z*-direction that contained pure bone were then selected to obtain a 3D volume of pure bone. In figure 4.3a, a square region is selected, shown on one of the images from the *xy*-planes. A threshold level was obtained by taking a fraction of the average signal intensity within the region (4.3b). The threshold level was then used to create a binary image (4.3c) that represents regions of pure water (white) and bone (black). The ratio of black to white pixels over the volume is calculated as the BVF. This accuracy and precision of this simple method to extract BVF relies on the images being at sufficient resolution and SNR to obtain an approximately binary distribution of pixel intensities.

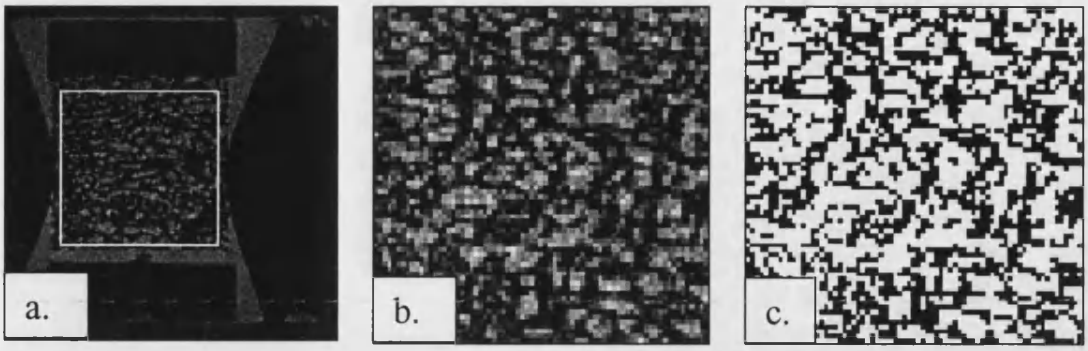

Figure 4.5 A simple calculation of BVF

a. A square region is selected. This is applied to all the slices containing pure bone to form a volume over which the BVF is calculated.
b. The region selected in 4.5a.
c. The bone (black) and water (white) components are selected with a threshold based on the mean signal intensity of the region in 4.5b. The BVF is then the ratio of black pixels to white pixels.

4.3.4.4 BMD and Stress Tests

The bone cube samples were weighed and measured to determine both their mass and size. The ratio of mass over the volume then gives the BMD (g/cm^3).

DEXA measurements were also performed on each sample with a Hologic QDR-4500A machine. A reading of BMD (g/cm^2) was obtained from the machine having manually selected a region of interest within the sample using a scout image. The regions were each of similar dimensions. A conversion factor of photon absorption/cm^2 to mass/cm^2 was used for the lumbar spine.

The measurement of BMD from directly weighing the bone samples was compared to measurements made using DEXA. To clearly visualise the level of consistency between the values, they were plotted against each other in figure 4.6.

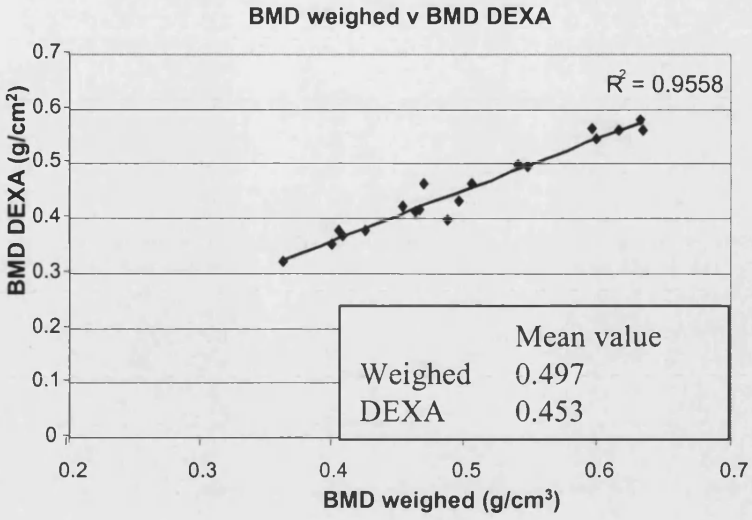

Figure 4.6 BMD calculated by weighing is compared to the values of BMD obtained from performing DEXA measurements for a subset of samples
In the plot of BMD a high correlation is seen between the two measures of BMD suggesting that consistent results are produced with the simple weighing method. The weighing method produced consistently higher values than DEXA for the BMD as seen by the mean values displayed in the figure

In figure 4.6, the difference between the two methods for measuring BMD was assessed. There was a high level of correlation between the two measures with the majority of the points lying close to the linear fit. The mean values for the two measures indicate that the BMD as measured by DEXA was consistently lower than the BMD measured by weighing. The source of this systematic underestimation was probably due to an error in the scaling factor used to obtain the bone density from the measured attenuation of the DEXA beam.

The weighed BMD was used for comparison with other parameters in all the following work. Due to the consistency between the measures of BMD, the results would be very similar if the DEXA BMD measurement had been used.

Mechanical tests were carried out on each sample with an actuated test machine (Lloyds M30K, UK). The load is applied in the direction of trabecular structure, replicating the direction of load applied in the human femur. Each sample is gradually loaded with an increasing force between 0 and 500 Newtons, while having the displacement of the sample measured. This yields a load-displacement curve that can be converted into a stress strain curve from knowledge of the samples dimensions. The Young's Modulus (YM) of the sample is then measured as the gradient from the linear region of the stress/strain curve. Though YM is not a direct measure of the load required for biomechanical failure, it is a direct measure of biomechanical strength. It is likely that biomechanical strength (and so YM) will be closely related to the risk of fracture [47-50].

4.4 Results

30 samples of bone were imaged with MRI, BMD was measured by weighing the samples and YM was measured using the stress test outlined above. The graphs, including the linear fits and R^2 values on the graphs were generated using Excel (Microsoft). For a summary of the R^2 values with their p-values to indicate the significance refer to table 4.2 at the end of the results section.

4.4.1 R_2/ R_2' v BMD

Three T_2 weighted images and three T_2* weighted images, obtained at different echo times, were used to calculate R_2 and R_2' as described in section 4.3.4.1. The values of R_2 and R_2' obtained for each sample were plotted against BMD in figures 4.7 and 4.8.

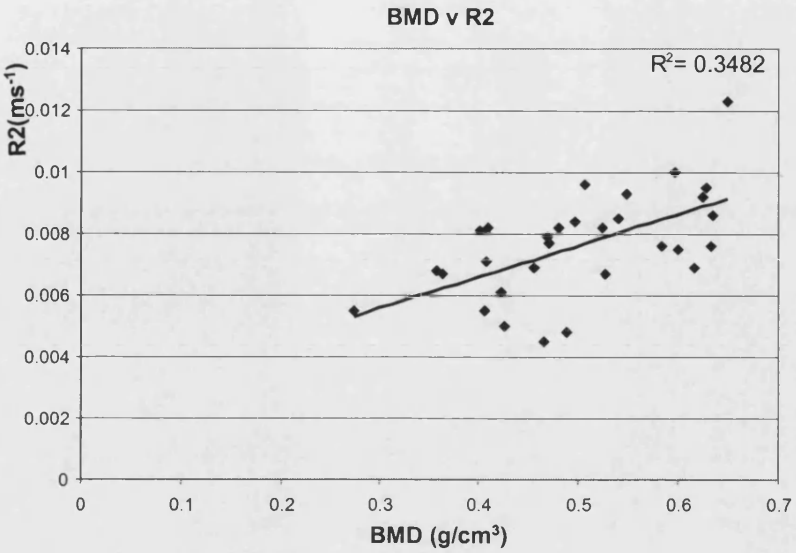

Figure 4.7 Graph of R2 against BMD
The transverse relaxation rate R2 is plotted against the BMD. A low level of correlation is seen between these two parameters as indicated by a value of R^2=0.3482 for the linear fit.

In figure 4.7, R_2 was not highly correlated to the BMD. Almost the entire signal used to calculate the R_2 value is from the water in the spaces of the bone. The R_2 of this water component is not dependent on the structure or volume of the bone. There is normally some contribution to R_2 from diffusion, which could relate to the size of the spaces within the bone. Hence, a low level of correlation between these parameters may be expected.

In figure 4.8, R_2', the relaxation rate from local temporally invariant magnetic fields, correlated strongly to the BMD. R_2' is dependent on the interaction between the bone structure and the main magnetic field. The susceptibility differences produced at the interfaces between bone and water will depend on the quantity of bone and its architecture. Hence, some correlation was expected between R_2' and BMD.

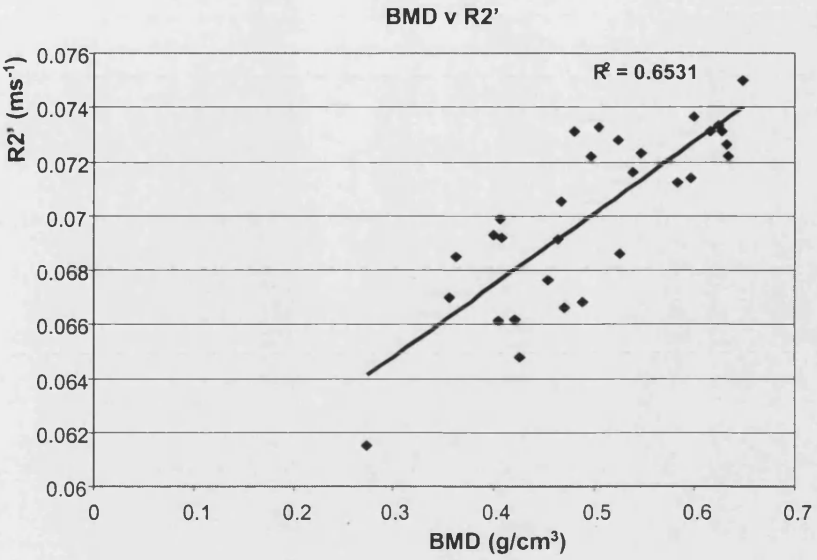

Figure 4.8 Graph of R2' against BMD
The transverse relaxation rate due to local (temporally invariant) magnetic fields R2' is plotted against the BMD. A reasonably high level of correlation is seen between these two parameters, indicated by a value of R^2=0.6063 for the linear fit.

4.4.2 R_2/ R_2' v YM

The values of R_2 and R_2' obtained for each sample were plotted against the YM in figures 4.9 and 4.10. R_2 was not correlated to the YM (see figure 4.9). Again, this result is not surprising because almost the entire signal is from water in the spaces between the bone. The R_2 of this water is unlikely to be related to either the structure or volume of bone within a sample and it is these factors that determine the YM of the samples.

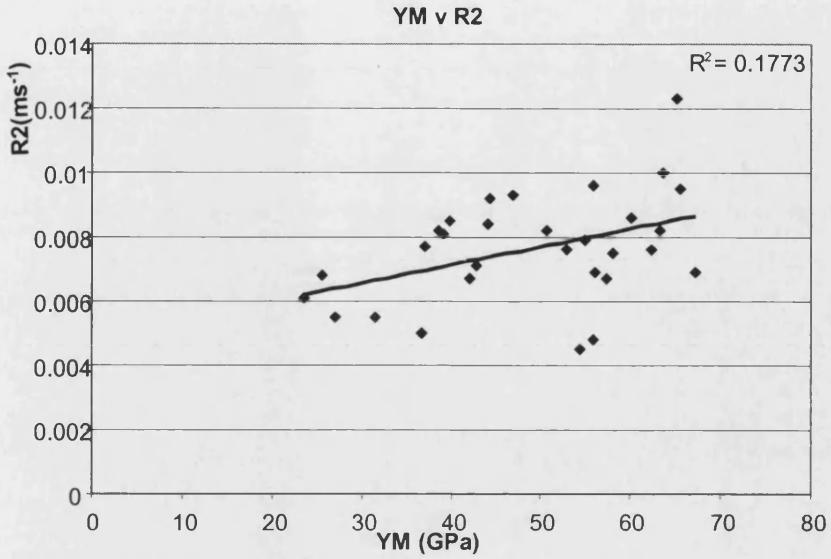

Figure 4.9 Graph of R2 against YM
The transverse relaxation rate R2 is plotted against the YM. No correlation is seen between these two parameters as indicated by a value of R^2=0.1773 from the linear fit.

In figure 4.10, the R_2' does appear to be correlated to the YM. Again, this might be expected from a consideration of local magnetic fields created by the interaction between the bone structure and the main magnetic field. The susceptibility differences produced at bone/water interfaces will be dependent on the quantity of bone and its architecture. Figure 4.10 suggests that while some measure of bone volume and architecture has been obtained, R_2' was not a strong enough correlate to bone strength to be used as a solely indicator of fracture risk. R_2' correlates more strongly to the density of bone than to its strength as measured by the YM.

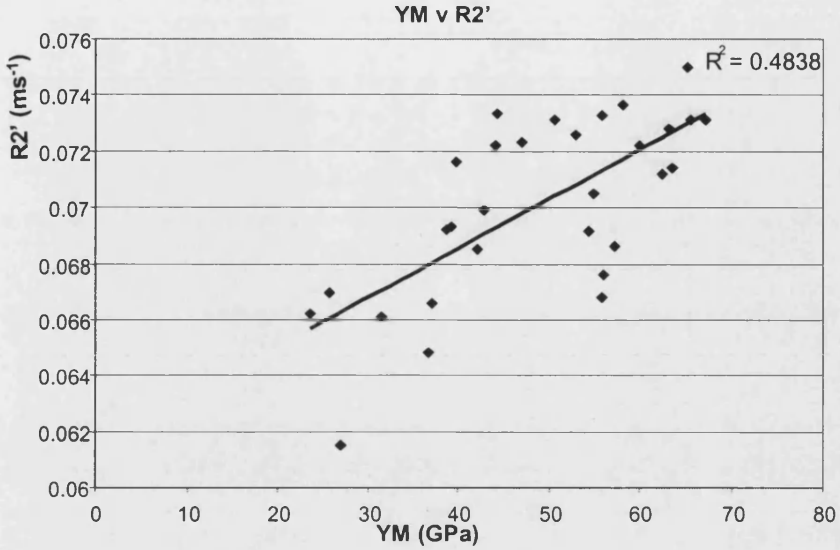

Figure 4.10 Graph of R2' against YM
The transverse relaxation rate due to local (temporally invariant) magnetic fields R2' is plotted against the YM. Some correlation is seen between these two parameters, indicated by a value of R^2=0.4073 for the linear fit.

4.4.3 SPENT v BMD

The N-SPENT signal was calculated over a region lying entirely within the bone cube and over the largest volume of pure bone possible. This process was performed for each SPENT direction (*x*,*y* and *z*) and for the combined directions (*x*y and *xyz*). The *x* and *y* directions lay in the imaging plane while the *z*-direction was used for slice selection. The bone cubes were cut and positioned so that the majority of their trabecular flow was in the *x*-direction. In figure 4.11, the average N-SPENT value was plotted against the BMD for each sample. Each direction was displayed using a marker of different colour and shape.

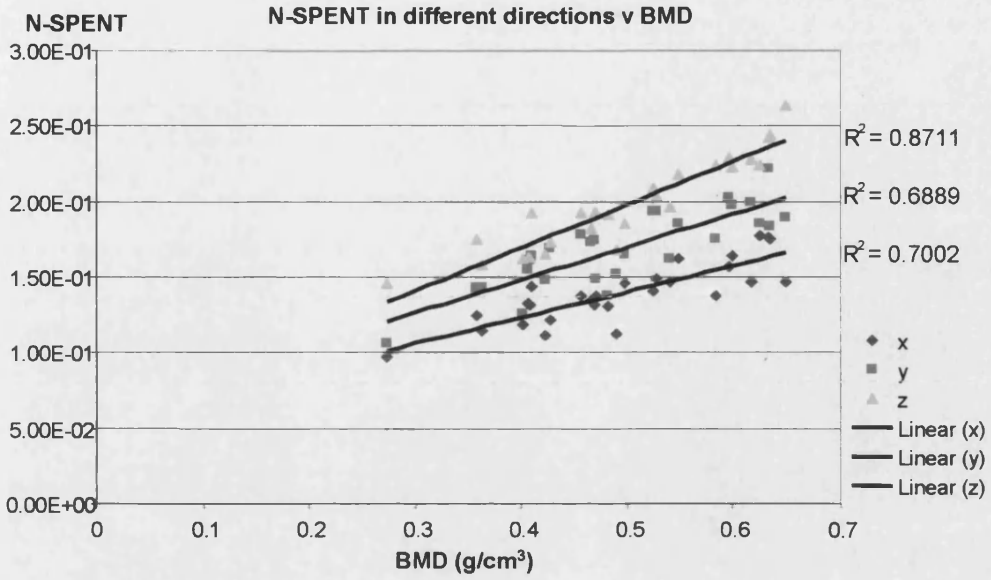

Figure 4.11 Graph of the Mean N-SPENT against BMD for each of the 3 directions that the N-SPENT is applied
The BMD is highly correlated with the N-SPENT in all three directions. The highest level of correlation is between BMD and N-SPENT in the z-direction. The mean value of the N-SPENT also appears different between directions.

Figure 4.11 showed a number of interesting trends. Firstly, the average N-SPENT signal was highly correlated to the BMD in all three directions. The slice direction shows the highest level of correlation and it was noted that the 1mm slice thickness was a different size to the in-plane resolution of 0.3125mm. This may account for some of the differences in the R^2 value between the N-SPENT *z*-direction v BMD and the N-SPENT *x* or *y*-directions v BMD. The increase in average signal level found in the *z*-direction may be due to a more consistent amount of signal being present in all pixels in the SPENT image. This could be due to a combination of the slice profile with a phase modulation that is not exactly 2π imposed across it, leading to some signal being present even in homogeneous regions of magnetisation. Secondly, while the in-plane directions *x* and *y* show a very similar level of correlation (R^2~0.7), the N-SPENT signal level was lower in the *x*-direction when compared to the *y*-direction. A higher level of N-SPENT

signal might be expected in directions perpendicular to the trabecular flow (*y* and *z*), because normally these will be less homogeneous.

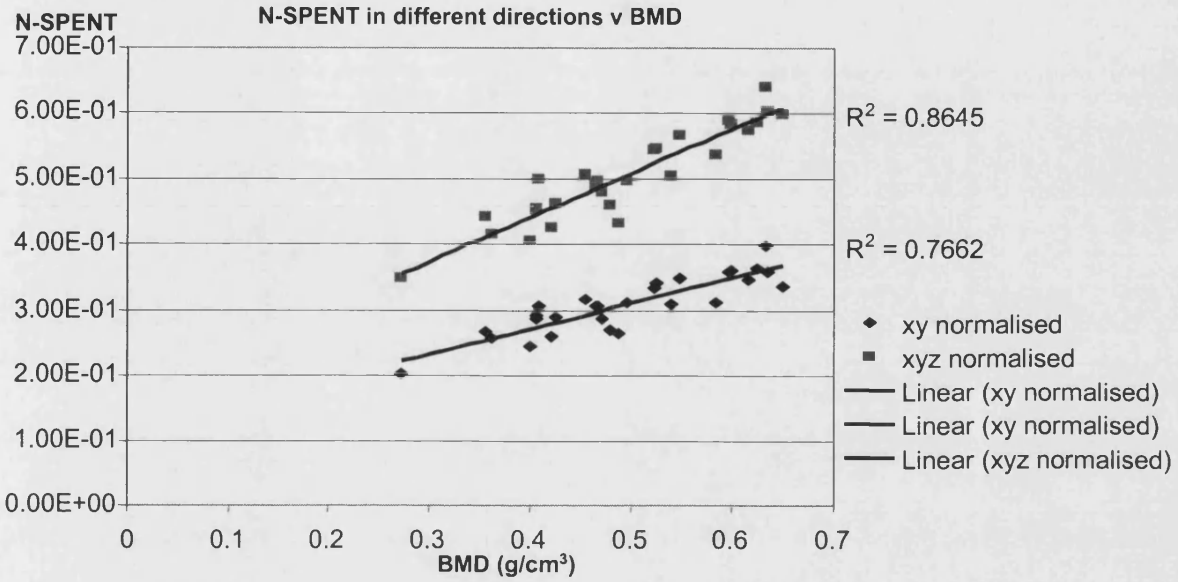

Figure 4.12 Graph of the Mean N-SPENT against BMD averaged over each direction (xyz)and over the in-plane directions (xy)
The BMD is very highly correlated with the N-SPENT in the combined directions. The level of correlation is highest when all the directions are combined together.

The N-SPENT signal from the different directions can be averaged to obtain an overall value. In figure 4.12, the N-SPENT signal is shown for the in-plane directions (*xy*) and for all the directions (*xyz*) averaged together. A very high level of correlation was seen between the combined directions and the BMD. The level of correlation was particularly high for the *xyz* directions combined. This measure of SPENT is independent of direction. Again, this result suggests that the slice direction contributes important information even though it is at a lower resolution and has extra factors such as slice profile and thickness that could potentially influence the result.

4.4.4 SPENT v YM

The N-SPENT signal was plotted against YM (in the same way as for N-SPENT with BMD in the previous section). In figure 4.13, the correlation between the individual *x*, *y* and *z* directions average N-SPENT signal and YM was displayed. All the N-SPENT directions suggested a relationship with the YM of the sample. The directions that ran perpendicular to the trabecular flow (*y* and *z*) provided a stronger relationship seen by the higher R^2 values. This was probably due to the sensitivity of the SPENT signal to the more frequent edges and discontinuities (inhomogeneity) in these directions.

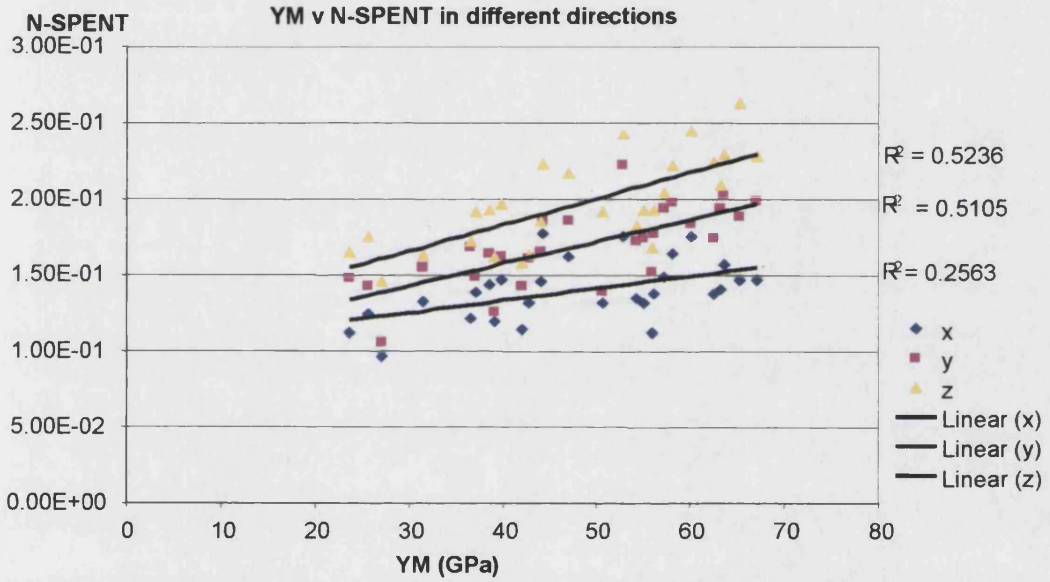

Figure 4.13 Graph of the Mean N-SPENT against YM for each of the 3 directions that the N-SPENT is applied
The YM is correlated with the N-SPENT in all the directions. The level of correlation is higher in directions that are against the trabecular flow.

The most important differences between the results shown in figure 4.13 (N-SPENT v YM) compared to figure 4.11 (N-SPENT v BMD) were i) that the strength of the relationship was lower for YM v N-SPENT and ii) while N-SPENT and BMD are highly correlated in all directions, the YM is correlated highly only in the directions perpendicular to the trabecular flow. This demonstrates that the N-SPENT was more

sensitive to changes in bone volume than bone strength. Additionally, whatever the N-SPENT images have actually measured (i.e. homogeneity), while this correlates to BVF in all directions, it does not correlates to bone strength in the direction of the trabecular flow.

In figure 4.14, the combined *xy* and *xyz* N-SPENT image signal levels were plotted against YM. The graph was similar to that for BMD (figure 4.12); both combined directions suggested a relationship, with the combination of all three directions providing a stronger R^2 value. The strength of the relationships, as with the individual directions, was weaker for N-SPENT v YM than for N-SPENT v BMD.

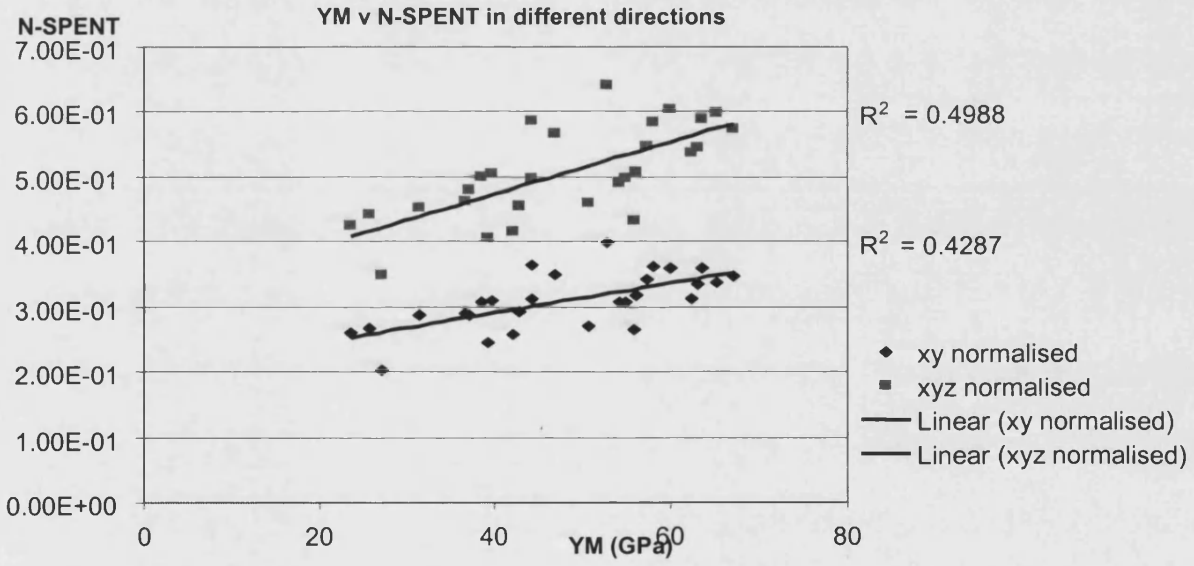

Figure 4.14 Graph of the Mean N-SPENT against YM averaged over each direction (xyz)and over the in-plane directions (xy)
The YM is correlated with the N-SPENT in the combined directions. The level of correlation is highest when all the directions are combined together.

4.4.5 SPENT and the Effects of Resolution

The relationship between the average N-SPENT signal and BMD was investigated using 3D images at different resolutions. Four different 3D data sets were created with a

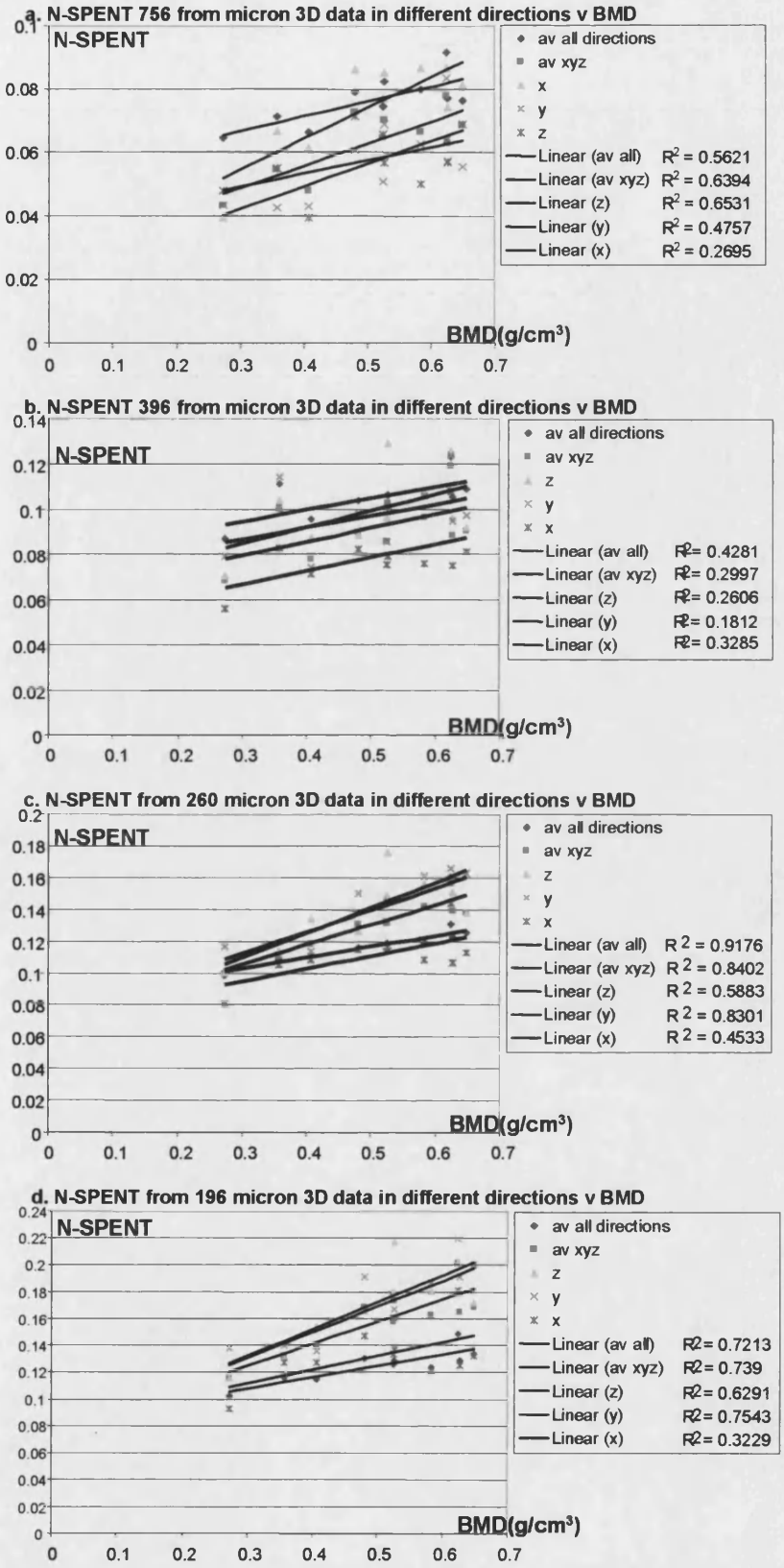

Figure 4.15 Global N-SPENT signal v BMD at 4 different resolutions

Each graph shows the N-SPENT signal v BMD for 3 different SPENT directions. In addition, two combinations of the N-SPENT directions are displayed. The resolutions is different in a-d with the resolution given being that for the 3D data set used i.e. SPENT images have a resolution of 1/3 of the value of the data set used that is given above.

resolution of 196, 260, 396 and 756 (to 3s.f.) microns respectively. The N-SPENT images produced from each of these data sets have a resolution of 1/3 of the resolution of the whole data set given above. The N-SPENT signal was calculated for each of the 26 SPENT directions obtained from the 3D data set (see figure 4.4), the x, y and z direction N-SPENT values were displayed against BMD in figure 4.15. Some of the 26 SPENT directions showed a much higher correlation to BMD than others. Again the y and z directions displayed a higher correlation to BMD than the x-direction, probably the result of the increased structure perpendicular to the direction of trabecular flow producing reduced homogeneity on the scale of the pixel. This was not true for the 396 resolution, however a low level of correlation was seen for all directions at this resolution.

The level of correlation between the BMD and the combined N-SPENT directions was highest for the 260 micron data set. This may be an effect of the resolution, or alternatively it could be due to improved levels of SNR between the 196 and 260micron data. Interestingly, the performance of the lowest resolution data was better than for the second lowest resolution data. This suggests that lower resolution data can be used, and that it is important to choose a resolution that reflects the size of the structure. It is not clear whether there is a direct relationship between the resolution and the N-SPENT signal level. If the N-SPENT images pick up structures of different sizes, it could be the prevalence of the structures that is in turn related to the BMD. It was also noted that the average N-SPENT signal level increased consistently with resolution. This could be because the N-SPENT was picking up more of the structure at higher resolutions. It is noted that even at the highest resolution of 196 microns the N-SPENT images have 1/3 of this resolution (i.e. 588 microns). This means the increase in N-SPENT signal is not

likely to be due to pixels that have large values due to division using a standard image with pixels containing very low signal intensity (e.g. from pure bone).

It was found that for certain individual N-SPENT directions the correlation to BMD was as strong as for all the directions combined together. The difference between the various directions, a kind of structural anisotropy, may contain further useful information.

4.4.6 BMD v YM

To help determine the relationship between the density of bone and its strength for our samples the BMD was directly compared to the YM. A strong relationship was found between these parameters in figure 4.16. However, there are samples with similar BMDs that exhibit quite large differences in YM. This suggests that it is not only the quantity of bone but also it is architecture that is important for the strength of the bone.

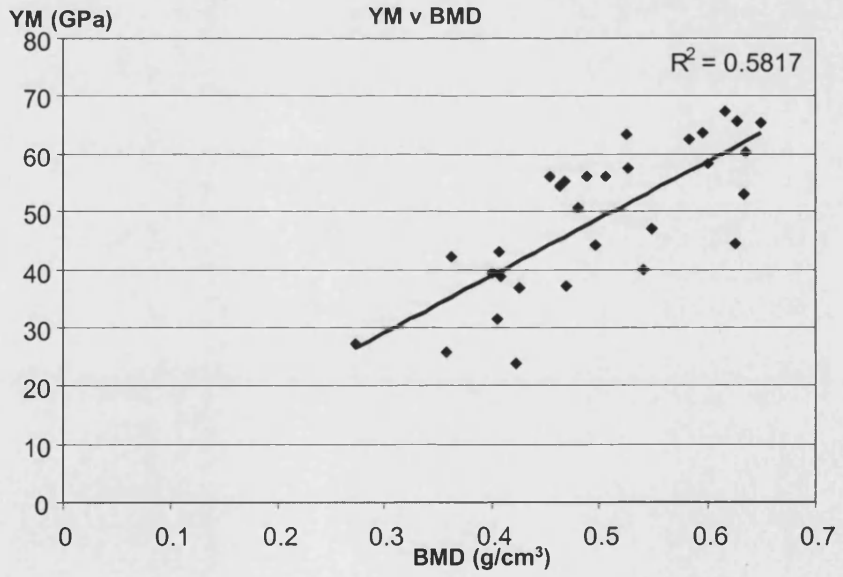

Figure 4.16 Graph of BMD against YM
The YM is strongly correlated to the BMD, indicating that greater bone density generally will give more strength. This is not the whole story however, the scatter in the results indicates that different bone samples with similar BMD can have widely varying strength. This is due to the bone architecture.

4.4.7 Image Based BVF Measurement

The BVF was calculated using the process described in section 4.3.4.3. In figure 4.17, the BVF was seen to correlate very closely to the BMD for the 10 samples. This indicates that even with the simple calculation of BVF used, the values of BVF obtained accurately reflected the BMD of the samples. The BVF measured using higher resolution images (176 microns) correlated slightly more strongly to the BMD. This is most likely due to a reduction in the number of pixels containing a partial volume and being incorrectly assigned as containing either pure bone or water.

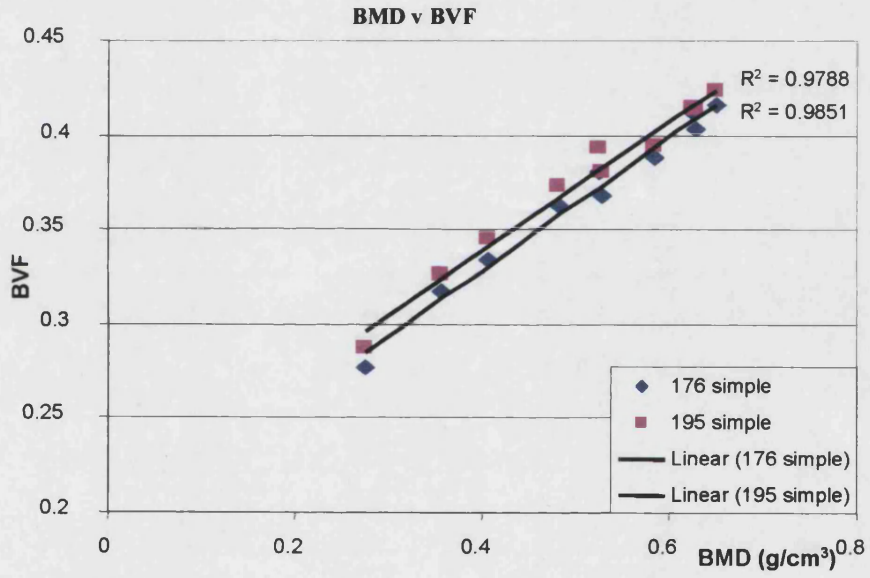

Figure 4.17 Graph of BMD v BVF
The BVF measured from 176 micron and 195 micron 3D images is compared with BMD for the first 10 samples. The level of correlation is very high demonstrating that, at the resolution used here, MR images accurately give the fraction of bone in a sample.

4.4.8 Summary of Results

The different parameters were entered into the JMP statistics package (SAS institute, Cary, NC, USA). The r^2 value was calculated to obtain a measure of the strength of the relationships between the different parameters and the p-value was calculated to

determine the significance of these results. The r^2 value is the same parameter as the R^2 value given previously in this chapter. The R^2 was calculated in excel from the linear fits shown in figures 4.6-4.17, the r^2 is calculated using the JMP package. The results were summarised in table 4.2 with the different parameters compared to both the Young's Modulus and BMD.

Results Table	YM r^2	YM p-value	BMD r^2	BMD p-value
R2	0.178	0.0205	0.348	0.0006
R2'	0.484	<0.0001	0.653	<0.0001
SPENT xy	0.431	<0.0001	0.768	<0.0001
SPENT xyz	0.499	<0.0001	0.865	<0.0001
SPENT x	0.260	0.0056	0.702	<0.0001
SPENT y	0.508	<0.0001	0.689	<0.0001
SPENT z	0.523	<0.0001	0.866	<0.0001
SPENT yz	0.570	<0.0001		
YM			0.582	<0.0001

Table 4.2 The relationships between the different parameters are summarised

Key points

1. YM and BMD correlate strongly (r^2=0.582, p <0.0001). YM closely describes the strength of bone and the BMD describes the bone density. This result confirms that the strength of bone is strongly related to its density. However, samples with a similar density did have quite different strengths, which must be due to their architecture.

2. R_2' correlates with both BMD (r^2=0.653, p<0.0001) and a little more weakly with YM (r^2=0.484, p<0.0001). This result suggests that, while the value of R_2' is related to the bone architecture, it is more strongly influenced by the density of the bone.
3. R_2 correlates weakly with BMD (r^2=0.348, p<0.001). However, R_2 does not correlate significantly with YM and so it is not a useful parameter for assessing bone strength.
4. SPENT correlates very highly with BMD in *all* directions *x*,*y* and *z*. The *z*-direction is best (r^2=0. 866, p<0.0001).
5. SPENT correlates with YM, though not as highly as with BMD and *not in all* directions. The *x*-direction (with the trabecular flow) was not significantly correlated to YM.

The results that have been obtained in this study were compared to previous work in table 4.3 below.

Majumdar et al 1991	R_2* v BMD	r=0.92, p<0.0001	Lumbar Samples in saline
Kang et al 1999	R_2'/ R_2* v density from qCT images	r=0.87 / 0.90 p<0.0005 / 0.0002	Sheep vertebra samples
Wehrli et al 2000	R_2' v Fracture risk	r^2=0.3, p<0.001	In vivo Femoral neck
"	BMD v Fracture risk	r^2=0.48, p<0.001	In vivo Ward triangle
"	Combined BMD and R_2' v Fracture risk	r^2=0.60, p<0.001	In vivo, BMD Ward triangle, R_2' trochanter
Link 2002	BMD v Biomechanical strength	r=0.69, p<0.01	In-vitro, BMD Ward triangle, Biomechanical strength of the femur

Table 4.3 Some literature values of the relationships between various parameters

4.5 Discussion

The key questions raised in this section are: i) how do the results obtained in this chapter compare with previous findings, ii) can SPENT provide a simple MR correlate of BMD, and iii) what prospects are there for MRI to become the most accurate and safe way of assessing bone in diseases such as osteoporosis.

4.5.1 How do the Results Compare with Previous Studies?

The MR parameters previously measured with any great frequency in bone have been R_2, R_2' and BVF. More complicated structural parameters have also been calculated from high resolution images [16,19,23-29]. These were not considered in this chapter because the resolution, SNR and uniformity of the images required for their accurate calculation would not be available on a standard clinical machine. Images have been obtained with sufficient quality in the heel and wrist but even here it is still a technical challenge [15]. In addition, the level of image processing that many of these methods require prevents them being applied easily in a more clinical setting. The other parameter that was measured in this, and previous studies, was bone density (or BMD). In this chapter Young's Modulus (YM) was used as a measure of biomechanical strength, and so a close correlate to fracture risk.

The relationship between bone strength, described here by the YM and the BMD was investigated. A strong relationship was established between these parameters that confirmed the previous findings in references [19,51] displayed in table 4.3. However, figure 4.12 showed that some samples with similar BMD have different YM. This is mainly thought to be due to a difference in the architecture of different bone samples although some difference in mineral content is also a factor [23]. YM should be a better measure of bone fracture risk than BMD because it is a direct measure of biomechanical strength. The YM is a measure of the amount that the bone contracts with load before reaching mechanical breakdown. While this is not a direct measure of ultimate load (the maximum load before breaking), the YM will normally be strongly related to the ultimate load in bone [47-50].

The correlation between R_2' and BMD/YM was seen to be consistent with previous findings (see tables 4.2 and 4.3). R_2' is highly correlated to BMD, especially in-vitro where there is less likelihood of results being contaminated by surrounding structures that may create local fields and so change R_2'.

Primarily, the BVF gives a known MR correlate to BMD. In figure 4.13, the MR images produced a measure of BVF similar to BMD using a simple method. The values of BVF produced were not very accurate due to systematic errors arising from the use of a gradient echo sequence [52] and from the simple method used to calculate the BVF. However, the correlation between the BMD and the BVF indicated that the same information was obtained.

Why has BVF measurement using MRI not yet become a reality in a clinical setting? This is mainly due to the difficulty of performing MRI at the high resolution required, and additionally, because complex image processing is also normally needed. Despite a lot of work at clinical field strength to find an MR method for accurately obtaining BMD/BVF [15,16], sites other than the distal radius or heel have not yet been used. BVF has been investigated using low resolution MRI [22], though in this work the limitations of performing this technique in sites with B_1 non-uniformity (such as in the trunk) were noted.

Overall the results presented in this chapter were consistent with those previously found. Despite much effort at clinical field strengths, accurately obtaining BMD/BVF [15,16] using MRI is still the primary objective of work in this area.

4.5.2 SPENT as a Simple MR Parameter to Determine BMD

The N-SPENT signal averaged over a region correlated highly with BMD both in individual directions and in different directions combined together. The *xyz* directions combined gave a high correlation to BMD while being independent of direction. This could be useful in vivo where the trabecular orientation may not be known. The highest correlation was found between BMD and N-SPENT in the *z*-direction. This may indicate that only one SPENT direction would be required to gain a reasonable measure of BMD. If so, benefits in SNR or time may be found by sampling a smaller region of k-space as discussed in the previous chapter. In addition, the *z*-direction was the slice select direction, indicating that 1mm slices can be used to determine the bone volume using this method. This provides encouragement for the possible use of SPENT in vivo for BVF assessment.

N-SPENT correlated highly with the measure of bone strength used in this chapter - YM. Improvements in the level of correlation were seen when the *y* and *z* directions were combined. The N-SPENT in the combined *yz* directions, correlated nearly as highly with YM as the calculated BMD correlated with YM. This is despite the fact that the BMD could be measured in the samples to a very high degree of accuracy by weighing them; BMD cannot be measured in vivo with the accuracy by any method.

Interestingly, the average N-SPENT signal did not correlate as highly to YM in all the individual directions. The *x*-direction, the direction of trabecular flow, displayed a weaker, less significant relationship. In contrast, the BMD displayed a high correlation to N-SPENT in all the individual directions. This may indicate that, while the N-SPENT is highly correlated with BMD, it is measuring something slightly different. SPENT

tends to highlight edges, so perhaps this difference in the *x*-direction is due to the strength of the bone being less dependent on the amount of structure in *x*, while the BMD still varies in a similar manner to the amount of structure in *any* direction.

4.5.3 Can MRI Produce a Better Assessment of Fracture Risk than DEXA?

It should be noted that BMD as measured by DEXA has limitations; it imparts a radiation dose and cannot avoid contamination in its results from cortical bone and other tissue. Furthermore, DEXA produces an area density as opposed to a true density that reduces its accuracy.

As stated previously, N-SPENT for the *y* and *z* directions combined produced a level of correlation to YM that was comparable to the correlation of BMD with YM. N-SPENT in the z-direction also provided a close correlate to both BMD and YM. These results suggest that N-SPENT is a simple way to extract the BMD from images of a sample.

In vivo, SPENT will have a number of obstacles to overcome. The most important issue is SNR and resolution, which can of course be traded for each other. SPENT has a number of advantages in this respect when compared to normal image acquisition. For normal image acquisition a full area of k-space must be acquired, requiring a certain time period. SPENT allows a reduced area to be targeted and so a time saving or corresponding SNR increase could be made. In addition, the N-SPENT images that were obtained should remove (by division) any variability in B_1 transmission and the receiver sensitivity on reception. This avoids the problems that other MR methods for BVF calculation encounter when non-uniform images are obtained. Perhaps more importantly, the insensitivity to B_1 could allow surface coils (both individually and in

arrays) to be used for optimal signal reception in sites such as Wards triangle. This would provide greatly enhanced SNR and may also allow FOV reduction, particularly if imaging of just one femur is required for overall fracture risk assessment.

If SPENT was proved effective in obtaining BMD/BVF measurements in vivo then it could be combined with measurements of R_2' or R_2*. R_2' may give a measure of bone architecture as well as BMD, providing complimentary information. R_2' has been shown to have a dependence on the angle of the trabecular bone relative to B_0. If SPENT is used with R_2', it may be preferable to obtain N-SPENT images that are independent of direction.

4.5.4 Translation of Results to In Vivo Data at Clinical Field Strengths

The N-SPENT signal averaged over region gives a very close correlation to BMD in samples. More work is needed to determine how useful SPENT will be in vivo for assessing bone fracture status. This involves two main differences from the work carried out in this study. Firstly, the composition of real bone marrow is different; it contains a mixture of fat, as opposed to water, in the spaces within the trabecular. Imaging of fat instead of water should not be difficult; high resolution images of bone have already been acquired in vivo at peripheral sites in the body [15,16,21,53]. In addition, human geometry and the SNR/resolution available at clinical field strength must be overcome.

N-SPENT images have the following characteristics that should allow their acquisition at clinical field strength: 1mm multislice images were used, indicating that high quality and time efficient multislice sequences such as the Fast Spin Echo (see section 2.9) could be used to obtain N-SPENT values. The ability of N-SPENT images to be used

for BMD / bone strength assessment appears to be possible at resolutions lower than those required for image based techniques. Normally, 3D images of around 200 microns resolution are used to try to extract the structural information. In figure 4.14, a 260 micron data set was used to accurately obtain BMD. The high correlation between N-SPENT and BMD for the individual directions corresponded to using two 'tiles' of k-space. This showed that a smaller region of k-space could be used to extract a measure of BMD. Sampling a reduced area of k-space could save enough time to get higher SNR data, at the necessary resolution. N-SPENT images and their average intensity within an object should be tolerant to transmit/receive variations in sensitivity. This allows RF coils with the best SNR (i.e. surface coils and array coils) to be used in vivo with N-SPENT to maximise SNR performance.

Though SPENT has not been proven to work in vivo for BMD calculation, the technique does appear to provide reasons to believe that it should yield similar results. The measurement of R_2' or R_2* with SPENT may in combination yield a practical MR based index of fracture risk.

4.5.5 Wider Implications – Information and K-space Regions

This work has demonstrated that by reconstructing regions of k-space certain information about the object may be obtained. While a large amount of work has been performed in the analysis of the information contained in images, less has been done on the information present in k-space. While an object in image space shows the local signal intensity, a local k-space area provides an indicator of the amount of structure throughout the object around a certain size. In objects containing regular structures,

perhaps a more specific area of k-space could provide distinct structural information, which would otherwise require full data sets at a higher resolution to be extracted.

4.6 Conclusions

In general, the average N-SPENT signal in a region produces a measure of BMD. The N-SPENT signal in a single direction also appears to offer a good measure of the BMD of a bone sample. The average N-SPENT signal has been shown to produce a close correlate to BMD/BVF using a multislice sequence, without requiring very high resolution images. A smaller area of k-space can be obtained for N-SPENT images when compared to high resolution images making the technique more efficient. The N-SPENT images should remove the sensitivity to B_1 transmit/receive non-uniformity that other methods can suffer from. R_2'/R_2^* measurements may give additional information about bone strength and structure. Further work is required to translate the promising results displayed here into a useful in vivo method for assessing bone fracture risk.

4.7 References

1. Cummings, S. R. & Melton, L. J. 2002, "Epidemiology and outcomes of osteoporotic fractures", *Lancet*, vol. 359, no. 9319, pp. 1761-1767.

2. Ray, N. F., Chan, J. K., Thamer, M., & Melton, L. J., III 1997, "Medical expenditures for the treatment of osteoporotic fractures in the United States in 1995: report from the National Osteoporosis Foundation", *Journal Of Bone And Mineral Research: The Official Journal Of The American Society For Bone And Mineral Research*, vol. 12, no. 1, pp. 24-35.

3. Shier, C. K., Ellis, B. I., Kleerekoper, M., & Jurisson, M. L. 1987, "Disseminated migratory osteoporosis: an unusual pattern of osteoporosis", *Can.Assoc.Radiol.J.*, vol. 38, no. 1, pp. 56-59.

4. Cummings, S. R., Kelsey, J. L., Nevitt, M. C., & O'Dowd, K. J. 1985, "Epidemiology of osteoporosis and osteoporotic fractures", *Epidemiol.Rev.*, vol. 7, pp. 178-208.

5. Majumdar, S., Kothari, M., Augat, P., Newitt, D. C., Link, T. M., Lin, J. C., Lang, T., Lu, Y., & Genant, H. K. 1998, "High-resolution magnetic resonance imaging: three-dimensional trabecular bone architecture and biomechanical properties", *Bone*, vol. 22, no. 5, pp. 445-454.

6. Grampp, S., Henk, C. B., & Imhof, H. 1999, " [Bone densitometry: comparative value and limitations of different techniques]", *Wien.Med Wochenschr.*, vol. 149, no. 16-17, pp. 472-478.

7. Parfitt, A. M. 2002, "Misconceptions (2): turnover is always higher in cancellous than in cortical bone", *Bone*, vol. 30, no. 6, pp. 807-809.

8. Seeman, E. 2002, "Pathogenesis of bone fragility in women and men", *Lancet*, vol. 359, no. 9320, pp. 1841-1850.

9. Cummings, S. R., Black, D. M., Nevitt, M. C., Browner, W. S., Cauley, J. A., Genant, H. K., Mascioli, S. R., Scott, J. C., Seeley, D. G., Steiger, P., & . 1990, "Appendicular bone density and age predict hip fracture in women. The Study of Osteoporotic Fractures Research Group", *JAMA*, vol. 263, no. 5, pp. 665-668.

10. Lu, Y., Genant, H. K., Shepherd, J., Zhao, S., Mathur, A., Fuerst, T. P., & Cummings, S. R. 2001, "Classification of osteoporosis based on bone mineral densities", *J.Bone Miner.Res.*, vol. 16, no. 5, pp. 901-910.

11. Cummings, S. R., Bates, D., & Black, D. M. 2002, "Clinical use of bone densitometry: scientific review", *JAMA*, vol. 288, no. 15, pp. 1889-1897.

12. Odgaard, A., Kabel, J., van Rietbergen, B., Dalstra, M., & Huiskes, R. 1997, "Fabric and elastic principal directions of cancellous bone are closely related", *J.Biomech.*, vol. 30, no. 5, pp. 487-495.

13. Goulet, R. W., Goldstein, S. A., Ciarelli, M. J., Kuhn, J. L., Brown, M. B., & Feldkamp, L. A. 1994, "The relationship between the structural and orthogonal compressive properties of trabecular bone", *J.Biomech.*, vol. 27, no. 4, pp. 375-389.

14. Genant, H. K., Engelke, K., Fuerst, T., Gluer, C. C., Grampp, S., Harris, S. T., Jergas, M., Lang, T., Lu, Y., Majumdar, S., Mathur, A., & Takada, M. 1996, "Noninvasive assessment of bone mineral and structure: state of the art", *J.Bone Miner.Res.*, vol. 11, no. 6, pp. 707-730.

15. Wehrli, F. W., Hwang, S. N., Ma, J., Song, H. K., Ford, J. C., & Haddad, J. G. 1998, "Cancellous bone volume and structure in the forearm: noninvasive assessment with MR microimaging and image processing", *Radiology*, vol. 206, no. 2, pp. 347-357.

16. Link, T. M., Majumdar, S., Augat, P., Lin, J. C., Newitt, D., Lu, Y., Lane, N. E., & Genant, H. K. 1998, "In vivo high resolution MRI of the calcaneus: differences in trabecular structure in osteoporosis patients", *J.Bone Miner.Res.*, vol. 13, no. 7, pp. 1175-1182.

17. Chung, H. W., Wehrli, F. W., Williams, J. L., Kugelmass, S. D., & Wehrli, S. L. 1995, "Quantitative analysis of trabecular microstructure by 400 MHz nuclear magnetic resonance imaging", *J.Bone Miner.Res.*, vol. 10, no. 5, pp. 803-811.

18. Kang, C., Paley, M., Ordidge, R., & Speller, R. 1999, "R'2 measured in trabecular bone in vitro: relationship to trabecular separation", *Magn Reson.Imaging*, vol. 17, no. 7, pp. 989-995.

19. Wehrli, F. W., Hopkins, J. A., Hwang, S. N., Song, H. K., Snyder, P. J., & Haddad, J. G. 2000, "Cross-sectional study of osteopenia with quantitative MR imaging and bone densitometry", *Radiology*, vol. 217, no. 2, pp. 527-538.

20. Wehrli, F. W., Hilaire, L., Fernandez-Seara, M., Gomberg, B. R., Song, H. K., Zemel, B., Loh, L., & Snyder, P. J. 2002, "Quantitative magnetic resonance imaging in the calcaneus and femur of women with varying degrees of osteopenia and vertebral deformity status", *J.Bone Miner.Res.*, vol. 17, no. 12, pp. 2265-2273.

21. Kang, C., Paley, M., Ordidge, R., & Speller, R. 1999, "In vivo MRI measurements of bone quality in the calcaneus: a comparison with DXA and ultrasound", *Osteoporos.Int.*, vol. 9, no. 1, pp. 65-74.

22. Fernandez-Seara, M. A., Song, H. K., & Wehrli, F. W. 2001, "Trabecular bone volume fraction mapping by low-resolution MRI", *Magn Reson.Med.*, vol. 46, no. 1, pp. 103-113.

23. Borah, B., Dufresne, T. E., Cockman, M. D., Gross, G. J., Sod, E. W., Myers, W. R., Combs, K. S., Higgins, R. E., Pierce, S. A., & Stevens, M. L. 2000, "Evaluation of changes in trabecular bone architecture and mechanical properties of minipig vertebrae by three-dimensional magnetic resonance microimaging and finite element modeling", *J.Bone Miner.Res.*, vol. 15, no. 9, pp. 1786-1797.

24. Borah, B., Gross, G. J., Dufresne, T. E., Smith, T. S., Cockman, M. D., Chmielewski, P. A., Lundy, M. W., Hartke, J. R., & Sod, E. W. 2001, "Three-dimensional microimaging (MRmicroI and microCT), finite element modeling, and rapid prototyping provide unique insights into bone architecture in osteoporosis", *Anat.Rec.*, vol. 265, no. 2, pp. 101-110.

25. Majumdar, S., Genant, H. K., Grampp, S., Newitt, D. C., Truong, V. H., Lin, J. C., & Mathur, A. 1997, "Correlation of trabecular bone structure with age, bone mineral density, and osteoporotic status: in vivo studies in the distal radius using high resolution magnetic resonance imaging", *J.Bone Miner.Res.*, vol. 12, no. 1, pp. 111-118.

26. Majumdar, S. & Genant, H. K. 1997, "Assessment of trabecular structure using high resolution magnetic resonance imaging", *Stud.Health Technol.Inform.*, vol. 40, pp. 81-96.

27. Majumdar, S. 1998, "A review of magnetic resonance (MR) imaging of trabecular bone micro-architecture: contribution to the prediction of biomechanical properties and fracture prevalence", *Technol.Health Care*, vol. 6, no. 5-6, pp. 321-327.

28. Wehrli, F. W., Gomberg, B. R., Saha, P. K., Song, H. K., Hwang, S. N., & Snyder, P. J. 2001, "Digital topological analysis of in vivo magnetic resonance microimages of trabecular bone reveals structural implications of osteoporosis", *J.Bone Miner.Res.*, vol. 16, no. 8, pp. 1520-1531.

29. Gomberg, B. R., Saha, P. K., Song, H. K., Hwang, S. N., & Wehrli, F. W. 2000, "Topological analysis of trabecular bone MR images", *IEEE Trans.Med.Imaging*, vol. 19, no. 3, pp. 166-174.

30. Majumdar, S., Link, T. M., Millard, J., Lin, J. C., Augat, P., Newitt, D., Lane, N., & Genant, H. K. 2000, "In vivo assessment of trabecular bone structure using fractal analysis of distal radius radiographs", *Med.Phys.*, vol. 27, no. 11, pp. 2594-2599.

31. Majumdar, S., Lin, J., Link, T., Millard, J., Augat, P., Ouyang, X., Newitt, D., Gould, R., Kothari, M., & Genant, H. 1999, "Fractal analysis of radiographs: assessment of trabecular bone structure and prediction of elastic modulus and strength", *Med.Phys.*, vol. 26, no. 7, pp. 1330-1340.

32. Majumdar, S. 1991, "Quantitative study of the susceptibility difference between trabecular bone and bone marrow: computer simulations", *Magn Reson.Med.*, vol. 22, no. 1, pp. 101-110.

33. Ford, J. C., Wehrli, F. W., & Chung, H. W. 1993, "Magnetic field distribution in models of trabecular bone", *Magn Reson.Med.*, vol. 30, no. 3, pp. 373-379.

34. Engelke, K., Majumdar, S., & Genant, H. K. 1994, "Phantom studies simulating the impact of trabecular structure on marrow relaxation time, T2'", *Magn Reson.Med.*, vol. 31, no. 4, pp. 380-387.

35. Jergas, M. D., Majumdar, S., Keyak, J. H., Lee, I. Y., Newitt, D. C., Grampp, S., Skinner, H. B., & Genant, H. K. 1995, "Relationships between young modulus of elasticity, ash density, and MRI derived effective transverse relaxation T2* in tibial specimens", *J.Comput.Assist.Tomogr.*, vol. 19, no. 3, pp. 472-479.

36. Majumdar, S. & Genant, H. K. 1992, "In vivo relationship between marrow T2* and trabecular bone density determined with a chemical shift-selective asymmetric spin-echo sequence", *J.Magn Reson.Imaging*, vol. 2, no. 2, pp. 209-219.

37. Chung, H., Wehrli, F. W., Williams, J. L., & Kugelmass, S. D. 1993, "Relationship between NMR transverse relaxation, trabecular bone architecture, and strength", *Proc.Natl.Acad.Sci.U.S.A*, vol. 90, no. 21, pp. 10250-10254.

38. Wehrli, F. W., Hwang, S. N., & Song, H. K. 1998, "New architectural parameters derived from micro-MRI for the prediction of trabecular bone strength", *Technol.Health Care*, vol. 6, no. 5-6, pp. 307-320.

39. Beuf, O., Newitt, D. C., Mosekilde, L., & Majumdar, S. 2001, "Trabecular structure assessment in lumbar vertebrae specimens using quantitative magnetic resonance imaging and relationship with mechanical competence", *J.Bone Miner.Res.*, vol. 16, no. 8, pp. 1511-1519.

40. Fernandez-Seara, M. A., Wehrli, S. L., & Wehrli, F. W. 2003, "Multipoint mapping for imaging of semi-solid materials", *J.Magn Reson.*, vol. 160, no. 2, pp. 144-150.

41. Yablonskiy, D. A., Reinus, W. R., Stark, H., & Haacke, E. M. 1997, "Quantitation of T2' anisotropic effects on magnetic resonance bone mineral density measurement", *Magn Reson.Med.*, vol. 37, no. 2, pp. 214-221.

42. Augat, P., Link, T., Lang, T. F., Lin, J. C., Majumdar, S., & Genant, H. K. 1998, "Anisotropy of the elastic modulus of trabecular bone specimens from different anatomical locations", *Med.Eng Phys.*, vol. 20, no. 2, pp. 124-131.

43. Haase, A., Odoj, F., Von Kienlin, M., Warnking, J., Fidler, F., Weisser, A., Nittka, M., Rommel, E., Lanz, T., Kalusche, B., & Griswold, M. 2000, "NMR Probeheads for In Vivo Applications", *Concepts in Magnetic Resonance*, vol. 12(6), pp. 361-388.

44. Allday, A. W. & Farquharson, M. J. 2002, "In-vitro Preperation and Demineralisation of Trabecular Bone as a tool for the Assessment of Bone Mineral Density Techniques", *Calcif.Tissue Int.*

45. Cummings, S. R. 1991, "Epidemiologic studies of osteoporotic fractures: methodologic issues", *Calcif.Tissue Int.*, vol. 49 Suppl, p. S15-S20.

46. Frahm, J., Haase, A., & Matthaei, D. 1986, "Rapid three-dimensional MR imaging using the FLASH technique", *J.Comput.Assist.Tomogr.*, vol. 10, no. 2, pp. 363-368.

47. Currey, J. D. 1999, "What determines the bending strength of compact bone?", *J.Exp.Biol.*, vol. 202 (Pt 18), pp. 2495-2503.

48. Currey, J. D. 1988, "Strain rate and mineral content in fracture models of bone", *J.Orthop.Res.*, vol. 6, no. 1, pp. 32-38.

49. Hodgskinson, R. & Currey, J. D. 1990, "Effects of structural variation on Young's modulus of non-human cancellous bone", *Proc.Inst.Mech.Eng [H.]*, vol. 204, no. 1, pp. 43-52.

50. Hodgskinson, R. & Currey, J. D. 1990, "The effect of variation in structure on the Young's modulus of cancellous bone: a comparison of human and non-human material", *Proc.Inst.Mech.Eng [H.]*, vol. 204, no. 2, pp. 115-121.

51. Link, T. M. & Bauer, J. S. 2002, "Imaging of trabecular bone structure", *Semin.Musculoskelet.Radiol.*, vol. 6, no. 3, pp. 253-261.

52. Genant, H. K. & Majumdar, S. 1997, "High-resolution magnetic resonance imaging of trabecular bone structure", *Osteoporos.Int.*, vol. 7 Suppl 3, p. S135-S139.

53. Link, T. M., Vieth, V., Langenberg, R., Meier, N., Lotter, A., Newitt, D., & Majumdar, S. 2003, "Structure Analysis of High Resolution Magnetic Resonance Imaging of the Proximal Femur: In Vitro Correlation with Biomechanical Strength and BMD", *Calcif.Tissue Int.*, vol. 72, no. 2, pp. 156-165.1.

5. Development of Multiple Receiver Imaging Hardware and Software for use at 4.7 T

In this chapter a prototype array coil, designed in conjunction with Pulseteq (Guilford, Surrey, UK) is evaluated.

High field strengths enable higher resolution images to be obtained. For the greatest improvements in resolution to be achieved the best possible SNR performance is required from RF receivers. Array coils have been used increasingly because they enable the higher sensitivity of a surface coil to be achieved over a larger volume. Array coils are also used to speed up image acquisition with techniques such as SENSE [1] and SMASH [2]. The efficacy of the prototype array coil for this purpose is also investigated.

Array coils have varying sensitivity and so they produce multiple images with a variation in intensity across them. To form an image of uniform sensitivity and optimal SNR, accurate maps of the individual coil sensitivities must be obtained and the multiple images combined having been weighted on a pixel-by-pixel basis according to their sensitivity. The software that will be described here, developed to reconstruct images from both fully sampled and reduced Fourier data sets, is also used to evaluate the coil design and performance.

The work of Navjeet Chhina, responsible for the design and production of the array coils and Mark Cooper and Colin Sunderland, responsible for the electronics (from Pulseteq, Guilford, Surrey) in the array coil used in this section is acknowledged.

5.1 Background and Introduction

5.1.1 Surface Coils

It has long been realised that surface coils, so called because they are applied to the surface of an object, provide a very efficient way of receiving signal. These coils can be positioned very close to the object of interest and are very sensitive to signal originating from their vicinity. In addition, because most of the noise in a coil originates from the sample (this is especially true at higher field strengths) a coil that only picks up signal from a small, localised region will only pick up noise from a small, localised region. This has the overall effect of producing a coil that has a very high SNR performance in its vicinity.

The main disadvantages of a surface coil are that the coil can only effectively cover a certain volume and that over this volume the sensitivity to signal from the object will vary (though, as we will see both of these characteristics can be used to provide distinct advantages). Due to the principle of reciprocity [3] the sensitivity to signal produced in a receiver coil from a field B_1 has the same spatial dependence as the B_1 field generated by the coil when current is being driven around it. This means that surface coils produce a spatially varying B_1 field when used to transmit RF pulses and correspondingly produce a flip angle that varies with spatial position. Hence, for many routine applications, where uniform flip angles and uniform sensitivity over a volume are desirable, coils such as the birdcage [4] have become the clinical workhorses.

5.1.2 Using Multiple Surface Coils Simultaneously

While surface coils have been used throughout the development of NMR/MRI, one relatively recent development made by Roemer et al in 1990 [5] has meant that surface

coils can be used with greater scope; this was the ability to simultaneously receive signal from multiple surface coils. Receiving from multiple coils simultaneously requires a separate receiver channel incorporating the usual receiver circuitry for each coil. In addition, the coils have to be non-interacting. When a receiver coil is placed near a sample that has been excited by an RF pulse a current is induced in it by the field from the sample. This current is the signal that is measured during an acquisition. A current in a coil produces a field, which in turn induces a current in any secondary receiver coils that experience the field. This interaction means that the coils pick up signal and noise from one other. Hence, the coils lose their highly localised sensitivity to signal and noise from the sample and reduce their high, local SNR performance. If multiple surface coils are used together they must not interact if they are to incorporate the high, local SNR performance of the individual elements, while together provide coverage over a large volume.

A larger volume coil used around an array of surface coils can provide uniform RF transmission, which is important in most applications. This also requires careful decoupling between the transmit and receive coils to prevent the RF power being deposited directly into the receivers as opposed to the sample. Pin diodes are normally used to actively switch the receiver array into a detuned mode during RF transmission. The correspondence between the multiple receivers used in NMR/MRI, and phased array ultrasound and radar, led Roemer to call his array coils 'The NMR Phased Array'.

5.1.3 High Field and High Speed Applications

Two factors have catalysed both further developments in, and the increased use of, array coils. Methods such as spectroscopic imaging [6,7] and the desire for ever higher

resolution images have demanded coils that produce the highest SNR at the expense of SNR uniformity. In addition, imaging of constantly moving systems such as the bowels and the heart has made it desirable to shorten even the most rapid imaging sequences. One other tendency has been the continuous move to higher field strengths throughout the development of NMR and MRI, to provide greater SNR and, more recently, increased sensitivity to BOLD contrast. The main reasons that array coils are required at higher fields (as at lower field strengths) are to maximise SNR performance and to increase acquisition speed. At higher field strengths, the increase size of magnetic susceptibility gradients causes the faster decay of T_2* weighted signal during image acquisition in sequences such as Gradient Echo EPI. In this example, image quality is reduced at higher field strengths due to increased levels of blurring and distortion. To improve the image quality, faster imaging is required and array coils can be used to achieve this goal. It is also noted that at higher field strengths many volume coil designs no longer provide uniform RF reception due to dielectric resonance effects (see section 2.10 for a brief description).

It was realised that the simultaneous acquisition of data could be utilised for increasing the speed of image acquisition [8] even before Roemer had published his paper that enabled the use of multiple receivers in parallel. Increased speed may be achieved because the amount of information per unit time acquired by parallel receivers is greater. Each view of an object provided by a different coil gives the same information about the object modulated by the spatial sensitivity function of the coil. If the sensitivity functions of the coils are sufficiently different over the same region of an object, knowledge of the spatial sensitivity functions can be used to localise where the signal has come from. If spatial localisation can be partially achieved by the coils, the

demands of spatial localisation using Fourier encoding have been reduced. This allows a reduction in the density with which k-space must be sampled [1]. With a reduction in sampling density, for most sequences, comes a reduction in the length of the k-space trajectory, without increasing hardware demands (such as gradient amplitudes / switching rates).

To map the array elements spatial sensitivities, images must be obtained from each of the coils in the array. A further reference image of the same contrast and spatial region of the object is then required. The division of the images will then produce a ratio of coil sensitivities. If an approximately uniform reference image is used, then the ratio of the coil sensitivities will be a good estimate of the absolute sensitivity of the array coil element, scaled relative to the coil used to obtain the reference image. It is normally necessary to measure the sensitivity data for each different subject due to different loading of the coils producing inter-scan variability in the coils sensitivities. The time required to map the coil sensitivities is minimal in dynamic studies where the maps can be used for the subsequent generation of many images. For conventional imaging the time required for pre-scanning can be minimised and in some cases removed altogether [9,10].

The extra information available from array coils has also been exploited in other ways by, amongst others, Bydder et al to correct for motion corrupted data by regenerating affected k-space lines or to produce navigators from the data already acquired [11,12], and to remove ghosting by Kellman et al [13]. These techniques have shown some promise but have yet to be introduced into routine use in a clinical setting.

The coil desired for the SMIS MR5000, 4.7 T / 90cm bore system is a 4-channel receive only dedicated head coil that can improve the SNR of imaging when used as a standard array coil over the whole brain volume. This should enable an improvement in the resolution available for high resolution imaging. Furthermore, the coil should be able to speed up imaging by at least a factor of 2 in either of two dimensions without significant geometry related noise enhancement in SENSE images (see section 2.7.1 and 5.2.5). The coil also needed to be compatible with audio and visual communication apparatus used to both communicate with the subject and to present audio and visual stimulus (e.g. in functional MRI studies).

5.2 Methods

In this section the array coil design, and the methods used to evaluate it, are summarised. The process used to map the array coils sensitivity and to estimate the coils performance is described. In addition, an FSE sequence optimised for use at 4.7 T is illustrated and the experimental details are given.

5.2.1 Array Coil Requirements

The requirements of the array coil designed for use on the SMIS MR5000, 4.7 Tesla / 90cm bore system are distinct. The receiver system comprises of four channels; the array is dedicated to head imaging; and it will be used as a receive-only phased array coil. A body volume coil often provides RF transmission. However, in the system used the head gradient coil inserts restrict the space available. This means a dedicated head volume coil must be used for RF transmission.

The volume coil used for transmission was a 28cm diameter, 16 rung, high-pass, birdcage coil (see reference [14] for a summary of birdcage coil design). The birdcage was a transmit / receive coil to enable a reference image to be obtained with a reasonably uniform sensitivity for sensitivity mapping. The array coil had to fit within the 28cm birdcage while allowing enough space for the subject, making space a premium. The array coil was required to provide up to 3 times the SNR at the edges of the brain, while maintaining the SNR performance of the birdcage in the centre of its FoV. In addition, the array coil elements needed to have sensitivity profiles that would allow the coil to be used as a SENSE array to speed up imaging in either of the principal gradient directions, while maintaining acceptable SNR performance throughout the imaging volume.

5.2.2 The 4-element 200MHz Array Coil

The design features incorporated into the array coil are given below (see figure 5.1 for pictures that illustrate the coil design):

- The efficiency of surface coils is dependent on their close proximity to the tissue being imaged. Hence, the coils were made to follow the contours of the head to achieve close coupling over the majority of the irregularly shaped imaging volume.
- The size of each of the array elements was designed to have approximately the same penetration as a 12.5cm diameter circular surface coil. In the head, this should provide enough penetration for imaging in the centre, while providing higher sensitivity to the peripheral regions. The localised sensitivity profiles necessary for SENSE imaging should also be provided by coils of these dimensions.

N.B. Using smaller more highly localised coils for SENSE imaging can reduce local regions of degraded SNR performance (i.e. reduce the g-factor in equation 2-40, section

2.7) that can result from the coils inability to separate aliased signals at a particular position. However, if the overall SNR performance of the array coil is also reduced by changing the coil size there may be no net gain in SNR performance for SENSE imaging (i.e. if the SNR_{full} performance is reduced so is SNR_R in equation 2-40, section 2.7). A balance must therefore be made between providing the highest possible SNR over the volume and having sensitivity profiles that are effective in separating aliased signals.

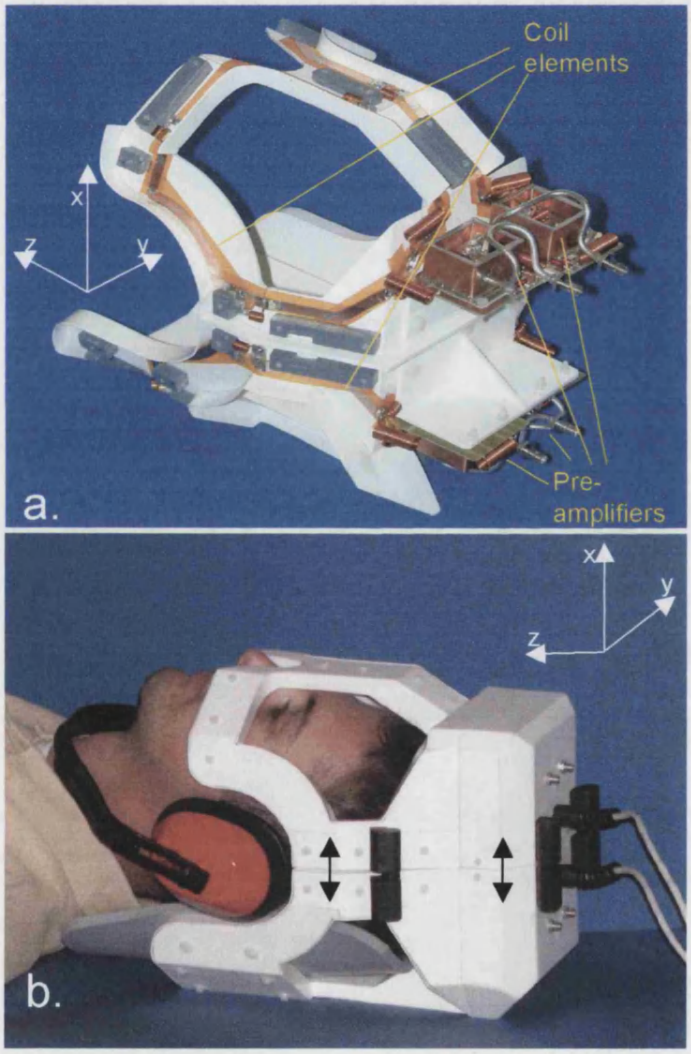

Figure 5.1 The Prototype Four-Element Array Coil
a.The array coil is displayed on the plastic former without its covering. The individual elements of the array can be clearly seen. Each coil has its own pre-amplifier.

b.The sealed array coil is seen with a subject inside. Spaces are left to allow audio and visual communication to be maintained. The top half of the coil may be removed to allow easier access for a subject. The whole array coil with the subject inside sits on the standard bed and headrest, which then slides into the 28cm diameter birdcage coil in the magnets centre.

- The array was designed to fit within a standard 28cm birdcage transmit / receive coil.

- The plane of the coils was not clear because they are formed by the contours of the head. However, the approximate plane of the coils was offset by around 45° to the principal gradient axes (x and y). This means that each coil has a spatial sensitivity profile that varies both in magnitude and phase when either of the principal axes is chosen for reduced Fourier encoding. Furthermore, this coil arrangement should allow the achievement of higher speed up factors when using 2D SENSE [15].
- Good audio and visual communication with the patient was also required. Gaps were left around the ears to incorporate the use of ear defenders. The position of the coils also enables clear vision out of the coil.
- Small gaps were left between the coils of 2-4cm. This should avoid high local regions of noise enhancement when the coils are used to speed up imaging as demonstrated by Weiger et al [16]. This may slightly reduce the SNR performance of the array coil when it is used as a phased array, especially in the centre of the head where smaller coils will not penetrate as effectively.
- The top of the coil could be separated from the bottom to gain easy access to the coil.
- Mutual coupling was minimised solely via high impedance matching to the 2 stage pre-amplifiers [5].
- Pin diodes were used to actively decouple the array and volume coils.

5.2.3 Mapping Sensitivity

Accurate mapping of array coil sensitivity values has been achieved by Preussmann et al in their original SENSE paper [1], drawing on their earlier work [17] and the work in references [18-20]. The mapping procedure described below draws heavily on this work, although it is entirely composed of procedures that have been independently

written and tested. The requirements of sensitivity mapping are that accurate maps can be produced easily on different subjects in a reasonable time scale.

A number of simple image processing tools were required for the sensitivity mapping to be performed. These were programmed in MatLab (Mathsworks, Natick, MA), along with the map generation and reconstruction routines, and provided a basis for the description of a protocol for sensitivity map determination that follows.

5.2.3.1 Masking

In this context, masking images is a simple process that involves the differentiation between pixels that lie within an object from the pixels that lie outside the object. A binary image (or mask) can be created that reflects the status of a pixel; normally the pixel has a value of '1' within the object and '0' outside. Many methods have been used to calculate the masks. One of the simplest (and most frequently used) relies on a signal-intensity-based threshold of the magnitude data (see figure 5.3). Most magnitude images contain a wide range of pixel intensity values and their distribution is multi-modal. However, this distribution can be simplified to being bimodal. There is one peak due to pixels that lie in regions of pure noise and another with pixels containing signal from the object. This means, with an appropriate choice of the threshold level, the pixels above the threshold can be assigned as lying within the object and a reasonably accurate mask created.

The threshold value can be chosen in a number of ways, however, this choice is dependent on the image that is being used to generate a mask. In a noisy image with low SNR, the distinct peaks that are from the signal in the object and the pure noise overlap.

In this low noise regime it is inevitable that some pixels will be incorrectly assigned from both within and outside the object.

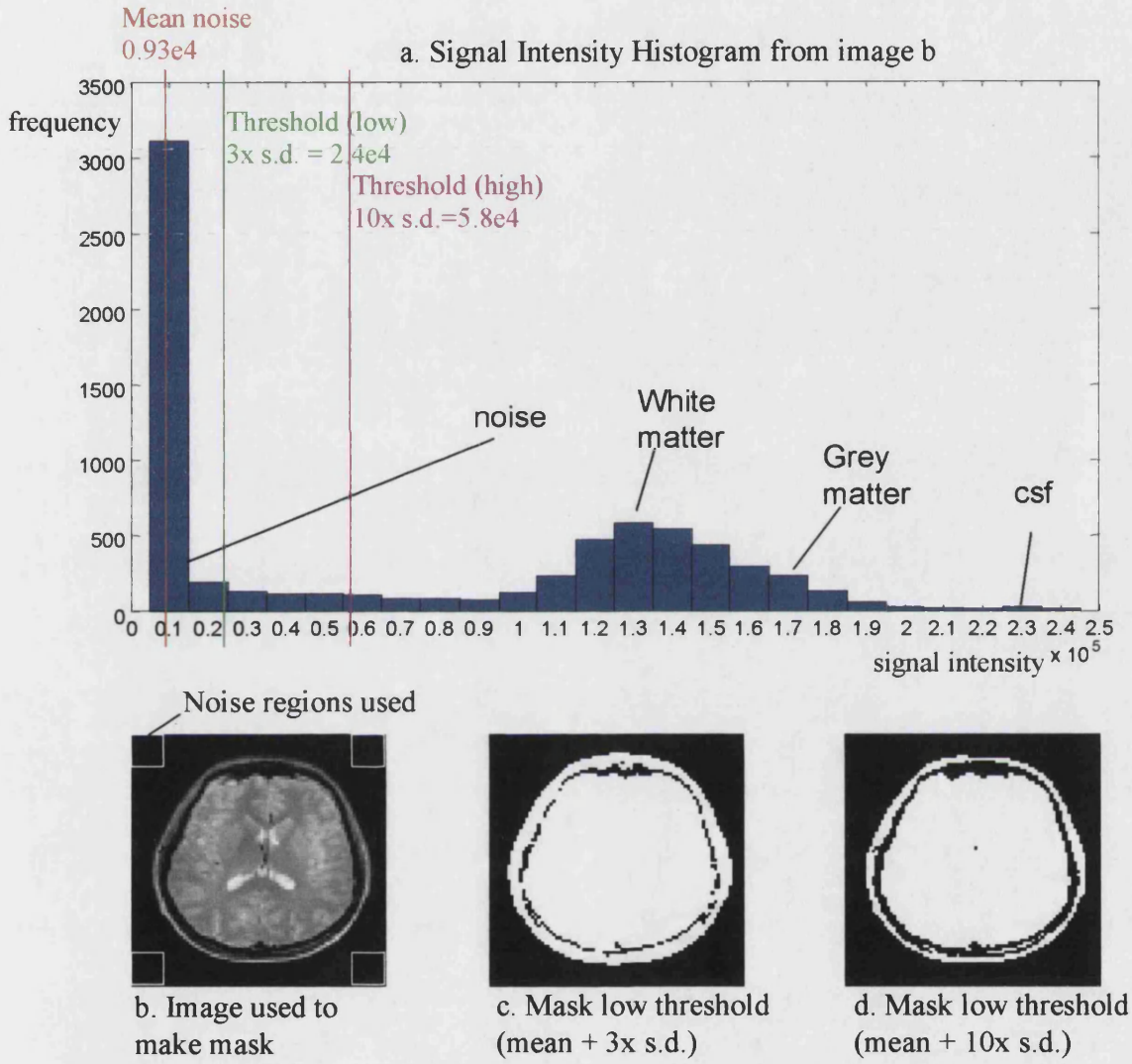

Figure 5.2 Thresholding an image to create a mask
The image *a* on the bottom left is used to create mask images by thresholding using different intensity values. The histogram of pixel intensities is shown; it displays two distinct peaks one from pixels inside the object and another from those outside containing pure noise. A threshold based on the mean and standard deviation (s.d.) of the noise from the 4 corners is demonstrated: the red line gives the mean value of a group of pixels known to contain pure noise, the standard deviation (s.d.) is also calculated from the same group. By adding a number of standard deviations of the noise to the mean value two threshold levels are chosen. Masks are created with these thresholds in *c* and *d* where pixels greater than the chosen level appear white.

The threshold used in this work was produced by taking regions in the corners of the magnitude image that in almost all situations will lie outside the object. The mean and standard deviation of the noise can then be calculated. A threshold level was then chosen by adding a number of standard deviations of the noise to the mean noise level. The rectified noise follows a Rician distribution. Hence, both the mean and the standard deviation of the noise in the magnitude image are proportional to the standard deviation of the noise in the complex image. This process excluded the noise regions effectively in most situations. The strength of the threshold can be varied depending on the purpose of the mask, the object properties and the SNR of the image.

When there are regions of low signal intensity within the object they will often be masked out (e.g. see single pixel in the centre of figure 5.2d). The SNR of the image used will determine if the threshold can be lowered to include them. Ghosting in the background of an image (that sometimes is not visible due to the scaling applied to display an image) can cause inaccurate values of mean and s.d. of the noise. Ghosting can often cause pixels outside the object to also be wrongly assigned.

5.2.3.2 Accurate Masking from Ghosted Array Coil Images

The procedure outlined in this section was developed to gain accurate masks from array elements in the presence of ghosting. Array coil images can be liable to suffer ghosting artefact in some circumstances. Surface coil elements receive signal very strongly from their local region, so the signal level can still be significant far out in k-space. Due to the discontinuity created between the significant signal-level and the edge of the discrete area of k-space sampled, ringing artefact is sometimes found. This artefact is

usually removed, or at least significantly reduced, by applying a filter to the data in k-space. A Hanning filter was used in this work [21].

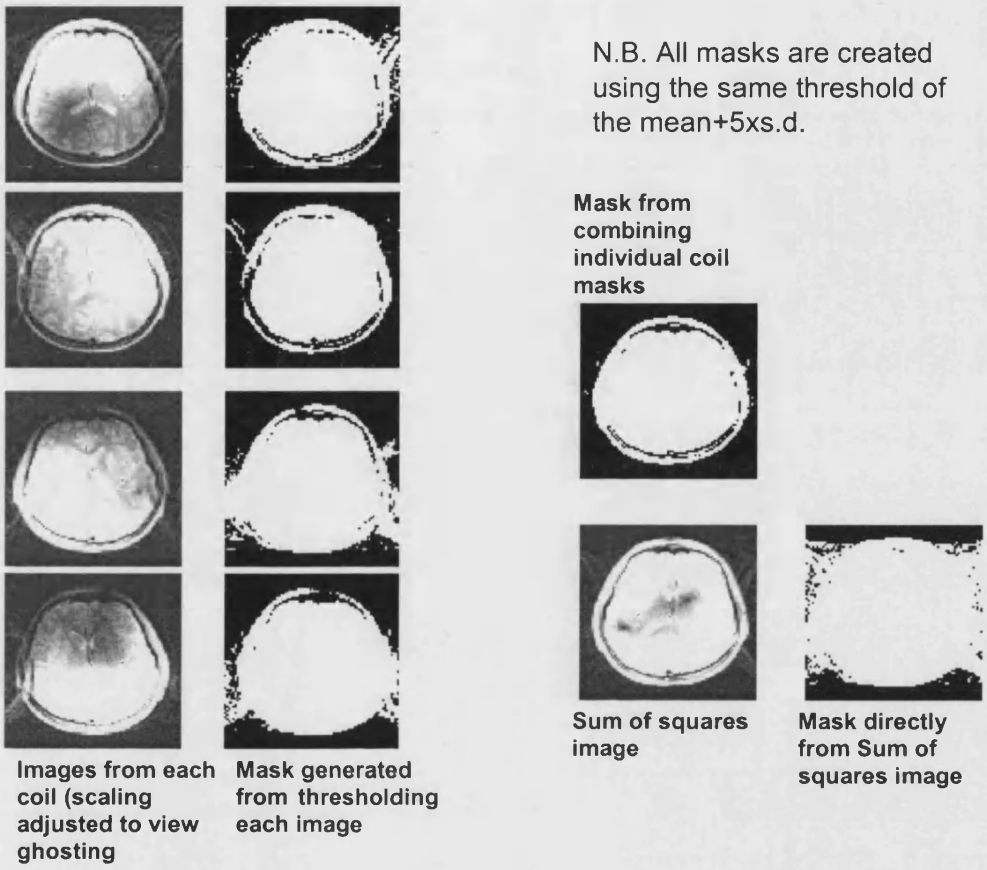

Figure 5.3 Masking array coil images
A mask can be made from all the individual masks (on the left hand side) by assigning a pixel to be inside the image when it has a value of one in a given number of the individual masks (here the pixels had to be present in 3 or more of the masks). On the right hand side a comparison is made between the 'sum of squares' image, a mask created directly from it, and the mask made from combining the individual element masks.

Furthermore, with the Fast Spin Echo (FSE) technique that will be described in more detail in section 5.2.6, significant ghosting can arise from a combination of the imaging technique's PSF, and regions of very high, localised signal intensity produced in the individual array element's images. When a mask is created from the sum of squares of the individual element images there is a further complication of regional variation in image intensity making the choice of threshold level more difficult.

When significant inaccuracies were found in the simple threshold determined mask, an individual mask was created from each individual image from each coil. An examination of these images (see figure 5.4) revealed that the regions of ghosting were different in each image, and so the regions of background assigned as lying within the object in each mask were also different. However, the majority of the object was assigned correctly in each of the individual masks. Using this observation a second criterion could be set for the inclusion of a pixel in a final mask. If we look at a pixel in a given position in the FoV, in each mask the pixel has been assigned a value. If the pixel contains a value of 1 in a certain number of the masks (that can be set depending on the quality and number of images) it is assigned 1 in the final mask, otherwise it is assigned zero. Two choices are then usually possible for creating the mask: a) A low threshold level is used but the pixels must equal '1' in a high number of the masks. b) A high threshold level is used but a lower number of masks must agree for the pixel to be included. In figure 5.3, this masking procedure is shown to provide a more accurate mask than using a simple threshold on the sum of squares image. Generally, values for the threshold level were between *mean+2xs.d.* and *mean+8xs.d.* of the noise. The pixels had to be classified as within the object for either 2 or 3 of the individual masks.

5.2.3.3 Density filling and Erosion or Region Growing

Density filling involves the assessment of the environment of a pixel. Namely, is the pixel isolated (also called sparse) or is it part of a larger object? Most objects that are imaged using MRI are part of a large body that normally takes up a central region in the FoV. Thus, pixels that occupy a sparse environment are unlikely to lie within the object.

This can serve as a further criterion for the removal or addition of pixels to the masked region that have already been assigned using an intensity level threshold.

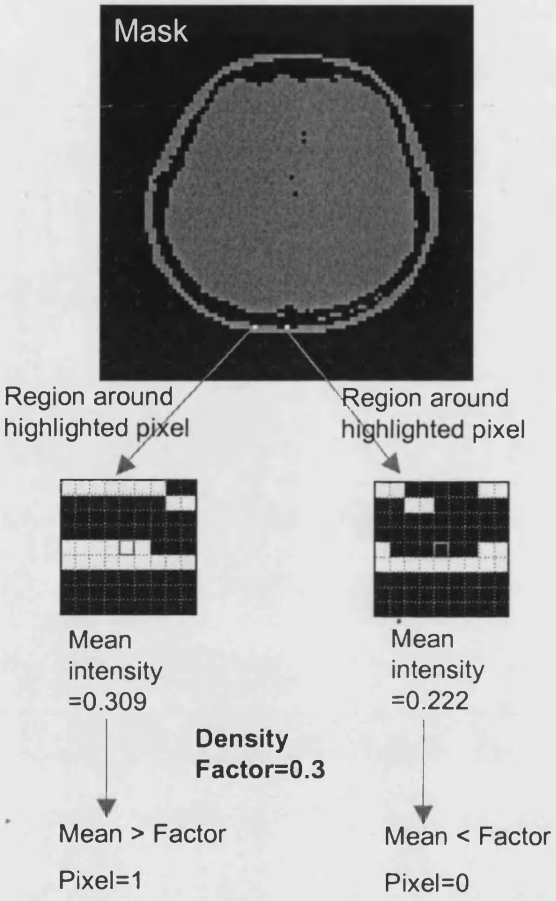

Figure 5.4 Density Filling
The process of density filling is demonstrated opposite on a binary mask shown at the top. A pixel is considered as belonging within the object (pixel intensity=1) when its surrounding region has a mean pixel intensity above the density factor. Alternatively, the pixel is excluded (pixel intensity=0).

N.B. The pixel itself may be either 1 or 0; it is then sparseness of the local region around the pixel that determines whether it is assigned 1 or 0.

The process of density filling is described in figure 5.4. For each pixel a sub-matrix is created from the its surrounding environment. A different sized sub-matrix may be selected but here a 9x9 pixel region was used. The mean value of the pixel's sub-matrix indicates how sparse the environment of the pixel is. A threshold can then be chosen based on the mean value of the pixel's sub-matrix. Pixels that have a mean sub-matrix value above a certain factor (here called the density factor) are considered not to be in a sparse environment and so remain assigned to the object (pixel intensity=1). On the contrary, if the mean of the sub-matrix falls below the density factor they will be considered sparse and so are excluded from the object (pixel intensity=0).

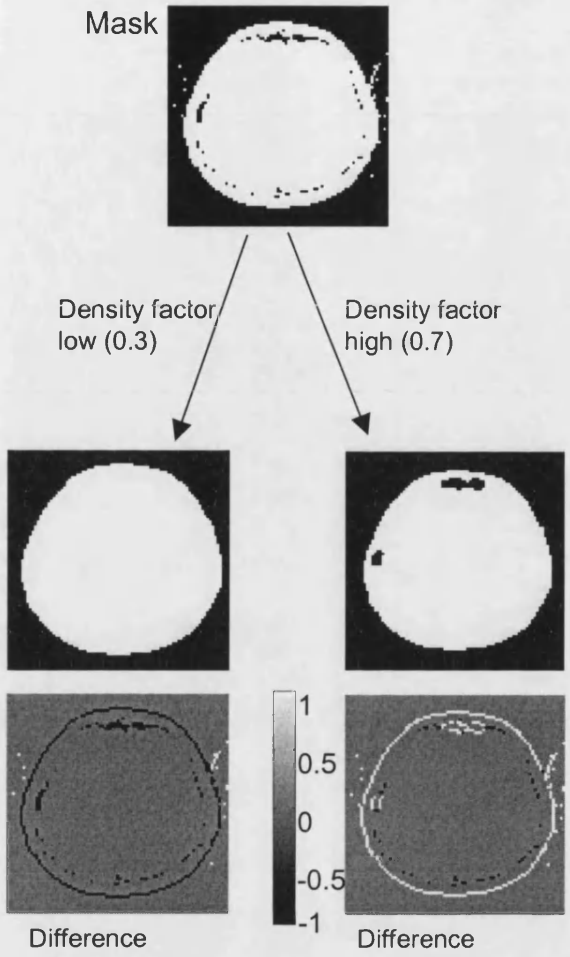

Figure 5.5 Using Density Filling to Grow or Erode Regions
A density filter is applied to a mask (top). A low density factor is used to create the mask on the left hand side, while a high density factor is used on the right hand side. The resulting new masks have had very isolated pixels removed. Additionally, the mask is either eroded (right hand side) or grown (left hand side) depending on the density factor used.

The density filling procedure can be used to erode or grow regions (see figure 5.5 above) by controlling the level of the density factor. If a low density factor is chosen then pixels on the edge of a structure are likely to be included within the object and so 'grow' the region. Alternatively, if a high density-factor is chosen then pixels on the edge of a structure are likely to be removed and excluded from the object (or eroded). Pixels that lie in a region of pure noise are highly likely to be in a sparse environment, and so are normally removed even when a low density factor is chosen.

5.2.3.4 Sensitivity Map Generation

Sensitivity maps are obtained by image division followed by a refinement procedure. The division of an array coil image 'I_A' of sensitivity '$S_A(x,y)$' by another image 'I_{REF}'

of sensitivity '$S_{REF(x,y)}$' removes all of the contribution to the signal intensity in the images from the magnetisation, leaving purely the ratio of the coil sensitivities. This happens provided that both I_A and I_{REF} have sampled the same spins 'ρ' in the same way (i.e. that relaxation / pulse sequence parameters were identical), the spins contrast is given by 'C'.

$$\begin{aligned} \mathbf{I_A(x,y) = S_A(x,y) \cdot \rho(x,y) \cdot C(x,y)} \\ \mathbf{I_{REF}(x,y) = S_{REF}(x,y) \cdot \rho(x,y) \cdot C(x,y)} \end{aligned} \qquad (5\text{-}1)$$

hence

$$\mathbf{I_A(x,y) \Big/ I_{REF}(x,y) = S_A(x,y) \Big/ S_{REF}(x,y)} \qquad (5\text{-}2)$$

There are various choices that can be made for the reference image [1,5,22]. The best solution is to use a separately acquired volume coil image. The advantage of this approach is that the sensitivity of the reference is highly uniform. This means the resulting sensitivity information will be similar to the absolute sensitivity of the coil, scaled to the sensitivity of the coil used to take the reference image. The main drawbacks of this approach are practical issues. The coil used to gain the reference must be capable of performing in transmit and receive modes while being decoupled from the array coil. This is normally achieved by pin diode decoupling. The second disadvantage of using a separate reference image is the additional time penalty for the acquisition of a separate image. This penalty can be minimised by acquiring fast, low resolution images to obtain the sensitivity information.

An alternative solution is to use the square root of the sum of squares of the array coil images (this will be referred to as the 'sum of squares' or '*SSQ*' image from now on). This is a pragmatic alternative that provides a reasonable solution, although the images

produced will have the sensitivity variation present in the sum of squares reference [5]. Another alternative is to use one of the individual element images as a reference [22].

N.B. For standard array coil imaging the *SSQ* image can be easily formed from the individual element images without knowledge of the coil sensitivity functions. This avoids the need for sensitivity mapping while producing an image with a high level of SNR [5].

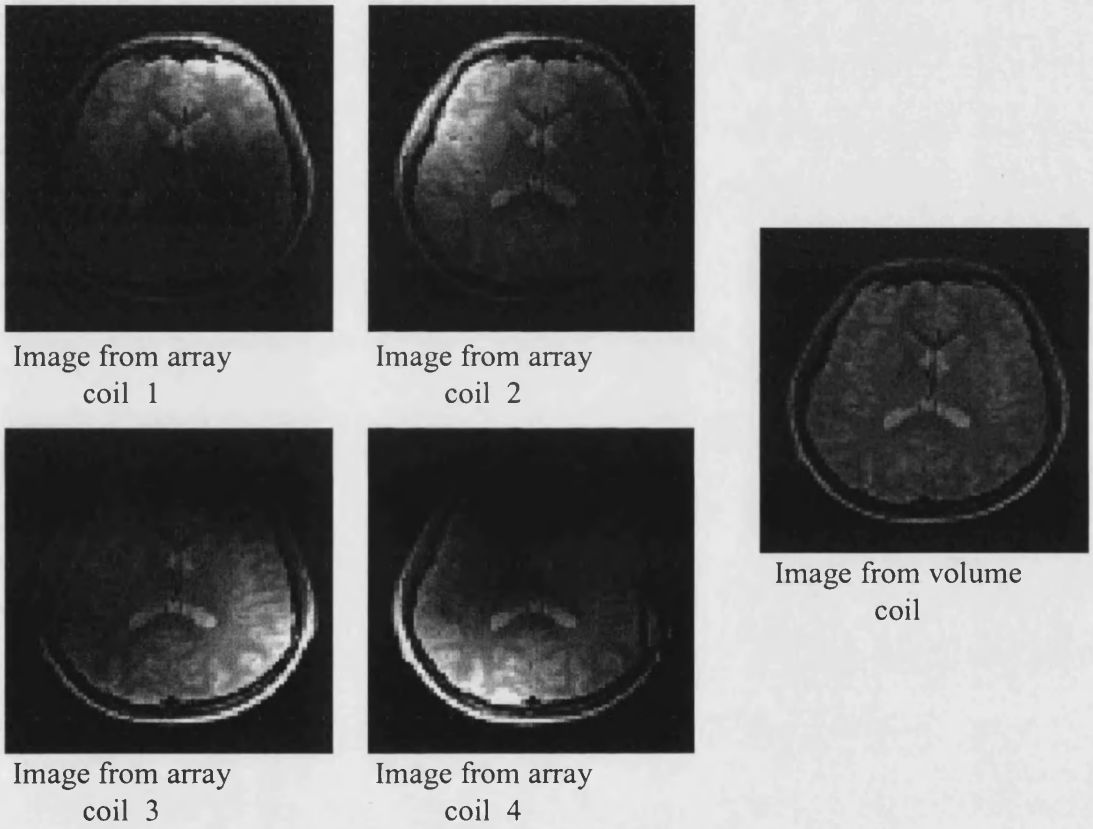

Figure 5.6 Array coil and volume coil images for sensitivity map generation
All the images are displayed with the same scaling and exhibit the same contrast behaviour. The difference in coil performance between the individual array elements can be clearly seen. The highly localised regions of increased signal intensity in the array element images indicates the respective position of the array element. While the volume coil image displays a more uniform signal level, it also exhibits a lower maximum signal level.

As stated above sensitivity map generation requires array element images and a reference image. Both array coil images and a volume coil image were acquired such as

those in figure 5.6. Exactly the same the pulse sequence parameters and instrument settings were used between acquisitions. In this way the volume and array coil data was characterised by the same spin relaxation behaviour and image contrast.

There are two factors that are also important for the acquisition of the images. The first is speed, because the time required for pre-scanning reduces the time available for useful data acquisition in a limited examination period. Secondly, gross movement between the acquisition of the reference and array coil images will produce errors in the sensitivity information that are more difficult to eliminate by processes such as smoothing.

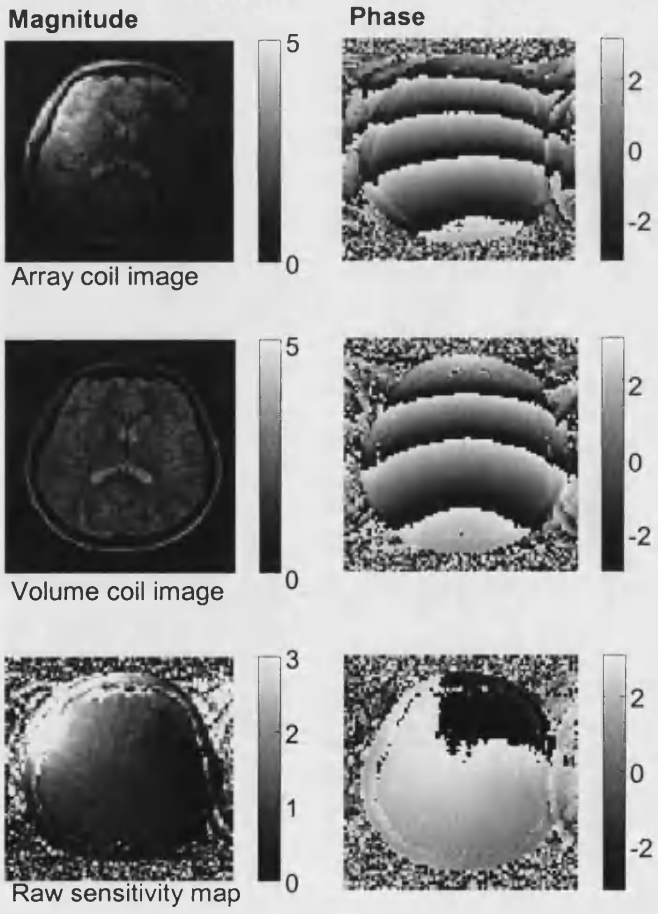

Figure 5.7 Generating Raw Sensitivity Maps
On the Left Hand Side (LHS) is magnitude data; on the Right Hand Side (RHS) is the phase information. The top row displays the complex data from one array coil element. The middle row shows the complex data from the volume coil. The bottom row shows the complex raw sensitivity data formed by the division of the complex array coil images (top) by the complex volume coil images (middle).

The mapping procedure was demonstrated here on a single array element to avoid unnecessary complication. The data chosen for the demonstration in figures 5.7 and 5.8 exhibited some ghosting to better illustrate the refinement procedure.

The creation of raw sensitivity maps by complex image division is shown in figure 5.7. The raw sensitivity map exhibits little of the structure or contrast seen in the image above it. The values seen in the map show that the array element has around 3 times the sensitivity of the volume coil in its local vicinity, but that it only covers a small region of the volume with a sensitivity greater than 1. It is also clear that the sensitivity of the coil has a phase component that is slowly varying across the object. If the volume coil reference is assumed to have a spatially uniform sensitivity function (i.e. $S_{REF}(x,y)=1$ in equation 5-2), the ratio of the images is then a close approximation to the absolute sensitivity of the array element both in magnitude and phase but its value is scaled relative to the volume coil.

The raw sensitivity maps need to be refined for several reasons. Primarily, the noise in the raw maps needs to be removed so that additional noise is not propagated into the final image during the reconstruction process. Smoothing is applied to the sensitivity maps to remove any noise. Extrapolation of sensitivity information can be used to prevent errors at the edges of an object created by smoothing. This is because the averaging effect of smoothing at discontinuities causes errors in the sensitivity values. In addition, the maps need to be extrapolated over a region large enough to allow for subject movement during the course of an examination.

A Binary mask formed from thresholding the array coil images followed by the application of a density filter as described in section 5.2.3.2-5.2.3.3. The object is seen as white pixels with a value of 1. Noise/low value regions are seen as black pixels with a value of 0.

B Binary mask formed from thresholding the volume coil image as described in section 5.2.3.1 followed by the application of a density filter.

C Binary mask image formed from multiplying the two masks A and B, thus eliminating all the pixels identified by either A or B as potentially unreliable i.e. if 1=true and 0=false, & is the logical operator then C=(A=1)&(B=1).

D Mask is 'grown' by a process of repeatedly density filling the mask seen in A (though any of A to C could have been used). 3 density fills were performed here using a 3x3 sub-matrix and density factors of 0.1, 0.3, 0.3.

E By calculating |D-A|-1, regions that require sensitivity information but do not contain it reliably in the raw data have been identified (black pixels).

Figure 5.8 Identification of regions for extrapolation of sensitivity information
A process of masking and region growing using the masking and density filling procedures outlined in preceding sections is used to identify a region over which sensitivity information is required but where the information obtained directly from the raw maps is considered to be unreliable.

Masking was used to identify regions of the sensitivity maps that contain poor sensitivity information. Regions of low signal intensity within the object, and regions containing pure noise outside the object, were identified by masking and density filling

as described in sections 5.2.3.1-5.2.3.3. In figure 5.8, the process of identifying pixels with unreliable sensitivity data in the raw maps is described. Masking was used to eliminate all pixels containing low signal or pure noise in either set of data used for making the maps. The region around the object was identified by region growing to create a new mask. Subtraction of the two masks (figure 5.8 D & A), yielded a region over which sensitivity information must be extrapolated (figure 5.8 E).

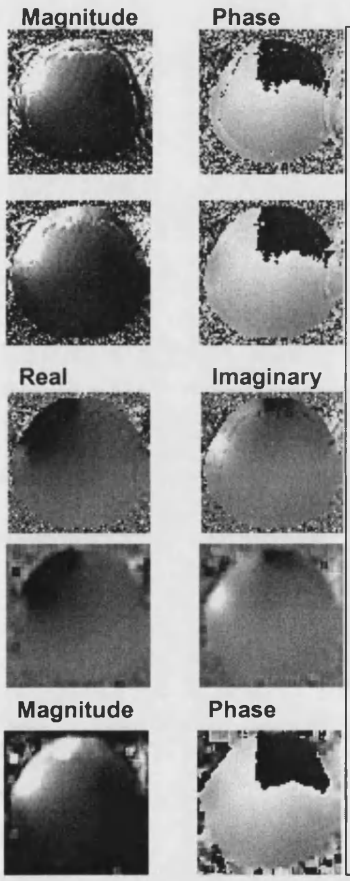

A The raw sensitivity maps for one of the array elements

B Regions on the edges of the object or that contain unreliable sensitivity information are identified using the masking procedure outlined in figure 6.8. These pixels are then filled with the nearest pixels sensitivity values. The resulting maps are shown here.

C Complex data is separated into real and imaginary components because they do not contain discontinuities.

D Smoothing is applied using a 5x5 kernel of 1/25s.

E Refined maps magnitude and phase components are shown.

Figure 5.9 Processing the sensitivity maps by smoothing real and imaginary components
The raw sensitivity maps are processed to remove noise via a process of smoothing. The real and imaginary components of the signal are smoothed individually. This produces refined magnitude and phase sensitivity maps without requiring any phase unwrapping procedures. Errors are avoided at the object edges by filling regions lying on the edge of the object with reliable sensitivity information from within the object.

The refinement procedure applied to the raw maps was illustrated in figure 5.9 & figure 5.10. A choice between the components of the data that were smoothed was allowed. In figure 5.9, smoothing was applied to both the real and imaginary components of the sensitivity maps. Alternatively in figure 5.10, smoothing was applied to the magnitude data only.

The raw sensitivity maps are shown at the top of the figures 5.9 & 5.10. Pixels identified as requiring sensitivity information, but that did not contain reliable values in the raw maps were identified (as described in figure 5.8). The pixels identified were then assigned a more accurate estimate of the coils sensitivity at that position. The nearest neighbours' pixel intensity was used to 'fill in' the missing data to give more accurate values in these pixels. This process should give good results when the sensitivity information is missing from a few pixels within the object. The sensitivity information does not vary rapidly over the short distances, so the nearest neighbour value used for the extrapolation is unlikely to have a large error prior to refinement using smoothing. The averaging effect of the smoothing tends to produce a final sensitivity value in an 'identified' pixel that is an interpolation between the nearest reliable values. This process will also produce reasonable results at the edges of the object; further from the objects edges the sensitivity functions will tend to level off and so become less accurate. Large low resolution pixels were used for obtaining the sensitivity maps. Hence, the sensitivity values typically used here lie within a region exhibiting a high degree of accuracy, even when there is subject movement of several millimetres.

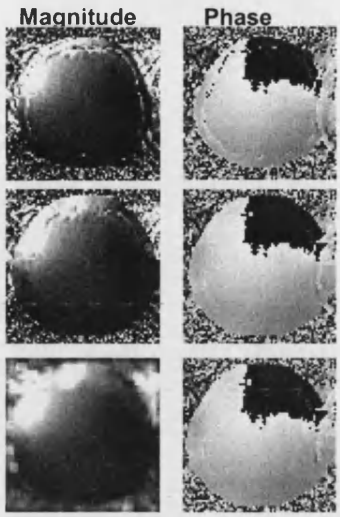

A	The raw sensitivity maps for one of the array elements
B	Regions on the edges of the object or that contain unreliable sensitivity information are identified using the masking procedure outlined in figure 5.8. These pixels are then filled with the nearest pixels sensitivity values. The resulting maps are shown here.
C	Refined maps magnitude and phase components are shown.

Figure 5.10 Processing the sensitivity maps by smoothing the magnitude component
The magnitude component of the raw sensitivity maps was smoothed. This produces refined magnitude maps without changing the phase information. As in figure 5.9 errors are avoided at the object edges by filling regions lying on the edge of the object with reliable sensitivity information from within the object.

There are a number of parameters that have to be chosen for the generation of sensitivity maps. These have different effects on the accuracy of the final maps, and will also depend on the pulse sequence and imaging parameters used. A full discussion of this is not presented here however some of the various parameters and implications are outlined.

1. ***Threshold for masks to make maps:*** here it is important to remove the regions that could contain inaccurate values in the raw maps so a reasonably high threshold is preferred. However, if too many pixels are removed then large regions within the object may need to have sensitivity information recovered. The greater the distance over which the extrapolation must be made, the greater the possible error.
2. ***The size and shape of the smoothing kernel used on the maps:*** a greater level of smoothing will reduce random noise but may introduce systematic error especially

where a function is changing rapidly. The shape of the kernel can be changed to allow more or less averaging and to control its special extent. A simple box filter (e.g. a square of identical values and zero outside) was generally found acceptable. The kernel can also be changed on a pixel wise basis (for an example see reference [1]).

3. ***Smooth real and imaginary data or just magnitude:*** If the real and imaginary components of the sensitivity information have a high frequency variation just the magnitude data may be smoothed to avoid introducing systematic error.
4. ***Reference image:*** A volume coil reference can be acquired and used; alternatively, a sum of squares reference can be generated and employed as a reference.
5. ***Final mask to apply to the processed sensitivity maps from all the array elements:*** As discussed previously parts of the FoV that are far away from the object do not contain reliable sensitivity information. In addition, the images that are reconstructed contain regions of noise. For pixels that are not aliased, treating them as being aliased with a region outside the object means that some of the signal originating from a position will be assigned as lying outside the object. Thus, in SENSE reconstruction, masking the background reduces noise in the image. In addition, if parts of the object are masked out incorrectly, the signal from a position outside the masked region will appear as artefact at the aliased position inside the masked region.

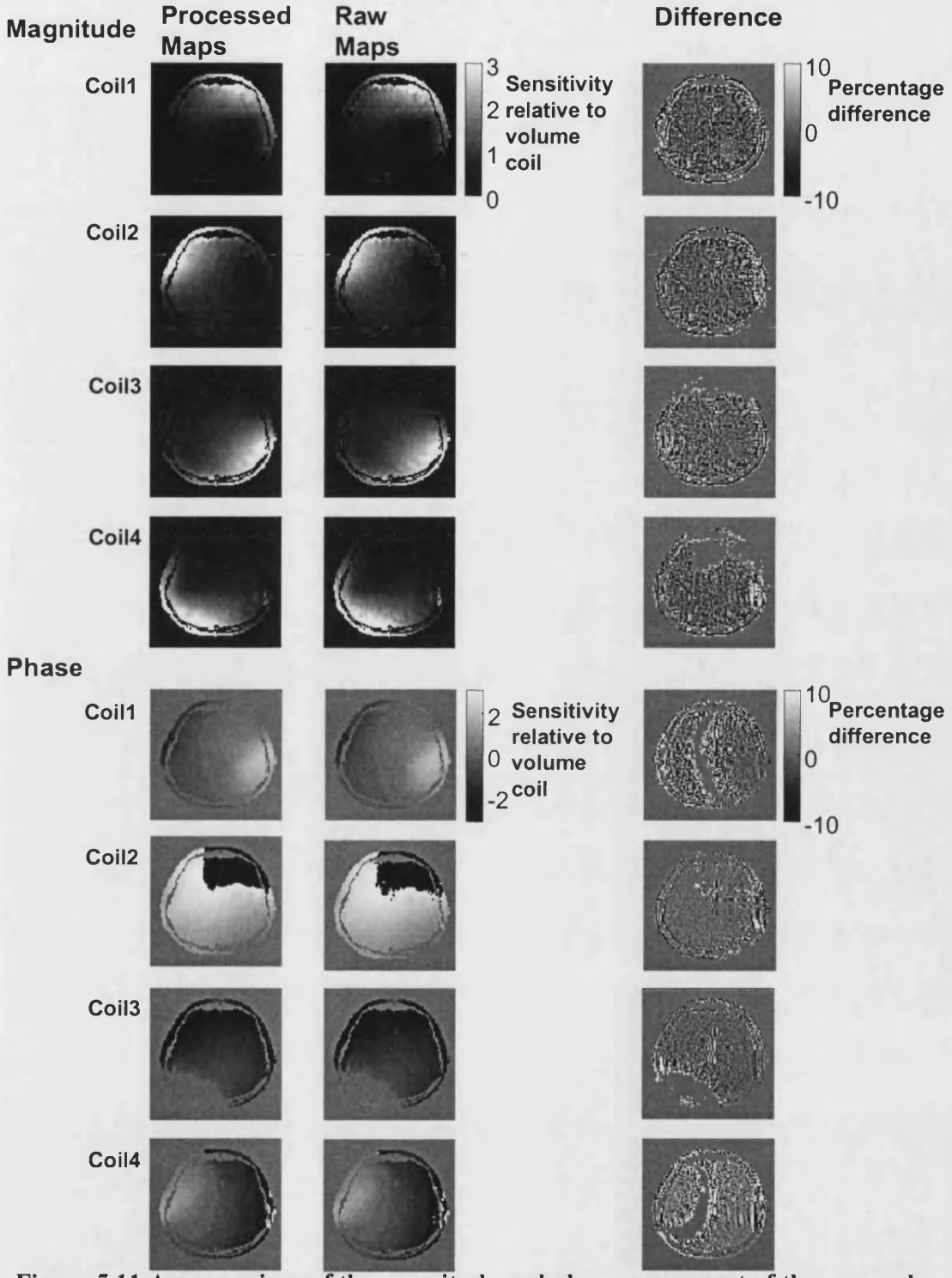

Figure 5.11 A comparison of the magnitude and phase component of the raw and refined sensitivity maps

On the left hand side are the refined masked sensitivity maps from each of the individual array elements. In this example maps were processed with a 3x3 smoothing kernal applied to the real and imaginary data. Next to these are the raw sensitivity maps. On the right hand side are difference images. The difference images demonstrate the refinement procedure has removed noise from the maps seen in the speckled appearance of the difference images. The maps do not exhibit any obvious systematic error from the smoothing.

To display the effect of the sensitivity map refinement 'difference' images are taken between the raw sensitivity maps and the refined versions in figure 5.11. In both the magnitude and phase components of the sensitivity maps random noise and local fluctuations in the maps have been removed without introducing any obvious systematic error to the information. This is demonstrated in the percentage difference images that show isolated pixel differences of up to 10% (white and black pixels). Only in the regions at the edges of the object that exhibit ghosting are consistent differences from the raw sensitivity maps found.

5.2.4 Combining the Multiple Images

In Roemer's original paper on combining images from array coils [5] the optimal way to combine the array images (I_{array}) was derived. The individual coils signals are combined by weighting them according to their particular sensitivity ($S(x,y)$) at a given spatial position. As noted by Bydder et al [22] this is equivalent to a SENSE reconstruction (see section 2.7) with no speed up factor.

$$\mathbf{I}_{comb} = \mathbf{S}^{-1} \cdot \mathbf{I}_{array} \qquad (5\text{-}3)$$

5.2.5 Calculating SNR

We want to assess the SNR performance of the array coil relative to the volume coil for standard imaging; here this is called the 'basic' performance of the array. The coil images are combined by weighting them optimally according to the sensitivity of the coil at that particular spatial position. This means the signal is effectively scaled to one and the relative SNR is proportional to 1/noise (see equation 5–4 below).

The 'basic' SNR performance of the array (relative to the volume coil) was estimated from the coil sensitivity maps using the following expression [1,16]

$$\mathbf{SNR}_{full}(\mathbf{r}) \propto \frac{1}{\mathbf{Noise}_{full}} = \sqrt{\left(\mathbf{S(r)}^{H}\boldsymbol{\Psi}^{-1}\mathbf{S(r)}\right)} \qquad (5\text{-}4)$$

Where S is the encoding matrix (made from the sensitivity map values), which here is simply a vector containing the coil sensitivity values at a given position r. Ψ is the receiver noise matrix containing the level and correlation of the noise. The superscript H denotes the transposed complex conjugate (sometimes called hermitian conjugate).

Ψ can be calculated by taking the average over sets of simultaneously acquired samples of noise in different coils where the coils are counted by the subscripts γ and γ', where γ,γ'=1:number of coils [16]

$$\psi_{\gamma,\gamma'} = \mathbf{mean}\left(\eta_{\gamma} \cdot \eta_{\gamma'}^{*}\right) \qquad (5\text{-}5)$$

Equation 5-5 takes an average over many samples of the product of the pure noise signal in one coil η_{γ} multiplied by the complex conjugate of the pure noise signal in a second coil $\eta_{\gamma'}$. The noise amplitude can usually be described by a normal distribution with a mean value of zero. If the coils signals are independent of each other then the mean of the product yields a value of zero. In contrast, if the coils sample similar noise then, on average, the product of the signals will sum to a value reflecting their level of correlation. Ψ is then a matrix with the diagonal components containing the relative level of noise in each channel, with the cross term reflecting the correlation of noise between the different coils. In some cases a unit matrix can be used to approximate Ψ because the noise in each channel is made to be equal so the diagonal values of Ψ are equal (and could be normalised to one). Additionally, when the level of correlation between the different channels is low the cross terms in Ψ are small and can be

approximated by zero. Ψ can be calculated by taking a region of pure noise in images from the different coils, the individual pixel values are then used as the values of η entered into equation 5-5.

The SNR performance of the array at a speed up factor (R) can also be estimated from the coil sensitivity information as (see section 2-7)

$$\mathbf{SNR_R} = \frac{\mathbf{SNR_{full}}}{\mathbf{g} \cdot \sqrt{\mathbf{R}}} \qquad (5\text{-}6)$$

SNR_{full} is the basic SNR from equation 6-4. The g-factor 'g' (where $g \geq 1$) describes the ability of the coil sensitivity functions to separate aliased signals.

The g-factor is calculated in a similar manner to the 'basic' SNR using the encoding matrix S (formed from sensitivity profiles) and the receiver noise matrix Ψ

$$\mathbf{g_x} = \sqrt{\left(\mathbf{S^H \Psi^{-1} S}\right)^{-1}_{x,x} \left(\mathbf{S^H \Psi^{-1} S}\right)_{x,x}} \qquad (5\text{-}7)$$

Where 'x' counts the aliased positions i.e. for a pixel in the reduced FoV: x counts the aliased positions in the full FoV, and $S^H \Psi^{-1} S$ forms a matrix whose diagonal values are selected by x and the value put in the correct position g_x, the g-factor over the full FoV.

It is worth noting that the 'basic' noise also needs optimisation when the coil is used for SENSE. Using smaller more highly localised coils for SENSE imaging can provide reduced geometrical noise enhancement, however, if the basic SNR performance of the array is reduced there may be no net gain in the SNR performance for SENSE imaging. A balance must therefore be made between providing the highest possible SNR over the volume and having sensitivity profiles that are effective in separating aliased signals.

5.2.6 The FSE Technique

The original Fast Spin Echo (FSE) sequence (introduced in section 2.9) originally provided by the manufacturer of the 4.7 T system (SMIS Ltd, Guilford, UK) was significantly developed and optimised by our group [23,24]. This section should provide an impression of the problems associated with the FSE and some of the possible solutions. The implementation of the FSE used here, aims to strike a good balance between the various parameters available, to maximise contrast and image quality while keeping within SAR and hardware limitations.

The FSE technique employs a series of refocusing pulses that are normally 180° see figure 2.16 (though lower flip angles can be employed e.g. FLARE/UFLARE [25]). The 180° pulses will refocus the magnetisation to produce a spin echo (*SE*) with the multiple pulses producing a chain of SEs at different echo times. At 4.7 T there is considerable B_1 non-uniformity (see section 2.10 for a brief description of the reasons for this). This means that some parts of the object will experience a repeated refocusing pulse of flip angle $\alpha°$ rather than the expected 180° pulse. The amplitude of the signal that has received m $\alpha°$ pulses rather than 8 or more 180° pulses will be smaller, by a factor $[sin^2(\alpha/2)]^m$. If the stimulated echo (*STE*) components are refocused at exactly the same time as the *SE*, they will partially compensate for this loss of magnetisation. This procedure yields images of even signal intensity, although some difference in contrast with respect to a standard *FSE* image of the same echo time will be present due to the STE contributions.

Each echo in the FSE echo train is formed at a different echo time. The echo time reported for the FSE image (called the effective echo time T_{eff}) is given by time of the

echo used for encoding the central lines in k-space, but, what is the effect of acquiring different lines of k-space with echoes formed at different times? It causes the formation of echoes with different intensities due to T_2 decay (see figure 5.12). This is equivalent to the application of a filter on the k-space data that is dependent on the first echo times, the echo train length and the order in which the k-space lines are acquired. These effects are well documented in references [26-30].

From section 2.6.4 we know that applying a filter in k-space translates into a Point Spread Function (PSF) for signal in image space that differs from a simple comb (or δ) function. In the implementation of the FSE described here rotated centric-type phase encoding was used [27], this means the centre of k-space is covered using the first echo, the next sections by the second echo and so on (see figure 5.12). The inter-echo spacing was 22ms (for reasons discussed later) which is significant in length when compared to T_2 (of 50-60ms for grey and white matter in the human adult brain at 4.7 T). This means that there is a significant drop in signal intensity between adjacent k-space lines that have been acquired at different echo times. The changes in the intensity of the signal are equivalent to the application of a filter in k-space, which causes significant sidebands in the PSF that will in turn cause artefacts in the images. These artefacts were reduced by a technique called 'feathering' the k-space data [24].

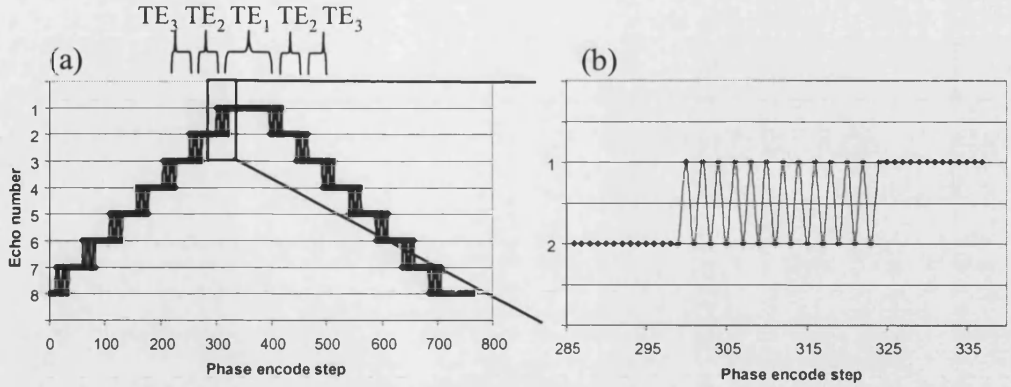

Figure 5.12 K-space filtering by the FSE in the phase encoding direction and the feathering technique

Adapted with permission from E. De Vita, Development and Optimisation of High Field Techniques, PhD Thesis, 2003. The filtering window applied by the FSE in k-space is seen in figure (a). The steps in the filter correspond to the different intensities of the echoes used to generate the k-space lines due to their different echo times. To avoid the problems caused by these steps the k-space lines are 'feathered' with each line alternating in intensity over a period around the step.

Feathering is the interleaving of adjacent k-space lines that have been acquired with different echo times. This is performed at the steps in the k-space filter; present because of the echoes, with different amplitudes, used to acquire the different k-space lines (see figure 5.13). The odd sidebands of the PSF are effectively moved to the edges of the image and if a large FoV is used they will not affect the part of the image containing the object. Another method that is used to mitigate this problem is to offset the echo times used for each k-space line. This avoids obtaining any large discontinuity in signal magnitude in k-space. The extra time delay needed to offset the echo times of each of the echoes within the train can cause *STE* coherences to be refocused at unwanted times. This can cause problems in the FSE implementation described here, because some *STE* components are refocused at the time of the *SE* for removing sensitivity to B_1 non-uniformity.

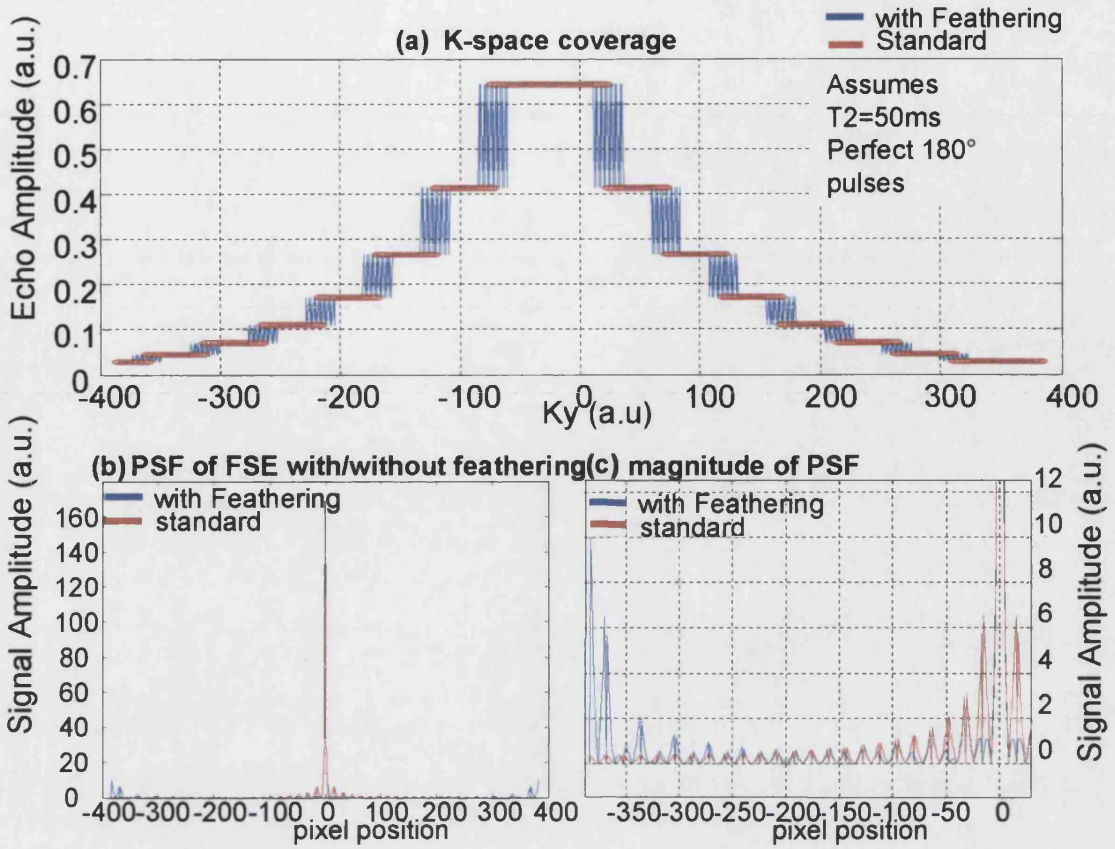

Figure 5.13 K-space filtering in the FSE acquisition, the effect of the filter on the PSF and its mitigation by feathering in the phase encoding scheme
Adapted with permission from E. De Vita, Development and Optimisation of High Field Techniques, PhD Thesis, 2003. a) The two filters that are applied to the k-space data in the phase encoding direction are demonstrated with and without feathering. b) and c) The PSF of the FSE with and without feathering is demonstrated showing that the high intensity side bands are shifted to the image edges when feathering is employed.

The implementation used here had an inter-echo spacing of 22ms. This is fairly long compared to some implementations and adds to the problems described above of large discontinuities in the k-space filter due to significant T_2 decay between echoes. However, this value does provide a lower Specific Absorption Rate (SAR) of RF power due to the reduced density of refocusing pulses, necessary at 4.7 T where larger RF powers are required to obtain a given flip angle than at lower fields. To refocus the *STE* component of the magnetisation the echo time of the first echo is the same as the inter-echo spacing. The first echo time is also the effective echo time and 22ms provides a

good balance between contrast and SNR performance determined by the receive bandwidth (here 50kHz). With this inter-echo spacing an echo train of 8 echoes was selected. Longer echo trains would have increased blurring, while shorter echo trains suffer a serious time penalty because they require more excitations of the magnetisation (or shots). Additionally, the echo train length determines the number of slices that may be obtained with a given *ETS* and recovery time *TR*.

5.2.6.1 Phase Correction for the FSE Technique

Each echo in the echo train may have a slight difference in echo time, due to small differences the timing of RF pulses A difference in time in k-space produces a phase shift in image space. Furthermore, having lines in k-space effectively shifted in time can cause ghosting artefacts in the image.

To remove this problem a phase correction was applied. One complete echo train was acquired without phase encoding; the relative phase of each of the subsequent echoes in the train can be established relative to the first. This was calculated by taking the data from each echo and Fourier transforming it to produce a 1D spatial profile. The phase difference between each 1D profile relative to the first is calculated for each echo. These values are then used to correct all subsequent k-space lines by the same amount so each echo is aligned with the first.

5.2.7 Experimental Details

Experiments were performed on a SMIS MR5000, 4.7 T /90cm system supported by Philips Medical Systems. Imaging was performed with a Fast Spin Echo (FSE) procedure with 8 echoes spaced 22ms apart, effective TE=22ms, 2mm slice thickness

and an image array of 1024x768, field of view 360x270mm, producing an isotropic in-plane resolution of 0.35mm. The total scan time was 5mins 40s. All volunteers were healthy and were imaged after informed consent had been gained. Approval was obtained from the University College London Hospital Ethics committee. Images were obtained from the 28cm birdcage coil (transmit/receive) and the 4-channel receive array (with the same birdcage coil for RF transmission).

Software developed in house using MatLab (Mathsworks, Natick, MA) was used to process the complex raw data acquired by the scanner. For each slice the raw complex data was read-in before having a phase correction applied (as described previously). The raw data was then re-ordered according to the scheme used to acquire the lines, which included 'feathering' the data. A Hanning filter was then applied to the k-space data to remove any ringing artefact. The slice of k-space data was then 2D Fourier transformed to produce an image.

5.3 Results

The SNR performance of the array coil is calculated from FSE data acquired using the protocol outlined in section 5.2.7. Low resolution sensitivity maps are then obtained from this data using the (sensitivity mapping) procedure described in section 5.2.3. The sensitivity maps can then be used to estimate the SNR performance of the array coil for both standard and SENSE imaging (as detailed in section 5.2.5).

5.3.1 Individual Array Element Performance

Low resolution sensitivity maps were created from FSE images using the processing described in the previous section, the real and imaginary components of the sensitivity

maps were smoothed with a 3x3 pixel box filter unless otherwise indicated. The threshold level entered for the mask used within the mapping procedure was the mean+(5*s.d.).

The sensitivity information was displayed as a contour plot of sensitivity relative to the volume coil in figure 5.14. The sensitivity of the volume coil was not uniform and this additional sensitivity dependence should be noted [31]. The FSE technique is relatively insensitive to variations in flip angle on transmission caused by B_1 non-uniformity. However, the maps do contain some of the B_1 variation present at 4.7 T because the volume coil image, used as a reference, contained variation in its receive sensitivity. N.B. Birdcage coils loaded with a human head at 4.7 T tend to drop off in sensitivity at the edges of the head, so absolute sensitivity profiles are probably a little greater in centre and a little lower at the edges.

The coil profiles were highly localised in figure 5.14, demonstrating that the decoupling between the coils is effective. The coils have high signal in their vicinity (e.g. high signal in the top left corner of the head from the top left coil etc). The coils were around 3 times more sensitive relative to the volume coil in local areas as indicated by the red colours in the contour map, yet still 0.5-1 times as sensitive in the centre indicated by the green and light blue regions.

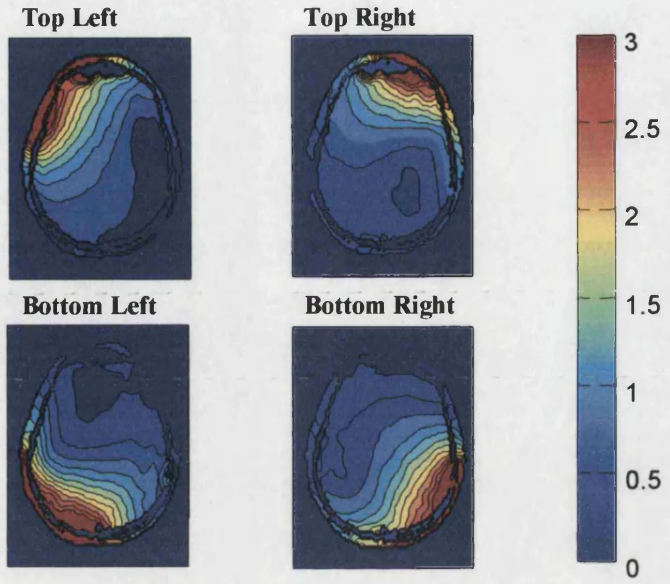

Figure 5.14 Sensitivity Maps from the individual array elements
The sensitivity of each array element relative to the transmit/receive volume coil is shown in the form of a contour plot. Regions of high SNR performance appear red and are localised to the position of the coil. Regions of lower SNR are blue.

Despite the coils used being symmetrical in shape, the B_1 field (or sensitivity due to their reciprocal nature) shows some non-symmetric behaviour. This non-symmetric behaviour is often found in RF fields at high field strengths due to dielectric resonance / wavelength effects and provides an interesting challenge for coil design [32-34].

When the coils are used for SENSE imaging, they need to possess significantly different sensitivity information in the spatial positions that are likely to aliased. This is necessary for the aliased signals to be separated without enhancing noise. Significant drop off with distance was seen in the sensitivity profiles which should provide the significantly different sensitivity values required over the head.

5.3.2 Decoupling and the Receiver Noise Matrix

In the following sections the array performance will be calculated using expression 5-4 from section 5.2.5. This uses Ψ the receiver noise matrix, which can be calculated from the expression 5-5. In some cases the unity matrix can be used to approximate Ψ

because the noise in each channel is adjusted to be equal, and the level of correlation between the noise in the different channels is low. The value of Ψ was investigated to determine the actual level and correlation of noise between the channels to see if the approximation of Ψ as a unit matrix is reasonable.

In figure 5.14, the coil elements were seen to be highly decoupled with regions of high sensitivity highly localised to their spatial position, so the noise that each coil receives from the sample should be quite different. The level and correlation of noise between the images used to create the sensitivity maps in figure 5.14 was calculated using equation 5-5. A typical result of this calculation (see below) yields a matrix with values very close to 1 down its diagonal; this means that noise level is very similar in each channel. The off diagonal terms are small, indicating a small level of correlation between the noise picked up by each coil.

$\Psi_{calculated}=$

1.0001	-0.0332 + 0.0301i	-0.0163 + 0.0061i	0.0064 + 0.0284i
-0.0332 -0.0301i	1.0006	-0.0075 - 0.0023i	0.0064 + 0.0424i
-0.0163 -0.0061i	-0.0075 + 0.0023i	1.0025	0.0352 + 0.0299i
0.0064 -0.0284i	0.0064 - 0.0424i	0.0352 - 0.0299i	1.0000

In figure 5.15, two maps of the SNR performance calculated using different values for Ψ are shown. In 5.15a $\Psi=unity$, in 5.15b $\Psi= \Psi_{calculated}$. The difference between the SNR performance calculated for each Ψ is very small, the largest difference is only a 2% reduction in the SNR. This indicates that to estimate the SNR and g-factor with the array coil, making the approximation $\Psi=unity$ gives acceptably accurate results.

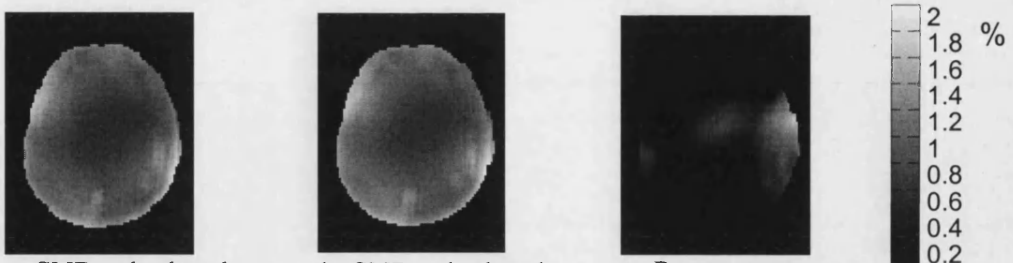

a. SNR calculated using Ψ= unity

b. SNR calculated using Ψ from images

c. Percentage difference

Figure 5.15 Relative SNR calculated with two different values for the receiver noise matrix

a. The SNR is calculated with a unit matrix for the receiver noise matrix.
b. The SNR is calculated with a receiver noise matrix calculated from noise in the receivers.
c. The difference between the two measurements of SNR (a-b).
In this figure the effect of using a value 1 (a unit matrix) for the receiver noise matrix in calculations of SNR is assessed. The SNR is lower in *b* than *a*, however, the difference is very small with values of 1-2 percent at most.

5.3.3 Basic SNR Performance

The relative noise performance of the array coil was determined for each slice. The resulting SNR maps are displayed using contour plots in figure 5.16. The axial slices begin at the top of the head in the top left hand corner, then we travel down through the head towards the feet from top left to bottom right viewing every other slice. The FoV is 240x180mm.

The SNR regions displayed in the contour plots as red values are in the peripheral brain areas. This indicates around a 3-fold improvement in SNR. It is worth noting that this three-fold improvement is relative to the birdcage, which has some drop off in performance in similar regions.

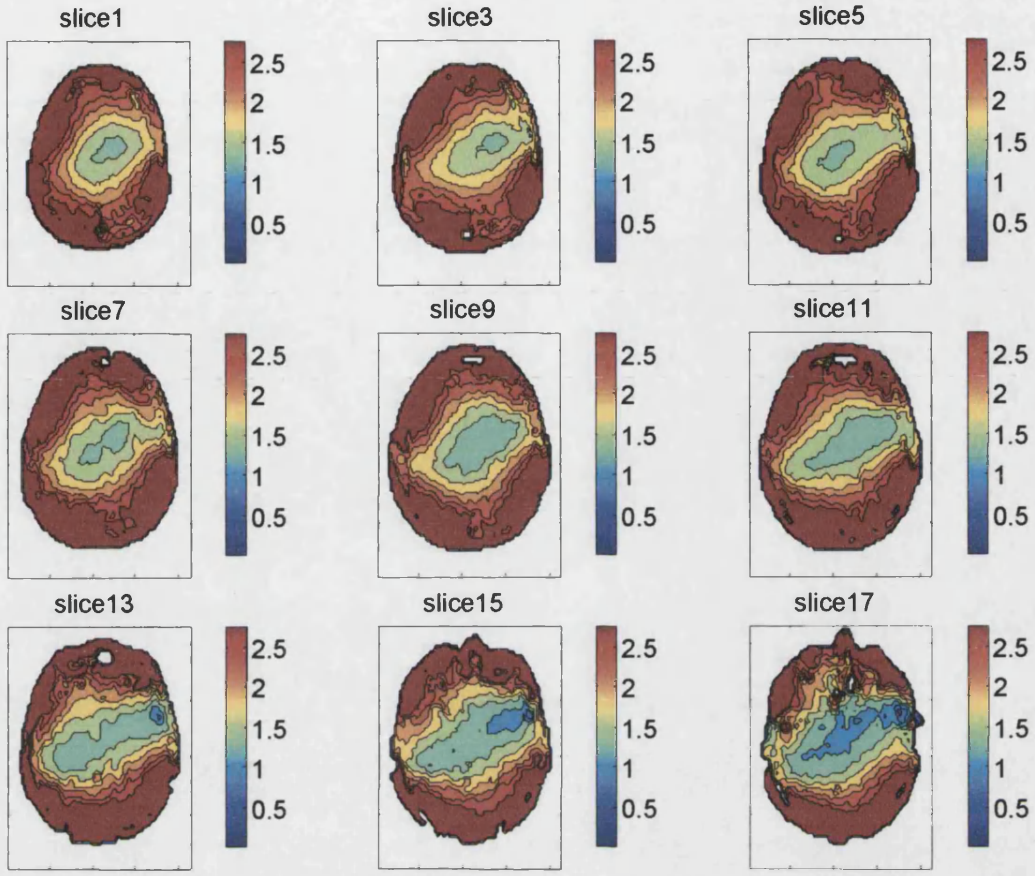

Figure 5.16 The basic SNR performance of the array coil relative to the birdcage coil over a volume
Contour plots showing the SNR of the array coil relative to the birdcage are shown for different slices. The slices are axial and are from the top of the head in the (top left) to lower in the head (bottom right). Overall the maps show an increase in SNR performance that is more marked in peripheral regions of the head. Going down the head there is some reduction in SNR performance though even the lowest slice shown maintains SNR performance in the centre while improving SNR by a factor of 2-3 over much of the slice.

In the centre of the brain there is still some SNR improvement, the contour maps show green and turquoise colours indicating a 1.25-1.5 improvement in the SNR performance. In the lower slices (e.g. 15 & 17) there is some reduction in the coil performance compared to the top slices (e.g.1 & 3). This drop in performance is mainly present in the central regions of the head. The coils perform best in their own close

proximity; the coils are on average furthest away from the lower central regions of the head, so a lower performance in these regions is expected.

The SNR plots exhibit some non-symmetric behaviour with a small region on the right hand side of slice 17 showing a regional dip in performance. This appears to be related to the non-symmetrical form of the individual array elements seen in figure 5.12, where it was clear that the top right coil profile is rotated and does not cover the centre right region with the sensitivity that might be expected. Indeed, all of the coil profiles exhibit some degree of rotation. However, the SNR performance in the back of the head in the lower slices remained very high and the overall SNR performance on the lower slices was still improved. Overall, the SNR maps from different slices demonstrated an improved level of performance over a large volume.

The SNR performance was similarly calculated for several different subjects with comparable results (data not shown).

5.3.4 FSE Images

A comparison between two FSE images acquired using the volume coil and the array coil was made (see figure 5.17). The FSE images had a resolution of 0.35 millimetres in-plane with a 2mm slice thickness. The effective TE was 22ms and 17 slices were acquired in 5mins 40s. Low resolution sensitivity maps were obtained as previously described. These were interpolated using Matlabs 2D cubic interpolation function to produce sensitivity maps of the same resolution and FoV as the high resolution array coil images. The Hanning filtering and phase correction described earlier was applied to the individual array element raw data. This was reconstructed to produce an image from

each element by performing a 2D FT. The array element images were then combined according to their sensitivity on a pixel-by-pixel basis to produce images of approximately uniform sensitivity.

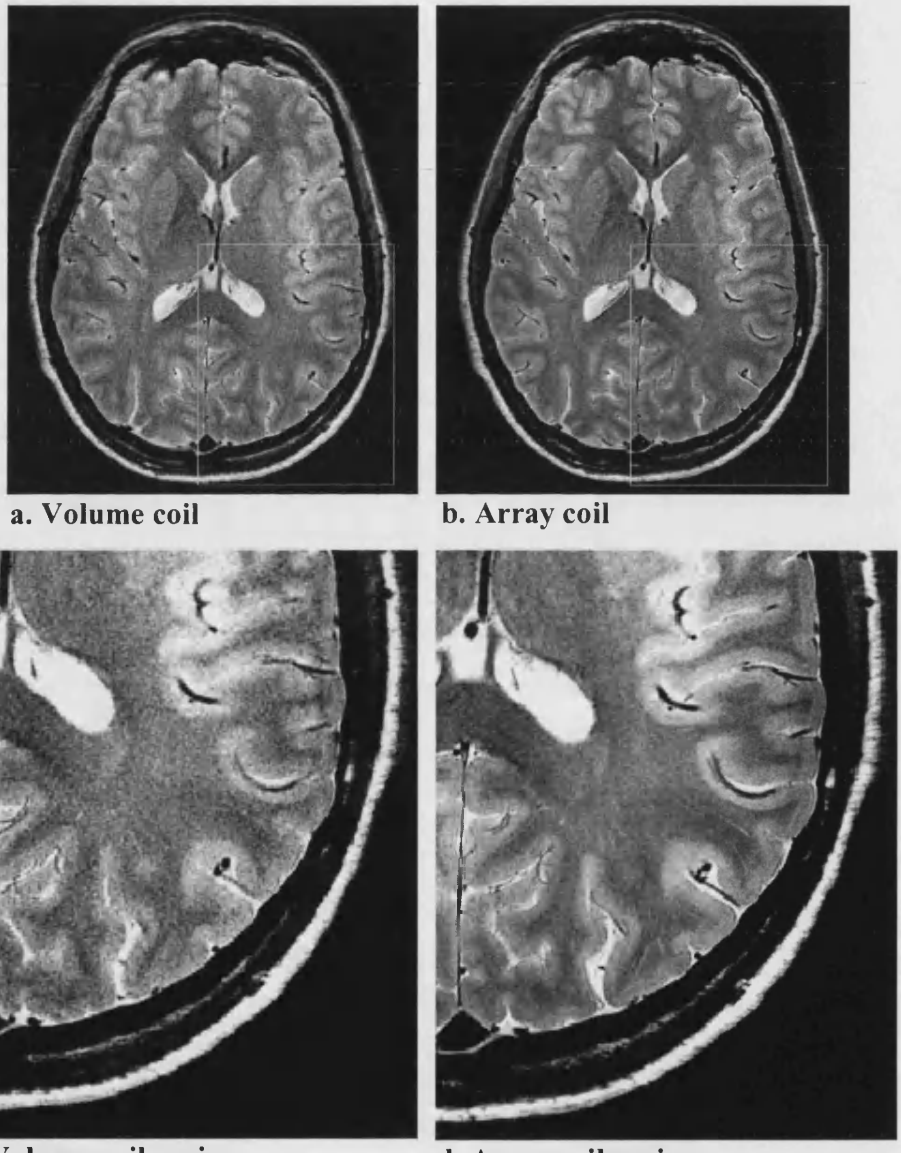

a. Volume coil **b. Array coil**

c. Volume coil region **d. Array coil region**

Figure 5.17 A comparison of FSE images acquired with different coils at 4.7T
Effective TE=22ms, 2mm slice thickness and an image array of 1024x768, FoV 360x270mm, in-plane resolution 0.35mm. The total scan time was 5min 40s. Images are cropped in this figure.

In figure 5.17, on the left is a volume coil image (5.17a) and on the right is an image of the same slice, obtained after appropriate processing, with the array coil (5.17b).

Though both of these images are of high quality, when a region is blown up (5.17c & d) the SNR improvement is clearly visible in the array coil image. There was a large improvement in performance from using the array coil in the peripheral regions, there also appears to be some improvement in SNR in more central regions of the head confirming the SNR improvements predicted by the contour plots (figure 5.16).

The combination of the FSE's high level of contrast and the high level of image quality, provided by the array coil, enables excellent discrimination of anatomical structures in the brain (see figures 5.18 & 5.19 on the next pages). A high in-plane resolution of 0.35 microns was achieved in a short experiment of 5mins 40s duration. Good quality images could be obtained at this resolution due to the high SNR provided by the high field strength together with the array coil. The choice of an echo train length of 8 refocusing pulses (echo spacing 22ms) enabled i) SAR, often a problem at high field, to be kept below the recommended limit, ii) the acquisition bandwidth to be kept low to maximise SNR, and iii) 17 slices to be obtained in a TR of 3.5s and total scan time of 5mins 40s at the desired in-plane resolution of 0.35 microns.

The higher SNR performance of the array coil enabled the clear visualisation of some brain structures that previously have not been seen in images taken in similar acquisition times. The array coil gives a large increase in performance, particularly in the peripheral regions of the head. For example, striation in the visual cortex is clearly visualised (see figure 5.19).

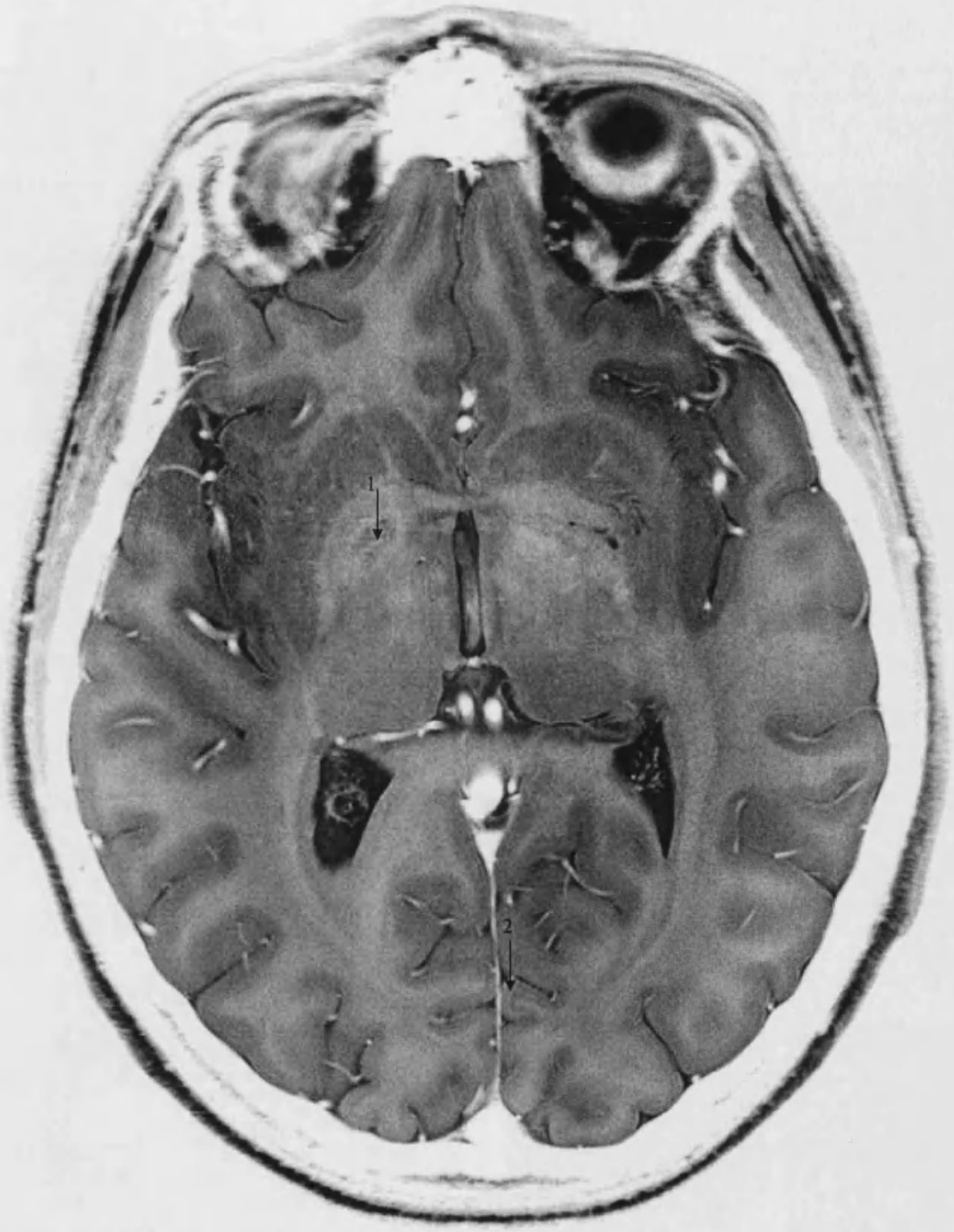

Figure 5.18 Inverted contrast FSE at 4.7T using the Array Coil
Images of high quality were obtained from the FSE with the array coil on a 25year old male volunteer. One slice (out of 17) is displayed, (TE_{eff} / TR=22ms / 3500ms, resolution 0.35x0.35x2 mm, scan time 5min 40s, contrast inverted so low signal is displayed white). Arrow 1 indicates one of the medullary laminae, separating the different segments of the globus pallidus. Arrow 2 indicates a striated fold of the visual cortex.

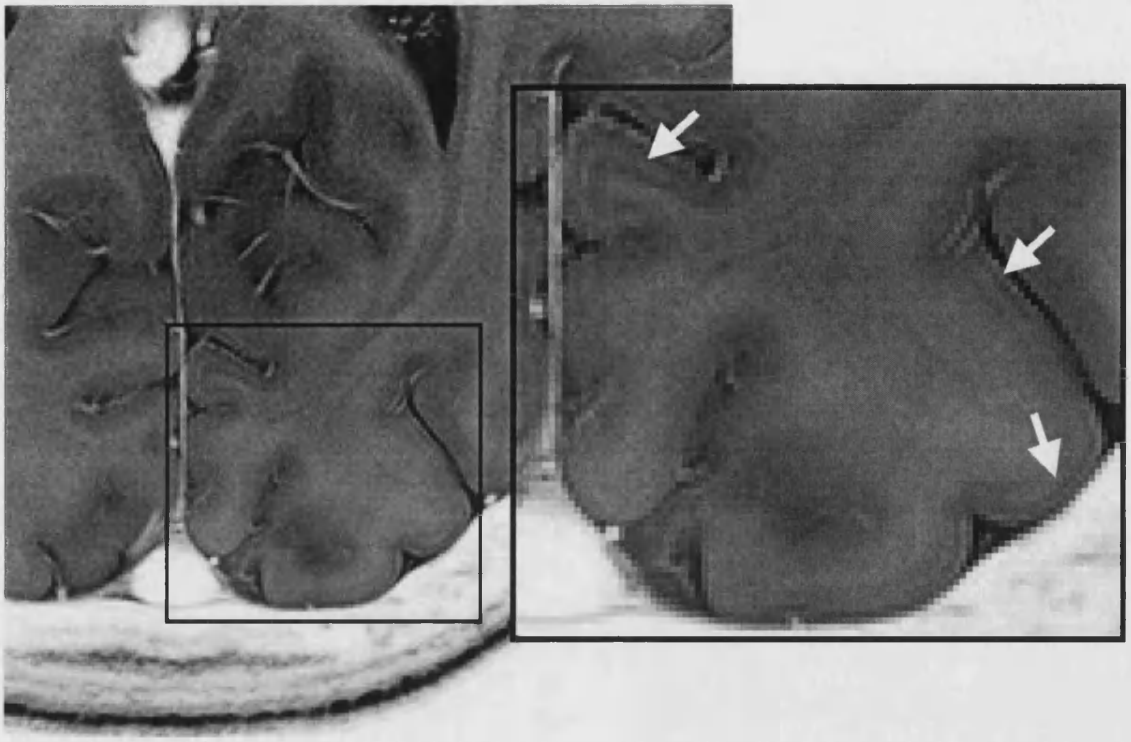

Figure 5.19 Inverted contrast FSE at 4.7T using the Array Coil: cortical regions
Regions of the inverted contrast FSE image in figure 5.18 taken with the array coil are displayed with greater magnification. There are two main points to note; firstly, the SNR is clearly very high, especially at the edges of the head, allowing a large degree of magnification without 'granulation' of the image. Secondly, alternate bright and dark bands indicated by the white arrows are clearly visible. These striations follow the folds of the brain over large regions of the visual cortex.

5.3.5 SENSE Performance

The SNR performance of the array coil was evaluated for different levels of speed up in both of the principal gradient directions (left-right and anterior-posterior) using the coil sensitivity information derived from the FSE images and the expressions given in section 5.2.5.

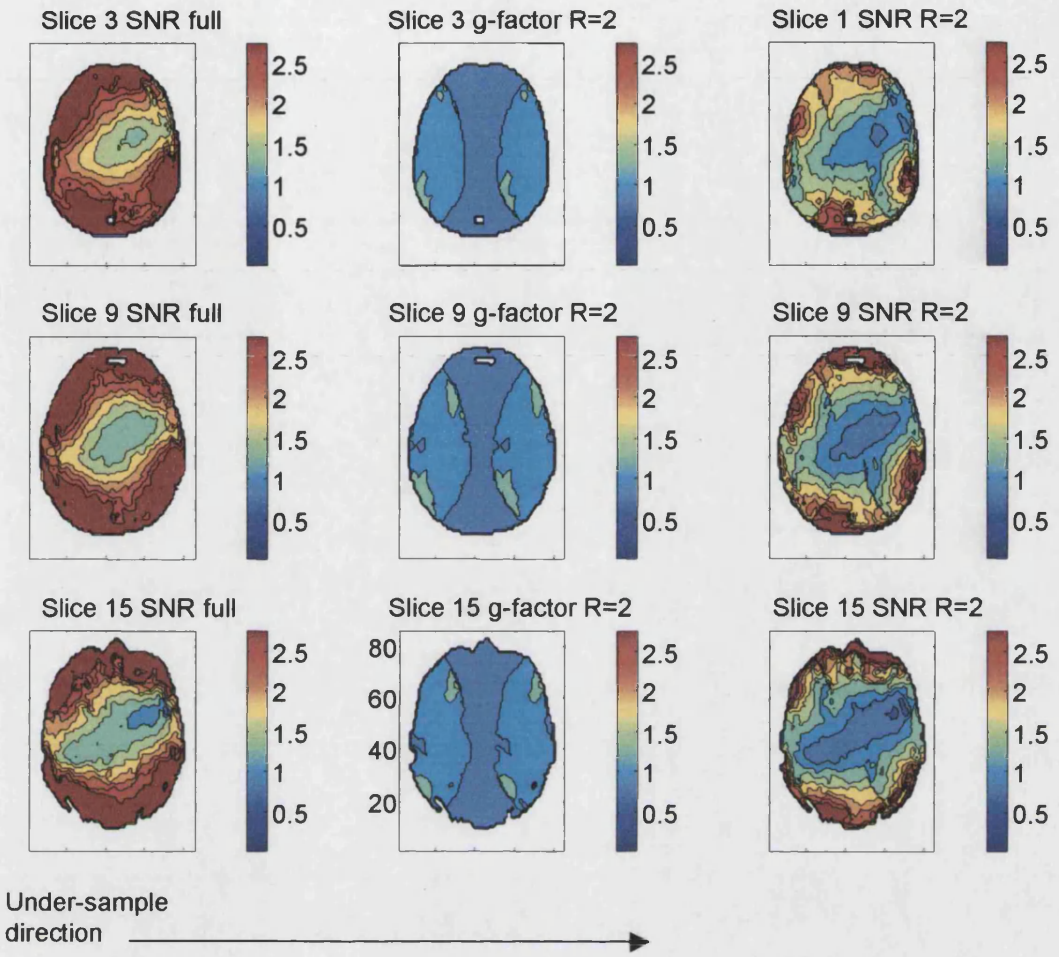

5.20 Assessing the SNR performance of the array coil using SENSE at a speed up factor of 2 in left-right direction
The figure shows the SNR performance for three representative slices (3,9 and 15). The basic SNR performance is shown on the left hand side while in the centre the g-factor is shown. Using $SNR_{red}=SNR_{full}/(R^{0.5}*g)$, the SNR estimated for SENSE at a speed up factor of R=2 is shown on the right hand side.

In Figure 5.20, the SNR performance for SENSE at a speed up factor of 2 (in the left-right direction) was displayed. The SNR performance was calculated for three axial slices (3,9 and 15) corresponding to different positions in the head, with slice 3 near the top and slices 9 and 15 lower down. The FoV is 240mm in the anterior-posterior direction and 180mm in the left-right direction. For each slice in figure 5.20, on the left hand side the basic SNR is displayed, in the middle the g-factor is shown at a speed up factor of *R*=2 and on the right hand side the SNR is displayed at *R*=2. The g-factor plots

demonstrate that there are no 'hotspots' where the noise is locally enhanced by a large factor. This translates into the SNR plot where a global reduction in SNR is visible but no smaller regions contain a very large SNR reduction. A large proportion of the head still exhibited improved SNR performance relative to volume coil even at R=2, seen by the regions that are still green-red in colour.

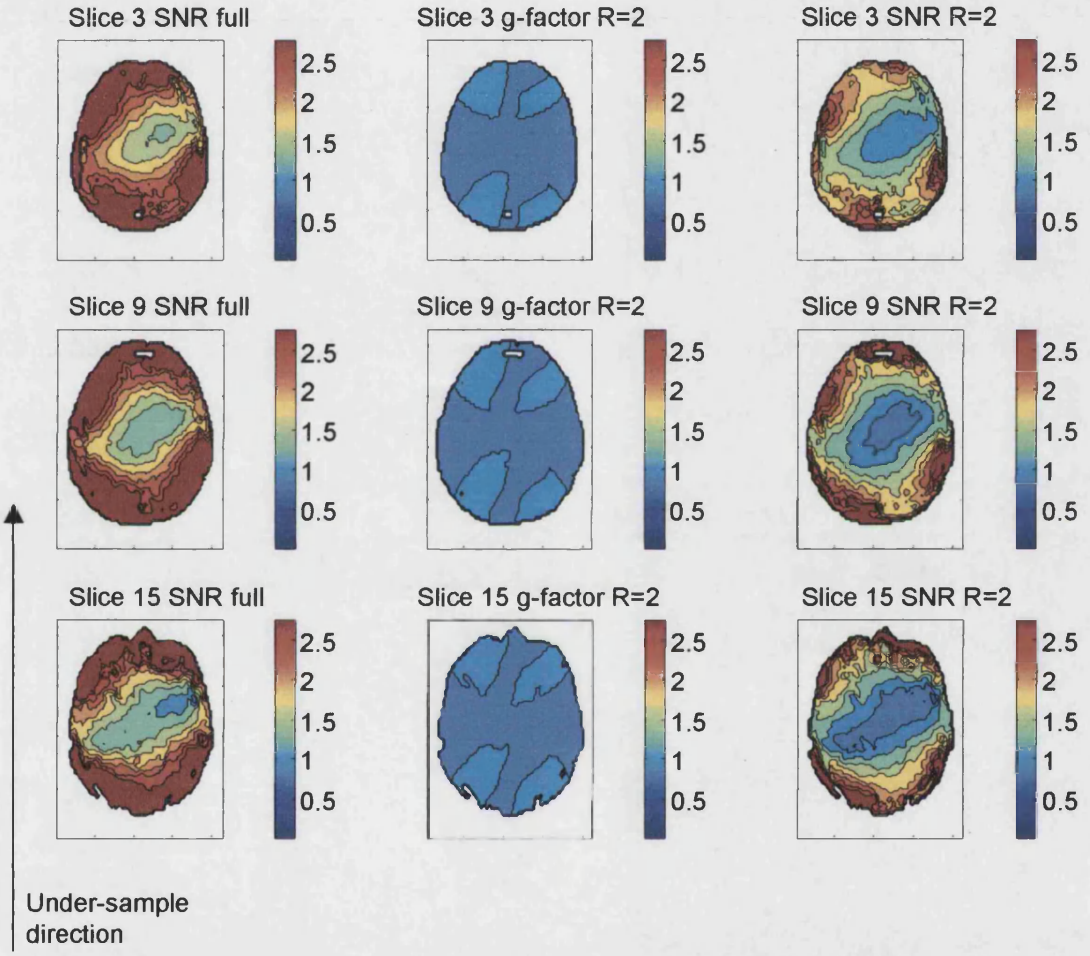

5.21 Assessing the SNR performance of the array coil using SENSE at a speed up factor of 2 in anterior-posterior direction
The figure shows the SNR performance for three representative slices (3,9 and 15). The basic SNR performance is shown on the left hand side while in the centre the g-factor is shown. Using $SNR_{red}=SNR_{full}/(R^{0.5}*g)$, the SNR estimated for SENSE at a speed up factor of R=2 is shown on the right hand side.

Figure 5.21 shows similar plots to figure 5.20, only this time for under sampling in the anterior-posterior direction (vertical in the images shown). The g-factor is very low

throughout the head, so the SNR reduction in the slices is the minimum expected from sampling the signal less densely (the square root of the speed up factor: $\sqrt{2}$). The difference in the g-factor between the two directions can be attributed to the narrower FoV in the left-right direction (180mm as opposed to 240mm). The FoV was made narrower deliberately, so that the same degree of wrap-up occurred in the images in both directions. The g-factor is overall slightly higher in the left-right direction because the aliased pixels are closer together. The sensitivity profiles however, have a similar drop off in both directions so the aliased pixels in the left-right direction have more similar sensitivity values. This makes the aliased signals more difficult to separate.

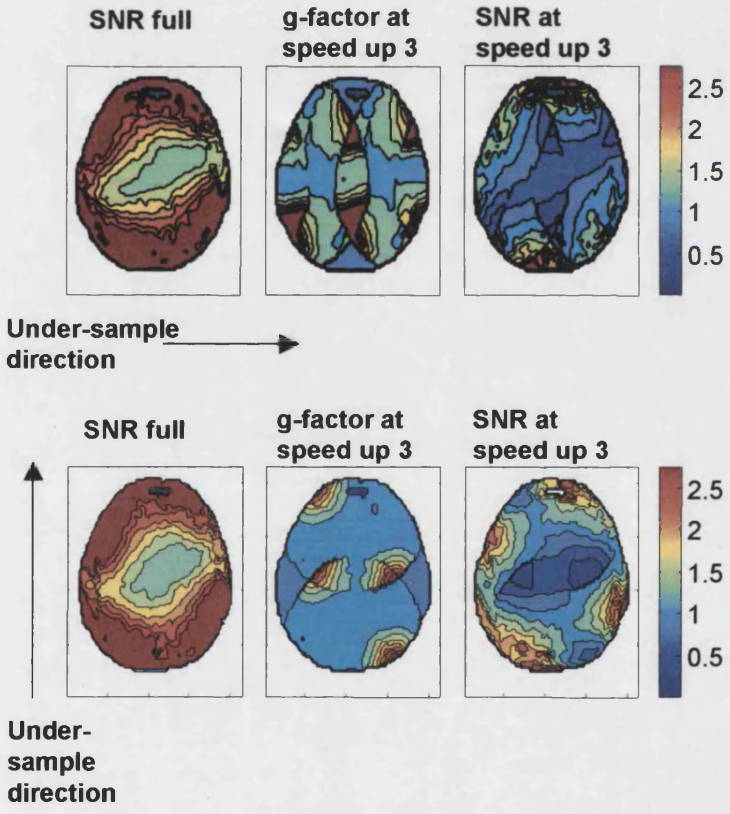

5.22 Assessing the SNR performance of the array coil using SENSE at a speed up Factor of 3

Figure 5.22 shows the SNR performance for a central slice in both gradient directions. On the left hand side the basic SNR performance is shown, in the centre the g-factor is shown. The basic SNR, g-factor and level of speed up are then used to obtain the SNR estimate for SENSE at a speed up factor of 3.

In figure 5.22, the SNR performance at a speed up factor of 3 is shown for a single slice in each either of the 2 possible under-sampling directions. The g-factor exhibits regions of high noise enhancement – above a factor of three (red) in large regions. Again, the left-right direction shows worse g-factor behaviour, though in both directions the SNR is drastically reduced, as indicated by the deep blue regions in the SNR plots. The level of local SNR degradation is prohibitively high for the use of SENSE at a speed up factor of 3 in either direction for most applications.

To examine the level of speed up possible with the array, the maximum and average g-factor was calculated for speed up factors between 1 and 4. The maximum g-factor measures the worst level of local noise enhancement and subsequent SNR degradation. The mean value of the g-factor gives a value representative of the global increase in the noise and corresponding reduction in SNR.

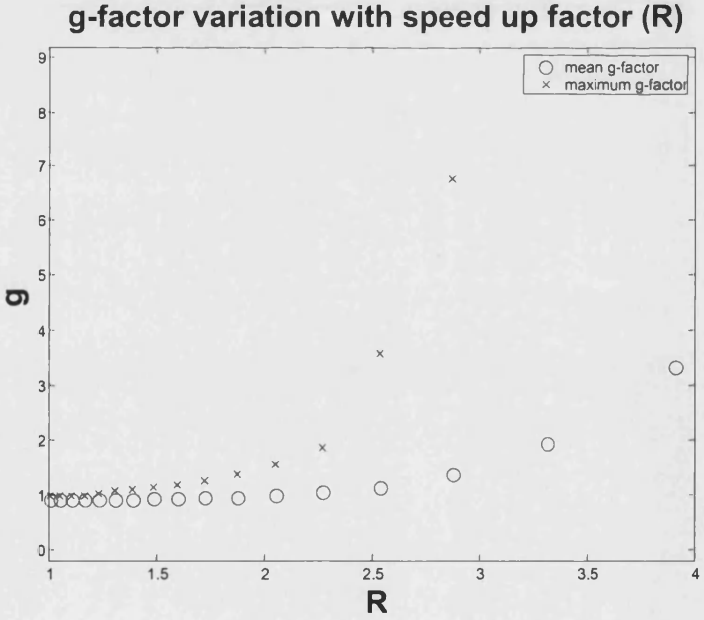

Figure 5.23 The mean and maximum g-factor with speed up factor R in left-right direction
The g-factor describes the enhancement of noise due to SENSE reconstruction at a given speed up factor. The mean (o) and maximum (x) values give a measure of global and local noise enhancement respectively. The speed up direction is left-right as in figure 5.20. N.B. last two crosses are off the scale

The cost of speeding up image acquisition in either direction was examined. The g-factor was calculated versus *R* for both gradient directions. In figure 5.23, the calculated

g-factor is plotted against R for under-sampling in the left-right direction. The mean g-factor ('o' in figure 5.21) showed a slow rate of increase over most of the range of R, it should be noted that R=4 is the maximum level of speed up possible using a 4 coil array. Towards the higher R-values the mean g starts to increase more sharply, but this value also indicates that, on average, the SNR would not be unduly reduced by R-values up to 3. The maximum g-factor ('x' in figure 5.23) showed a much steeper rise, with an increasing gradient as the R-value increased. Due to this sharp increase in the maximum g-factor it is clear that small regions have a much greater reduction in performance, even when on average the coil is performing without large-scale SNR degradation. The maximum g increases faster at higher speed up factors indicating that the cost in SNR is greater for the same increment in R at higher values of R. Up to a value of R~2.25 in figure 5.23, the maximum g factor remains below 2, above this R-value the g-factor increases rapidly. This indicates the level of speed up that should be possible, without local regions developing prohibitively poor SNR performance.

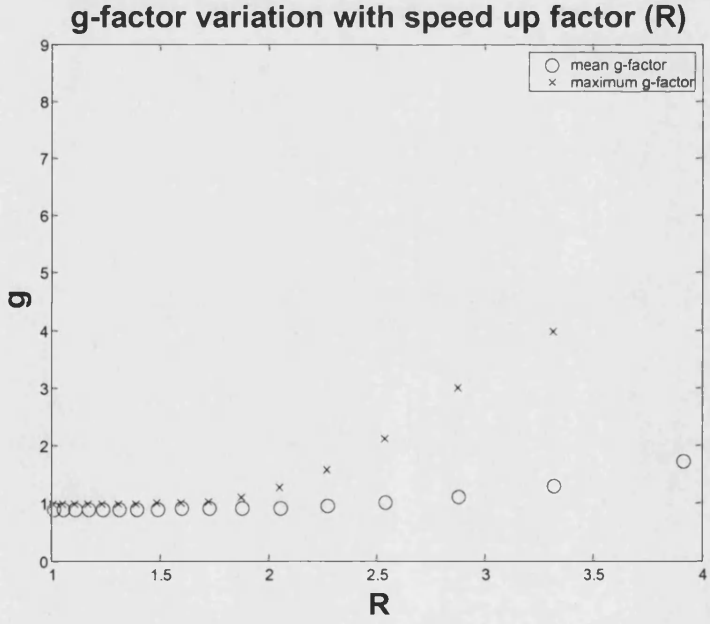

Figure 5.24 The mean and maximum g-factor with speed up factor R in anterior-posterior direction The g-factor describes the enhancement of noise due to SENSE reconstruction at a given speed up factor. The mean (o) and maximum (x) values give a measure of global and local noise enhancement respectively. The speed up direction is anterior-posterior as in figure 5.21. N.B. last cross is off the scale

In figure 5.24, the calculated g-factor was plotted against R for the anterior-posterior under-sampling direction. Both the mean g-factor ('o' in figure 5.24) and the maximum

g-factor ('x' in figure 5.24) have curves with the same shape as for the left-right plot in figure 5.23. The mean g-factor in the anterior-posterior direction showed a slower rate of increase over all the *R*-values when compared to the left-right direction, demonstrating that the SNR is not globally reduced by the geometry factor, even at the highest speed up factors. However, the maximum g-factor again showed a much steeper rise with increased *R* at higher *R*-values. The maximum g-factor does not rise as fast in the anterior-posterior direction as for the left-right speed up direction. Up to a value of *R*~2.5, the maximum g-factor remains below 2, above this *R*-value the g-factor increases more sharply with *R* in figure 5.24. This indicates the level of speed up that should be possible, without local regions developing prohibitively poor SNR performance.

5.3.5.1 SENSE in 2 Dimensions (2D)

To allow the maximum speed up factors possible with a 4-coil array the efficacy of 2D SENSE [15] was investigated in the same way as in the previous section. In figure 5.25, the g-factor is calculated for three speed up factors *R*=3, 3.5 and 4 displayed going from left to right in the figure. This provides an estimate of the noise enhancement / SNR reduction when an equal reduction in sampling is applied in both of the indicated directions. The g-factor is low both for all the *R*-values used, and over the whole head region, with a maximum of *g*=1.58 for a speed up factor of *R*=4. This indicates a large improvement in local performance when compared to the maximum g-factors seen in figures 5.23 and 5.24 for 1D SENSE at *R*=3-4. The plots of SNR reflect the fact that some global reduction in SNR is inevitable due to the reduction in the density of k-space sampling that is performed in a SENSE experiment. However, when the g-factor is maintained at a reasonable level (e.g. 1.5-2) over the entire object, a maximum level

of speed up can be achieved from the four-coil array using 2D SENSE, because this arrangement minimises geometry related noise enhancement.

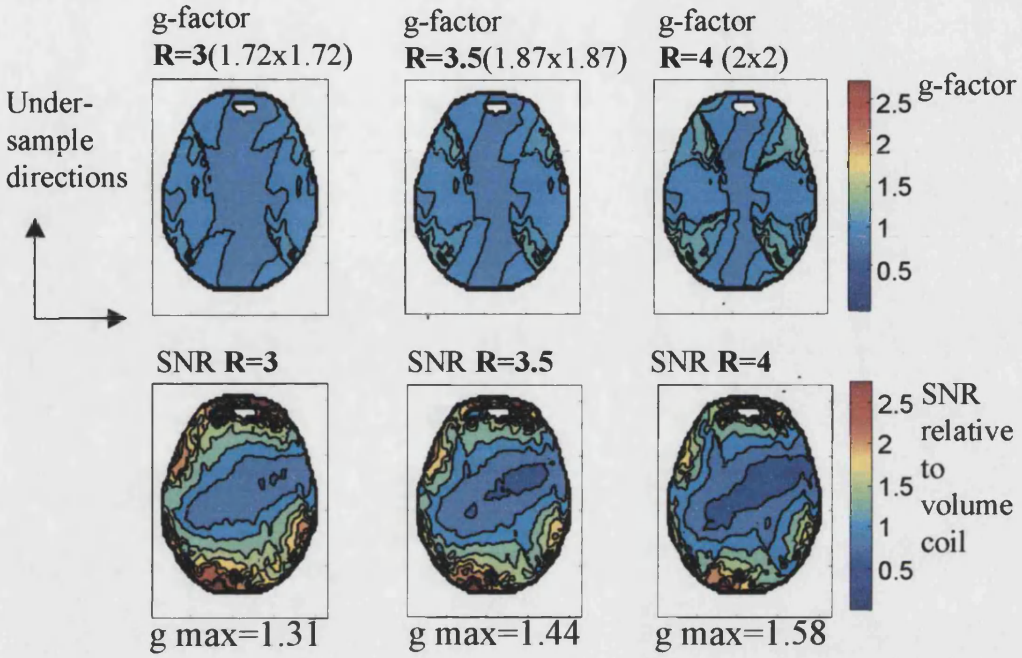

Figure 5.25 2D SENSE should allow greater speed up factors to be realised by reducing geometric noise enhancement
The g-factor and SNR performance is calculated for three speed up factors 3, 3.5 and 4 using under-sampling in 2 dimensions. The geometry factor is low globally in all the plots, even at maximum speed up factor of R=4. The most notable difference for 2D SENSE (c.f. 1D SENSE R=3 in figure 5.22) is the maximum g-factor. There are no regions that suffer prohibitively high noise enhancement with a maximum g of 1.3-1.6. This is translated into SNR maps that show a global reduction in SNR with a similar level of SNR uniformity as seen in the basic SNR performance of the array.

The design of the four coil array effectively placed a coil offset at approximately 45° to the main gradient axes in each of the four corners. This arrangement favours 2D SENSE because each pixel is aliased with pixels from each of the quadrants of the full FoV. Each quadrant is covered uniquely by one of the coils. This permits effective unfolding of the images and so the g-factor is low. 2Dd SENSE is most likely to find application where two phase encoding directions are used such as 3D imaging and CSI.

5.3.6 SENSE Images

Here, an example of using SENSE at a speed up factor of two was obtained using a 2DFT sequence.

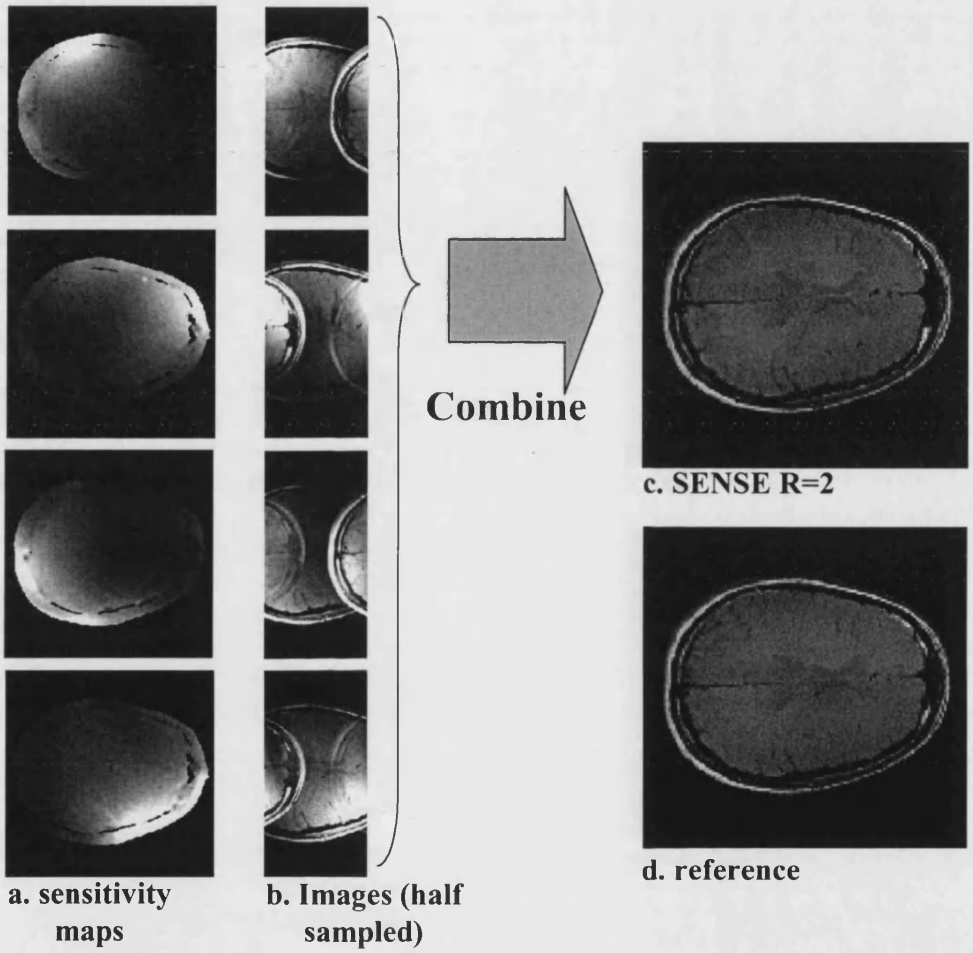

Figure 5.26 SENSE at a speed up factor of 2
This figure demonstrates the SENSE technique at a speed up factor of 2 using a 2DFT imaging protocol. Full FoV images were acquired with the array coil and with a birdcage coil. These were used to create the sensitivity maps (a). Half FoV images can then be acquired with reduced sampling (b) and combined to form an image with the aliasing removed (c). The image from the birdcage coil is provided as a reference (d).

On the left-hand side of figure 5.26, the sensitivity maps from each coil are displayed. These were obtained from full FoV, 2DFT, array coil images from each element and from a full FoV, 2DFT, volume coil image via image division followed by processing as described in section 5.2.3. Half FoV images were then acquired from each coil. The

half FoV images were combined using the sensitivity maps to create a full FoV image with the aliasing removed. The full FoV image can be compared to the volume coil reference image on the right hand side of figure 5.26. The SENSE image provides similar image quality in half the time.

5.4 Discussion

The array coils design was described and then its performance evaluated. The assessment of the array coils performance was broken down into several sections.

The first consideration for the array performance was how efficiently the array elements were decoupled. This is crucial to the SNR performance of the array, because coupling between the coils introduces a large level of correlation between the signal and noise that they sample. The coupling between the coils was verified as being low by the highly localised sensitivity of the individual elements in the sensitivity maps seen in figure 5.14. Some asymmetry could be seen in the elements sensitivity profiles. While this behaviour is expected at high field, it is hard to predict without complicated modelling, due to the interactions that occur between the coil and the sample.

The most important test of the array coil was its basic SNR performance. This is crucial to its performance as an array, but it also should be the primary feature of a SENSE coil because the SNR of the SENSE coil at any speed up factor is proportional to the basic SNR. The coils were shaped to fit the contours of the head (see figure 5.1). While their shape may not have had quite the same efficiency as a similarly sized circular surface coil, it allowed the array coil elements both to be in close proximity to the head and for parts of the head to sit inside them. This enabled a high sensitivity to be achieved over a

larger irregular volume than a set of circular surface coils would have allowed. In addition, the coils could be kept to a minimum size and did not overlap each other, which is advantageous when the array coil is used with SENSE [16].

The array coil provided a considerable gain in SNR over the majority of head when compared to a standard 28cm head Birdcage coil. The SNR was around 3 times better at the edge of the head and 1-1.5 times better in the centre of the head. The array coil had no regions of markedly reduced performance in the brain regions of the head because the elements were shaped to fit together to cover the whole volume.

The SNR improvements seen in the basic SNR plot can be traded for speeding up the acquisition time using SENSE. A factor of speed up of R=2.2-2.5 was shown to be achievable in either of the two principal gradient directions while maintaining acceptable SNR performance over the whole imaging volume. The array coils perform slightly better for SENSE applied in the anterior-posterior direction. This is attributed to the size of the coils and the larger FoV used in this direction, which favour SENSE because aliased pixels have a larger difference in sensitivity, are easier to separate and so have a lower g-factor. Smaller coils would reduce the g-factor for SENSE in the left-right direction. However, more coils would be required to maintain the volume coverage and basic SNR performance of the array described here.

The coils were offset at approximately 45° with respect to the principal gradient axes. This provides good geometry for separating pixels that have been aliased from each quadrant - exactly what happens when 2D SENSE is performed. Speed up factors up to 4 (the maximum theoretically possible) appear achievable when 2D SENSE is

performed. This will be particularly advantageous when used with pulse sequences that require phase encoding in 2 dimensions such as 3D imaging and Chemical Shift Imaging (CSI).

The first practical application for the array is likely to be high resolution imaging. Some of the preliminary FSE images shown in this chapter (figures 5.17-5.19) demonstrate that the coil enables imaging to be performed at a much greater resolution, particularly in cortical regions.

With the in-plane resolution reaching 0.35mm in this work, it is increasingly important to reduce motion. Any motion on this scale is likely to reduce the effective resolution of the final image. Furthermore, severe artefacts can result from small movement during periods of data acquisition. Further developments of this work are likely to focus on motion correction. The ability of the extra information obtained using array coils for motion correction has already been investigated [11,12]. The combination of these parallel imaging based approaches, with the acquisition of navigator echoes [35] and interactive reacquisition techniques [36], should lead to image resolutions beyond those achieved here being realised routinely in vivo at 4.7 T.

One of the main applications of SENSE at high field strengths may prove to be with EPI. This is because SENSE can shorten the length of the readout and so reduce blurring. Perhaps more importantly, the phase encoding bandwidth per pixel may also be increased to reduce levels of image distortion. Thus, the main benefits of reducing the sampling density are found in the phase encoding direction. This is typically chosen to be the direction we called left-right. Increasing the level of speed up beyond 2.5 is

difficult using coil arrays because the geometric flexibility of the coils is limited and the sensitivity functions they produce are fixed. To speed up by a greater factor in the phase encoding direction new pulse sequence designs such as Common SENSE (that will be presented in the next chapter) may need to be combined with SENSE.

5.5 Conclusions

An efficient head array coil design has been presented. The coil fits into a 28cm birdcage transmit / receive coil while allowing audio-visual communication to be maintained with the subject.

The coil produces improved SNR performance over almost the entire head while producing large gains in SNR in peripheral regions. This was used to obtain high resolution images using an FSE sequence optimised for use at 4.7 T. Structural images of very high resolution, quality and contrast were produced.

The coil is compatible with SENSE to allow imaging to be sped up by a factor of 2.25-2.5 using 1D SENSE or by a factor of 3-4 using SENSE in 2D.

5.6 References

1. Pruessmann, K. P., Weiger, M., Scheidegger, M. B., & Boesiger, P. 1999, "SENSE: sensitivity encoding for fast MRI", *Magnetic Resonance In Medicine*, vol. 42, no. 5, pp. 952-962.

2. Sodickson, D. K. & Manning, W. J. 1997, "Simultaneous acquisition of spatial harmonics (SMASH): fast imaging with radiofrequency coil arrays", *Magnetic Resonance In Medicine*, vol. 38, no. 4, pp. 591-603.

3. Hoult, D. I. & Lauterbur, P. C. 1976, "The signal to noise ratio of the nuclear magnetic resonance experiment", *J.Magn Reson.*, vol. 34, pp. 425-433.

4. Hayes, C. E., Edelstein, W. A., Schenck, J. F., Mueller, O. M., & Eash, M. 1985, "An efficient, highly homogeneous radiofrequency coil for whole-body NMR imaging at 1.5T", *Journal Of Magnetic Resonance*, vol. 63, pp. 622-628.

5. Roemer, P. B., Edelstein, W. A., Hayes, C. E., Souza, S. P., & Mueller, O. M. 1990, "The NMR phased array", *Magn Reson.Med.*, vol. 16, no. 2, pp. 192-225.

6. Maudsley, A. A., Hilal, S. K., Perman, W. H., & Simon, H. E. 1983, "Spatially resolved high resolution spectroscopy by "four-dimensional" NMR", *Journal Of Magnetic Resonance*, vol. 51, pp. 147-152.

7. Axel, L. 1988, "Chemical shift imaging," in *Magnetic Resonance Imaging*, D. D. Stark & W. G. Bradley, eds., Mosby, pp. 229-243.

8. Hutchinson, M. & Raff, U. 1988, "Fast MRI data acquisition using multiple detectors", *Magn Reson.Med.*, vol. 6, no. 1, pp. 87-91.

9. McKenzie, C. A., Yeh, E. N., Ohliger, M. A., Price, M. D., & Sodickson, D. K. 2002, "Self-calibrating parallel imaging with automatic coil sensitivity extraction", *Magn Reson.Med*, vol. 47, no. 3, pp. 529-538.

10. Jakob, P. M., Griswold, M. A., Edelman, R. R., & Sodickson, D. K. 1998, "AUTO-SMASH: a self-calibrating technique for SMASH imaging. SiMultaneous Acquisition of Spatial Harmonics", *MAGMA*, vol. 7, no. 1, pp. 42-54.

11. Bydder, M., Larkman, D. J., & Hajnal, J. V. 2002, "Detection and elimination of motion artefacts by regeneration of k-space", *Magn Reson.Med*, vol. 47, no. 4, pp. 677-686.

12. Bydder, M., Atkinson, D., Larkman, D. J., Hill, D. L., & Hajnal, J. V. 2003, "SMASH navigators", *Magn Reson.Med*, vol. 49, no. 3, pp. 493-500.

13. Kellman, P. & McVeigh, E. R. 2001, "Ghost artifact cancellation using phased array processing", *Magn Reson.Med*, vol. 46, no. 2, pp. 335-343.

14. Haase, A., Odoj, F., Von Kienlin, M., Warnking, J., Fidler, F., Weisser, A., Nittka, M., Rommel, E., Lanz, T., Kalusche, B., & Griswold, M. 2000, "NMR Probeheads for In Vivo Applications", *Concepts in Magnetic Resonance*, vol. 12(6), pp. 361-388.

15. Weiger, M., Pruessmann, K. P., & Boesiger, P. 2002, "2D SENSE for faster 3D MRI", *MAGMA*, vol. 14, no. 1, pp. 10-19.

16. Weiger, M., Pruessmann, K. P., Leussler, C., Roschmann, P., & Boesiger, P. 2001, "Specific coil design for SENSE: a six-element cardiac array", *Magnetic Resonance In Medicine*, vol. 45, no. 3, pp. 495-504.

17. Pruessmann, K. P., Weiger, M., Scheidegger, M. B., and Boesiger, P. 1998, "Coil sensitivity maps for sensitivity encoding and intensity correction.", *Proc.6th Annual Meeting of ISMRM* 2087.

18. Murakami, J. W., Hayes, C. E., & Weinberger, E. 1996, "Intensity correction of phased-array surface coil images", *Magn Reson.Med.*, vol. 35, no. 4, pp. 585-590.

19. Carlsen, I. C. and Jensen, D. 1994, "Reconstruction algorithm for images obtained with flexible multi-element synergy coils.", *Proc.2nd Meeting of the Society of Magnetic Resonance* 835.

20. Brey, W. W. & Narayana, P. A. 1988, "Correction for intensity falloff in surface coil magnetic resonance imaging", *Med.Phys.*, vol. 15, no. 2, pp. 241-245.

21. Haacke, E. M., Brown, R. W., Thompson, M. R., & Venkatesan, R. 1999, "Filtering and resolution in Fourier Transform Image Reconstruction," in *Magnetic Resonance Imaging Physical Principles and Sequence design*, 1 edn, E. M. Haacke et al., eds., John Wiley and Sons, New York, USA, pp. 265-299.

22. Bydder, M., Larkman, D. J., & Hajnal, J. V. 2002, "Combination of signals from array coils using image-based estimation of coil sensitivity profiles", *Magn Reson.Med*, vol. 47, no. 3, pp. 539-548.

23. De Vita, E., Thomas, D. L., Roberts, S., Parkes, H. G., Turner, R., Kinchesh, P., Shmueli, K., Yousry, T. A., & Ordidge, R. J. 2003, "High resolution MRI of the brain at 4.7 Tesla using fast spin echo imaging", *Br.J.Radiol.*, vol. 76, no. 909, pp. 631-637.

24. Thomas, D. L., De Vita, E., Roberts, S., Turner, R., Yousry, T. A., and Ordidge, R. J. "High Resolution Imaging of the human Brain at 4.7 T: Implementation and Sequence Characteristics", *Magn Reson.Med*, submitted 2003

25. Hennig, J. 1988, "Multiecho imaging sequences with low refocusing flip angle", *Journal Of Magnetic Resonance*, vol. 78, pp. 397-407.

26. Mulkern, R. V., Wong, S. T., Winalski, C., & Jolesz, F. A. 1990, "Contrast manipulation and artifact assessment of 2D and 3D RARE sequences", *Magn Reson.Imaging*, vol. 8, no. 5, pp. 557-566.

27. Mulkern, R. V., Melki, P. S., Jakab, P., Higuchi, N., & Jolesz, F. A. 1991, "Phase-encode order and its effect on contrast and artifact in single-shot RARE sequences", *Med.Phys.*, vol. 18, no. 5, pp. 1032-1037.

28. Constable, R. T., Smith, R. C., & Gore, J. C. 1992, "Signal-to-noise and contrast in fast spin echo (FSE) and inversion recovery FSE imaging", *J.Comput.Assist.Tomogr.*, vol. 16, no. 1, pp. 41-47.

29. Constable, R. T. & Gore, J. C. 1992, "The loss of small objects in variable TE imaging: implications for FSE, RARE, and EPI", *Magn Reson.Med.*, vol. 28, no. 1, pp. 9-24.

30. Constable, R. T., Anderson, A. W., Zhong, J., & Gore, J. C. 1992, "Factors influencing contrast in fast spin-echo MR imaging", *Magn Reson.Imaging*, vol. 10, no. 4, pp. 497-511.

31. De Vita, E. 2003, *Development and Optimisation of High-Field MRI Techniques.*

32. Kangarlu, A., Baertlein, B. A., Lee, R., Ibrahim, T., Yang, L., Abduljalil, A. M., & Robitaille, P. M. 1999, "Dielectric resonance phenomena in ultra high field MRI", *J.Comput.Assist.Tomogr.*, vol. 23, no. 6, pp. 821-831.

33. Ibrahim, T. S., Lee, R., Abduljalil, A. M., Baertlein, B. A., & Robitaille, P. M. 2001, "Dielectric resonances and B(1) field inhomogeneity in UHFMRI: computational analysis and experimental findings", *Magn Reson.Imaging*, vol. 19, no. 2, pp. 219-226.

34. Sled, J. G. & Pike, G. B. 1998, "Standing-wave and RF penetration artefacts caused by elliptic geometry: an electrodynamic analysis of MRI", *IEEE Trans.Med.Imaging*, vol. 17, no. 4, pp. 653-662.

35. Ordidge, R. J., Helpern, J. A., Qing, Z. X., Knight, R. A., & Nagesh, V. 1994, "Correction of motional artefacts in diffusion-weighted MR images using navigator echoes", *Magnetic Resonance In Medicine*, vol. 12, no. 3, pp. 455-460.

36. Nguyen, Q. 2001, *Quantative Diffusion Weighted Imaging:Techniques and Applications to Perinatal Asphyxia.*

6. Common SENSE, TRAIL and TWIST

In this chapter, new methods are presented that enable image acquisition to be segmented into two readouts. Both of the readouts are performed in rapid succession after a single excitation of the magnetisation (i.e. two readouts are performed per shot). This is achieved using new pulse sequences that create two components of magnetisation with different spatial profiles. Each component of the magnetisation is measured in one of the readouts. This produces two images with complimentary 'sensitivity profiles' and near identical contrast. The images can be acquired with a reduced data matrix that corresponds to shorter periods of data acquisition. The reduced matrix images are then combined to produce a full matrix image.

The most promising application for these techniques is in improving the performance of Gradient Echo-Echo Planar Imaging (GE-EPI) at high field. Single-shot Gradient Echo-Echo Planar Imaging (GE-EPI) has a single, long period of data acquisition (or readout) and a low bandwidth per pixel in the phase encoding direction. This causes blurring and distortion in the GE-EPI images when magnetic field susceptibility gradients are present (see section 2.8). One way to reduce these problems is to segment the acquisition into several shorter periods. This can be achieved using Common SENSE, TRAIL and TWIST, the new methods investigated in this chapter,

The author would like to acknowledge the work that has gone into this chapter from members of the group. The chapter is broken into two sections. The first features Common SENSE that is a technique originally proposed by R. J. Ordidge before being

developed by the author. Common SENSE using EPI readouts at 4.7 T benefited from the work of D.L. Thomas who programmed and developed EPI on the system and E. De Vita who assisted in both the extra pulses programming required for Common SENSE and in data acquisition. Simulations of Common SENSE were developed by the author having been based on initial work by A.N. Priest. The second section features three techniques. Firstly there is ROCS, a high frequency variant of Common SENSE that is entirely the authors work. Secondly there is TRAIL; A.N. Priest mainly developed this method, though the author programmed the pulse sequence used. Lastly there is TWIST, the co-work of E. De Vita is acknowledged in this section.

6.1 Introduction to Common SENSE

MR imaging applications have found a continued need for increased speed of image acquisition. The use of MRI in the observation of dynamic systems has made it desirable to shorten even the most rapid imaging sequences. One such application is fMRI [1] where a local change in blood volume and oxygenation causes a change in T_2* contrast called Blood Oxygenation Level Dependent contrast or BOLD [2,3]. The observation of this regional change with time can be used to chart brain activity. The current imaging method of choice for making these measurements is Gradient Echo-EPI [4] (GE-EPI, see section 2.8) due to its speed and contrast. BOLD contrast is increased by the use of higher field magnets; however, EPI suffers from increased distortion and blurring with field strength. The challenge is to reduce the level of distortion and blurring whilst maintaining the increased BOLD sensitivity afforded by higher fields.

Summarising section 2.8.1 'EPI problems', distortion in GE-EPI images is the result of local susceptibility gradients and chemical shifts that cause an error in the assignment of spin position. To reduce this problem, the bandwidth per point along the phase encoding axis must be increased. Blurring of image detail occurs because of T_2* decay over the length of the acquisition, this is a greater problem at higher field where T_2* is shorter. Shortening the total readout length reduces this problem leading to a sharper image. Ghosting is produced by a mismatch in amplitude or phase between adjacent lines of k-space data. Gradient inconsistencies, eddy currents and susceptibility gradients can all contribute to this mismatch. Hardware improvement or corrections can both be used to reduce the artefact level [5].

The simplest method to reduce distortion and blurring is to shorten the length of the readout. The rate at which the read gradient can be switched is limited. This is due to physiological constraints; rapidly varying magnetic fields can induce currents in nerves large enough to cause stimulation. Additionally, the desired gradient waveform is only accurately produced when both its amplitude and switching rate lie within certain limits. Therefore, one option available is to reduce in the number of phase encoding steps in the acquisition window, necessitating the recovery of a full set of image information by some other means. There are a number of different techniques to perform this function that can be classified into two approaches.

Firstly, there is the segmentation of k-space (see section 2.8.2); different lines of the standard k-space coverage are acquired in separate readouts. The signal amplitude and phase must remain precisely the same between the readouts. Otherwise, when data from different readouts is combined in k-space, ghosting is produced in the images reconstructed from it. There are two different kinds of segmented image acquisition: single-shot and multi-shot. Multi-shot segmented EPI requires more than one excitation of the magnetisation producing a penalty in temporal resolution that would be unacceptable for many applications. Furthermore, any motion between the shots can result in severe ghosting artefacts. Single-shot segmented EPI is rarely performed because the data must be combined to produce a smoothly varying function across k-space [6]. One method to obtain the segments consecutively is to use a 45° RF pulse-readout followed directly by a 90° RF pulse-readout. This method suffers from ghosting due to discontinuities in signal phase and amplitude between segments that are difficult to eliminate.

The second approach uses prior information to recreate full images from reduced data sets. Partial Fourier methods that exploit the conjugate symmetry of k-space have been used [7], but, because they do not increase the phase encoding bandwidth, there is no reduction in distortion. In EPI, due to magnetic susceptibilities, k-space is often not symmetrical which can cause reconstruction errors.

In recent years, a new group of methods has allowed a considerable increase in acquisition speed. These Parallel Imaging (PI) methods all rely on the simultaneous use of receiver coils with different spatially varying sensitivities (see section 2.7 and chapter 5). Knowledge of the sensitivity functions of these coils gives information that is complimentary to standard Fourier encoding. This allows a reduction in the density with which k-space must be sampled [8]. For EPI, employing the reduction in sampling in the phase encoding direction increases the bandwidth and correspondingly reduces distortion in this direction. The data from the multiple coils can be combined in either k-space or image space. SENSE, which combines the data from separate coils in image space, has been used for fMRI with some success in references [9-11]. The time required to map the sensitivity is minimal in dynamic studies where the same maps can be used for the subsequent generation of many images.

As illustrated by chapter 5, each coil arrangement used for PI possesses its own non-uniform sensitivity profile and SNR performance. The maximum degree of speed up is limited by coil geometry (i.e. by the g-factor) that can reduce the SNR prohibitively in certain regions and for some slice geometries even with a low degree of speed up. For the array in chapter 5, the maximum speed up factor along one dimension was ~2.5, which is similar to the values reported in reference [8]. It is unlikely that significantly

greater speed up factors will ever be achieved using SENSE in 1D because of the geometry of the head, and the limited positions at which surface coils may be arranged around it. This means that the sensitivity profiles that the coils can produce are also limited. It would be advantageous if the sensitivity profiles could be optimised further, either by using hardware or by using new imaging methods. N.B. there is little obvious advantage from performing SENSE in 2D for 2D-EPI.

There have been some other approaches to minimise the amount of phase encoding needed to produce a full image; these include a reduction in the size of the FoV using 2D RF pulses [12], saturation [13] and stepped B_0 fields [14,15].

Though there are many approaches to EPI that enable a reduction in distortion and blurring, a robust method to perform a single-shot segmented acquisition is desirable. This method must maintain temporal resolution and robustness to ghosting, while using conventional hardware with its more uniform SNR characteristics and absence of geometric constraints. In this chapter 'Common SENSE' is presented as such a method. The technique is demonstrated using both EPI and standard two-dimensional Fourier transform (2DFT) scans, where Common SENSE may also prove to be effective in reducing imaging times. The high quality, artefact free images obtained by the 2DFT technique are used here to facilitate the clear presentation of Common SENSE.

At high field strength, it is likely that a combination of the techniques outlined above will be necessary to obtain GE-EPI images of optimal quality, especially if any improvement in resolution is to be achieved.

6.2 Theory

In this section, the Common SENSE pulse sequence is described in terms of the development and manipulation of magnetisation. This should lead to an understanding of the how two images are produced in rapid succession and how the spatial variation in sensitivity is imposed upon them.

6.2.1 Pulse Sequence and Magnetisation

The principle underlying Common SENSE is that the magnetisation may be split into two different components; these components vary in magnitude and phase as a function of position across the object. Each component of the magnetisation is used to acquire an image that has a spatially varying sensitivity function across the FoV corresponding to the underlying, spatially varying magnitude and phase of the magnetisation.

The pulse sequence is similar to that used in TRAIL (Two Reduced Acquisitions InterLeaved) [16,17]. The spatial responses are produced by imposing a linear phase shift on the transverse magnetisation with a gradient after the first 90° RF pulse (see the pulse sequence in figure 6.1 and the corresponding development of magnetisation with position in figure 6.2). This creates two components of magnetisation M_x and M_y, that vary cosinusoidally and sinusoidally respectively across the FoV. The second 90° pulse then selectively rotates a portion of the magnetisation into the z-axis where it can be stored. In this state, the longitudinal magnetisation is only affected by a small amount of T_1 relaxation. The component that remains in the transverse plane is used to acquire an image. A third 90° pulse recalls the z-component of magnetisation, and a second image can be taken with a response of the same spatial frequency but with a phase difference of $\pi/2$. The two images obtained using the Common SENSE pulse sequence can be

acquired with a reduced FoV. The reduced FoV images can then be combined using reconstruction methods used in SENSE to form a full FoV image.

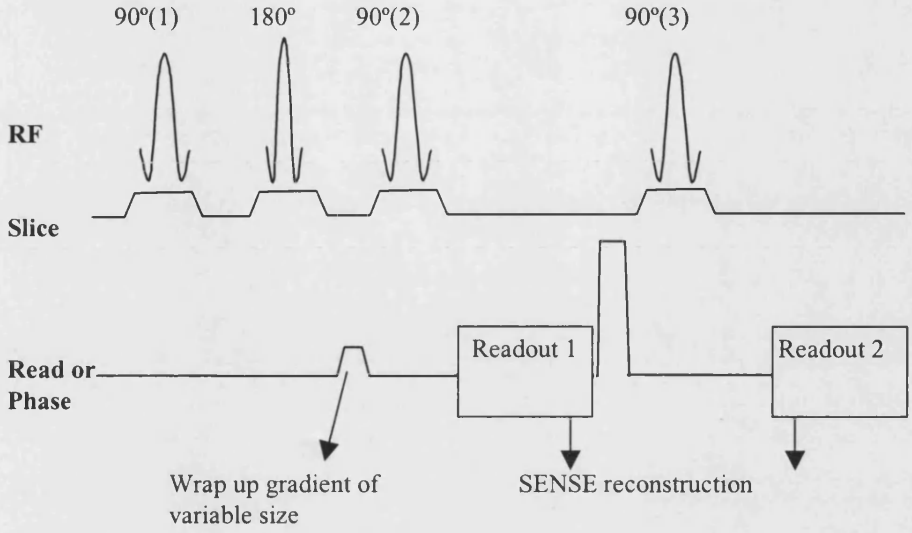

Figure 6.1 The Common SENSE pulse sequence
All RF pulses are slice selective. The readout may be a 2DFT or EPI acquisition.

The pulse sequence has two other important features. Firstly, a 180° RF pulse is used to ensure that any dephasing due to B_0 inhomogeneities is refocused immediately prior to the second 90° pulse. Secondly, the magnetisation in the transverse plane is spoiled after the first readout. This prevents any interference from the first component of magnetisation in the second readout (where the second component of magnetisation is measured). The phase of the 90° pulses determines the spatial phase of the response functions, and the size of gradient determines the spatial frequency, making the spatial profiles easy to control. The profiles may be imposed in the read or phase directions, though they are used in the phase encoding direction here, as this is where the greatest gains in time or quality can be realised.

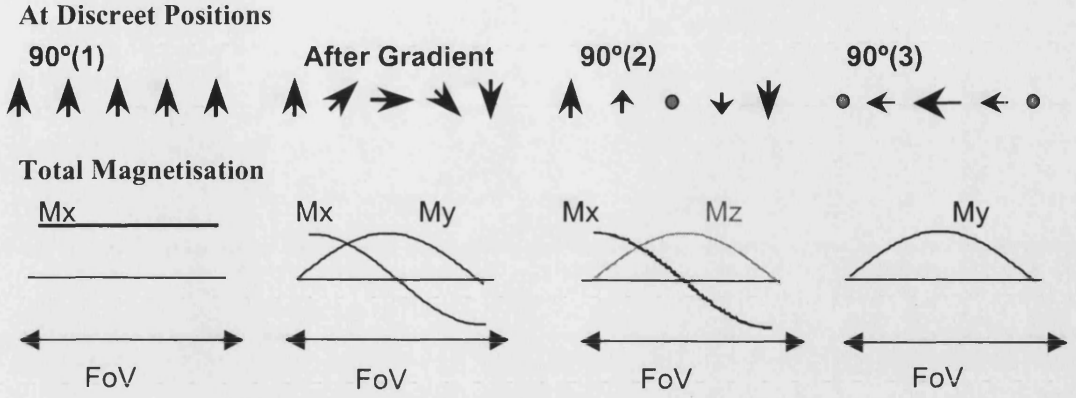

Figure 6.2 The progression of magnetisation during the Common SENSE pulse sequence
After the first 90° pulse the magnetisation is coherent and lies along M_x. A gradient is applied to split the magnetisation into two components. The second 90° pulse then puts one component onto the z-axis and an image may be gained from M_x. The third 90° pulse then recalls M_z and an image is gained with M_y.

Common SENSE can also be understood by examining the phase graph in figure 6.3 for the pulse sequence shown in figure 6.1. The first 90° RF pulse (90_1) brings the magnetisation into the transverse plane where the magnetisation is dephased by T_2* relaxation. The 180° RF pulse then reverses the phase of the magnetisation and the T_2* dephasing is reversed by the same processes that created it. The magnetisation would be completely refocused (pass through the (u,v) signal line) immediately before the second 90° pulse (90_2) because the time between the 180° pulse and both 90_1 and 90_2 is equal. This makes the magnetisation decay by T_2 relaxation only between the 90_1 and 90_2 pulses, typically the amount of time between these pulses is short compared to T_2, so dephasing due to this decay is negligible. However, a gradient is applied between the two 90° pulses that causes the magnetisation to be dephased, with the area of the gradient determining the degree of dephasing. At the second 90 degree pulse some of the magnetisation effectively experiences a 180° pulse, it is converted to an F* coherence and forms a spin echo (SE) when it crosses the signal line. A second

component of the transverse magnetisation effectively experiences no RF pulse, it remains an *F* coherence and forms a second *SE* when it crosses the signal line. The coherences are made to passes through the signal line by the application of the appropriate readout gradients.

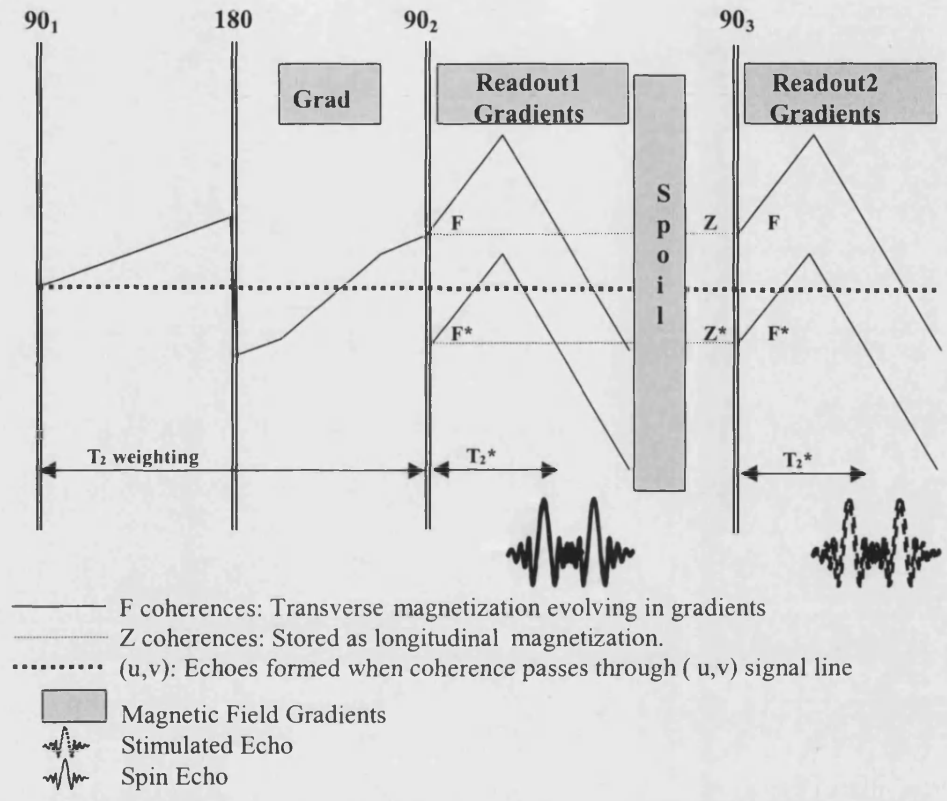

Figure 6.3 A Phase Graph description of the Common SENSE pulse sequence
A 90-180-90 series of RF pulses forms the preparation period of the Common SENSE pulse sequence. This forms two components of magnetisation. The first is a super position of the F and F* states. These are used to perform the first readout and obtain the first image. The interference between the F and F* states produces a sinusoidal oscillation in the magnetisation profile. The second component is the combined Z and Z* states. This longitudinal magnetisation is stored on the z axis after the 90_2, it is then brought back into the transverse plain by the 90_3. A second readout is then performed with a second sinusoidal oscillation in the magnetisation profile.

There are also components of the magnetisation that experience the 90_2 as a 90° pulse. This converts the transverse magnetisation to longitudinal magnetisation represented by the two states *Z* and *Z**. These states will not be dephased by any gradients but they do

decay via T_1 relaxation. Because the time between the second and third 90° pulses is typically much shorter than T_1 this decay is small. After the first readout the transverse magnetisation (*F* and *F** states present after the 90_2) is spoiled. The longitudinal magnetisation, *Z* and *Z**, is brought back to the transverse plane by the third 90° pulse to form *F* and *F** coherences. These coherences are used for a second readout and two further echoes are measured, these are stimulated echoes (*STE*). Though the echoes from each readout are termed *SE* and *STE* they both have the same relaxation weighting. The size of the gradient between the first two 90° pulses determines the separation of the coherences and the interference between them causes the spatial modulation in sensitivity response described above.

In Common SENSE, for each readout the *F* and *F** coherences are nearly on top of one another and both are seen as a single combined echo in the centre of the readout. Similar sequences with three 90° pulses have been used [18-20] with a much larger gradient between the first two 90° pulses, causing an oscillation in sensitivity below the size of a pixel. These are used to obtain two images that are very similar in appearance without doubling the number of shots required to obtain the data. However, the underlying oscillation of the magnetisation is not visible in the images produced. If each image is deliberately given a different contrast the sequence can be used for various measurements [19,20] such as chemical shifts [21] T_1 [22], and diffusion [23-26]. These sequences have not previously been used to create a variation in sensitivity across an image for the purpose of segmenting an acquisition as described here.

6.3 Methods

In this section, the 2DFT experiments performed to investigate Common SENSE are described. The EPI pulse sequence adapted to perform the Common SENSE experiment is also detailed. A simulation to model the signals produced by the Common SENSE pulse sequence is also described. This was further developed to determine the optimal way to reduce the readout length in terms of the SNR of the final image produced.

6.3.1 Simulations

The sequence described above was simulated using code written in MatLab to investigate the SNR behaviour of Common SENSE images. A uniform sample was modelled as a discrete set of magnetic moments. Gradients and RF pulses were treated as vector rotations of the magnetisation. T_1 and T_2 relaxation were not considered. The SNR was modelled by the addition of pseudo-random noise to the simulated signal at a constant level. The noise was calculated for each pixel by taking the standard deviation of the signal for a set of two hundred images, the signal being the mean value over the same set. This was done for both a reconstructed full FoV Common SENSE image (speed up factor R=2) and standard image (R=1) for comparison. There will be some additional noise due to inaccuracies in the sensitivity maps though these are assumed to be small in comparison to noise in the images.

N.B. Common SENSE images will be referred to as having a 'speed up factor R'. This is not exactly the same as the R described for SENSE. The SENSE R gives a reduction in the overall time taken to obtain the image data from sampling k-space with reduced density. For Common SENSE R describes the reduction in sampling density in k-space for each consecutive readout, though this does not correspond to a reduction in the overall time taken to obtain the image data.

The sensitivity of Common SENSE to B_1 inhomogeneity was investigated by altering the flip angle of all the 90° RF pulses seen in figure 6.1. The 180° RF pulse was assumed to be uniform. A set of 200 images was generated for a full FoV Common SENSE acquisition (speed up factor R=2) and a standard acquisition (R=1) with the same flip angle. This was repeated with values of flip angle ranging between 45° and 90°. The SNR per pixel was calculated for the Common SENSE and standard images (as above) for each flip angle.

6.3.2 2DFT Methods

2DFT experiments were performed on a 40cm bore, Bruker Biospec, 2.35 T, Avance system running under Paravision 2.0 using a standard birdcage coil supplied by the manufacturer. Processing was performed offline, using software developed by the author in MatLab (Mathworks, Natick, MA). Images were acquired using the Common SENSE sequence shown in figure 1. The sequence allowed the option of adding an extra 180° pulse before each readout to obtain T_2 weighted images.

Full FoV Common SENSE images with the desired sinusoidal sensitivity modulation (of π across the FoV, see section 6.4) were taken. These correspond to the images obtained from the individual array coil elements in chapter 5. However, the Common SENSE images were obtained consecutively by the same coil as opposed to the images obtained simultaneously by multiple coils in chapter 5. The sensitivity functions imposed on the Common SENSE images can be mapped as described in section 5.2.3. A reference image is required for the mapping process. This may be acquired using a 'standard' pulse sequence, characterised by the same image contrast as produced in the

Common SENSE images. Alternatively, the root of the sum of squares of the Common SENSE images (*SSQ*) may be used as a reference image. The *SSQ* image will have an approximately uniform sensitivity because the profiles in the two images vary as a cosinusoid and sinusoid respectively and $cos^2(x) + sin^2(x) = 1$ for any value of x. Reduced FoV images can then be acquired and combined with the sensitivity maps to obtain full FoV images.

A tomato was imaged using 'standard' 2DFT and Common SENSE 2DFT pulse sequences. The following parameters were used Te / Tr~40 / 2000ms, 3mm slice, full FoV=9x9cm, full matrix=96x96, half FoV=9x4.5cm, half matrix=96x48. A sinusoidal response with a period of π radians was generated across the full FoV. This response was produced by the gradient pulse, applied before the second 90° RF pulse in figure 6.1, which created a π radian linear phase shift across the full FoV. The reasons for using a π radian linear phase shift are discussed later.

6.3.3 EPI Methods

EPI experiments were performed on a SMIS MR5000, 4.7 T / 90cm system supported by Philips Medical Systems utilising a head gradient set (Magnex, UK) and a standard birdcage coil. The maximum gradient strength on the system is 35mT/m with a maximum slew rate of 195mT/m/ms. The slew rate used was significantly less than this maximum. All volunteers were healthy and were imaged only after informed consent had been gained. Approval was obtained from the University College London Hospital Ethics committee.

The EPI sequence featured blipped phase encoding gradients with sinusoidal readout gradients [6]. The k-space data (100x64) was re-gridded to a uniform (64x64) Cartesian matrix before being Fourier transformed to produce an image. Acquisitions performed with read gradients of opposite polarity were used to eliminate ghosting from mismatches between echoes [27,28]. Maps of the sensitivity profiles imposed by the Common SENSE pulse sequence were generated using full FoV Common SENSE images and a reference image. The *SSQ* of the two full FoV Common SENSE images gave an approximately uniform reference image without the need for a separate acquisition. To ensure the sensitivity maps contain the same level of distortion as the half FoV images, a two shot interleaved sequence was used. This method provides the same signal bandwidth per point along the phase encoding direction. Half FoV Common SENSE images were then acquired in a single-shot and full FoV images reconstructed (speed up factor R=2) using the sensitivity maps as previously described. Reference images were taken using a single-shot, single segment acquisition (R=1) and a two shot, two interleaved segment technique for comparison. A volunteer's head was imaged using the following parameters TR / TE=3500 / 20ms, FoV=20cm, 3mm slice thickness; for a 64x64matrix the full-length acquisition window was 26ms.

	Acquisition	Further Details / figure	Time (a.u.)
2DFT	Full FoV 'standard' acquisition	figure 6.7h	2 units of time
	Full FoV Common SENSE acquisition	figure 6.7a & b	2 units of time
	Half FoV Common SENSE acquisition	figure 6.7e & f	1 unit of time
EPI	Full FoV 'standard' acquisition	1-shot, BW_{pe}=1a.u. figure 6.8c	1 unit of time
	Full FoV 'standard' segmented acquisition	2-shot 2-segment, BW_{pe}=2a.u, figure 6.8d	2 units of time
	Full FoV Common SENSE segmented acquisition	2-shot 2-segment, BW_{pe}=2a.u, SSQ reco. in figure 6.8b	2 units of time
	Half FoV Common SENSE acquisition	1-shot, BW_{pe}=2a.u SENSE reco. in figure 6.8a	1 unit of time

Table 6.1 A summary of the Common SENSE image acquisitions

6.4 Results

In this section the results obtained from simulating the pulse sequence are presented with particular reference to SNR performance and sensitivity to B_1 non-uniformity. Common SENSE and 'standard' images are then presented obtained using both 2DFT and EPI imaging methods.

6.4.1 Simulation of SNR Results

The spatial sensitivity functions generated by the pulse sequence determine the SNR of the final image. The simulation was run for various spatial responses of different frequency and phase by changing the gradient size and RF pulse phase. The best SNR performance for Common SENSE images (reduction in the FoV of R=2, reconstructed from a pair of half FoV images) was produced when the frequency of the sinusoidal response was π radians across the FoV. This was expected because it produces the

maximal variation in sensitivity across the FoV without the function repeating. This is compared to the SNR of a standard image with a full FoV in figure 6.4a. The simulation shows the SNR to be uniformly $\sqrt{2}$ worse across the entire FoV. 2DFT phantom results confirmed this finding (data not shown).

The SNR performance of Common SENSE with different '90°' RF pulse angles was investigated to model RF non-uniformity. In figures 6.4a-c the RF pulse flip angles used for the '90°' RF pulses in figure 6.1 were 90°, 70° and 50° respectively. The SNR performance of the standard images decreases with flip angle, as expected from a consideration of the reduction in the amount of magnetisation available in the transverse plane for image acquisition. The flip angle is uniform across the FoV and so in the standard image the SNR is also uniform.

In the Common SENSE images the flip angle has a less direct effect on the SNR, because the flip angle changes the sensitivity functions imposed on the half FoV images. The sensitivity functions then influence the SNR of the final image. Figures 6.4a-c demonstrate that the Common SENSE images have a greater variability in SNR across the FoV as the flip angle deviates further from the ideal of 90°. However, figure 6.4b shows that the level of SNR uniformity in the Common SENSE image is still high at a flip angle of 70°, with the drop in SNR being around $\sqrt{2}$ across the entire FoV compared to the standard image acquired with the same flip angle. Figure 6.4c shows that the SNR is becoming non-uniform at a flip angle of 50° with the SNR varying from above a $\sqrt{2}$ reduction at the edges to a factor of nearly 2 in the centre, again, as compared to the SNR of the standard image at the same flip angle.

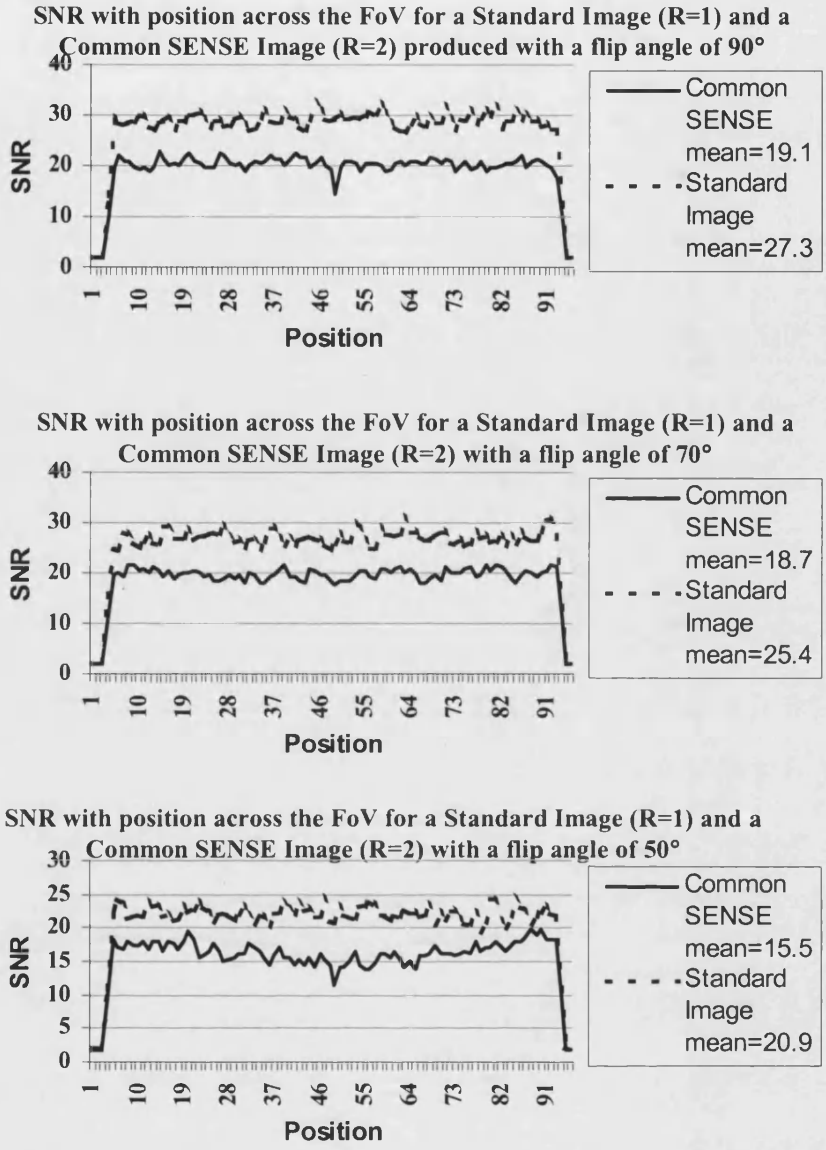

Figure 6.4 The Simulated SNR Performance of Common SENSE and Standard Imaging with position across the image FoV for several flip angles

The average SNR performance across the FoV with flip angle of Common SENSE and standard imaging was compared in figure 6.5. The SNR performance of the standard image (triangle points) drops with the size of the reduced flip angle (square points). The average SNR for Common SENSE falls with flip angle in a similar manner to the SNR fall for standard imaging. The crosses show the standard image SNR divided by $\sqrt{2}$. This is in close agreement with the simulated Common SENSE SNR. In summary the

average SNR in Common SENSE is $\sqrt{2}$ worse at a speed up factor of 2, even when there is some variation in the flip angle away from the ideal 90°. When the pulse angle is far away from 90°, Common SENSE images do have some variation in SNR across the FoV that is not present in the standard images. However, the overall SNR performance of Common SENSE is affected by RF pulse flip angle in a similar manner to standard imaging.

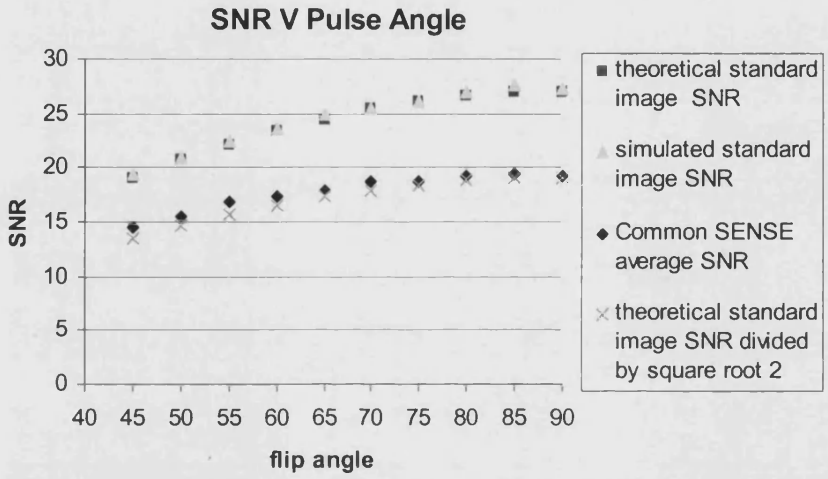

Figure 6.5 The Simulated Average SNR Performance of Common SENSE and Standard Imaging with RF pulse flip angle

6.4.2 2DFT Images

Images were taken of a water phantom to demonstrate the control that can be exerted on the sensitivity profiles across the FoV of the image. In figure 6.6a, the modulus of the sinusoidal response is seen in the magnitude image, which was taken using readout 1 in figure 6.1 and a gradient that, in this case, produces a 2π linear phase difference over the FoV. Figure 6.6b has a phase difference of $\pi/4$ in its spatial response profile from a corresponding $\pi/4$ phase change in the second 90° RF pulse, compared to figure 6.6a. An increase in the frequency of the response by a factor of two is generated in figure 6.6c by doubling the gradient evolution following the first 90° RF pulse. The gradient

can be increased still further, until the frequency of response is over the scale of a pixel rather than over the scale of the object, this is demonstrated in figure 6.6d (and will be revisited later in this chapter). The second readout produces images with the same frequency but with a phase difference of $\pi/2$ in the spatial response functions.

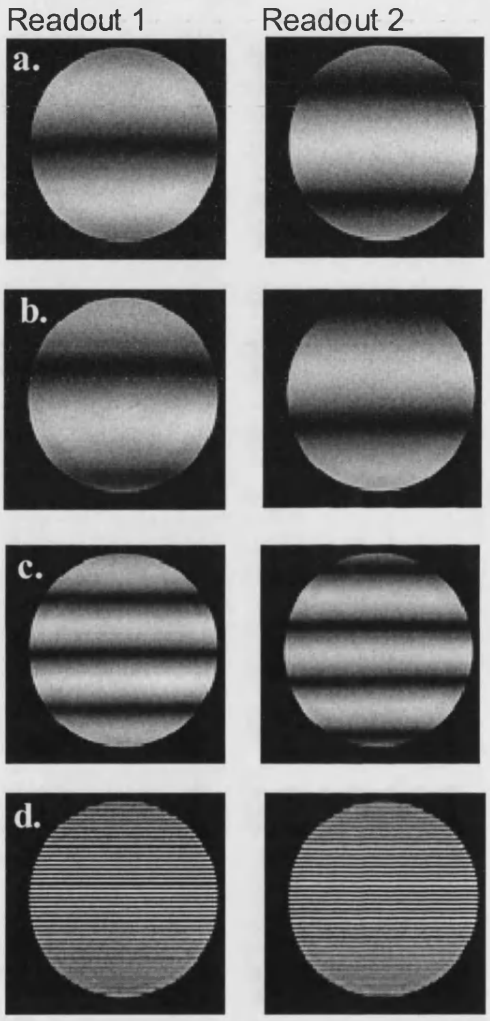

a. A 2π period sinusoidal function is imposed on the images over the FoV. There is a phase difference of 90 degrees between the functions imposed on the images acquired in each readout.

b. As in *a* but with the phase of the $90°_2$ RF pulse in figure 6.1 changed by $\pi/4$.

c. As *a* but with the 2x gradient area between the first two 90° RF pulses in figure 6.1.

d. As a. but with the a much larger gradient area imposing approximately a $\pi/2$ period over each pixel.

Figure 6.6 Manipulation of Sensitivity Functions on a Water Phantom
All images are produced using the Common SENSE pulse sequence

A full FoV 2DFT image of a tomato was obtained from a pair of half FoV 2DFT images (see figure 6.7). Full FoV images, figure 6.7a and figure 6.7b, were acquired in two consecutive full-length readouts and show the same contrast, modulated by different spatial response profiles. Figure 6.7c & figure 6.7d are the sensitivity maps generated

with these full FoV images after division by a standard full FoV image with a near identical relaxation weighting. The images shown in figure 6.7e & figure 6.7f have had the FoV reduced by one half in the phase encoding direction. A full FoV Common SENSE image, figure 6.7g, is generated using the information in figure 6.7c-f. The Common SENSE image maintains a high of level of image quality and identical contrast when compared to the reference, figure 6.7h, despite being produced from the half FoV images. The difference between these images is shown to be pure noise by the difference image figure 6.7j.

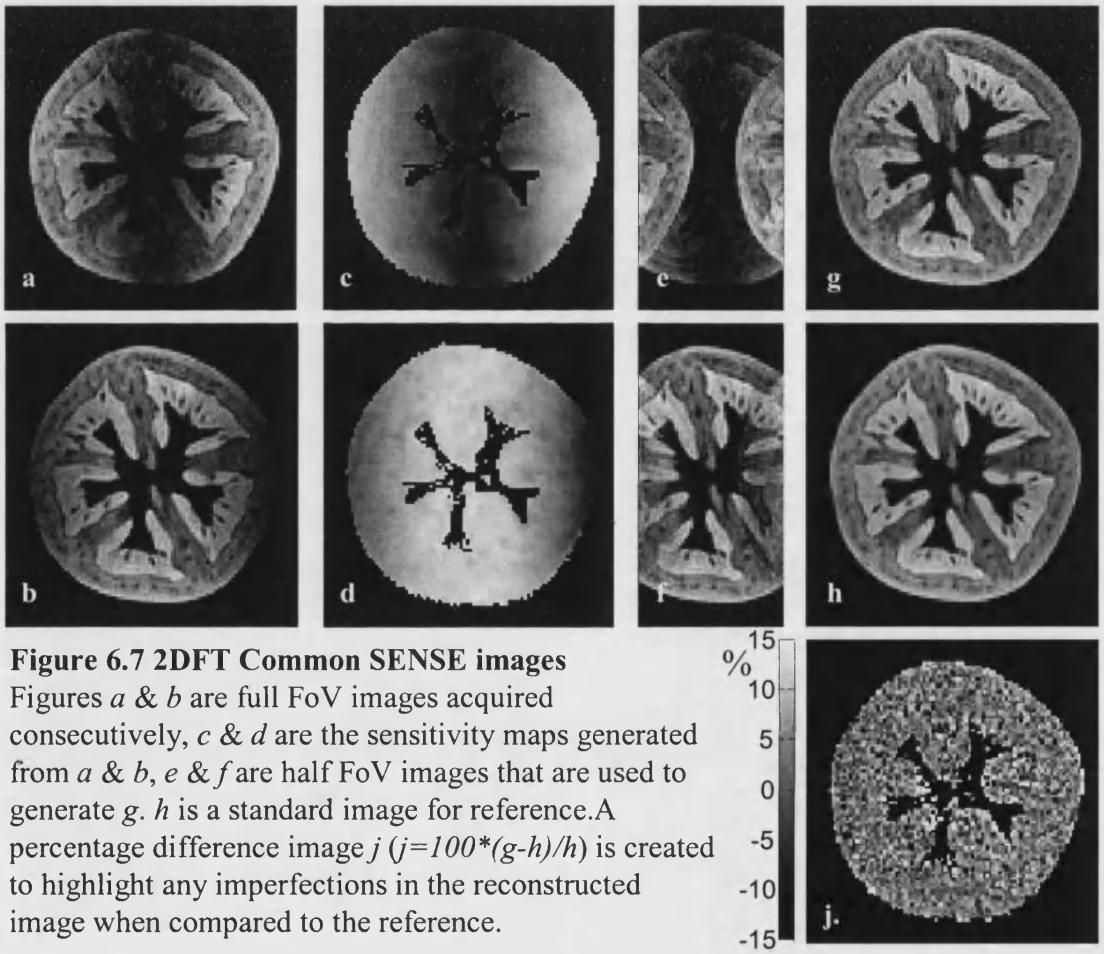

Figure 6.7 2DFT Common SENSE images
Figures *a* & *b* are full FoV images acquired consecutively, *c* & *d* are the sensitivity maps generated from *a* & *b*, *e* & *f* are half FoV images that are used to generate *g*. *h* is a standard image for reference.A percentage difference image *j* (*j=100*(g-h)/h*) is created to highlight any imperfections in the reconstructed image when compared to the reference.

6.4.3 EPI Images

A comparison of Common SENSE and standard EPI techniques is shown in figure 6.8. Figure 6.8a shows a Common SENSE image reconstructed from half FoV data. Figure

6.8b is the square root of the sum of squares reference that is produced in the generation of the sensitivity maps. A standard EPI image obtained in one shot is shown in figure 6.8c, with a two shot interleaved image in figure 6.8d. The Common SENSE image has the same level of distortion and blurring as the two shot references, while maintaining the temporal resolution of the single-shot reference. The Common SENSE image, figure 6.8a, most closely resembles the Common SENSE reference, figure 6.8b, because this is the reference image used to form the sensitivity maps. Figures 6.8a and 6.8b demonstrate that Common SENSE can be used in vivo to produce images of two shot quality in a single-shot.

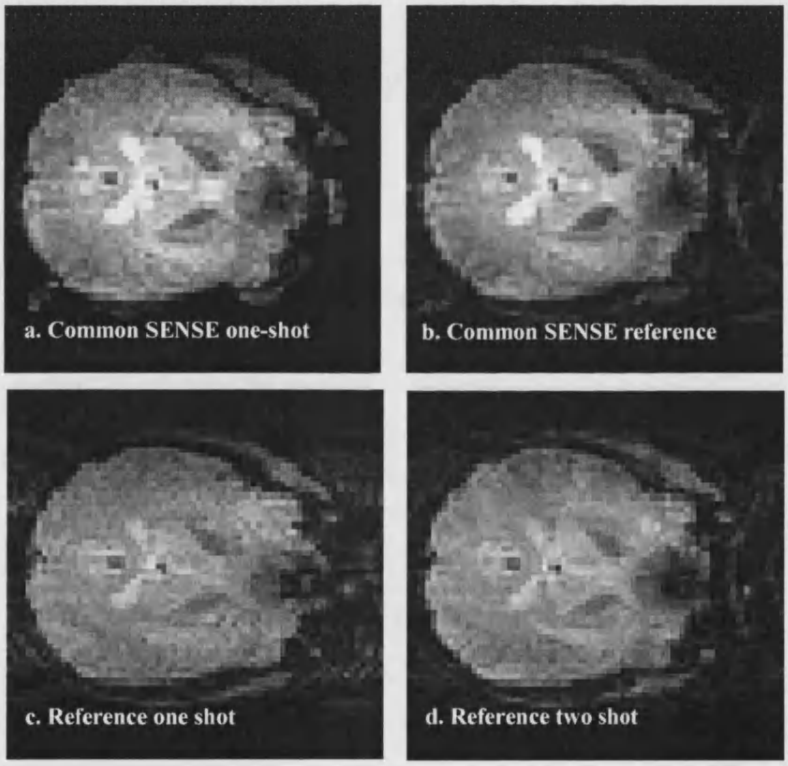

Figure 6.8 A Comparison of Standard and Common SENSE EPI images

The contrast throughout the white and grey matter appears consistent between the Common SENSE and 'standard' EPI images. However, the CSF appears brighter in the Common SENSE images. This is thought to be due to the flow of CSF during the

Common SENSE sequence. Any CSF that flows into the slice between 90° RF pulses will be excited by the next 90° RF pulse and fully contribute to the signal. Whereas CSF that has remained in the slice will be attenuated in each readout according to the sensitivity function imposed on the magnetisation by the Common SENSE pulse sequence. More work is required to fully investigate, quantify and, if necessary, ameliorate this effect.

6.5 Discussion

In this section, the Common SENSE method is described as a technique to create pairs of images with different sinusoidal sensitivity functions. Common SENSE is first illustrated with the 2DFT imaging technique and its possible application here is discussed. Common SENSE is primarily concerned with segmenting the EPI readout for reducing image distortion and blurring and this is the subject of the remainder of this section. Particular reference is made to SNR performance, time efficiency and the differences and similarities between SENSE and Common SENSE.

6.5.1 Common SENSE and the 2DFT Technique

The Common SENSE method has been demonstrated with the 2DFT technique. The phantom experiments in figure 6.6 show the degree of control that can be exerted over the spatial response using easily varied gradient and RF parameters. This ability enables the method to be used like any conventional experiment, allowing geometric factors such as the desired FoV and slice orientation to be freely chosen. It also permits use of Common SENSE with a wide variety of standard RF coils.

Full FoV 2DFT Common SENSE images can be generated from a pair of images obtained in rapid succession, with a half FoV and the same contrast. When applied in the phase encoding direction, the scan time was halved. However, the level of pre-scanning necessary to accurately process these images determines the total time saving that is possible. The generation of a reference image can easily be avoided by using the convenient fact that the root of the sum of squares of the image pair should produce an even intensity image with the same contrast as in a standard reference scan. For the sensitivity functions to be mapped, full FoV images with the desired sensitivity profiles need to be obtained in addition to the reference image. For SENSE and SMASH it has been demonstrated that pre-scanning can be eliminated by acquiring a few extra lines in the centre of k-space to obtain a low resolution, full FoV image from the same data [29,30]. For Common SENSE the inter-subject variation in the sensitivity functions, imposed by RF pulses and gradients alone, may be small enough in spin echo images to use the same maps on many subjects thus eliminating the need for a pre-scan. There are already methods for obtaining T_2/T_1 weighted images in a reduced time such as RARE [31] and its derivatives that are highly efficient, robust and are not compatible with Common SENSE. However, where 2DFT images are used, Common SENSE could provide a reduction in scan time.

6.5.2 SNR and Sensitivity to B_1 Inhomogeneity

The penalty in SNR for producing a full FoV image from two half FoV images obtained using the Common SENSE method is $\sqrt{2}$ compared to a 'standard' image acquisition. This is achieved by imposing a half wavelength (π radian) sinusoidal modulation across the FoV. Some small extra variation in SNR due to RF inhomogeneity is likely, as is the case with conventional images. The average SNR performance of Common SENSE

with reduced flip angle is similar to standard imaging. Common SENSE is robust to RF inhomogeneities because they simply cause a slight change in the sensitivity functions that, when mapped correctly, will still produce a uniform image. Any changes in the sensitivity functions due to RF inhomogeneity can in turn affect the SNR performance of Common SENSE, however, it is found that a very large change in the flip angle away from an ideal 90° pulse is required to cause significant SNR non-uniformity.

It should also be noted that the ability to use different pulse strengths for the three 90° RF pulses in Common SENSE is a further way to eliminate the effects of any RF inhomogeneity. This can compensate for flip angle non-uniformity by ensuring that at every spatial position all the magnetisation sees at least one '90°' pulse that is close to 90°. The majority of magnetisation is then brought into the transverse plane and so contributes to the acquired signal. Unlike the SENSE method, the g-factor for Common SENSE is nearly always $g \approx 1$ due to the imposition of near ideal sensitivity functions independent of any geometric factor. This is because the optimum sensitivity variation can easily be imposed across the object. As with SENSE, unaliased pixels in Common SENSE images have a higher SNR due to the $\sqrt{R}$ factor present in equation 2-40.

6.5.3 Common SENSE with EPI

The use of Common SENSE with EPI can reduce the length of the acquisition window (or effective readout time) by a factor of two. This produces a corresponding reduction in both blurring and distortion. The advantage of Common SENSE over two shot, segmented EPI or a 45-readout-90-readout-type acquisition is that there is maintenance of both temporal resolution and robustness to ghosting. This is because the two sets of data are acquired within a few tens of milliseconds and then recombined in image space.

Common SENSE requires two consecutive half length readouts and a short preparation period (see figure 6.9) compared to a single readout in a 'standard' EPI acquisition. This means the time required to acquire the data from one slice (T_{total}) is different. In fMRI, it is important to maintain the same volume coverage (acquire the same number of slices) at a certain scan repetition rate. This means that T_{total} must not be significantly greater for Common SENSE than for a 'standard' acquisition. The respective lengths of the TE and *TACQ* determine how much longer the Common SENSE acquisition will take. The shorter the echo time used in an EPI experiment, the less time (*TW*) that is wasted between the RF pulse and the start of the readout. Thus, Common SENSE is suited to experiments that require a shorter TE, because it has two such *TW* periods. Common SENSE may be useful for obtaining EPI images where the readout length is too long to allow a very short echo time (i.e. where *TE<TACQ/2* in a 'standard' readout).

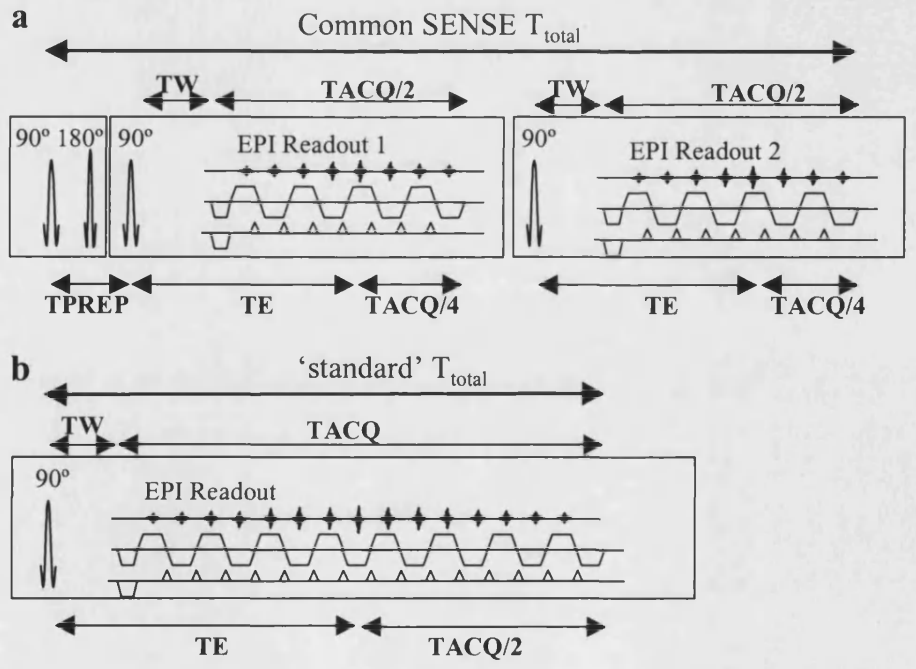

Figure 6.9 Schematic of time considerations for the the Common SENSE pulse sequence
The time required for performing Common SENSE and its two half length EPI readouts (*a*) is compared to single 'standard' EPI readout of double the duration (*b*).

For fMRI, there is an optimum echo time that produces maximum sensitivity to BOLD contrast. This optimum echo time is lower at higher field strength. Additionally, a slightly lower echo time than the optimum for BOLD contrast is sometimes used to reduce the dropout of signal from regions of the head containing strong susceptibility gradients. From figure 6.9, T_{total} for Common SENSE is approximately *TPREP+2TE+TACQ/2* and T_{total} for a 'standard' is approximately *TE+TACQ/2*. On the 4.7 T system described in section 6.3.3, TE~20ms (the approximate T_2* of grey matter at 4.7 T), TPREP~10ms and TACQ~26ms giving T_{total} Common SENSE~63ms and T_{total} standard~33ms. This should allow both methods to acquire at least 48 slices of data in a TR of 3.5s. The TPREP time could be made shorter though this would entail a reduction in the length of the RF pulses. This results in a higher deposition of power (SAR). SAR is an important consideration in the design of pulse sequences at high field because more power is required to produce the same flip angle. Common SENSE uses three 90° RF pulses and one 180° RF pulse in a time of approximately 66ms. While this is an increase relative to the 'standard' EPI readout it does not exceed the SAR limits. When compared to the FSE sequence in chapter 5, which utilises a train of 8, 180° RF pulses with an inter-echo spacing of 22ms and a similar repetition time, the SAR of Common SENSE EPI is lower.

Higher field strengths are being used increasingly for fMRI because of the greater sensitivity to BOLD contrast. Common SENSE is likely to be more useful at higher field strengths because it favours shorter echo times and reduces the effective length of the readout.

6.5.4 SENSE and Common SENSE

The application of both SENSE and Common SENSE to EPI is more beneficial at higher field strengths, because they both incur a penalty for reducing blurring and distortion. The main penalty from using these methods is the reduction in SNR of the final images by a factor of $\sqrt{2}$, for halving the effective readout duration. Additionally, there is a time penalty from performing a pre-scan for sensitivity mapping. Dynamic studies performed with EPI suffer a minimal time penalty from performing the short pre-scan required before a much longer acquisition.

Common SENSE does not need the extra hardware that SENSE requires. This means it can maintain the greater level of SNR uniformity that standard volume coils may provide. The SNR performance of Common SENSE is also independent of slice and phase encoding geometry, whereas for SENSE the fixed geometry of the coils allows for less flexibility in this respect. As discussed previously, there is an additional time penalty from the greater total acquisition length necessary for Common SENSE. This time penalty is reduced for shorter echo times. Thus, Common SENSE is most useful for fMRI at higher field strengths where shorter echo times are preferred. SENSE has been used with some success for fMRI [9,10], Common SENSE could provide similar advantages, but, with a greater flexibility in the choice of geometry and more uniform SNR performance.

When applied with parallel imaging methods, Common SENSE could allow a greater reduction in scan time. In parallel imaging the manipulation of sensitivity functions afforded by Common SENSE could be used to reduce geometry dependent noise levels and variance. With the array coil described in chapter 5, a maximum speed up factor of

2-2.5 was produced. The combination of SENSE and Common SENSE should allow the effective readout time to be reduced by double this factor. The modulation of sensitivity profiles by RF pulses has already been explored to improve k-space based parallel imaging reconstruction methods [32], Common SENSE is possibly a method to do this using standard slice selective RF pulses.

6.6 Further Related Ideas: ROCS, TRAIL and TWIST

The Common SENSE method was described previously as a pulse sequence that could improve EPI image quality, while maintaining temporal resolution and robustness to ghosting and using conventional hardware with its more uniform SNR characteristics. There are two other methods and a second mode of operation for Common SENSE that have been developed at the same time by our group to fulfil the same criteria, these are described in the following section.

6.6.1 High Frequency Mode Common SENSE and TRAIL

In the implementation of the Common SENSE method described above a low frequency, sinusoidal, spatial sensitivity profile was imposed with a of period π radians over the FoV on the images. This frequency modulation was used because it produces the best SNR performance, a result expected because at this frequency the sensitivity functions exhibit the maximal variation across the FoV without repeating. However, there are further modes of operation that should also produce optimal SNR performance; these modes are investigated in the following section.

In addition, at this frequency of modulation, the coherences (F & F^*) in figure 6.3 were nearly on top of one another. As the size of the dephasing gradient in figure 6.1 is increased, so the coherences move further apart, and the frequency of the modulation imposed on the magnetisation increases. When the function imposed on the magnetisation experiences a period over a scale of the order of a pixel (rather than over the FoV) the F & F^* coherences are nearly separate. This allows the potential for each coherence to be used individually or together to obtain more information from the same readout than might normally be available.

6.6.1.1 Theory

When a larger dephasing gradient is applied between the first two 90° RF pulses in figure 6.1 the coherences described in figure 6.3 move apart until they appear separate. When the two readouts in figure 6.1 are full length, they produce images with alternate dark and light stripes corresponding to maxima and minima of the applied modulation; with the positions of signal maxima and minima reversed between the two images. If the gradient is set to produce a $\pi/2$ linear phase shift per pixel (as shown in figure 6.6d), and the pixels are centred on the maxima and minima of the applied modulation, the stripes correspond to alternate pixels containing full signal and minimum signal.

In figure 6.12 (see section 6.6.1.3), the signal and images produced with a $\pi/2$ linear phase shift per pixel are simulated using the method described in section 6.2.4. The readouts 6.12a and 6.12b contain two distinct echoes at ¼ and ¾ of the readout duration. The image pixels contain alternately maximum and minimum signal. This is in contrast to the standard acquisition that produces a uniform image in figure 6.12c. The two striped images contain redundant information, as they have no signal in half of the image pixels. This pair of images can be acquired with some reduction in the points in k-space that are sampled, and using the redundancy in information, enable an increase in image quality or scan time as described previously.

The first way in which to reduce the distance through k-space that must be traversed is to sample only one of the two possible coherences (F or F^* as seen in figures 6.3 & 6.12) with full density. The particular coherence selected is determined by the polarity of the applied read gradient. The single coherence, sampled in each half length readout, forms a half resolution image. The underlying sinusoidal modulation of the

magnetisation, shown in figure 6.10, means that the majority of the signal has come from only one side of the half resolution pixel. In each image (obtained from readouts 1 and 2) the signal has come from the opposite side of each pixel, thus the two images can be interleaved to obtain a near full resolution image. This is TRAIL: Two Reduced Acquisitions InterLeaved [16].

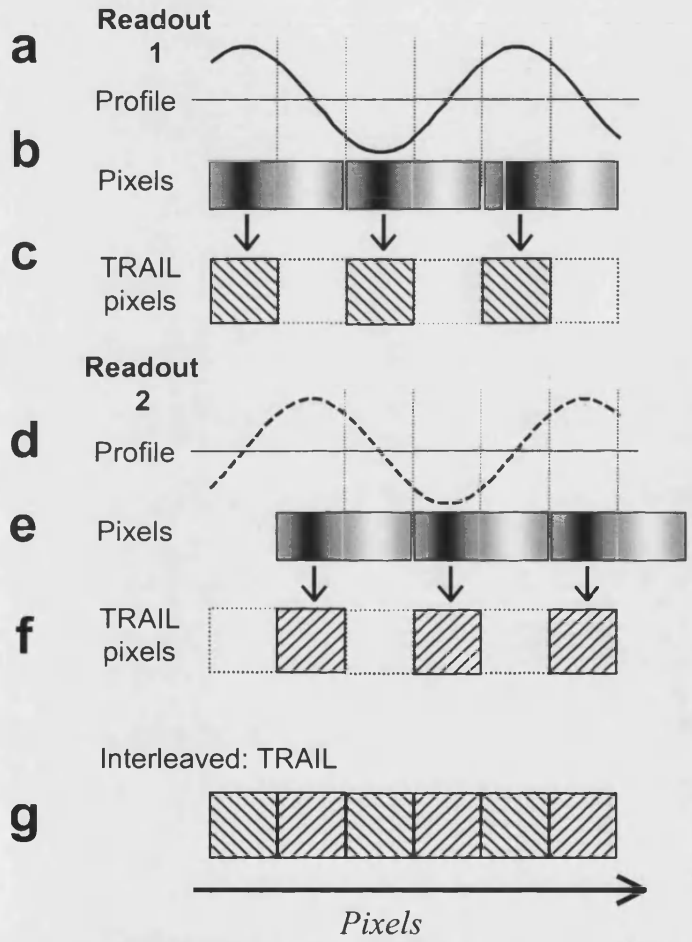

Figure is reproduced from Priest, A.N. et al A Method to Halve EPI readout times: TRAIL (Two Reduced Acquisitions InterLeaved), submitted to Magn. Reson. Med. 2003

Figure 6.10 The Principle of TRAIL
Distribution of signal relative to pixels for the readout1 'spin echo' and readout2 'stimulated echo' images acquired using the pulse sequence in figure 6.1. Each readout samples with half the desired final resolution. The readout1 image has a sinusoidal magnetisation profile (**a**) with a period of four pixels, so the magnetisation is concentrated in the left half of each pixel (**b**); the magnetisation distribution is indicated by the the shading across each 'pixel'. The signal from the right half is nulled, so the signal from the left half can be assigned to a half-sized pixel (**c**). Similarly the readout2 image has a co-sinusoidal magnetisation (**d**), also with signal concentrated in the left half of each pixel (**e**), but with the pixel positions displaced by half a pixel relative to the readout1 image. Again the signal is assigned to a half-sized pixel (**f**). Since only half each pixel contributed any net signal, the pixels of the readout1 and readout2 images can be interleaved, to give the TRAIL image (**g**).

Alternatively, both coherences may be measured with a full length readout. This forms a full resolution image with alternate dark and light stripes. The second way in which to reduce the distance through k-space that must be traversed is called high frequency mode Common SENSE, which has been termed Rapidly Oscillating Common Sense (ROCS). Here, both the coherences are sampled with a reduced density; this is in contrast to TRAIL that samples one coherence with full density. If the FoV is reduced by the correct amount and an odd number of pixels are used, the pixels containing maxima will be aliased with those containing minima, as shown in figure 6.11. This maximises the information content in each pixel. Full FoV images can be reconstructed from the reduced FoV pair of images by simply rearranging the pixels as shown in figure 6.11. For the pixels to be correctly arranged while reducing the FoV by the maximum amount possible, the FoV reduction factor R is given by

$$\mathbf{R_{max}} = \frac{\mathbf{N}}{\left(\frac{\mathbf{N-1}}{\mathbf{2}}\right)+\mathbf{1}} \qquad (6\text{-}1)$$

where R_{max}=maximum possible reduction factor, N is odd and is the number of pixels in the full FoV in the direction of the FoV reduction. When N is large (typically N=256 in a MR image) $R \approx 2$.

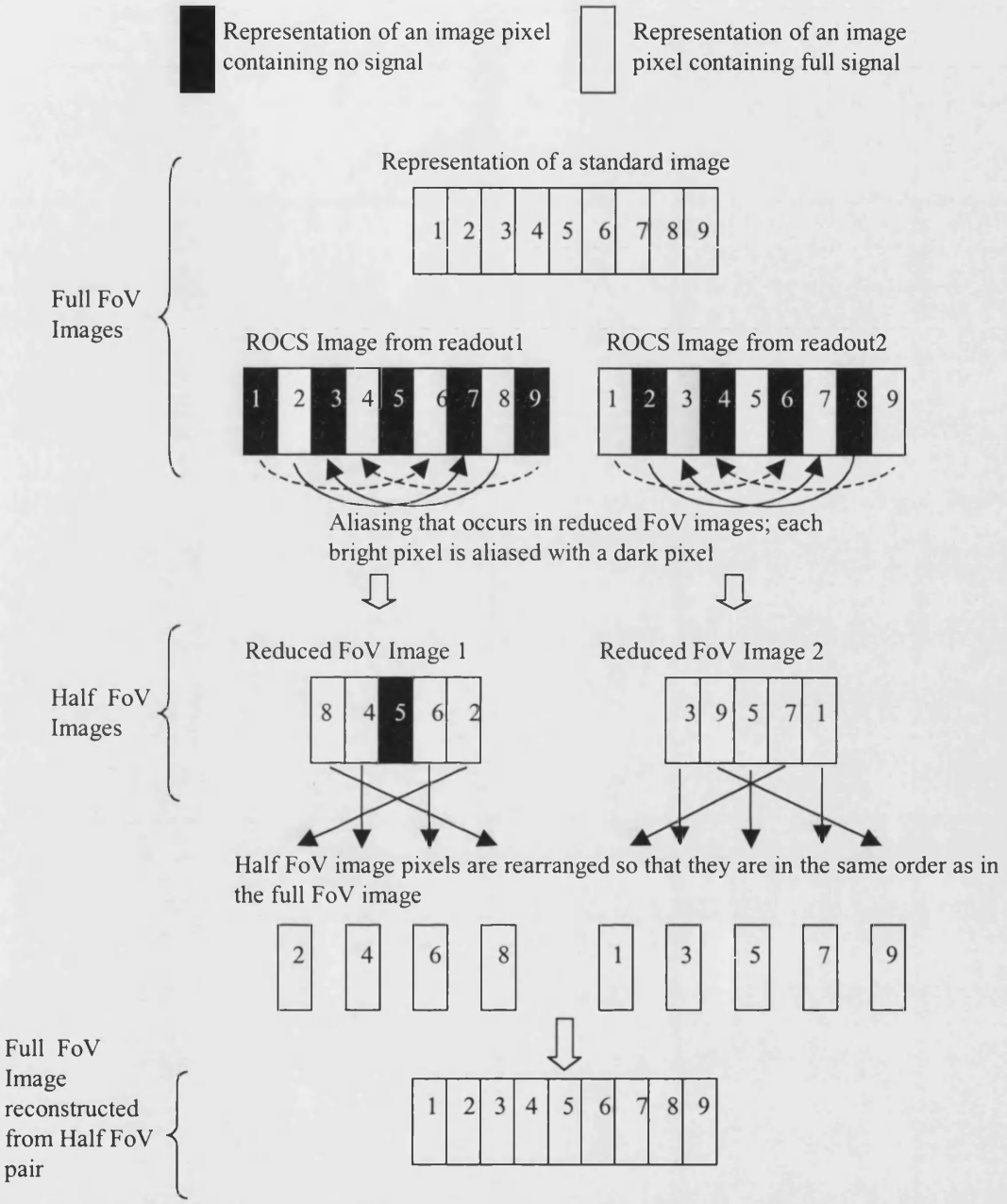

Figure 6.11 ROCS - A High frequency mode for Common SENSE and a way of performing a reconstruction without sensitivity maps
Pixels are represented by rectangles and these are put together to represent 1D images. Full and half FoV 'standard' and ROCS images are then represented using light and dark pixels. The half FoV ROCS image pixels may be rearranged to produce a full FoV image.

6.6.1.2 Methods

The sequence in figure 6.1 was simulated using the program described in section 6.2.4. The gradient applied between the first two 90° pulses was increased until there was a $\pi/2$ phase difference applied across the distance corresponding to one pixel. Full FoV images with and odd number of pixels were obtained. The pixels were aligned with the maxima and minima of the sinusoidal modulation so that the image would appear striped.

2DFT, TRAIL and ROCS images of a tomato were acquired on a 40cm bore, 2.4T, Bruker Avance spectrometer using the manufacturer's birdcage coil. Parameters were TE = 13.2 ms, TR = 3 s, FoV 9 cm, slice thickness 2 mm. TRAIL images were taken at 'full resolution', 128 × 128 pixels, 9x9 cm FoV and 'half-resolution', 128 × 64 pixels, 9x9 cm FoV. ROCS images were acquired at 'full FoV', 128×129 pixels, 9x9.07cm FoV and 'half FoV', 128×65 pixels, 9x4.57cm FoV.

6.6.1.3 Results

The simulation was run with a gradient applied to create a phase difference of $\pi/2$ across a distance corresponding to one pixel. In figure 6.12 the acquired signal is displayed on the left hand side with the 1D profile formed from the same data on the right hand side. The two full length readouts, performed consecutively with the same excitation of the magnetisation, show two separate coherences within them. The full FoV profiles can be seen to contain maxima and minima in alternate pixels. The position of the maxima and minima is reversed between the two readouts. Figure 6.12c shows the signal and 1D profile formed from a standard acquisition for comparison.

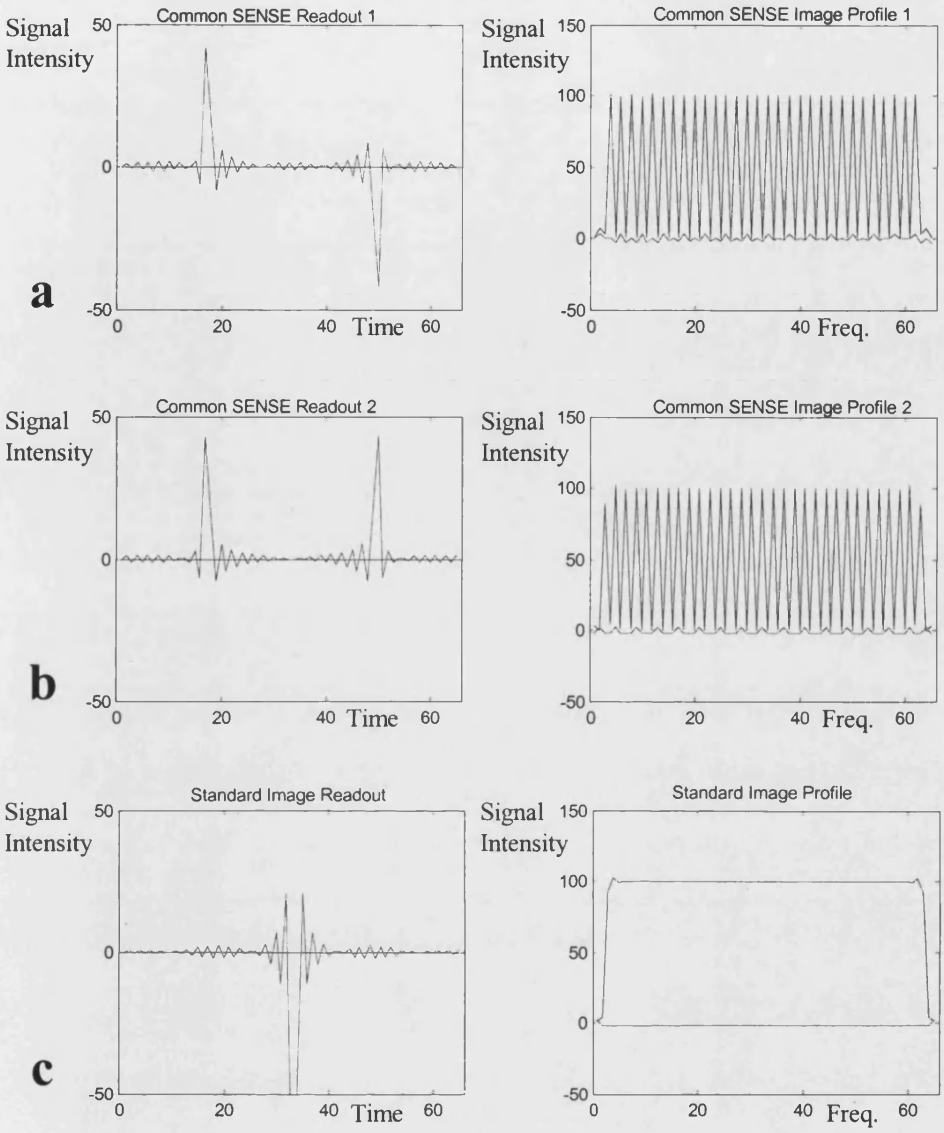

Figure 6.12 A simulation of the change in the image and time domain signal produced when a π/2 per pixel phase shift is applied between the first two 90 degree pulses in the Common SENSE pulse sequence

In figure 6.13a and b, full resolution TRAIL images (128 × 128 pixels) are shown that were obtained from full length readouts 1 and 2. In these images a striped appearance was seen due to the underlying magnetisation that has maxima and minima corresponding to the positions of alternate image pixels. In figure 6.13c and d, half resolution images (128 × 64 pixels) are shown that were obtained from half length readouts 1 and 2. In figure 6.13e the two half resolution images were interleaved to

produce a full resolution image (128 × 128 pixels). This was compared to an image obtained using a standard 2DFT acquisition and the same imaging parameters.

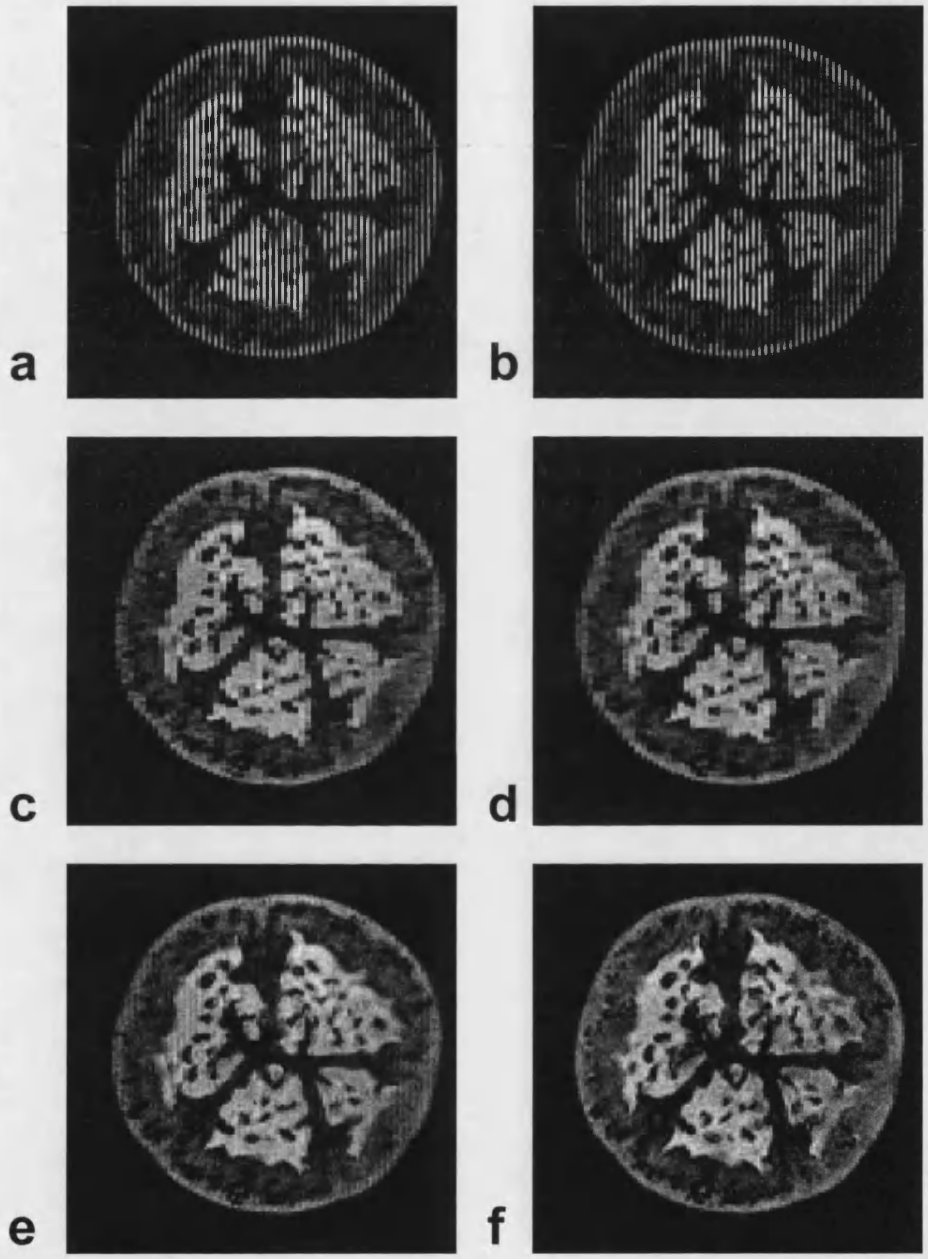

Figure 6.13 TRAIL images
Figure is reproduced from Priest, A.N. et al A Method to Halve EPI readout times: TRAIL (Two Reduced Acquisitions InterLeaved), submitted to Magn. Reson. Med. 2003. Top, figures *a* and *b*; full resolution images (128 × 128 pixels) gained from readouts 1 and 2 respectively. Middle, figures *c* and *d*; half resolution images (128 × 64 pixels) formed from readout 1 and readout 2 respectively. Bottom *e*; an interleaved image formed from *c* and *d*. For comparison, *f*, a conventional gradient echo image (128 × 128 pixels).

The TRAIL image was seen to exhibit improved resolution from the half FoV images. However, when closely compared to the standard image of full resolution there appears to be some loss in resolution. The main source of this resolution degradation is from the slight difference in intensity between spin echoes used in readout 1 and the stimulated echoes used in readout 2. This can occur when the RF pulse non-uniformity and causes a slight difference in the magnitude images. This also causes the appearance of some striping in the reconstructed TRAIL image (figure 6.13e). There is also a loss in image quality associated with the reduction in the image SNR by a factor of $\sqrt{2}$. This factor is the SNR loss in each half FoV image associated with reducing the number of sampled points by a factor of 2. Some differences between the TRAIL and standard image could be the result of a difference in slice profile. This is because the application of repeated RF pulses of the same bandwidth results in the excitation of a different slice profile than a single RF pulse would excite.

Full resolution ROCS images (9×9.07cm FoV, 128x129 matrix) obtained from full length readouts 1 and 2, are shown in figure 6.14a and b. In these images the expected striped appearance is seen. This was due to the underlying magnetisation that has maxima and minima corresponding to the positions of alternate image pixels. In figure 6.14c and d, half FoV images (9×4.5cm FoV, 128x65 matrix) are shown that were obtained from half length readouts 1 and 2. The reduction in FoV was calculated using equation 6-1. Sensitivity maps formed from the full resolution images are displayed in 6.14e & f. The bottom four images compare full FoV ROCS images (reconstructed in different ways from the half resolution images 6.14c & d) with a reference image.

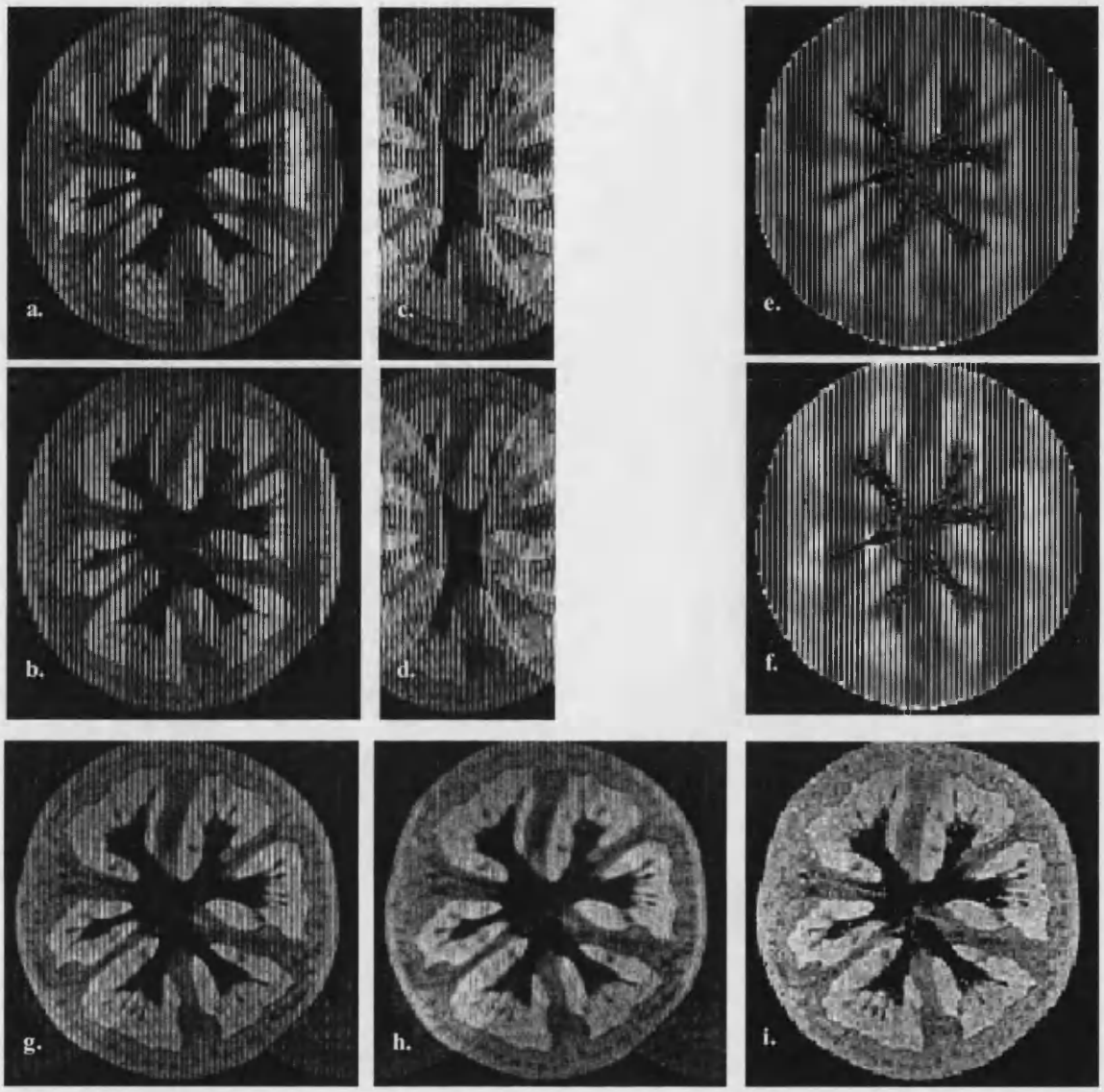

Figure 6.14 ROCS images
From the top left, *a* & *b*; full resolution ROCS images formed from readouts 1 and 2 respectively. Top middle, *c* & *d*; half resolution images formed from readouts 1 and 2 respectively. Top right, *e* & *f*; Sensitivity maps formed from the full resolution images *a* & *b*. The bottom four images *(g-i)* are full FoV ROCS images reconstructed from the half resolution images (*c* & *d*). Figure *g*, shows the simplest reconstruction of the data (illustrated in figure 6.11) where the pixels in *c* & *d* are simply re-arranged. Figure *h*, shows the same reconstruction with two extra corrections that do not require a pre-scan. Figure *i*, shows a SENSE reconstruction of the half FoV data using sensitivity maps (*e* & *f*). Figure *j*, shows reference image gained from a standard acquisition.

In figure 6.14g, the simplest reconstruction of the two half resolution images was performed by simply rearranging the pixel positions (as described in figure 6.11), to produce a full resolution image. This image (6.14g) contains a stripe artefact due to mismatches in signal intensity between images formed from readout 1 and readout 2. To reduce this problem the half FoV images were normalised to have the same mean value. In addition, there is some ghosting both inside and outside the image. This aliased signal is due to a non-perfect sinusoidal modulation imposed on the magnetisation. In the images this will produce maxima and minima that are not equal to 1 and 0 respectively in alternate pixels. The imperfections in the sinusoidal modulation are caused by a variation in flip angle away from the 'perfect' 90° pulses seen in figure 6.1. The incorrect flip angle is manifested as signal that has not seen the first 90° pulse, or, that has not seen the second 90° pulse. In the phase graph (see figure 6.3) either of these eventualities can be seen to produce a third state of transverse magnetisation that will lie between the F and F^* states shown.

The signal produced in the middle of the readout can be removed by filtering the data in the time domain. Here, a Hannig filter was applied to k-space data before it was reconstructed to form half FoV images. The filtered images were then normalised to have approximately the same sensitivity to signal. This was achieved by making mean (magnitude) pixel intensity consistent between the two images formed from each readout. A reconstruction was then performed by simply rearranging the pixel positions (as described in figure 6.11) to produce the full FoV image in figure 6.14h. This image has been obtained without the need for a prescan thus reducing the experiment time by a factor of 2.

There is some residual artefact in image 6.14h, even after the filtering and normalising corrections have been applied. All of these errors can be more accurately corrected by using a prescan that has also been applied to TRAIL images, described in detail in reference [17]. Briefly, by acquiring two pairs of images with the phase of the $90°_2$ RF pulse offset by $\pi/2$ radians between acquisitions, the maxima and minima of the applied modulation are reversed (a $\pi/4$ change to the same pulse is shown in figure 6.6a-b). The difference in the images obtained in readouts 1 and 2 (in separate acquisitions) with the same magnetisation modulation produces a correction for the intensity of each pixel. A further correction is obtained to remove the extra coherence present from RF inhomogeneity that lies in the centre of the readout (i.e. between the echoes seen in figure 6.12a & b). By acquiring images with the phase of the $90°_2$ RF pulse offset by π radians between acquisitions, the phase of the unwanted coherence is reversed. The two complex data sets may be combined to create an image free of this artefact. A correction can be made to all subsequent images by comparing the difference between the original image containing the artefact and the corrected image from the combined data.

An alternative is to use the full FoV ROCS images (6.14a & b) to generate sensitivity maps. A SENSE reconstruction of the half FoV data (6.14c & d) was performed using sensitivity maps (6.14e & f) to obtain the full FoV image (6.14i). This image exhibits a much lower artefact level and a closer resemblance to the reference image than the other reconstructed images. However, the SENSE reconstruction of the data does appear to further degrade the SNR of the final image.

6.6.1.4 Discussion

Both TRAIL and ROCS were used to reduce the effective scan time by half for 2DFT images, and can be used to reduce the effective readout time in EPI by half. Also, both methods used two half length readouts to form a pair of images that were combined to obtain a single full image. The reduction in SNR associated with this process is $\sqrt{2}$, due to the reduction in the number of sampled points in each readout by a factor of 2. More work is needed to discover if ROCS can be used effectively to obtain spin echo 2DFT images in half the time without pre-scanning.

For the simple implementation of TRAIL and ROCS described, it was important that the maxima and minima of the spatial modulation imposed on the magnetisation were aligned with the pixels correctly. The application of a linear phase shift in k-space can be used to move the positions of the pixels relative to the magnetisation for correct alignment. It was also important that the modulation was near to the ideal sinusoidal and cosinusoidal functions that should be produced by the Common SENSE pulse sequence. Inconsistencies in the imposed modulation caused image artefacts in the reconstruction. In ROCS, the artefact is produced by aliased signal from a different spatial position that causes a Nyquist ghost in the image. In TRAIL the artefact amounts to a blurring of the information from the two sides of a pixel leading to a reduction in the true resolution of the images.

A further problem can arise due to signal intensity differences between the first and second readouts, which leads to a stripe artefact in the final image. A number of corrections have been successfully applied to TRAIL images to reduce these problems [17,33,34]. However, when these corrections entail a prescan, the time saving for 2DFT

imaging from reduced phase encode k-space sampling is diminished. The corrections that have been applied to TRAIL could also be applied to ROCS, however, all the image artefacts in the ROCS images can be corrected by reassigning the aliased signal using a SENSE-type strategy. Sensitivity maps can be obtained from full FoV images and SENSE reconstruction performed on the half FoV data, as shown in figure 6.14. This appears to entail a reduction in the SNR of the ROCS image suggesting the correction methods outlined in the previous section may be the best approach.

The rest of the discussion is focused on the application of TRAIL and ROCS to EPI. TRAIL and ROCS can be used with EPI readouts to improve the level of blurring in the images. This is due to the shorter acquisition window that reduces filtering effect of T_2* relaxation over the length of the readout. It should be noted that both TRAIL and ROCS maintain the point spread function of an equivalent 'standard' image. For the implementation of TRAIL described here, there is no improvement in the level of distortion in the phase encoding direction because the phase encoding bandwidth is not increased by acquiring a half resolution image. ROCS exhibits the same improvement in distortion as the low frequency Common SENSE method described previously. The full resolution acquisitions (like those in figures 6.13a & b and 6.14a & b) can be used to correct for distortion and provide an effective correction for amplitude mismatches between the two readouts and RF non-uniformity in both TRAIL [17,33] and ROCS. Alternatively, the full resolution acquisitions can provide sensitivity maps for ROCS in the event of signal being aliased due to the imposition of a non-ideal sinusoidal sensitivity function. A SENSE reconstruction may be used with the sensitivity maps to assign the signal to its correct spatial position, at some cost in SNR that will depend on the level of aliasing (i.e. how far the sensitivity functions are from being ideal).

When methods are used for acquiring a time series of EPI images, a pre-scan is easily accommodated. In this case, the intrinsic reduction in distortion and blurring provided by Common SENSE is an advantage over TRAIL. Motion or distortion may cause differences between the reference data, obtained for sensitivity mapping or for correcting the data, and the reduced FoV images to be reconstructed. A slow variation in the sensitivity functions will mean that any movement over the scale of a few pixels will not result in the use of inappropriate sensitivity values. However, because the sensitivity function imposed in ROCS and TRAIL is a function of spatial position, and is independent of the position of the object within the FoV, these methods should also be reasonably tolerant to patient motion. The same considerations must be applied to TRAIL and ROCS that were discussed for Common SENSE, both for the total acquisition length and the SAR (see section 6.5.3 and figure 6.9).

It is possible to use the two coherences produced using full FoV TRAIL and ROCS to correct for distortion on a shot-by-shot basis because they provide two images at different TE times. If it were possible to extract this information from reduced FoV ROCS acquisitions it would provide a distinct advantage over the low frequency Common SENSE variant. It is likely that Common SENSE can readily be combined with SMASH or SENSE to provide a higher speed up factor without a prohibitively high reduction in SNR. The flexibility to produce the optimal frequency sensitivity function for the a given FoV and degree of speed up makes Common SENSE appear a strong method for reducing the effective readout time for the GE-EPI.

6.6.2 TWIST (Tilted Wedge Inclined Slice Technique)

TWIST (Tilted Wedge based on Inclined Slices Technique) is another method that allows the production of full resolution images from pairs of images acquired with half the number of phase encoding steps and conventional hardware. TWIST differs from TRAIL and Common SENSE in that it does not use separate sinusoidal components of magnetisation to create spatial sensitivity profiles. Instead, TWIST uses the excitation of overlapping slices to gain images of the same slice but with different spatially varying 'sensitivity profiles'. As with Common SENSE, TWIST images can be combined using reconstruction methods based on those used in SENSE. This allows the production of a full Field of View (FoV) image with uniform sensitivity from two half FoV images. In this section TWIST is explored as another technique that may be employed to reduce the effective readout time for GE-EPI to improve image quality.

6.6.2.1 Theory

The basic principle behind TWIST is to selectively excite slices with wedge-shaped profiles of magnetisation. The acquisition of each conventional rectangular slice is replaced with the acquisition of two separate wedge shaped slices. If the conventional slice has a near uniform spin density through the slice plane, the wedge shaped slice profile will be a good approximation to the conventional rectangular slice modulated by a sensitivity profile.

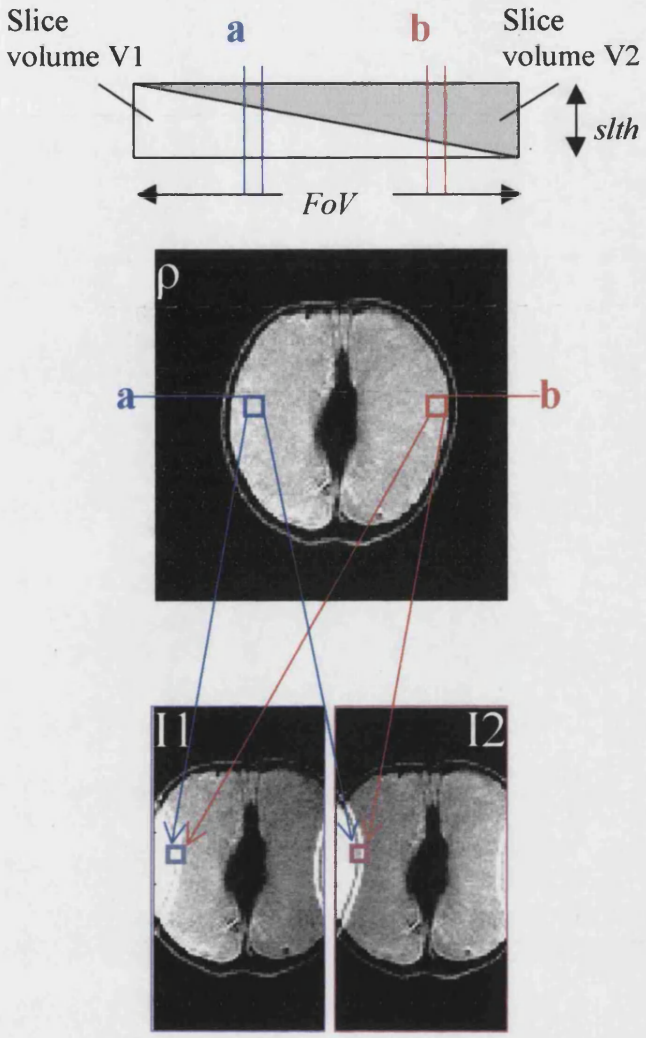

Figure 6.15 The principle of TWIST
Two different triangular volumes of a standard slice are exciting in rapid succession. When images are taken with a reduced FoV the signal in each image, I1 and I2, is a product of the slice volume excited, V1 and V2, and the spin density ρ within that volume. If the spin density through the slice is uniform the slice volumes may be used as sensitivity profiles to separate aliased signals such as those from positions a and b.

A slice of an object with a spin density distribution of ρ is imaged, as shown in figure 6.15, with triangular slice volumes *V1* and *V2* each excited in turn. If the images *I1* and *I2* are taken with a reduced FoV, such that positions *a* and *b* across the FoV are aliased, then the equations for the signal in the highlighted pixels of *I1* and *I2* are

$$\begin{aligned} \mathbf{I1} &= \rho_{a1} \cdot \mathbf{V}_{a1} + \rho_{b1} \cdot \mathbf{V}_{b1} \\ \mathbf{I2} &= \rho_{a2} \cdot \mathbf{V}_{a2} + \rho_{b2} \cdot \mathbf{V}_{b2} \end{aligned} \qquad (6\text{-}1)$$

Where ρ is the spin density and V is the volume, both counted over the positions a and b and slice excitations *1* and *2*. The excited volumes can be estimated as triangles with one side equal to the *FoV* and the other the slice thickness *slth*. Alternatively, the profiles can be measured by taking full FoV wedge images and dividing by a standard slice; this removes the spin density ρ to leave values of V. The two equations 6-1 contain 4 unknown values of ρ. However, if we assume that the slice has a uniform spin density through its *slth* then

$$\rho_{a1} \approx \rho_{a2} \approx \rho_a \quad , \quad \rho_{b1} \approx \rho_{b2} \approx \rho_b \qquad (6\text{-}2)$$

Substituting this into equation (6-1) gives a set of equations that can be solved for ρ.

$$\begin{aligned} \mathbf{I1} &= \rho_a \cdot \mathbf{V}_{a1} + \rho_b \cdot \mathbf{V}_{b1} \\ \mathbf{I2} &= \rho_a \cdot \mathbf{V}_{a2} + \rho_b \cdot \mathbf{V}_{b2} \end{aligned} \qquad (6\text{-}3)$$

These can be compared with equation 2-37 in chapter 2 (section 2.7) for SENSE; the difference is the substitution of sensitivity profiles for slice volumes. As with SENSE, if the spatial sensitivity functions (or spatial slice volumes) are known, aliasing can be removed effectively from reduced FoV images. SENSE samples all the magnetisation with a varying sensitivity; TWIST samples a varying fraction of the spins. Hence, for TWIST to work effectively equation 6-2 must be a reasonable assumption: the spin density through the slice must be reasonably uniform.

The excitation of the triangular profiles is achieved by an appropriate combination of gradients and RF pulses, as illustrated in figure 6.16. Consecutive slices are separated by half the slice thickness (*slth*) and are acquired alternately along the conventional slice-select direction (slices 0, 2, 4,...) and tilted by an angle θ along the phase encoding (*pe*) direction. (slices 1,3,5,..., where $\theta = atan\ [slth/FoV]$). Due to the

overlapping of successive excitation profiles, partial saturation of signal from each slice occurs, resulting in the excitation of wedge-shaped slice profiles. In this way, signal intensity is linearly modulated across the FoV with the gradient of the applied modulation reversed between odd and even wedge slices (e.g. excited profile of slices 1 and 2). With ideal saturation, adding the complementary signals obtained at full FoV from a pair of slices (e.g. slices 1 and 2) produces a sum of wedges (SoW) image equivalent to a 'conventional' acquisition (a parallel slice with a rectangular slice profile of thickness *slth*).

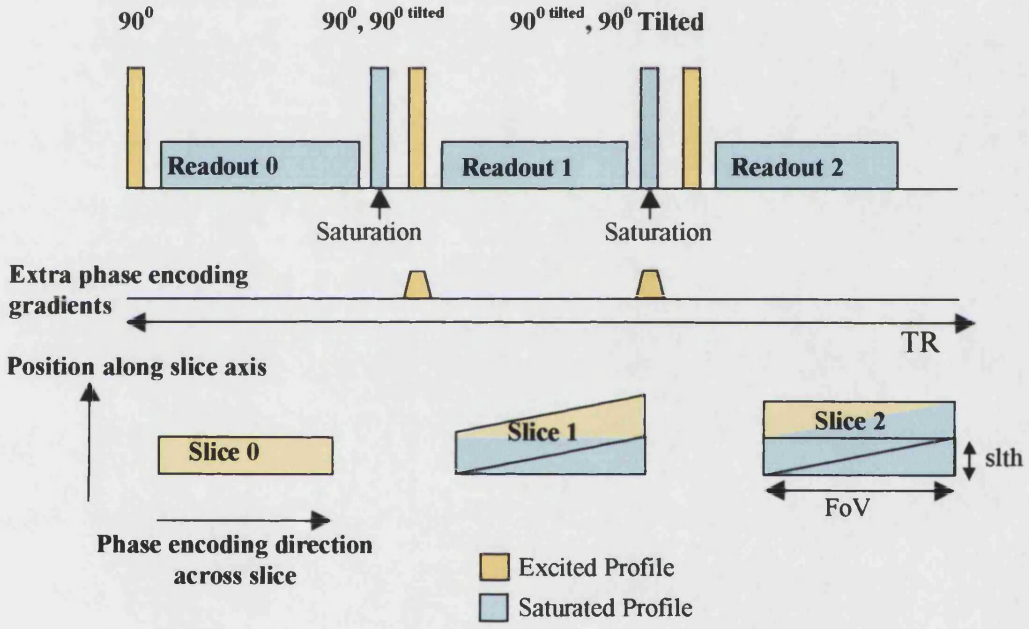

Figure 6.16 The TWIST Pulse Sequence
In TWIST slices are alternately excited with a conventional slice profile and a tilted slice profile. The tilted slices have an offset of a slice thickness in the phase encoding direction. This is achieved via the application of an extra gradient in the phase encoding direction. After each RF pulse and readout the slice just acquired is saturated with an additional RF pulse. This means from slice 1 onwards wedge shaped profiles are excited in rapid succession.

6.6.2.2 Methods

All experiments were performed on a SMIS MR5000, 4.7 T / 90cm system supported by Philips Medical Systems with a transmit / receive head birdcage coil and a head gradient set (Magnex, UK). Both 2DFT and EPI images were obtained.

For both the 2DFT-TWIST and the EPI-TWIST sequences that were implemented, an extra (sinc) 90° pulse similar to that used for imaging was applied in combination with spoiler gradients just before the excitation of the subsequent slice to improve saturation. Maps of the sensitivity profiles imposed by the TWIST pulse sequence were generated using full FoV TWIST images and a reference image. The sum of the two full FoV TWIST images gave a reference image with approximately uniform sensitivity without the need for a separate acquisition. The sensitivity maps could be processed to remove noise by smoothing as described in chapter 5, section 5.2.3.

2DFT images of a tomato were obtained using the following parameters TR / TE / flip-angle=1.5s / 27ms / 90°, slice thickness=3mm. Full FoV TWIST images (10x10cm, 256x96 matrix and 15nex) and half FoV TWIST images (10x5cm, 256x48 matrix and 30nex) were acquired. A full FoV standard 2DFT image was also acquired using the same parameters (10x10cm, 256x96 matrix and 15nex). Two approaches were used to obtain sensitivity maps. Firstly, full FoV images were used to obtain measured sensitivity profiles by dividing the full FoV TWIST images by the SoW. Alternatively, the need for preliminary scans was avoided by assuming an ideal sensitivity profile (a linear variation from 0 to 1 (odd slices) and 1 to 0 (even slices) across the full FoV). The reconstruction methods used in SENSE were applied to the pairs of half FoV TWIST images (using the sensitivity maps) to yield an unaliased full FoV image.

The GE-EPI sequence featured blipped phase encoding gradients with sinusoidal readout gradients [6]. The k-space data was re-gridded to a uniform 64x64 Cartesian matrix before being Fourier transformed to produce an image. Acquisitions performed with read gradients of opposite polarity were used to eliminate ghosting from non-perfect read gradient refocusing and B_0 inhomogeneity [27,28]. To ensure the sensitivity maps contain the same level of distortion as the half FoV images a two shot interleaved sequence was used. This method provides the same signal bandwidth per point along the phase encoding direction. Half FoV TWIST images were then acquired in a single-shot. Full FoV (speed up factor R=2) images were reconstructed from the half FoV images, using sensitivity maps as previously described. A volunteer's head was imaged using the following parameters Tr / Te=3.5s / 20ms, FoV=20cm, 4mm slice thickness, for a 64x64 matrix full FoV image the full-length readout duration was 26ms.

The theoretical SNR of TWIST was investigated using programs written in MatLab. Ideal wedge shaped profiles were used as input sensitivity functions. The ideal wedge shaped profiles were functions varying linearly from zero to one, and one to zero respectively, across the FoV. The SNR was calculated in the same way as described in chapter 5 section 5.2.5 using equation 2-40 restated here

$$\mathbf{SNR_R} = \frac{\mathbf{SNR_{full}}}{\sqrt{\mathbf{R}} \times \mathbf{g}} \qquad (6\text{-}4)$$

N.B. TWIST images will be referred to as having a 'speed up factor R'. This is not exactly the same as the R described for SENSE. The SENSE R gives a reduction in the overall time taken to obtain the image data from sampling k-space with reduced density. For TWIST R describes the reduction in sampling density in k-space though this does not correspond to a reduction in the overall time taken to obtain the image data.

To briefly recap, there are three factors taken into consideration to determine the SNR of TWIST using half FoV images (R=2). The first factor is the SNR performance of optimally combining full FoV TWIST images, given by SNR_{full} (this was the 'basic SNR' of the coil array in chapter 5), as compared to the SNR performance of a 'standard' image acquisition. When the full FoV TWIST images are reconstructed using the SENSE algorithm they produce an image with the same signal as a standard image (i.e. the signal is scaled to a factor of one). From chapter 5, the SNR_{full} was estimated from the sensitivity maps S at a position r using the following expression from references [8,35]

$$\mathbf{SNR}_{full}(\mathbf{r}) \propto \frac{1}{\mathbf{Noise}_{full}} = \sqrt{\left(\mathbf{S(r)}^{H}\boldsymbol{\Psi}^{-1}\mathbf{S(r)}\right)} \qquad (6\text{-}5)$$

H denotes the transposed complex conjugate of a matrix. Ψ is the receiver noise matrix that contains the level and correlation of noise between images used in the reconstruction. The level of noise in the full FoV TWIST images is uniform with spatial position. Additionally, the noise is not correlated between images acquired in consecutive readouts. This means Ψ is equal to unity hence

$$\mathbf{SNR}_{full} = \left(\mathbf{SS}^{H}\right)^{1/2} \qquad (6\text{-}6)$$

For full FoV TWIST images $\mathbf{S} = (\mathbf{V1} \quad \mathbf{V2})$

$$\mathbf{SNR}_{full} = \sqrt{\mathbf{V1}^2 + \mathbf{V2}^2} \qquad (6\text{-}7)$$

The above equation demonstrates how the noise is summed in an optimally weighted combination of the images. The noise in the combined image is equal to the square root of the sum of squares of the sensitivity weightings of the two TWIST images at a given position. The signal is made to be at the same level so the signal SNR_{full} is also equal to this expression.

The second factor to consider is the geometry factor g, at a pixel x, where S is the sensitivity matrix for given reduction factor. g is calculated using equation 5-7 again from reference [8], which with Ψ equal to unity is

$$\mathbf{g}_x = \sqrt{\left(\mathbf{S}^H\mathbf{S}\right)^{-1}_{x,x}\left(\mathbf{S}^H\mathbf{S}\right)_{x,x}} \qquad (6\text{-}8)$$

The third factor is simply the SNR cost of sampling k-space less densely that is given by the square root of the reduction factor R.

6.6.2.3 Imaging Results

Figure 6.17 shows 2DFT TWIST images. Half FoV images (6.17a & 6.17b seen at the top of figure 6.17) were obtained from the two consecutive half duration readouts, with each readout performed using a different wedge shaped profile of magnetisation. On the left-hand side the measured sensitivity maps (6.17c & 6.17d) are shown, these were generated from full FoV TWIST images and a SoW reference image. A full FoV image (6.17e, below the sensitivity maps) is displayed, which was reconstructed using the sensitivity maps shown. On the right-hand side the estimated triangular profiles (6.17f & 6.17g) are seen under the half FoV images. A full FoV image (6.17h) was reconstructed using the triangular profiles shown. Both of the full FoV reconstructed images are compared to a full FoV reference image (6.17h).

	Acquisition	Further Details / Figure	Time (a.u.)
2DFT	Half FoV TWIST acquisition	Figure 6.17a & b, SENSE reco. from these in figures 6.17e & h	1 unit of time
	Full FoV TWIST acquisition	Not shown, used to make maps in figures 6.17c & d	2 units of time
	Standard acquisition	Figure6.17i	2 units of time
EPI	Full FoV 'standard' acquisition	1-shot, BW_{pe}=1a.u. figure 6.18c	1 unit of time
	Full FoV 'standard' segmented acquisition	2-shot 2-segment, BW_{pe}=2a.u. figure 6.18d	2 units of time
	Full FoV segmented TWIST acquisition	2-shot 2-segment, BW_{pe}=2a.u figure 6.18a	2 units of time
	Half FoV TWIST acquisition	1-shot, BW_{pe}=2a.u figure 6.18b	1 unit of time

Table 6.2 A summary of the TWIST image acquisitions

The reconstructed 2DFT TWIST images show a reasonable correspondence with the reference image in figure 6.17. The TWIST image reconstructed without measured sensitivity maps (6.17e) shows a low level of ghosting within the image and in the background. This demonstrates that the estimated functions were able to separate the aliased signal with reasonable efficiency. There are several sources of error in the estimation of the wedge shaped profiles. Firstly, the slice profiles selected are unlikely to be perfectly rectangular, thus the wedges formed will also have a non-perfect triangular wedge shape. Secondly, any non-uniform spin density across the thickness of each slice will cause an additional, local deviation from the ideal triangular shaped function. The TWIST image that was reconstructed using the measured sensitivity maps (figure 6.17h) shows little ghosting within the image, demonstrating that the sensitivity maps can correct for most of these errors. If the sensitivity maps are smoothed or fitted, then any local sensitivity changes from the non-uniform spin density across the slice thickness is likely to be removed and an error will remain in the reconstructed image.

Half FoV images

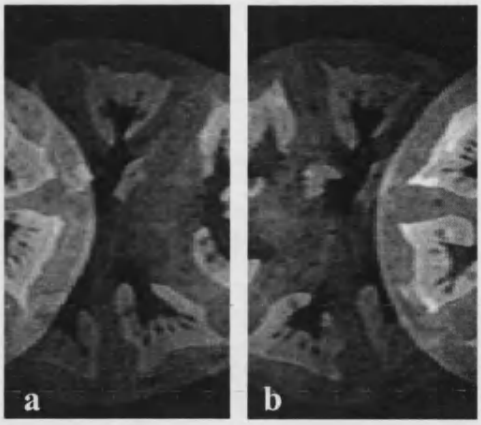

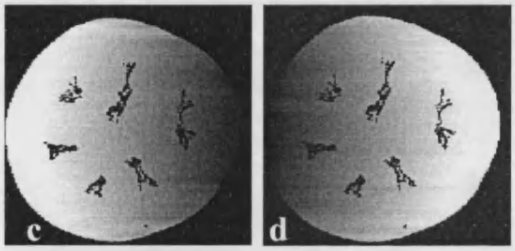

Measured TWIST Sensitivity Maps over the full FoV , used with a & b to make image e below

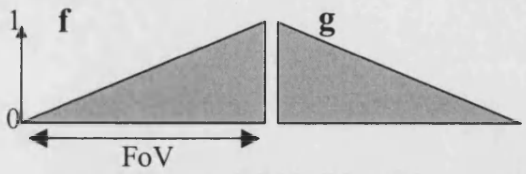

Estimated TWIST functions, used with a & b to make image h below

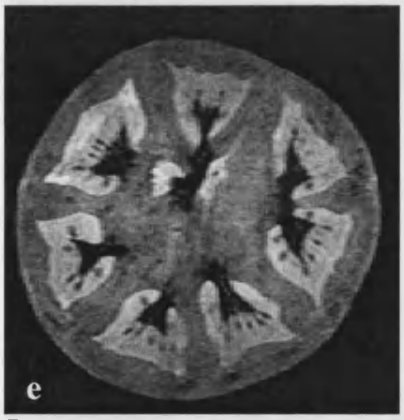

Reconstruction using estimated functions above and half FoV images

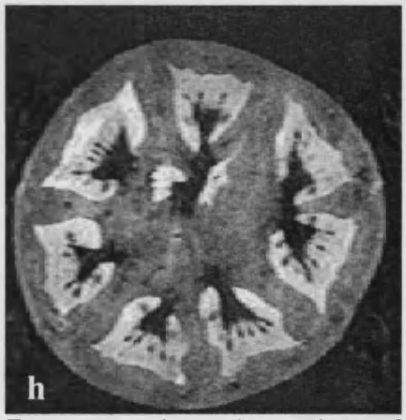

Reconstruction using estimated functions above and half FoV images

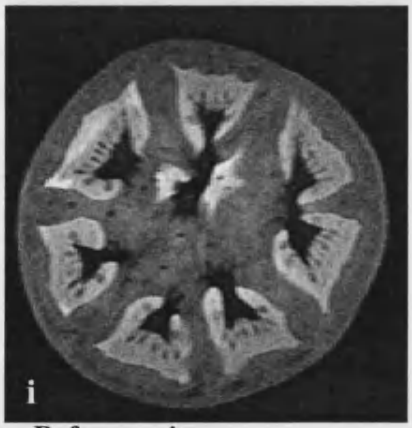

Reference image

Figure 6.17 TWIST 2DFT Images
Half FoV images (*a* & *b*) were obtained from the two consecutive readouts in TWIST, with each readout exciting a different wedge shaped profile. On the left hand side are the sensitivity maps (*c* & *d*) created from Full FoV TWIST images (not shown). These maps (*c* & *d*) are used to reconstruct a full FoV image (*e*). On the right hand the estimated profiles (*f* & *g*) are used to reconstruct a full FoV image (*h*). The full FoV reconstructed images (*e* & *h*) can be compared to a full FoV reference image bottom left. See table 6.2 for a summary of the details.

In figure 6.18, a TWIST-EPI image formed from a pair of half FoV images is compared to a Sum of Wedges (SoW) image (6.18b, obtained by summing a pair of full FoV TWIST-EPI images), a standard single-shot image (6.18c) and a two shot interleaved image (6.18d). The full FoV TWIST image (6.18a) closely matches the reference (6.18b) with no visible signs of Nyquist ghosting. The TWIST-EPI image also exhibits the same reduction in distortion and blurring as the two shot, interleaved image while maintaining the temporal resolution of the single-shot image. In addition, the TWIST image dropout is reduced in the temporal regions as well as in the vicinity of the frontal sinuses.

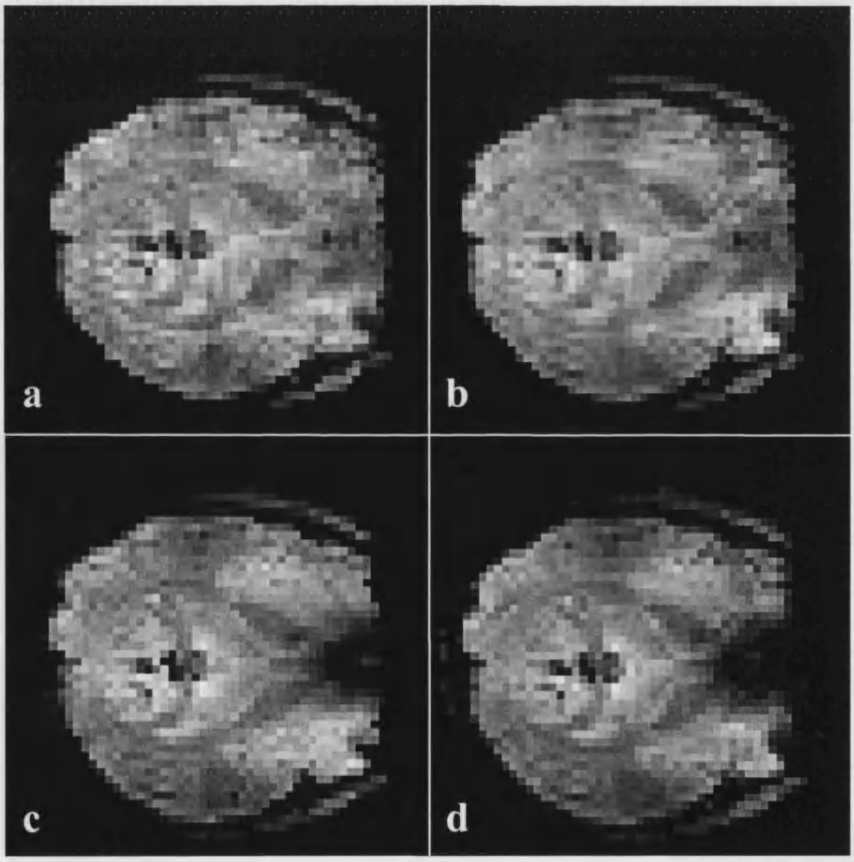

Figure 6.18 TWIST EPI images
A TWIST image formed from a pair of half FoV images is compared to a summed pair of full FoV TWIST images (b), a standard single shot image (c) and two shot interleaved image (d).

6.6.2.4 SNR Simulation Results

The SNR performance of a full FoV image, produced for the combination of half FoV TWIST images, is investigated in figure 6.19. The SNR of the TWIST image was scaled relative to the SNR of a standard image so that the standard image had a nominal uniform SNR of 1 across the FoV. The SNR of an optimum combination of the full FoV TWIST images (SNR_{full}) was not uniform, but varied from 1 at the edges of FoV to $1/\sqrt{2}$ in the centre. This is because in the centre of the FoV the sum of the signal has the same level as a standard image; however, the sum of the noise in the images is $\sqrt{2}$ greater.

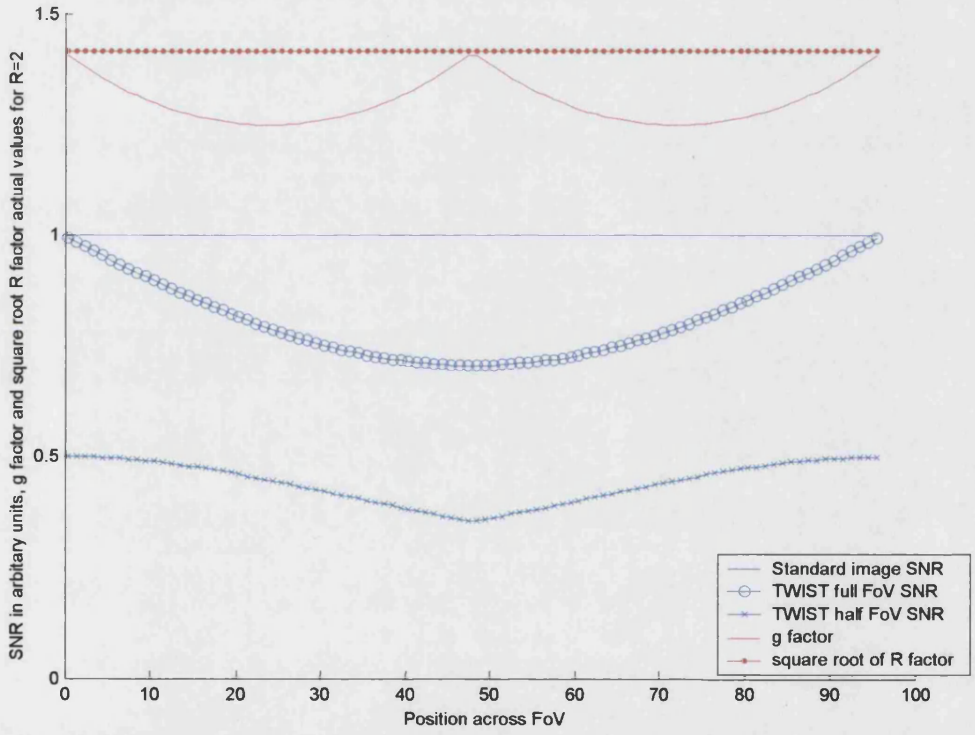

Figure 6.19 The SNR performance of TWIST
TWIST obtains a pair of images with wedge shaped sensitivity profiles. The SNR produced is investigated for the combination of both full FoV TWIST and half FoV TWIST images relative to the SNR of a standard image. The combination performed is a SENSE reconstruction for R=1 (full FoV) and R=2 (half FoV). All the factors that determine the overall reduction in SNR for reconstructing half FoV TWIST images are shown. These factors are the full FoV performance of TWIST, the g-factor that gives the noise amplification due to separating the aliased signals with the 'ideal' triangular TWIST functions and the reduction in SNR ($2^{0.5}$) due to reduced sampling (of R=2).

The SNR of a half FoV TWIST image combination ($SNR_{R=2}$) was governed by the factors described in the previous section. All the factors that determine the reduction in SNR when reconstructing half FoV TWIST images are shown in figure 6.19. These factors are the full FoV performance of TWIST (SNR_{full}), the g-factor that gives the noise amplification due to separating the aliased signals with the wedge shaped functions and the reduction in SNR due to reduced k-space sampling of $\sqrt{R}$. The triangular wedge functions have a significant g-factor that varies from $\sqrt{2}$ to around 1.25 with position across the FoV. The combination of this with the SNR_{full} and the $\sqrt{2}$ reduction factor leads to an SNR performance of between 1/2 to $1/2\sqrt{2}$ with the greatest reduction in the centre of the FoV compared to a 'standard' acquisition.

6.6.2.5 Discussion & Conclusion

The TWIST technique has been successfully tested on phantoms and healthy human volunteers with 2DFT and EPI methods. It can be readily used on any scanner as it only requires conventional hardware. In its simplest implementation, TWIST involves setting a separation between subsequent slices equal to half the slice thickness and tilting every other slice. TWIST can be applied to any multi-slice pulse sequence.

The value of TWIST may ultimately be limited by its SNR performance that is a factor of between 2 and $2\sqrt{2}$ worse than a standard image acquisition and is dependant on position with in the FoV. The SNR was estimated using ideal wedge shaped functions. The actual TWIST functions used will not be ideal wedges due to non-uniform slice excitation. There is also a phase component in the images that may not be consistent between each readout due to the excitation of different regions of magnetisation. Both of these factors may serve to improve the g-factor of the actual sensitivity functions

imposed by TWIST, helping to maintain the SNR at more acceptable level. Similar considerations must be made for TWIST, as discussed for Common SENSE, with regard to the total acquisition length and SAR (see section 6.5.3 and figure 6.9). The TWIST implementation described here fell within SAR limits, though by removing the extra saturation RF pulses in figure 6.16, SAR can be reduced further.

TWIST images have one additional problem to be overcome for correct image reconstruction in the presence of a non-uniform through-slice spin density. There are two choices:

i) The 'sensitivity' may be mapped by image division and local 'sensitivity' variations caused by a non-uniform spin density remain. This results in correct image reconstruction, at the expense of being able to process the TWIST sensitivity maps to remove noise. Hence, very high SNR images are required to produce maps that avoid incurring an additional SNR penalty from propagating additional noise into the final images. Furthermore, if the sensitivity maps do contain local variations due to local spin density non-uniformity, some sensitivity to subject motion is introduced. This is because any movement of the subject could significantly change the 'sensitivity' information.

ii) The 'sensitivity' maps produced do not take into account local variations in spin density non-uniformity and so do not completely remove aliasing in the reconstructed image. This will result in a systematic image artefact.

TWIST reduces the distortions introduced by magnetic susceptibility gradients in the slice volume; blurring is also reduced due to a smaller level of signal decay during the readout. This is achieved by acquiring pairs of half FoV images, to halve the effective

readout time while doubling the phase encoding bandwidth. In addition, through-slice image dropout is also reduced because of the smaller local effective slice thickness in the individual, wedge-shaped, half FoV images. This may make TWIST a useful sequence to employ for GE-EPI where brain regions of interest suffer from high levels of dropout such as the temporal lobes and frontal sinuses. However, SENSE can be used in the slice plane [36] to obtain twice as many slices in the same time period. This would allow slices to be obtained with half the slice thickness resulting in a similar improvement in levels of dropout as are provided by TWIST. The cost in SNR for SENSE in the slice plane is likely to be lower than for TWIST even for axial slices where the geometry of the head and neck may not allow ideal placement of array coil elements. With only a simple alteration of the GE-EPI pulse sequence TWIST can provide improvements in distortion, blurring *and* dropout making it a useful addition to existing methods that can provide some of these advantages.

6.6.3 Conclusions to 'Further Ideas' Section

TRAIL, ROCS and TWIST were used to reduce the effective scan time by half for 2DFT images, and can be used to reduce the effective readout time in EPI by half. Also, all these methods used two half length readouts to form a pair of images that were combined to obtain a single full FoV image. All the methods presented in this section entail an increase in SAR. However, SAR did not prove a limitation for the work presented here, even at field strength of 4.7 T where more RF power is required than at lower field strength. For TRAIL and ROCS the reduction in SNR associated with this process is $\sqrt{2}$, and is uniform across the image FoV. The reduction in SNR for TWIST is greater and is non-uniform lying between 2 and $2\sqrt{2}$ across the image FoV. For 2DFT image acquisitions the advantage of imaging with a reduced FoV would be a decrease in

scan time. For this advantage to be realised a lengthy prescan must be avoided. Further work is needed to determine if the techniques can be performed reliably without the need for a prescan. TRAIL and ROCS are more sensitive to RF non-uniformity because they tend to rely on an accurate sinusoidal magnetisation profile being created.

The main aim of the methods presented in this section was to improve GE-EPI image quality, which is made worse at higher field strengths due to increased susceptibility related problems. TRAIL, ROCS and TWIST (like Common SENSE) are all methods that require longer total acquisition times. This is less important at higher field strength; shorter echo times are normally used and so two readout periods in rapid succession may be performed while still allowing a high number of slices to be obtained per TR time. Both of these factors suggest that all the methods presented in this chapter are most likely to find application at high (>1.5T) field strength.

TWIST and ROCS both reduce the levels of distortion and blurring seen in an image; TRAIL does not improve the distortion or blurring significantly in the implementation presented here. TRAIL can be used to correct for distortion [33] or can be used to readout two k-space lines per gradient reversal [37]. TWIST has an advantage over the other techniques due to the reduction of dropout from through slice spin dephasing, but it also has the worst SNR performance.

It is also noted that, for TWIST, when there is a non-uniform spin density across the thickness of each slice it will correspond to a local change of the sensitivity functions. This is an extra consideration for accurate sensitivity mapping and subsequent correct reconstruction of the images.

6.7 Conclusions

Methods have been presented for reducing effective readout times through the consecutive generation of two images. Two half FoV images are acquired consecutively with the same contrast and complimentary sensitivity profiles. Unaliased images may then be created using processing methods from SENSE. The sensitivity profiles can be easily manipulated for best SNR performance. The minimum SNR penalty is $\sqrt{2}$ and is uniform across FoV independent of coil or slice orientation. No special hardware is required and quadrature signal detection is preserved.

The main application of these methods is to GE-EPI at high field strengths (>1.5T). Common SENSE and TWIST should be a useful means for significantly reducing blurring and distortion in EPI images, with little artefact, since recombination is performed in image space. TWIST also improves dropout from through slice dephasing, but this advantage is offset by worse SNR performance. Common SENSE and TWIST may be used in conjunction with partial Fourier and parallel imaging techniques to further increase the performance of GE-EPI.

Two modes of operation for Common SENSE have been described. For use with EPI, the low frequency variant of Common SENSE should provide greater robustness to movement and B_1 inhomogeneity. However, the strength of the Common SENSE (and TRAIL) pulse sequence is that any frequency of sensitivity modulation can be easily imposed across the object. This allows the use of the same pulse sequence to perform prescans for sensitivity mapping, distortion corrections, B_1 uniformity corrections and image acquisitions that are tailored to the subject and protocol. It is hoped that, in

certain situations, Common SENSE will also improve the performance of parallel imaging by augmenting SENSE array coils sensitivity functions.

6.8 References

1. Turner, R. & Ordidge, R. J. 2000, "Technical challenges of functional magnetic resonance imaging", *IEEE Eng Med Biol.Mag.*, vol. 19, no. 5, pp. 42-54.

2. Ogawa, S., Lee, T. M., Nayak, A. S., & Glynn, P. 1990, "Oxygenation sensitive contrast in magnetic resonance images of rodent brain at high magnetic fields", *Magnetic Resonance In Medicine*, vol. 14, pp. 68-78.

3. Ogawa, S., Lee, T. M., Kay, A. R., & Tank, D. W. 1990, "Brain magnetic resonance imaging with contrast dependent on blood oxygenation", *Proceedings Of The National Academy Of Sciences Of The United States Of America*, vol. 87, pp. 9868-9872.

4. Schmitt, F., Stehling, M. K., & Turner, R. 1998, *Echo-planar imaging* Heidelberg: Springer-Verlag, Berlin.

5. Fischer, H. & Ladebeck, R. 1998, "Echo-Planar Imaging Image Artefacts," in *Echo-planar imaging*, F. Schmitt, M. K. Stehling, & R. Turner, eds., pp. 180-200.

6. Wielopolski, P. A., Schmitt, F., & Stehling, M. K. 1998, "Echo-Planar Pulse Sequences," in *Echo-planar imaging*, F. Schmitt, M. K. Stehling, & R. Turner, eds., pp. 65-134.

7. Feinberg, D. A., Hale, J. D., Watts, J. C., Kaufman, L., & Mark, A. 1986, "Halving MR imaging time by conjugation: demonstration at 3.5 kg.", *Radiology*, vol. 161, pp. 527-531.

8. Pruessmann, K. P., Weiger, M., Scheidegger, M. B., & Boesiger, P. 1999, "SENSE: sensitivity encoding for fast MRI", *Magnetic Resonance In Medicine*, vol. 42, no. 5, pp. 952-962.

9. Weiger, M., Pruessmann, K. P., Osterbauer, R., Bornert, P., Boesiger, P., & Jezzard, P. 2002, "Sensitivity-encoded single-shot spiral imaging for reduced susceptibility artefacts in BOLD fMRI", *Magn Reson.Med.*, vol. 48, no. 5, pp. 860-866.

10. Preibisch, C., Pilatus, U., Bunke, J., Hoogenraad, F., Zanella, F., & Lanfermann, H. 2003, "Functional MRI using sensitivity-encoded echo planar imaging (SENSE-EPI)", *Neuroimage.*, vol. 19, no. 2 Pt 1, pp. 412-421.

11. Golay, X., Pruessmann, K. P., Weiger, M., Crelier, G. R., Folkers, P. J. M., Kollias, S. S., & Boesiger, P. 2000, "PRESTO-SENSE: an ultrafast whole-brain fMRI technique", *Magnetic Resonance In Medicine*, vol. 43, pp. 779-786.

12. Alley, M. T., Pauly, J. M., Sommer, F. G., & Pelc, N. J. 1997, "Angiographic imaging with 2D RF pulses", *Magn Reson.Med*, vol. 37, no. 2, pp. 260-267.

13. Paschal, C. B., Haacke, E. M., Adler, L. P., & Finelli, D. A. 1992, "Magnetic resonance coronary artery imaging", *Cardiovasc.Intervent.Radiol.*, vol. 15, no. 1, pp. 23-31.

14. Paley, M. N., Lee, K. J., Wild, J. M., Whitby, E. H., & Griffiths, P. D. 2002, "Interleaved pulsed MAMBA: a new parallel slice imaging method", *Magn Reson.Med.*, vol. 48, no. 6, pp. 1043-1050.

15. Lee, K. J., Paley, M. N., Wilkinson, I. D., & Griffiths, P. D. 2002, "Fast two-dimensional MR imaging by multiple acquisition with micro B(0) array (MAMBA)", *Magn Reson.Imaging*, vol. 20, no. 1, pp. 119-125.

16. Priest, A. N., Carmichael, D. W., and Ordidge, R. J. 2002, "TRAIL (Two Reduced Acquisitions InterLeaved)", *Proc.10th Meeting of the Society of Magnetic Resonance*, abs. 2381.

17. Priest, A. N., Carmichael, D. W., De Vita, E., & Ordidge, R. J. 2003, "A method which spatially interleaves two images to halve EPI readout times: TRAIL (Two Reduced Acquisitions InterLeaved)", *Magnetic Resonance In Medicine*, vol. submitted, p. na.

18. Sattin, W., Mareci, T. H., & Scott, K. N. 1985, "Exploiting the stimulated echo in nuclear magnetic resonance imaging. I. Method", *Journal Of Magnetic Resonance*, vol. 64, pp. 177-182.

19. Sattin, W., Mareci, T. H., & Scott, K. N. 1985, "Exploiting the stimulated echo in nuclear magnetic resonance imaging. II. Applications", *Journal Of Magnetic Resonance*, vol. 65, pp. 298-307.

20. Frahm, J., Merboldt, K.-D., Hanicke, W., & Haase, A. 1985, "Stimulated echo imaging", *Journal Of Magnetic Resonance* , vol. 64, pp. 81-93.

21. Franconi, F. & Akoka, S. 1995, "Chemical shift imaging from simultaneous acquisition of a primary and a stimulated echo", *Magn Reson.Med.*, vol. 33, no. 5, pp. 683-688.

22. Ropele, S., Stollberger, R., Kapeller, P., Hartung, H.-P., & Fazekas, F. 1999, "Fast multislice T_1 and T_{1sat} imaging using a phase acquisition of composite echoes (PACE) technique", *Magnetic Resonance In Medicine*, vol. 42, pp. 1089-1097.

23. Sotak, C. H. & Li, L. 1992, "MR imaging of anisotropic and restricted diffusion by simultaneous use of spin and stimulated echoes", *Magnetic Resonance In Medicine*, vol. 26, pp. 174-183.

24. Franconi, F., Lethimonnier, F., Sonier, C. B., Pourcelot, L., & Akoka, S. 1997, "Diffusion Imaging with a multi-echo MISSTEC sequence", *Journal of Magnetic Resonance Imaging*, vol. 7, pp. 399-404.

25. Lethimonnier, F., Franconi, F., & Akoka, S. 1997, "Three-point Dixon method with a MISSTEC sequence", *MAGMA.*, vol. 5, no. 4, pp. 285-288.

26. Franconi, F., Sonier, C. B., Seguin, F., Le Pape, A., & Akoka, S. 1994, "Acquisition of spin echo and stimulated echo by a single sequence: application to MRI of diffusion", *Magn Reson.Imaging*, vol. 12, no. 4, pp. 605-611.

27. Chen, C.-N. and Wyrwicz, A. M. 2000, "Single Shot and Segmented Ghost Artefacts Removal with 2-D Phase Correction", *Proc.Eighth Annual Meeting of ISMRM.*

28. Thomas, D. L., De Vita, E., Priest, A. N., Turner, R., and Ordidge, R. J. 2003, "Reducing motion-related artefacts caused by 2D phase correction in time course EPI of the human brain at 4.7 T", *Proc.12th Annual Meeting of ISMRM*, abs. 1026.

29. McKenzie, C. A., Yeh, E. N., Ohliger, M. A., Price, M. D., & Sodickson, D. K. 2002, "Self-calibrating parallel imaging with automatic coil sensitivity extraction", *Magn Reson.Med*, vol. 47, no. 3, pp. 529-538.

30. Jakob, P. M., Griswold, M. A., Edelman, R. R., & Sodickson, D. K. 1998, "AUTO-SMASH: a self-calibrating technique for SMASH imaging. SiMultaneous Acquisition of Spatial Harmonics", *MAGMA*, vol. 7, no. 1, pp. 42-54.

31. Hennig, J., Nauerth, A., & Friedburg, H. 1986, "RARE imaging: a fast imaging method for clinical MR", *Magnetic Resonance In Medicine*, vol. 3, pp. 823-833.

32. Kyriakos, W. E., Panych, L. P., Kacher, D. F., Westin, C. F., Bao, S. M., Mulkern, R. V., & Jolesz, F. A. 2000, "Sensitivity profiles from an array of coils for encoding and reconstruction in parallel (SPACE RIP)", *Magnetic Resonance In Medicine*, vol. 44, no. 2, pp. 301-308.

33. Priest, A. N., De Vita, E., Thomas, D. L., and Ordidge, R. J. 2003, "Distortion-free EPI with half the effective readout time using TRAIL", *Proc.11th Meeting of the Society of Magnetic Resonance*, abs. 1021.

34. Priest, A. N., Ordidge, R. J., and Carmichael, D. W. 2002, "TRAIL: a new imaging technique and its use with EPI", *Proc.6th Meeting of the British Chapter of ISMRM*, abs. 75.

35. Weiger, M., Pruessmann, K. P., Leussler, C., Roschmann, P., & Boesiger, P. 2001, "Specific coil design for SENSE: a six-element cardiac array", *Magnetic Resonance In Medicine*, vol. 45, no. 3, pp. 495-504.

36. Larkman, D. J., Hajnal, J. V., Herlihy, A. H., Coutts, G. A., Young, I. R., & Ehnholm, G. 2001, "Use of multicoil arrays for separation of signal from multiple slices simultaneously excited", *Journal of Magnetic Resonance Imaging*, vol. 13, no. 2, pp. 313-317.

37. Priest, A. N., De Vita, E., Thomas, D. L., and Ordidge, R. J. 2003, "Doubling EPI resolution with two k-space lines per gradient reversal", *Proc.11th Meeting of the Society of Magnetic Resonance*, abs. 0987.

7. Thesis Conclusions

In this section a brief summary of the important conclusions from this work are presented. These conclusions are discussed with reference to future work arising form the ideas presented here. The four main projects presented in each chapter of this thesis can be separated into two parts.

Firstly, there is SPENT and its application to bone imaging. In this section SPENT is discussed as a technique to obtain a global measure of structure. The future for its application in the assessment of bone is discussed. Furthermore, if SPENT can be useful for investigating bone can it be used in other applications?

Secondly, the use of the 4-coil array on the 4.7 T system is discussed with regard to the most beneficial applications, and further development. The array coil can be used to speed up imaging using SENSE [1] (or other related parallel imaging methods). The applications that would benefit from SENSE are summarised. One application of SENSE is to reduce the length of the GE-EPI readout. This is also the aim of Common SENSE, TRAIL and TWIST. The relative merits of these methods for the purpose of improving GE-EPI at high field strength are discussed.

7.1 SPENT and its Application to Imaging Bone

SPENT did not increase the ability to resolve individual structures and does not fundamentally increase the information gathered per unit time (i.e. the time taken to traverse k-space is not reduced and the SNR of the information gathered is the same). However, SPENT images do give some structural information about an object that would normally be displayed in an image of 3 times the resolution. Hence, if SPENT images can provide useful structural information about a sample, particularly in a single orientation relative to the structure, then a reduced area of k-space can be targeted. The subject for the next section is what structural information is being obtained - particularly in bone?

7.1.1 The Contrast Produced by SPENT

SPENT was found to give a signal that was dependent on the level of uniformity of magnetisation within a voxel. The level of uniformity in different directions could thus be investigated. While there appeared to be little benefit form performing SPENT to resolve individual structures, the global signal intensity produced by the SPENT images was thought to relate to the structure of an object in some way. By dividing SPENT images by the same resolution 'standard' image a Normalised SPENT (N-SPENT) image was obtained.

Simulations in section 3.4.1, showed that there was a non-linear relationship between the global N-SPENT signal and both the size and density of 'holes' placed in a uniform object. The exact correspondence between the structure and the N-SPENT signal was not clear. In contrast, for the bone samples, the N-SPENT signal gave a very high correlation to the BMD even when measured in a single direction. The N-SPENT global

signal is unlikely to be directly measuring BMD so further analysis is required to identify exactly what the N-SPENT global signal represents. Further simulation using different structures in the object should provide the answer to this question. Of particular interest would be to use the same amount of structure and change the level of order. This should simulate an object with the same density but different architecture. In addition, simulating a structure that is a closer correlate to bone should help to bring a greater understanding of what exactly has been measured.

7.1.2 Further Applications of SPENT

SPENT can be viewed in two ways. Firstly, (as discussed previously) it is a method to gain some measure of structure. This was found to be most useful as a global N-SPENT value; a measure of how homogeneous the pixel's magnetisation is on average in a certain direction. With improved understanding of exactly what the N-SPENT signal correlates to, a better idea will be gained of what additional structure or tissue SPENT may be useful for investigating. It seems likely that tissue such as bone that contain strong ordered structure, with two quite different tissue types (in terms of MR contrast), may also find application for SPENT.

SPENT may also be viewed in terms of k-space coverage. SPENT uses different k-space 'tiles' (see figure 3.4). If structural information is contained within a certain k-space region then SPENT is a way to target less of k-space. Interestingly, in highly ordered structure, such as a striped object, with stripes that are around the width of a pixel (somewhat like the imposed modulation deliberately created for TRAIL / ROCS in figure 6.12) more signal can be found further from the centre of k-space. If more 'phase wraps' are applied to the signal before image acquisition (i.e. a larger gradient

applied in figure 3.2 to put multiple phase wraps across each pixel as opposed to just one in figure 3.3) then a tile further from the centre of k-space will be obtained with a narrower width. This approach could target even smaller k-space regions containing the structural information desired, or alternatively, a larger region of k-space could be reconstructed in different sized tiles to attempt to extract more specific information.

One additional way to develop this work is to examine different ways to display the directional information obtained, especially by using 3D data sets that may be divided into separate 'cubes' (see section 4.3.4.2, particularly figure 4.4). This produces a value for the level of homogeneity in each direction and could be displayed as a 'tensor', somewhat like a diffusion tensors [2,3]. It is not known if this would yield additional information, particularly in anisotropic structure such as bone.

7.1.3 MRI Methods to Measure Bone Strength In Vivo

The global N-SPENT signal correlated very highly to BMD using a multislice spin echo sequence (1mm slice thickness 0.3125micron in-plane resolution). The global N-SPENT signal level should be able to be measured using receiver coils with non-uniform sensitivities and using relatively low resolution multislice slice images. These factors provide strong encouragement that the results found here using samples, a relatively uniform receiver coil and a field strength of 7 T, should be repeatable in vivo at clinical field strengths (~1.5T). R_2' has already been used to obtain an MR measure of bone strength [4,5] and in combination these parameters could give a better measure of bone status than BMD area measured by DEXA. As a result of the work presented here a grant application will be made to perform in vivo measurements of N-SPENT and R_2' using MRI, and BMD using DEXA, to study the prevalence of fracture.

7.2 Using the 4-element Array Coil: High Resolution Imaging

A 4-element array coil for use on the head at 4.7 T was evaluated in chapter 5. The array coil provided improved SNR over much of the head in comparison to a 28cm head birdcage coil. This allowed the acquisition of images with improved resolution using an FSE sequence developed by the group [6,7]. A clear application for the array coil is high resolution structural imaging of the brain. The in-plane resolution achieved was 0.35mm with a 2mm slice thickness and 17 slices in 5mins 40s. The high SNR that is apparent from visual inspection of these images (see figures 5.17-5.19) indicates a higher in-plane resolution or a smaller slice thickness could be used while maintaining an acceptable SNR throughout the image. Even higher resolution may be obtained in peripheral brain regions where work to examine cortical structure is currently being undertaken.

There are two main problems associated with images at this resolution that both occur from subject motion during the image acquisition. Firstly, it is likely that some blurring of image detail may occur from slight movements (tenths of a millimetre). In addition, gross movement of the subject during the scan, which may only be for a very short period before returning to approximately the same position, can result in severe ghosting image artefacts. Further development of high resolution imaging using the array coil will focus on these issues. The extra data obtained by coil arrays has been used for a number of related purposes. It may provide its own navigators echoes to determine if a line of k-space data has been corrupted [8], or be used to correct for motion [9]. The data that is defined as being corrupted may be regenerated using SENSE or SMASH reconstruction methods to reduce motion related artefacts. There

has also been some initial work towards determining and correcting for the motion that has occurred [10].

One further problem of image quality that is present in the FSE images is the ghosting created from the PSF of the FSE technique. To prevent large side lobes of the PSF creating blurring of signal from nearby voxels a technique called 'feathering' was used [7]. This moves strong side lobes of the PSF to the edge of an object. However this requires a wide FoV to be used so that the additional signal from the PSF lies outside the object. Array coils have been used to remove ghosting [11]. It should be possible to use the different array coil images to remove this artefact.

7.3 SENSE and Common SENSE with a TWIST

7.3.1 Using SENSE to Speed up Data Acquisition

The array coil can be used to speed up imaging. However, this always comes at a cost in SNR that has a minimum value of the square root of the speed up factor. Thus, it is important to identify those techniques that would benefit from using SENSE and those that, instead, demand the array to be used with the highest possible SNR. Standard spectroscopy methods such as PRESS [12,13] do not use Fourier encoding for spatial localisation. This means that SENSE cannot be used to 'speed up' the acquisition. However, the array coil can allow significant gains in SNR especially in voxels positioned in peripheral brain regions. A free choice of voxel position is also maintained, unlike a single surface coil that is limited by its localised sensitivity. Spectroscopic imaging (or Chemical Shift Imaging CSI as it is also known) [14] often uses two phase encoding directions to encode spatial position of spectra. Due to the long readout length and low concentrations of the metabolites of interest, a low spatial

resolution is typically obtained. The PSF associated with limited k-space coverage spreads far (spatially) across the image resulting in blurring of information. By applying SENSE in 2D a significant increase in the spatial resolution of the data could be obtained in the same total time. This would improve the PSF of the spectra. If an increase in SNR was required images from the different pixels could be averaged. This would still result in better spatial definition of the information when compared to a lower resolution acquisition of the same length. 2D SENSE with a speed up factor of 1.5-2 in each direction was demonstrated to be efficiently performed by the 4-coil array. Hence, the use of the array coil with SENSE is expected to improve the performance of CSI.

SENSE in 2D is also envisaged for improving the speed of 3D structural sequences such as 3D FLASH. There may be other circumstances when other structural sequences may be improved by using SENSE, because it enables a reduction in scan time, for example when patients cannot keep still for extended periods. The final goal for using the array coil for parallel imaging is to improve the image quality of GE-EPI at high field strength. This is to maximise the benefit of BOLD contrast increases found at high field for fMRI experiments [15,16] and will be discussed in the next section.

7.3.2 Methods to Improve GE-EPI

Increased levels of distortion, blurring and dropout are suffered at higher fields due to increased magnetic susceptibility gradients [17], and correspondingly, faster T_2* decay. All of the methods presented in this section are designed to decrease the effective readout time. Various methods to achieve this goal are presented with a qualitative assessment based on the literature [1,18] in table 7.1 below. It is noted that table 7.1

does not contain every method, or indeed, different implementations of these techniques to try to circumvent their limitations.

Method	Standard 1 shot	45/90 Fleet/Mesh	2-shot segmented	Partial Fourier	SENSE at speed up factor 2 along PE axis
Distortion (a.u.)	1	½	½	1	½
Blurring (standard / improved)	standard	improved	improved	may be slightly improved in some circumstances	improved
Ghosting (standard / worse / poor)	standard	poor	worse	worse	standard
Dropout (standard / improved)	standard	standard	standard	standard	standard
SNR (a.u.)	1	$1/\sqrt{2}$	1	$\sim 1/\sqrt{2}$	$1/\sqrt{2}$ (for most slice geometries)
Hardware	standard	standard	standard	standard	RF coil array and multiple receive channels
Temporal Res.(a.u)	1	1	2	1	1
Volume coverage (improved \ standard \ reduced)	standard	reduced (amount is TE dependent)	slightly improved	slightly improved	slightly improved
Motion sensitivity (standard / worse	standard	standard	worse	standard	standard

Table 7.1 Qualitative summary for various methods to reduce blurring and distortion in GE-EPI images

In table 7.1, various methods are presented for reducing the effective duration of the GE-EPI readout. To reduce distortion and dropout when compared to standard EPI, without decreased temporal resolution or increased ghosting, SENSE appears to be the only method available. SENSE entails the use of new hardware, a reduction in SNR of $\sqrt{2}$ (compared to an image using the same hardware with no speed up i.e. R=1) although this is increased for certain slice geometries. SENSE is generally limited to a reduction

in readout duration of 2-2.5 for its application in the phase encoding direction (there are no clear advantages from its employment in the readout direction).

Method	Common SENSE (low frequency)	Common SENSE (ROCS)	TRAIL (for the implementation described here)	TWIST
Distortion (a.u.)	½	½	1	½
Blurring (a.u.)	improved	improved	improved	improved
Ghosting (standard / worse / poor)	standard	standard	standard	standard
Dropout (standard / improved)	standard	standard	standard	improved
SNR (a.u.)	$1/\sqrt{2}$	$1/\sqrt{2}$	$1/\sqrt{2}$	~$2-2\sqrt{2}$
Hardware	standard	standard	standard	standard
Temporal Res.(a.u)	1	1	1	1
Volume coverage (improved \ standard \ reduced)	reduced (amount is TE dependent)	reduced (amount is TE dependent)	reduced (amount is TE dependent)	reduced (amount is TE dependent)
Motion sensitivity (standard / worse	standard	standard	standard	may be worse due to 'sensitivity' dependence on spin density

Table 7.2 Qualitative summary for new methods presented in chapter 6 to reduce blurring and distortion in GE-EPI images

In table 7.2 the methods developed in chapter 6 are summarised. Unlike the single-shot segmented sequences in Table 7.1 all of these methods should be robust to ghosting because the data is reconstructed in image space rather than k-space. In addition none of the methods in Table 7.2 require new hardware. Both Common SENSE and TWIST improve distortion and blurring, but they also maintain temporal resolution and have reasonable volume coverage at short TE times. Common SENSE has an SNR penalty of $\sqrt{2}$ (the same as SENSE) independent of slice geometry (unlike SENSE). However, different RF coils are normally used for SENSE and a direct, general comparison between the techniques is difficult. With the exception of worse SNR that varies between $2-2\sqrt{2}$, the performance of TWIST is similar to Common SENSE. However, TWIST is the only method to reduce dropout as well as distortion and blurring due to

the smaller effective slice thickness that it uses. Additionally, TWIST may suffer from either worse 'ghosting' if through slice spin density non-uniformity is not taken into account. Alternatively, motion sensitivity is introduced if the through slice spin density non-uniformity is introduced into the 'sensitivity maps'. Further work is required to determine if significant extra motion sensitivity or ghosting is introduced by through slice variation in spin density for TWIST.

Both Common SENSE and TWIST should have advantages (discussed above), particularly in certain situations. Thus, they should be regarded as additional methods to compliment those displayed in table 7.1 that require further investigation. There are many situations where Common SENSE could be used in addition to SENSE. SENSE coils are generally designed for imaging with a certain FoV and normally perform better in certain slice orientations. Common SENSE should be able to provide additional flexibility for choice of these parameters, or, provide a greater reduction in the effective readout time. TWIST is likely to be useful in providing similar gains in image distortion and blurring in applications where dropout is a particular problem, rendering the decrease in SNR an acceptable penalty.

TRAIL has been used to map B_1 and B_0 (for subsequent distortion correction) [19,20], to obtain two k-space lines per gradient reversal [21], and has been submitted for publication [19]. Common SENSE and TRAIL have been patented [22], additionally, papers are being prepared on both Common SENSE and TWIST.

All of the methods presented here need to be validated in future work using fMRI experiments at high field strength, where they are most likely to be employed.

7.4 References

1. Pruessmann, K. P., Weiger, M., Scheidegger, M. B., & Boesiger, P. 1999, "SENSE: sensitivity encoding for fast MRI", *Magnetic Resonance In Medicine*, vol. 42, no. 5, pp. 952-962.

2. Basser, P. J., Mattiello, D., & Le Bihan, D. 1994, "MR diffusion tensor spectroscopy and imaging", *Biophysical Journal*, vol. 66, pp. 259-267.

3. Basser, P. J., Mattiello, J., & Le Bihan, D. 1995, "Anisotropic diffusion: MR diffusion tensor imaging," in *Diffusion and Perfusion Magnetic Resonance Imaging: Applications to functional MRI*, 1st edn, D. Le Bihan, ed., Raven Press, New York, pp. 140-149.

4. Wehrli, F. W., Hopkins, J. A., Hwang, S. N., Song, H. K., Snyder, P. J., & Haddad, J. G. 2000, "Cross-sectional study of osteopenia with quantitative MR imaging and bone densitometry", *Radiology*, vol. 217, no. 2, pp. 527-538.

5. Kang, C., Paley, M., Ordidge, R., & Speller, R. 1999, "In vivo MRI measurements of bone quality in the calcaneus: a comparison with DXA and ultrasound", *Osteoporos.Int.*, vol. 9, no. 1, pp. 65-74.

6. De Vita, E., Thomas, D. L., Roberts, S., Parkes, H. G., Turner, R., Kinchesh, P., Shmueli, K., Yousry, T. A., & Ordidge, R. J. 2003, "High resolution MRI of the brain at 4.7 Tesla using fast spin echo imaging", *Br.J.Radiol.*, vol. 76, no. 909, pp. 631-637.

7. Thomas, D. L., De Vita, E., Roberts, S., Turner, R., Yousry, T. A., and Ordidge, R. J. "High Resolution Imaging of the human Brain at 4.7T: Implementation and Sequence Characteristics", *Magn Reson.Med*, submitted 2003

8. Bydder, M., Atkinson, D., Larkman, D. J., Hill, D. L., & Hajnal, J. V. 2003, "SMASH navigators", *Magn Reson.Med*, vol. 49, no. 3, pp. 493-500.

9. Bydder, M., Larkman, D. J., & Hajnal, J. V. 2002, "Detection and elimination of motion artefacts by regeneration of k-space", *Magn Reson.Med*, vol. 47, no. 4, pp. 677-686.

10. Atkinson, D., Batchelor, P. G., Larkman, D. J., Hill, D. L., and Hajnal, J. V. 2003, "Generalised Motion Correction in Parrallel Imaging", *Proc.11th Annual Meeting of ISMRM*, abs. 1063.

11. Kellman, P. & McVeigh, E. R. 2001, "Ghost artifact cancellation using phased array processing", *Magn Reson.Med*, vol. 46, no. 2, pp. 335-343.

12. Bottomley, P. A., Foster, T. H., & Leue, W. M. 1984, "In vivo nuclear magnetic resonance chemical shift imaging by selective irradiation", *Proc.Natl.Acad.Sci.U.S.A*, vol. 81, no. 21, pp. 6856-6860.

13. Akoka, S. 1992, "Localization," J. D. Certaines, W. M. M. J. Bovée, & F. Podo, eds., Oxford : Pergamon.

14. Decorps, M., Dupeyre, R., Remy, C., Le Fur, Y., Devoulon, P., & Bourgeois, D. 1992, "Spectroscopic Imaging," J. D. Certaines, W. M. M. J. Bovée, & F. Podo, eds., Oxford : Pergamon.

15. de Zwart, J. A., van Gelderen, P., Kellman, P., & Duyn, J. H. 2002, "Reduction of gradient acoustic noise in MRI using SENSE-EPI", *Neuroimage.*, vol. 16, no. 4, pp. 1151-1155.

16. Preibisch, C., Pilatus, U., Bunke, J., Hoogenraad, F., Zanella, F., & Lanfermann, H. 2003, "Functional MRI using sensitivity-encoded echo planar imaging (SENSE-EPI)", *Neuroimage.*, vol. 19, no. 2 Pt 1, pp. 412-421.

17. Fischer, H. & Ladebeck, R. 1998, "Echo-Planar Imaging Image Artefacts," in *Echo-planar imaging*, F. Schmitt, M. K. Stehling, & R. Turner, eds., pp. 180-200.

18. Schmitt, F., Stehling, M. K., & Turner, R. 1998, *Echo-planar imaging* Heidelberg: Springer-Verlag, Berlin.

19. Priest, A. N., Carmichael, D. W., De Vita, E., & Ordidge, R. J. 2003, "A method which spatially interleaves two images to halve EPI readout times: TRAIL (Two Reduced Acquisitions InterLeaved)", *Magnetic Resonance In Medicine*, vol. submitted, p. na.

20. Priest, A. N., De Vita, E., Thomas, D. L., and Ordidge, R. J. 2003, "Distortion-free EPI with half the effective readout time using TRAIL", *Proc.11th Meeting of the Society of Magnetic Resonance.*

21. Priest, A. N., De Vita, E., Thomas, D. L., and Ordidge, R. J. 2003, "Doubling EPI resolution with two k-space lines per gradient reversal", *Proc.11th Meeting of the Society of Magnetic Resonance.*

22. Carmichael, D. W., Priest, A. N., & Ordidge, R. J. 2003, *Common SENSE and TRAIL* (patent).